Universität Zürich
Physik-Institut

www.physik.unizh.ch

Wissenschaftlicher Jahresbericht

April 2004 - März 2005

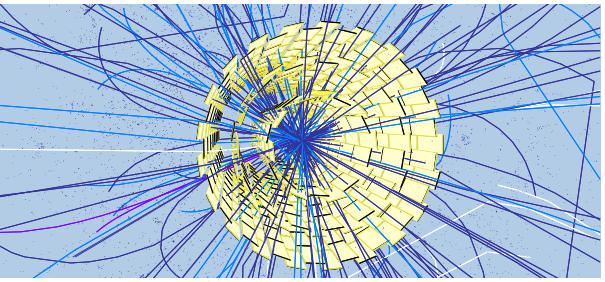
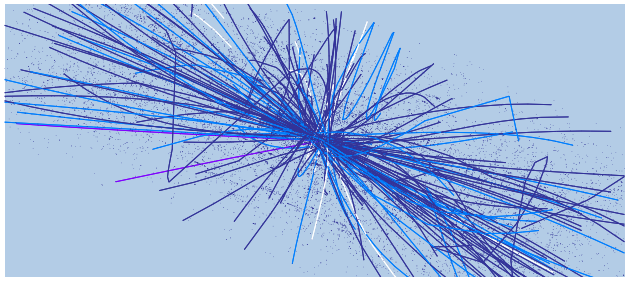
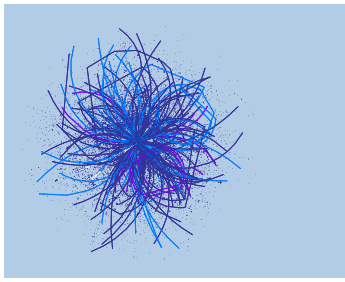

Winterthurerstrasse 190, CH-8057 Zürich/Schweiz

Universität Zürich
Physik-Institut
www.physik.unizh.ch

Wissenschaftlicher Jahresbericht

April 2004 - März 2005

Winterthurerstrasse 190, CH-8057 Zürich/Schweiz

The pictures on the cover page show a simulation of particle trajectories in the CMS detector as they will appear when a B_s meson produced in the collision of two proton-bunches at 14 TeV decays to $J/\psi\,\phi$, among several hundred background tracks. The pixel-detector (diameter of about 20 cm) to which the Physik-Institut is contributing is shown to the left (see Sec. 8 on CMS).

Sekretariat	044 635 5721	secret@physik.unizh.ch
Prof. C. Amsler	044 635 5784 022 767 2914	amsler@cern.ch
Prof. H.-W. Fink	044 635 5801	hwfink@physik.unizh.ch
Prof. H. Keller	044 635 5748	keller@physik.unizh.ch
Prof. P.F. Meier	044 635 4016	pfmeier@physik.unizh.ch
Prof. J. Osterwalder	044 635 5827	osterwal@physik.unizh.ch
Prof. A. Schilling	044 635 5791	schilling@physik.unizh.ch
Prof. U.D. Straumann	044 635 5768	strauman@physik.unizh.ch
Prof. P. Truöl	044 635 5777	truoel@physik.unizh.ch

The annual reports are available on the internet: http://www.physik.unizh.ch/reports.html.

Begleitwort

Mit seinen acht Forschungsgruppen deckt das Physik-Institut ein breites, national und international vernetztes Spektrum experimenteller Forschung ab, das von den Eigenschaften biologischer Makromoleküle bis zu jenen der elementaren Bestandteile des Universums in seiner Frühphase reicht. In den beiden etwa gleich starken Hauptbereichen, Physik der kondensierten Materie und Physik fundamentaler Systeme, finden sich Gruppen in der Bio-, der Oberflächen-, der Festkörper- und der Elementarteilchenphysik. Die Forschungsgruppen am Physik-Institut sind vom Nationalfonds durch 15 Forschungsprojekte und von Beiträgen aus der K. Alex Müller Stiftung und der Gebert-Rüf Stiftung unterstützt worden. Das Physik-Institut ist unter anderem an den Nationalen Forschungskompetenzzentren (NCCR) MaNEP (Materials with Novel Electronic Properties, Profs. H. Keller, A. Schilling) und Nanoscale Science (Impact on life sciences, sustainibility, information and communication technology, Prof. H.-W. Fink) beteiligt und gehört zu den Mitgründern des Swiss Institute of Particle Physics (CHIPP) (Profs. C. Amsler, U. Straumann, P. Truöl).

Einige wichtige Entwicklungen bei den Projekten der *Teilchenphysik* seien hier kurz erwähnt: Da sich die Inbetriebnahme des Large Hadron Colliders am CERN (2007) nähert, wird die Designphase für die Detektorteile, die die *Teilchenphysik-Gruppen* für die Experimente CMS und LHCb entwickeln, bald abgeschlossen sein. Die Konstruktions- und Testphase, die die zur Verfügung stehenden Ressourcen im technischen und personellen Bereich an ihre Grenzen stossen lässt, hat begonnen. Die laufenden Experimente, Antiwasserstofferzeugung (Athena, CERN), Protonstruktur und Quantenchromodynamik im Bereich hoher Energien und Impulsüberträge (H1, Elektron-Proton-Speicherring HERA am DESY) und kleinere Experimente am PSI und in Brookhaven beschäftigen wie bis anhin sowohl mit Datennahme als auch mit Datenanalyse die Gruppen intensiv, wie die Publikationsstatistik ausweist.

Im Forschungsbereich *Physik der kondensierten Materie* sind unter anderem folgende Fortschritte erzielt worden: Die Gruppe *Oberflächenphysik* konnte zum ersten Mal die Impulsverteilung von Elektronen in einer Flüssigkeit bestimmen. Der Gruppe *Physik Biologischer Systeme* ist es gelungen, mit einer neuartigen Methode die Energetik einzelner DNA-Moleküle zu untersuchen. Ein elegantes Modell zur Analyse von Kernspinresonanz-Daten in Kuprat--Supraleitern, welches eine neue Interpretation der antiferromagnetischen Fluktuationen in diesen Systemen zulässt, wurde von der Gruppe *Computer Assistierte Physik* entwickelt.

Im September 2003 wurde das Physik-Institut von einem internationalen Team von Expertinnen und Experten bezüglich Forschung, Lehre und Infrastruktur evaluiert. Der Gesamtbericht der Evaluationsstelle wurde uns im Juli 2004 zur Stellungnahme übergeben und im Februar 2005 mit der Universitätsleitung besprochen. Die Leistungen in Lehre und Forschung wurden als sehr gut und im internationalen Vergleich als überdurchschnittlich gut beurteilt.

Alle Forschungsgruppen profitieren von der exzellenten Unterstützung der mechanischen und elektronischen Werkstätten, sowie des technischen Personals und des Sekretariats. Alle helfen mit, einen reibungslosen Ablauf in Forschung und Lehre auf hohem Niveau zu garantieren.

Nach über 30 Jahren erfolgreicher Tätigkeit ist unser geschätzter Mitarbeiter Bernhard Schmid im März 2005 in den Ruhestand getreten. Von 1974 bis 2002 war Herr Schmid Werkstattchef. Im Jahr 2003 hat er die Leitung seinem langjährigen engen Mitarbeiter Kurt Bösiger übertragen, hat aber weiterhin in der Werkstatt tatkräftig mitgewirkt. Mit seinem engagierten Team hat Herr Schmid über die Jahre unsere mechanische Werkstatt stets erneuert und auf

einen im internationalen Vergleich hohen Standard gebracht. Mit dem Umzug des Physik-Instituts auf den Irchel im Jahre 1993 wurde die Werkstatt unter seiner Leitung wesentlich ausgebaut und von Grund auf modernisiert. Die in der Werkstatt ausgeführten Projekte umfassen ein breites Spektrum: Realisation des neuen Medizinerpraktikums, Bau von komplizierten Kryostaten und komplexen Hochvakuum-Kammern für die Festkörperphysik und Planung und Bau von zentralen Detektorsystemen für Grossprojekte in der Teilchenphysik an den grossen nationalen und internationalen Beschleunigeranlagen, um nur einige Beispiele zu nennen. Die hervorragenden mechanischen Arbeiten unserer Werkstatt geniessen nicht nur bei den Forschenden am Physik-Institut, sonderen auch in den grossen internationalen Kollaborationen in der Teilchenphysik grosse Anerkennung. Auch in der Ausbildung von jungen Leuten hat sich Herr Schmid sehr eingesetzt. Nicht nur 16 Lehrlinge haben über die Jahre in der Werkstatt eine solide Ausbildung genossen und vom fundierten Fachwissen von Herrn Schmid profitiert, sondern auch alle unsere Physik-Studierenden, welche den Werkstattkurs besucht haben. Herr Schmid hat die Werkstatt mit grossem Einsatz geführt und Dank seinem freundlichen Charakter ist es ihm gelungen seine Mitarbeiter immer wieder zu Höchstleistungen anzuspornen. Seine grosse Hilfsbereitschaft, seine Teamfähigkeit und seine zuvorkommende, bescheidene Art im Umgang mit Mitarbeitern und Mitarbeiterinnen, Lehrlingen und Studierenden werden von uns allen sehr geschätzt. Wir wünschen Herrn Schmid alles Gute im wohl verdienten Ruhestand und danken ihm für seinen enormen Einsatz am Physik-Institut.

Die Forschungsprojekte des Physik-Instuts findet man auf den Websites der Forschungsdatenbank der Universität Zürich [1]. Der wissenschaftliche Jahresbericht des Physik-Instituts wurde wie schon in den letzten Jahren in englischer Sprache abgefasst, um unsere Forschungstätigkeit einem internationalen Publikum besser zugänglich zu machen. Der vollständige Jahresbericht wie auch die Jahresberichte früherer Jahre können auf der Website des Physik-Instituts (http://www. physik.unizh.ch/reports.html) eingesehen werden. Eine allgemein verständliche Zusammenfassung (auf Deutsch) der laufenden Forschungsprojekte folgt auf den nächsten Seiten.

Zürich, im Mai

Prof. Dr. Hugo Keller

[1] http://www.research-projects.unizh.ch/math/unit71600/index.htm

Zusammenfassung der Forschungsprojekte

Teilchenphysik

Am CERN wurden 2002 erstmals kalte Antiwasserstoffatome in grossen Mengen hergestellt. Letztes Jahr hat die ATHENA Kollaboration die Produktionsrate auf etwa 100 Antiatome pro Sekunde erhöht und den Erzeugungsmechanismus studiert. Erste Versuche wurden unternommen, die Antiwasserstoffproduktion mit Hilfe eines CO_2 Lasers zu stimulieren.

Mit dem H1-Detektor werden Kollisionen von 27.4 GeV Elektronen oder Positronen mit 920 GeV Protonen studiert. Dabei sind die Struktur des Protons bis zu Distanzen unterhalb eines Attometers aufgeklärt und die durch die Quantenchromodynamik (QCD) beschriebene Wechselwirkung der Quarks (q) und Gluonen (g) erfolgreich untersucht worden. Folgenden Aspekte wurden studiert:

- qg-Dichteverteilungen,
- diffraktiv erzeugte Endzustände,
- Erzeugung schwerer Quarks (c,b: charm, beauty),
- Abhängigkeit der QCD-Kopplungskonstante α_S von Distanz und Impulsübertrag,
- Suche nach exotischen Zuständen ausserhalb des Standard-Modells,
- Pentaquark-Zustände.

Nach 2000 wurden Speicherring und Detektor für höhere Strahlströme aufgerüstet, wofür die Gruppe eine neue fünflagige Vieldrahtproportionalkammer und ein neues Triggersystem gebaut hat. Seit 2003 wird wieder gemessen, wobei jetzt auch polarisierte Elektronen- und Positronenstrahlen zur Verfügung stehen.

Seit 2001 wird am $p\overline{p}$ Beschleuniger TEVATRON in den USA bei einer Schwerpunktsenergie von 2 TeV nach Abweichungen vom Standardmodell gesucht. Die Gruppe konzentriert sich auf die Suche nach dem Prozess $B_s \to \mu^+\mu^-$, wo ein neuer Grenzwert publiziert wurde. Dies stellt ein zentrales Resultat der DØ Kollaboration im Jahre 2004 dar und erlaubt es insbesondere den Parameterbereich von Theorien, die über das Standard Modell hinausgehen, einzuschränken.

Physik der Kondensierten Materie

Neuartige Nanostrukturen in Form von ultradünnen Schichten, Quantendrähten und Nanonetzen werden mit Methoden der Oberflächenphysik kontrolliert hergestellt und charakterisiert. Dabei stehen Methoden der "Self-Assembly" im Vordergrund, wo man Prozesse sucht, durch welche sich solche kleinsten Strukturen spontan ausbilden. Da auf dieser Längenskala Quanteneffekte dominieren, kann man mit Hilfe geeigneter Strukturierung gezielt die elektronischen, magnetischen und katalytischen Eigenschaften von Oberflächen beeinflussen. Im vergangenen Jahr wurde weiter an atomaren Monolagen von Bornitrid und Fullerenmolekülen geforscht. Das im letzten Jahr entdeckte Bornitrid-Nanonetz wurde weiter auf seine Stabilität untersucht, und ob es sich auch auf anderen Metalloberflächen als Rhodium ausbildet. Ein EU-Forschungsprojekt mit neun europäischen Forschungsgruppen wurde zu diesem Thema bewilligt. Leicht schräg geschnittene Kristalle mit regelmässigen atomaren Treppenstufen im Abstand von etwa einem Nanometer eignen sich hervorragend, um lineare Ketten von C_{60} Molekülen herzustellen. Photoemissionspektren von solchen Fullerenketten deuten an, dass diese Molekülketten den elektrischen Strom entlang der Ketten leiten, nicht aber quer dazu.

Zur Erforschung der physikalischen Eigenschaften einzelner biologischer Moleküle dienen die in vergangenen Jahren entwickelten Methoden, wie temperaturabhängige Fluoreszenzmikroskopie zur Untersuchung einzelner DNS Moleküle in Flüssigkeiten, und Holografie mit langsamen Elektronen als neue Methode in der Strukturbiologie und Feldionen-Mikroskopie.
Lithografie mit fokussierten Ionenstrahlen wird zur Strukturierung auf der Nanometer-Skala und zur Verbindung biologischer Systeme mit Silizium-Strukturen verwendet.
Im vergangenen Jahr wurden Experimente zum quantitativen Verständnis der Energetik einzelner DNS Moleküle abgeschlossen. Ferner wurde die Entwicklung eines auf kohärenter Elektronenoptik basierenden Prinzips zur Vermeidung von Strahlenschäden bei der Strukturuntersuchung einzelner Bio-Moleküle abgeschlossen und eine neuartige Punkt-Ionenquelle aus einem Festkörper-Elektrolyten erfunden.

Die Gruppe beschäftigt sich mit der Theorie der Hochtemperatur-Supraleitung und macht dabei von zwei prinzipiell verschiedenen Konzepten Gebrauch. Einerseits versucht sie, basierend auf *ab initio* Berechnungen lokale elektronische Eigenschaften der Kuprate (Feldgradienten, Hyperfeinfelder und chemische Verschiebungen) unter massivem Computereinsatz numerisch zu bestimmen. Andererseits versucht sie auch, Modelle zu finden, welche experimentelle Resultate (insbesondere aus Magnetresonanz- und Neutronenstreu-Experimenten) erklären können. Neueste Erfolge waren unter anderem die Bestimmung der Feldgradienten und Hyperfeinfelder in Zink-dotierten Kupraten und damit die Erklärung der nuklearen Quadrupolspektren der Kupferkerne, die Auffindung eines Modells für die Erklärung der Spin-Gitter-Relaxationszeiten in optimal dotierten, unterdotierten und überdotierten Kupraten und die Erklärung der Inkommensurabilitäten in Neutronenstreuexperimenten.

Mitarbeiter

Wissenschaftliches Personal

Yves	Allkofer	CMS
Prof. Claude	Amsler	ATHENA, CMS
Ralf Patrick	Bernhard	DØ, LHCb
Jan	Becker	H1
Dr. Roland	Bernet	LHCb
Christophe	Bersier	CAP
Louis	Brandenberger	Oberflächenphysik
Dr. Vincenzo	Chiochia	CMS
Claudio	Cirelli	Oberflächenphysik
Martina	Corso	Oberflächenphysik
Raffaele	Dell'Amore	PTM
Dr. Daniele	Di Castro	Supraleitung & Magnetismus
Andrei	Dolocan	Oberflächenphysik
Andrei	Dorokhov	CMS
Dr. Andreas	Engel	PTM
Conrad	Escher	Bio-Physik
Dr. Dmitry	Eshchenko	Supraleitung & Magnetismus
Peter	Fierlinger	UCN
Prof. Hans-Werner	Fink	Bio-Physik
Ilaria	Foresti	H1
Dr. Johannes	Gassner	LHCb
Prof. Thomas	Greber	Oberflächenphysik
Dr. Matthias	Hengsberger	Oberflächenphysik
Stefan	Heule	UCN
Christoph	Hörmann	CMS
Dr. Ian	Johnson	ATHENA
Prof. Hugo	Keller	Supraleitung & Magnetismus
Nicolas	Keller	H1
Dr. Rustem	Khasanov	Supraleitung & Magnetismus
Martin	Klöckner	Oberflächenphysik
Stefan	Kohout	Supraleitung & Magnetismus
Dr. Michael	Krüger	Bio-Physik
Fabio	La Mattina	Supraleitung & Magnetismus
Dr. Jorge	Lobo-Checa	Oberflächenphysik
Christina	Lois Gomez	LHCb
Dr. Tatiana	Latychevskaia	Bio-Physik
Dr. Frank	Lehner	DØ, LHCb
Linus	Lindfeld	H1
Dr. Niels	Madsen	ATHENA
Alexander	Maisuradze	Supraleitung & Magnetismus
Dr. Mihael	Mali	Supraleitung & Magnetismus
Tamas	Mayer	CAP

Wissenschaftliches Personal (cont)

Prof. Peter F.	Meier	CAP
Prof. K. Alex	Müller	Supraleitung & Magnetismus
Dr. Katharina	Müller	H1
Dr. Matthias	Muntwiler	Oberflächenphysik
Dr. Matthew	Needham	LHCb
Dr. Hiroshi	Okamoto	Bio-Physik
Dr. Taichi	Okuda	Oberflächenphysik
Prof. Jürg	Osterwalder	Oberflächenphysik
Kirill	Prokofiev	CMS
Prof. Henk	Pruys	ATHENA, CMS
Dr. Christian	Regenfus	ATHENA, CMS
Mark	Reibelt	PTM
Dr. Samuel	Renold	CAP
Dr. Peter	Robmann	CMS, H1, $\pi \to e\nu$, KOPIO
Armand	Rochat	ATHENA
Dr. Josef	Roos	Supraleitung & Magnetismus
Rosmarie	Rössel	Studienberatung
Dr. Tariel	Sakhelashvili	LHCb, $\pi \to e\nu$
Prof. Andreas	Schilling	PTM
Dr. Richard	Schillinger	Oberflächenphysik
Dr. Stefan	Schmitt	H1
Carsten	Schmitz	H1
Prof. Toni	Schneider	Supraleitung & Magnetismus
Dr. Alexander	Shengelaya	Supraleitung & Magnetismus
Matthew	Siegler	LHCb
Dr. Thomas	Speer	CMS
Dr. Olaf	Steinkamp	LHCb
Dr. Erich	Stoll	CAP
Simon	Strässle	Supraleitung & Magnetismus
Prof. Ulrich	Straumann	H1, LHCb, $\pi \to e\nu$, UCN
Anna	Tamai	Oberflächenphysik
Sandra Pascale	Thomann	Bio-Physik
Prof. Peter	Truöl	H1, $\pi \to e\nu$, KOPIO
Dr. Anne-Christine	Uldry	CAP
Max	Urban	H1
Dr. Andries	van der Schaaf	$\pi \to e\nu$, KOPIO
Simon	Scheu	$\pi \to e\nu$, KOPIO
Achim	Vollhardt	LHCb
Dimitro	Volyanskyy	LHCb
Andreas	Wenger	LHCb
Nicole	Werner	H1
Dr. Stefania	Xella Hansen	H1

Technisches und administratives Personal

Cornel	Andreoli	Bio-Physik
Eva	Baby	Sekretariat
Kurt	Bösiger	Werkstatt
Tiziano	Crudeli	Dokumentation
Walter	Fässler	Dokumentation, Elektronik
Ruth	Halter	Sekretariat
Martin	Klöckner	Supraleitung & Magnetismus, Oberflächenphysik, PTM
Bruno	Lussi	Werkstatt
Reto	Meier	Werkstatt
Hanspeter	Meyer	Elektronik
Lucien	Pauli	Vorlesungsbetrieb
Rolf	Reichen	Werkstatt
Jacky	Rochet	ATHENA, CMS
Marcel	Schaffner	Werkstatt
Jacqueline	Schenk	Sekretariat
Silvio	Scherr	Werkstatt
Bernhard	Schmid	Werkstatt
Jürg	Seiler	Vorlesungsbetrieb
Peter	Soland	Elektronik
Stefan	Steiner	CAD, CMS, LHCb
Karoly	Szeker	Elektronik
Peter	Treier	Werkstatt
Ursula	Wolf	Sekretariat

Contents

1 Production and Spectroscopy of Antihydrogen

C. Amsler, I. Johnson, N. Madsen[2], H. Pruys, C. Regenfus, and J. Rochet

in collaboration with:
CERN, University of Aarhus, Brescia, Genoa, Pavia, RIKEN, Rio de Janeiro, Swansea, Tokyo

(ATHENA Collaboration)

1.1 Introduction

Following the first observation of cold antihydrogen ($\bar{H}$) in 2002 (1), the ATHENA collaboration continued to optimize the antihydrogen formation rate and to study the $\bar{H}$ production mechanisms when low energy antiprotons are merged with dense and cold positron plasma (2)-(5). In this report we summarize the results achieved in 2004. The Zurich group has developed a new technique to measure the Lorentz deflection angle in silicon microstrip detectors (6). We have also performed a feasibility study to measure the gravitational acceleration of antimatter. Two unforeseen obstacles have been encountered by ATHENA for spectroscopy experiments with cold $\bar{H}$: first, antihydrogen appears to be formed before thermalization in the nested Penning trap that we are using. The kinetic energy is then too high to confine the $\bar{H}$ atoms in the inhomogeneous magnetic field of e.g. a quadrupole or mutipole trap. Second, the $\bar{H}$ production mechanism (radiative or three-body combination) is still ambiguous. If three-body combination dominates ($e^+e^+\bar{p} \rightarrow \bar{H}e^+$) then 1s - 2s spectroscopy is not straightforward, since this mechanism populates the high Rydberg states of the $\bar{H}$ atom. Ways are in sight to solve these issues, but this will require significant time and R & D efforts.

The ATHENA positron-antiproton mixing trap comprises a series of hollow cylinders at 15 K generating the axial (z) potential configuration of a nested Penning trap. The radial confinement is provided by a 3 T axial magnetic field. The detector for $\bar{p}$ and e^+ annihilation built by the Zurich group (7) surrounds the mixing trap. It consists of two cylindrical layers of double-sided silicon strip detectors (radii of 4 cm and 5 cm) to register the charged annihilation pions and to reconstruct the annihilation vertex. Each layer contains 16 double-sided modules with active lengths of 16 cm. Antihydrogen is detected by requiring the spatial and temporal coincidence of the vertex with two back-to-back 511 keV γ's produced by the annihilation of the positron. The γ's are detected by a high granularity electromagnetic detector comprising 192 CsI crystals with avalanche photodiode readout. A detailed description of the ATHENA apparatus can be found in ref. (8).

1.2 Measurement of the Lorentz angle

We have measured the Lorentz deflection angle in microstrip sensors operated at a temperature of 130 K in a 3 T magnetic field. This measurement was performed with cosmic ray data and the ATHENA microstrip detector. The detector axis was parallel to the homogeneous 3 T solenoidal magnetic field. Thus the charge drift is perpendicular to the magnetic field.

Due to the propagation of charge carriers along the Lorentz angle, the charge spread at the

[2]Now at the University of Aarhus, Denmark

collection surface is distorted in length and displaced. Impact positions for charged particles are reconstructed with a center of gravity algorithm of charge collected by adjacent strips. Tracks that traverse the silicon parallel to the Lorentz deflection generate the shortest charge spread and have similar charge collection properties to tracks that cross perpendicular to the sensor plane in the absence of magnetic field. A geometric model that relates the track inclination to the average cluster width has been developed to measure the Lorentz angle (6).

Cosmic rays traversing both cylinders were reconstructed from the four 3D points by requiring charged particles to fully traverse both cylinders. The four spatial measurements were fitted with a helix for data with the magnetic field on, and a straight line for data without magnetic field. The Lorentz angle was measured by fitting the model to distributions of the average cluster size as a function of track inclination. The data sample was divided into ϕ and θ intervals (polar and azimuthal angle). Three distributions are shown in Fig. 1.1. As expected, the data taken without magnetic field are symmetric around θ = 0 (perpendicular incidence), while data taken with magnetic field are shifted towards positive values. The model fits are in excellent agreement with the measuered data. These measurements correspond to holes drifting in sensors operated at 130 K in a 3 T magnetic field, and with an average internal electric field of 1.3 kV/cm. The Lorentz angle was found to be 19.6 $^{+1.0}_{-0.6}$ degrees (6).

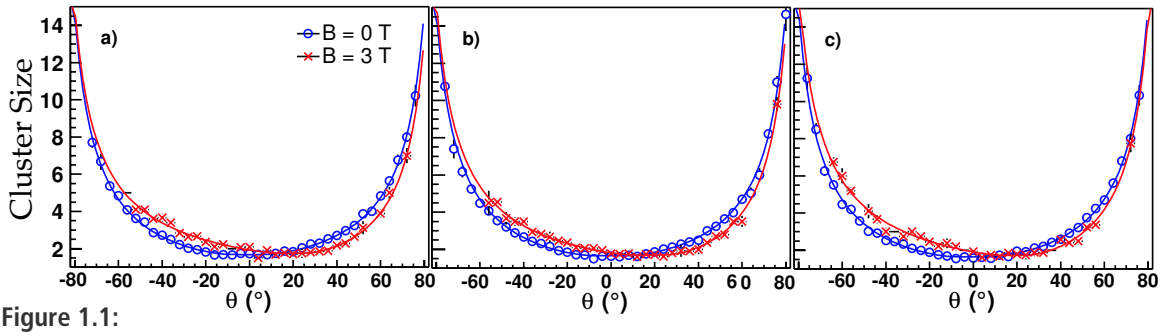

Figure 1.1:
Distribution of the average number of strips vs. inclination angle θ in three intervals of ϕ; around ϕ = -20°(a), 0° (b) and 20° (c) for field–off and field–on. The curves show the model fits.

1.3 $\bar{H}$ production mechanism

Antihydrogen production is carried out by first loading the mixing trap with 7×10^7 e^+ which cool to the ambient temperature of 15 K by the emission of synchrotron radiation, and then by injecting about 10^4 $\bar{p}$ that interact through the Coulomb interaction with the e^+ plasma. We let the antiprotons interact with the positrons for about 180 s before ejecting both species and restarting the cycle. Neutral $\bar{H}$ atoms drift towards the electrodes of the mixing trap where they annihilate.

The two relevant mechanisms for $\bar{H}$ formation are two-body radiative recombination (in which a photon removes the binding energy) and three-body combination (in which a second positron removes the excess energy). The two processes lead to different n-state populations, the former populating mainly the low n states (this is the relevant process for the 1s - 2s laser spectroscopy) and the latter mainly the high n states. The two processes have also different temperature dependences, $T^{-1/2}$ for the former and $T^{-9/2}$ for the latter. We have measured the temperature dependence of $\bar{H}$ formation (3) by changing the positron plasma temperature with a radio-frequency excitation. Neither of the two power laws gives

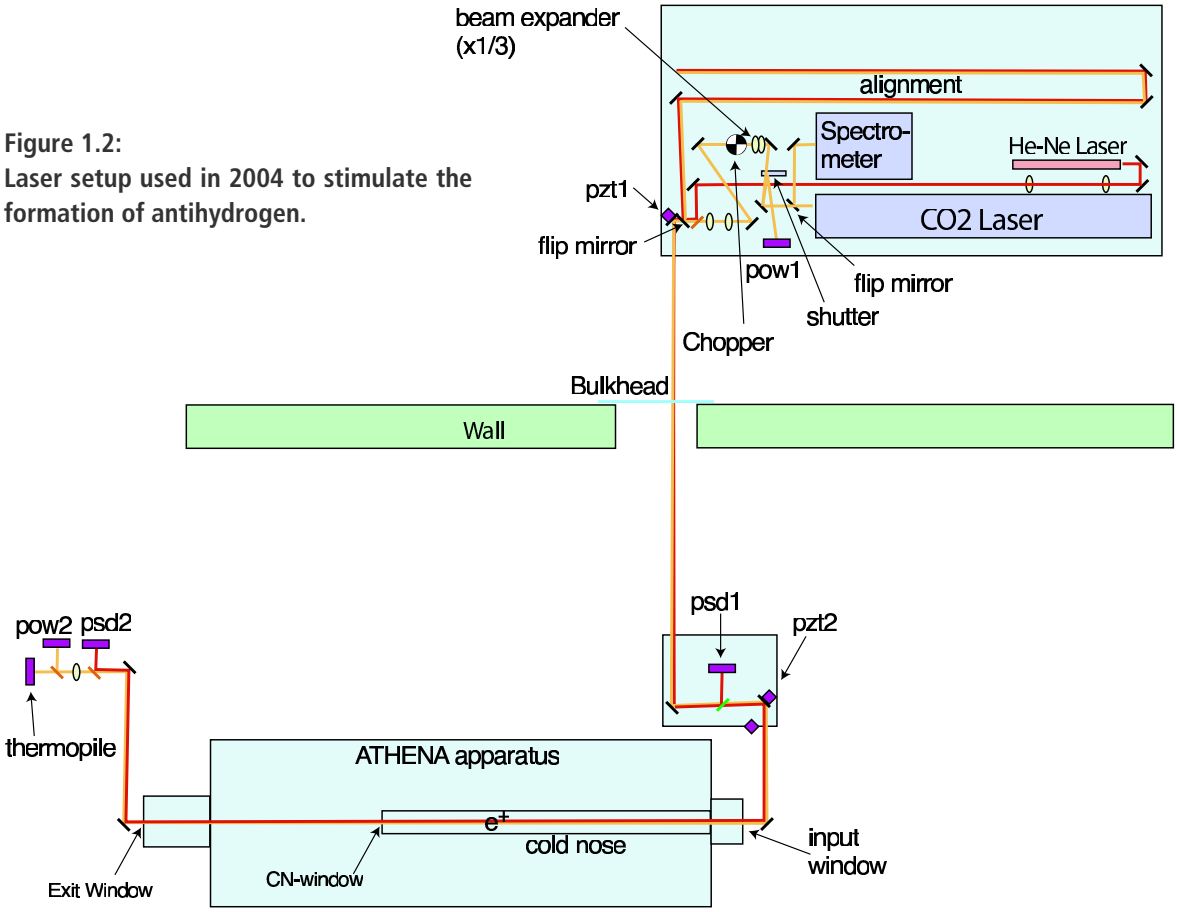

Figure 1.2:
Laser setup used in 2004 to stimulate the formation of antihydrogen.

a good fit to the data, although the $T^{-1/2}$ dependence provides a better description. Since $\bar{H}$ is still produced at room temperature, radiative combination is favored over three-body combination.

However, the observed high antihydrogen production rate (peak rate of 440 $\pm$ 40 Hz (2)) is incompatible with the much smaller rate ($<$ 40 Hz) predicted by the two-body radiative process. In fact, some recent Monte Carlo calculations based on the three-body process (9) are consistent with the observed high rate of antihydrogen production and the fraction of atoms ($\sim$ 15 %) that are sufficiently bound to escape the potential well and annihilate on the trap wall where they are detected.

Hence the cooling dynamics of the antiprotons in the mixing trap remains ambiguous and calls for more sophisticated measurements and calculations. To obtain further information on the recombination mechanism an attempt was made to stimulate radiative combination. We used a CO_2 laser to stimulate the two-body process from the continuum to the n = 11 antihydrogen bound state. The laser system in shown in Fig. 1.2. The laser beam was focused at the center of the positron cloud (beam waist 2σ = 2.0 mm). The wavelength of the laser was tuned by changing the angle of the grating which also served as the high reflecting mirror at one end of the laser cavity. The wavelength could be tuned from 9.5 μm to 11.2 μm. At the optimum wavelength of 10.96 μm the rate of stimulated two-body radiative combination was expected to be 60 Hz, a rate enhancement easily detectable by the Zurich detector. The laser power was 100 W $\cdot$ cm^{-2} and the transmission to the mixing trap 70 %, measured by a laser power meter at the end of the ATHENA main magnet, and directly at the exit of the laser.

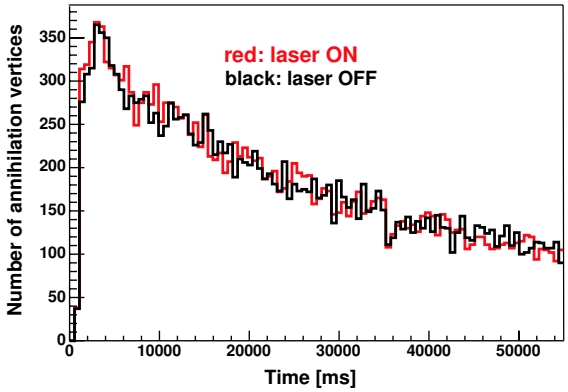

Figure 1.3:
Annihilation rate as a function of time for laser ON and laser OFF.

Figure 1.3 shows the time distribution of annihilation vertices with and without laser stimulation. There is no obvious enhancement, although the data still need to be analyzed in detail. The absence of stimulation favours the three-body recombination mechanism.

1.4 $\bar{H}$ angular distribution

We have shown that about 65 % of all observed annihilations were due to antihydrogen (2). Hence the detection of the two 511 keV γ's that led to the unambiguous observation of antihydrogen in ref. (1) (golden events) but which was inefficient ($\sim 2.5 \times 10^{-3}$) is not really required to study the production mechanism. Hence the spatial distribution of the emerging $\bar{H}$ atoms was studied without γ-coincidence to increase the size of the statistical sample (5). Figure 1.4 shows the vertex distribution along the z axis for all annihilations (a) and for $\bar{p}$ annihilations without e^+ mixing (b). Subtracting (b) from (a) (and applying a cut for the so-called hot spots in the transverse projection (10)) leads to the z distribution of annihilating $\bar{H}$ atoms (Fig. 1.4c). The distribution is in good agreement with the one obtained with the 2γ-coincidence.
Figure 1.5 shows that $\bar{H}$ atoms tend to move preferably along the z axis, although the distribution is not far from isotropy. The distribution is independent of the positron temperature (but the formation rate decreases with

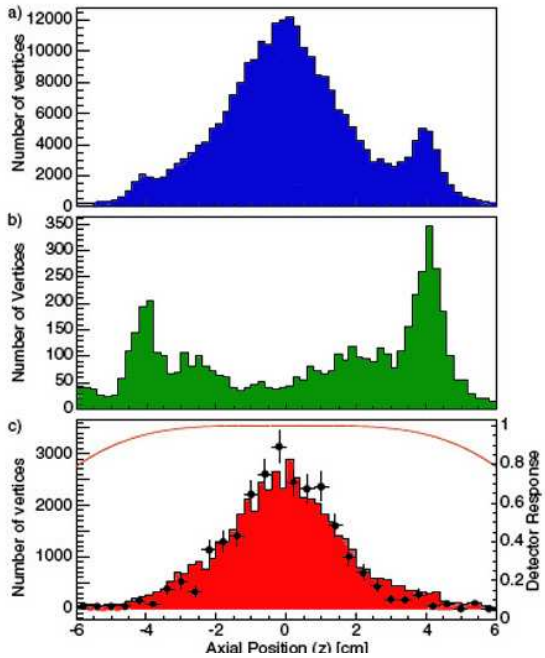

Figure 1.4:
Distribution of annihilations along the trap axis (z) (a) for all vertices during cold mixing (1.75 $\times 10^5$ events) and (b) for $\bar{p}$ annihilating in a nested trap without e^+ (5717 events). The colored area in (c) shows the difference after eliminating hot spots (4.9 $\times 10^4$ events). The full circles show $\bar{H}$ annihilations when two back-to-back 511 keV photons are required in coincidence. The solid line gives the detector acceptance.

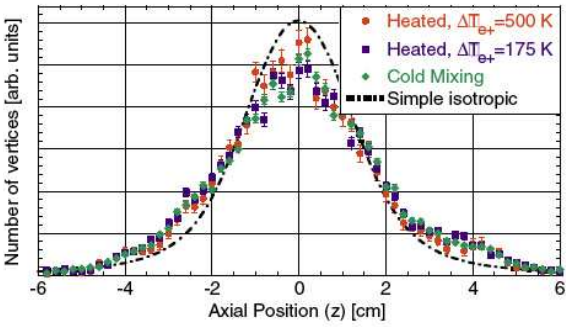

Figure 1.5:
Distribution of antihydrogen annihilation along the trap axis (z) for cold mixing and mixing with positrons heated to two different temperatures. The dot-dashed line is the prediction for isotropic emission from the positron plasma volume. The distributions have been normalized to the same area.

positron temperature). A model has been developed assuming a positron plasma rotating at a frequency of 80 kHz. The plasma was typically 2.5 mm in radius, 32 mm in length, and had a density of 1.7 $\times$ 10^8 cm^{-3}. The data in Fig. 1.5 are consistent with a two-temperature Maxwellian model for the velocities of the produced antihydrogen. In the axial direction the kinetic energy is typically an order of magnitude larger than in the transverse direction. The formation temperature is 150 K in the axial direction if the equilibrium temperature (15 K) is reached in the transverse direction. Hence antihydrogen is *not* produced at thermal equilibrium between the two plasma.

This is bad news for trapping antihydrogen and for performing $\bar{H}$ spectroscopy since typical neutral traps have depths of about 1 K. Therefore very few $\bar{H}$ will be trapped. To produce cold $\bar{H}$ it is thus necessary to have cold antiprotons before mixing with positrons.

1.5 Outlook

A possible solution to confine $\bar{H}$ could be to invert the current mechanism for formation and trap the antiprotons in the center of the nested trap, cooling them first with electrons. This means that the $e^+\bar{p} \rightarrow \bar{H}$ mechanism needs to be studied in a completely new configuration. The presence of the magnetic field gradient needed for the neutral trap also strongly influences the stability of the confinement of the charged particles. One of the major issues is the breaking of the rotational symmetry induced by the presence of the radial magnetic field having values comparable to the axial magnetic field of the charged particle trap.

The conceptual design that we are currently investigating foresees a mixing region that allows the confinement of positrons, antiprotons and the neutral antihydrogen atoms in the same volume. This is achieved by superimposing a trap for charged particle confinement with a trap for antihydrogen, made by a radial multipolar magnetic gradient together with an axial magnetic bottle. This issue is being pursued by our colleagues from Genoa with electrons and protons combining to form hydrogen. A Lyman-α laser with sufficient power for the laser cooling of antihydrogen atoms is being considered by collaborators from Florence.

1.5.1 Antimatter gravity

Assuming CPT symmetry antimatter $\bar{M}$ would fall on an anti-earth with the same acceleration g as matter M on the earth. However, CPT does not make any statement on the acceleration $\bar{g}$ of antimatter by the earth. In quantum field theories (QFT), forces mediated by the exchange of bosons with spin 1 may be repulsive or attractive (such as the γ of QED) while spin 0 and 2 exchanges are attractive. However, a QFT formulation of general relativity with a tensor T (the spin 2 graviton) is inconsistent. Extensions including supersymmetric partners of the graviton lead to vector V (spin 1) and scalar S (spin 0) exchanges. At least partial cancellation of V and S interactions is expected in MM while attractive coherence is predicted for $M\bar{M}$. Therefore antimatter will fall on earth with a larger acceleration than matter. The size of the effect depends on the relative strength between S and V exchanges. Measurements performed with Eötvös-type experiments on MM lead to predictions for the relative difference between g and $\bar{g}$ varying between 10 % and 2×10^{-6}.

We have investigated the feasibility of a pilot experiment with $\bar{H}$ atoms with energies of typically 1 K. For a 1 m flight distance the gravitational sag of a single, horizontally emitted, $\bar{H}$

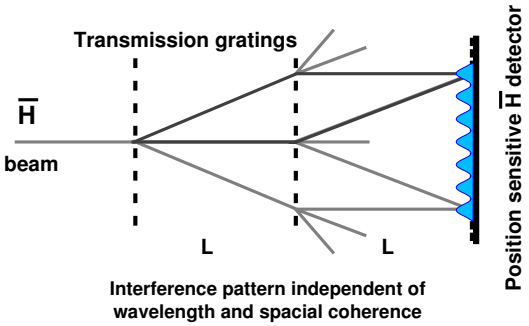

Figure 1.6:
Mach-Zehnder interferometer with two identical transmission gratings and position sensitive $\bar{H}$ detector.

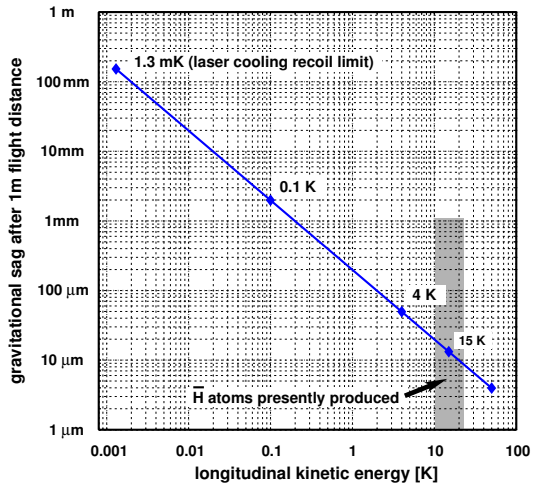

Figure 1.7:
Gravitational sag of $\bar{H}$ atoms in the gravitational field after 1 m flight distance (assuming $\bar{g}$= 9.81 m/s^2).

atom of 1 K kinetic energy could be measured to within a few percent if the emission point, initial flight direction and energy of the atom are known. Better precisions can be reached with $\bar{H}$ atoms with energies below 1 K. A possible experiment coupled to an $\bar{H}$ source would consist of horizontal slits and a position sensitive $\bar{H}$ detector to measure the sag of the interference pattern. The best solution uses a Mach-Zehnder matter wave interferometer consisting of two identical transmission gratings (Fig. 1.6). Such a device was used for measurements of g with cold atoms or neutrons (11). It does not require a monochromatic atomic source since the interference pattern is independent of wavelength. However, the divergence of the beam must be sufficiently small to avoid smearing.

The sag can be determined with high precision by rotating the setup around the beam axis by 90° (slits vertical). The gravitational sag for a distance L = 1 m is shown in Fig 1.7 as a function of temperature. A temperature of 0.5 K (typical for a multipole trap) corresponds to a sag of 400 μm.

We assume that a spatial resolution of 5 μm for the annihilation point on the detector surface can be achieved and plan to use a silicon microstrip detector detecting the $\bar{H}$ annihilations with spatial *and* time-of-flight information. The extraction of the atoms from the neutral trap could be done by either lowering one of the axial magnetic wells or kicking the $\bar{H}$ out with a magnetic pulse. Since the time of flight is in the range of 100 ms, only a moderate resolution on the kick-out time is required.

A proposal to the CERN Committees will be submitted in due time, depending on the results of the R&D efforts mentioned above. The ATHENA project itself was completed in December 2004 with the closure of the antiproton decelerator for at least 18 months.

[1] M. Amoretti *et al.* (ATHENA Collaboration), Nature **419** (2002) 456.
[2] M. Amoretti *et al.* (ATHENA Collaboration), Phys. Lett. **B 578** (2004) 23.
[3] M. Amoretti *et al.* (ATHENA Collaboration), Phys. Lett. **B 583** (2004) 59.
[4] M. Amoretti *et al.* (ATHENA Collaboration), Phys. Lett. **B 590** (2004) 133.
[5] N. Madsen *et al.* (ATHENA Collaboration), Phys. Rev. Lett. **94** (2005) 033403.
[6] I. Johnson *et al.*, Nucl. Instr. and Meth. in Phys. Res. **A 540** (2005) 113.
[7] C. Regenfus, Nucl. Instr. and Meth. in Phys. Res. **A 501** (2003) 65.
[8] M. Amoretti *et al.*, Nucl. Instr. and Meth. in Phys. Res. **A 518** (2004) 679.
[9] F. Robicheaux, Phys. Rev. **A 70** (2004) 022510.
[10] M. Fujiwara *et al.*, Phys. Rev. Lett. **92** (2004) 065005.
[11] M. Gruber *et al.*, Phys. Lett. **A 140** (1989) 363; D. W. Keith *et al.*, Phys. Rev. Lett. **66** (1991) 2693.

2 Particle Physics at DESY/HERA (H1)

J. Becker, Ilaria Foresti (until October 2004), N. Keller (until June 2004), L. Lindfeld, Katharina Müller, P. Robmann, S. Schmitt, C. Schmitz, U. Straumann, P. Truöl, M. Urban (until December 2004), Nicole Werner (until June 2004) and Stefania Xella Hansen

in collaboration with:
S. Baumgartner, N. Berger, W. Erdmann, C. Grab, B. List, S. Mangano, D. Meer, A. Schöning and R. Weber, Institut für Teilchenphysik der ETH, Zürich; S. Egli, R. Eichler, M. Hildebrandt, and R. Horisberger, Paul–Scherrer–Institut, Villigen, and 34 institutes outside Switzerland

(H1 - Collaboration)

2.1 Electron-proton collisions at a centre of mass energy of 320 GeV - summary

During the first nine years of successful operation of the HERA storage ring, which ended in the year 2000, the H1 - detector has studied collisions of 27.4 GeV electrons and positrons with up to 920 GeV protons with a total luminosity of $\approx$ 200 pb^{-1}. During this phase (HERA-I) both the H1 - and the ZEUS - Collaboration have explored the structure of the proton and tested quantum chromodynamics (QCD) predictions focusing on precise determinations of the neutral and charged electroweak current cross sections at high momentum transfer leading to parton density functions in pre-HERA inaccessible domains of Bjorken x and momentum transfer Q^2, diffractively produced final states, hidden and open charm and beauty production as well as searches for states outside the Standard Model. The analysis of the wealth of data accumulated during this period is by no means concluded, as evidenced by the continuous flow of publications.

Since the HERA-I luminosity was insufficient to obtain large event samples for electroweak processes at the highest momentum transfers ($Q^2 \approx M_W^2$) an upgrade program was started in 2000 and completed in 2001. After solving a series of technical difficulties, which required another longer shutdown in 2003, luminosity and beam currents have reached design values for positron runs with tolerable background levels in the H1- and the ZEUS-detectors in 2004. While HERA-I used only unpolarized beams, HERA-II allows beam polarisations up to 40 %. Present plans call for HERA-II running until 2007, with an expected integrated luminosity of $\approx$ 500 pb^{-1}, split between electron and positron running. This will considerably raise the discovery potential of the HERA machine for beyond the standard model physics in the largely unexplored mass region above 200 GeV/c^2.

The components which were built by us for the upgraded H1-detector (a new five-layer inner multiwire proportional chamber with finer granularity and increased redundancy, equipped with new electronics and a new optical readout delivering signals for an improved z-vertex trigger) are now fully operational, and hence require only maintenance. The focus of our work has therefore shifted to data analysis.

Four theses of Zürich graduate students have been concluded (1)-(4). Results from ongoing thesis projects concerning lepton flavor violation and the search for excited fermions and photons within jets are given below in Sec. 2.3.2 and 2.3.3, respectively. The other two projects concern τ-lepton production as a signal for W-production, and the appearance of prompt photons within jets.

The analysis of HERA-I data lead to nine publications (5)-(13), and six more have been submitted or are in print (14)-(19). Additional, however preliminary results have been communicated at the August 2004 high-energy physics conference in Beijing (20)-(29), among them first results from the HERA-II running with polarized positrons (30)-(32), to be discussed briefly in Sec. 2.3.1 below.

A large fraction of these publications deals with searches for states and interactions outside the Standard Model, either of general type (11), or dedicated to specific objects such as supersymmetric partners of light and top quarks (6; 10), gravitinos (15), or magnetic monopoles (16).

Using all e^+p and e^-p data collected during HERA-I running between 1994 and 2000 combined QCD fits have been performed to determine electroweak parameters taking properly into account the correlation with the parton density distributions. The results include among others an improved determination of the W-boson mass, a first determination of the weak couplings of the light quarks to the Z^0 boson at HERA either in a least model dependent way (a) or within the standard model (b). The results are being presented at the upcoming conference on deep-inelastic scattering. As an example we quote only the two results:

a) m_W = 82.87 ± 1.83 (stat.) $^{+0.30}_{-0.16}$ (syst.) GeV/c^2

b) m_W = 80.786 ± 0.207 (stat.) $^{+0.048}_{-0.029}$ (mod.) ± 0.025 (top) ± 0.033 (th.) ± 0.084 (Higgs) GeV/c^2

The latter value can also be interpreted in terms of the Weinberg angle via $\sin^2\theta_W = 1 - M_W^2/M_Z^2$ using the e^+e^--collider world average for M_Z as

$$\sin^2\theta_W = 0.2151 \pm 0.0040\ (\mathrm{exp.})\ ^{+0.0019}_{-0.0011}\ (\mathrm{th.}).$$

In scheme (b) the uncertainties quoted refer to the QCD-model (*mod.*) coming mainly from α_s and the starting point of the Q^2 evolution Q_0^2, the accepted ranges of the Higgs-boson and the top quark mass, and Δr (*the.*), the W propagator self energy correction.

Otherwise the parton density program of H1 broadens its kinematical base by including QED Compton scattering (9) and radiative events (23).

The other two areas, where our group has been active in the past, charm and beauty production (13; 14; 18; 19; 21; 22; 24) benefit strongly from the precise tracking information available from the silicon vertex detector, which was built almost exclusively by the Swiss groups within the H1-collaboration.

The studies of the diffractive component of deep inelastic scattering and photoproduction have been refined by going from inclusive to exclusive final states (25; 26) and also including the charged current data (28). Data on diffractive charm production, which was first studied in the Zürich thesis of S. Hengstmann on the basis of a handful of events recorded up to 1997, are now available over a larger kinematical region (25) which allows a more stringent test of the underlying QCD-predictions.

The H1 experiment has observed an excess of events with respect to the Standard Model W-production in the search for isolated, high p_T, single electrons and muons. Stefania Xella is working on the search for isolated, high p_T, single τ leptons from W-production, in the framework of the new object oriented software. The focus of the analysis is on hadronic decays of τ. First results from this analysis are available in (29).

Another Zürich project (C. Schmitz, K. Müller) is trying to determine the photon content of jets. The goal is first to identify photons inside a hadron jet and then to measure the energy fraction of the jet carried by the photon. This should allow to determine the quark-to-photon

fragmentation function (35) which is not yet measured in the kinematic regime of HERA and can not be estimated by QCD calculations due to its non-perturbative component. If successful this analysis will yield important input to the simulation of physics processes at LHC, especially background processes for the Higgs search in the $\gamma\gamma$ channel.

2.2 Data taking

2.2.1 Status of the HERA accelerator

Since the end of the HERA shutdown in September 2003 the vacuum and background situation has significantly improved. This was achieved by the installation of an additional ion getter pump, increased pumping power and lead shielding around the beam pipe for better synchrotron radiation protection. From January 2004 to August 2004 HERA–II was running with positrons and delivered 90 pb^{-1}, of which 60 pb^{-1}were useful for physics analysis with average beam currents $I_p = 80$ mA ($I_p^{max} = 122$ mA) and $I_e = 25$ mA ($I_e^{max} = 53$ mA). In 2005 HERA–II runs with electrons, but background conditions have so far limited the beam currents and only 35 pb^{-1}of the about 50 pb^{-1}were useful for physics analysis. The slope of the curves displayed in Fig. 2.1 showing the integrated luminosity versus time however is promising and vacuum conditions are bound to improve. The maximum instantaneous and specific luminosity, $3.65 \cdot 10^{31}$ cm^{-2}/s and $1.72 \cdot 10^{30}$ cm^{-2} mA^{-2}/s, respectively, have reached the HERA-II upgrade design values.

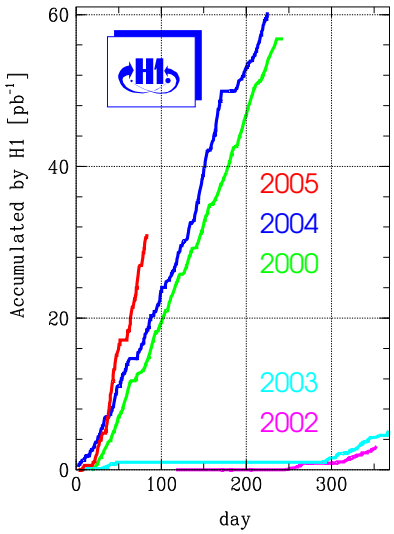

Figure 2.1:
Integrated luminosity produced by HERA–I (2000) and HERA–II (since 2002) as a function of day of the year. In the years 2000 - 2004 positrons were accelerated, in 2005 electrons.

2.2.2 Status of the H1 experiment

This years short summer shutdown was used to exchange electronics on the central silicon vertex detector, which suffered from radiation damage. Since this required access to the inner detector our group used the opportunity, too, to exchange a few CIP preamplifier and readout cards. Unfortunately the backward silicon detector had to be removed completely and will, after replacement of its radiation damaged components be reinstalled next year. Data taking resumed in October 2004, but useful electron running only started in 2005. Otherwise all H1-components function satisfactorily. The new z-vertex trigger built by us (34) is an essential component of nearly all trigger elements for regular data taking and cosmic calibration runs.

2.3 Results from recent analyses

2.3.1 First results from measurements with polarised beams

In the past years the HERA electron ring was tuned such that the electrons acquired a transverse polarisation of 50-60 %. After 2000 two pairs of spin rotators were installed around the H1 and ZEUS interaction regions, and the compensating magnets were removed. In autumn 2002 the latter spin rotators were switched on and polarized positrons were produced successfully. In spring 2003 HERA demonstrated a high degree of polarisation (45-50%) with both experiments taking data. Under typical running conditions in 2004 values around 35 ± 5 % have been reached.

The lepton polarisation is measured with two Compton polarimeters:

- the transverse polarimeter (TPOL) located near HERA-B outside the spin rotators, where the longitudinal component is zero, measures the transverse component of the beam polarisation.
- the longitudinal polarimeter (LPOL) located between the spin rotators near HERMES measures the longitudinal component at a place, where the transverse component of the polarisation is zero.

Both polarimeters detect Compton scattered laser light from the colliding the lepton beam. The polarisation is determined by comparing the cross section for left- and right-circularly polarized laser light. The polarimeter activities are coordinated by the POL2000 group with members from H1, ZEUS, HERMES, and DESY. Stefan Schmitt from our group was the speaker of this group from August 2002 to September 2004.
One of the main physics topics with longitudinally polarized leptons at H1 is the direct search for right-handed charged currents using the relation $\sigma_{CC} = (1 \pm P) * \sigma_L + (1 \mp P) * \sigma_R$. The linear dependence on the polarisation is quite evident from the data presented by the H1-collaboration at ICHEP04 (30; 32), which are shown in Fig. 2.2. The data are consistent with those of the ZEUS-collaborations, agree with standard model predictions and do not require right-handed charged currents.
A linear fit to the positron data points at large momentum transfer ($Q^2 > 400$ GeV^2) and inelasticity $y < 0.9$ yields a result consistent with the SM prediction $\sigma_{CC}(RH) = 0$:

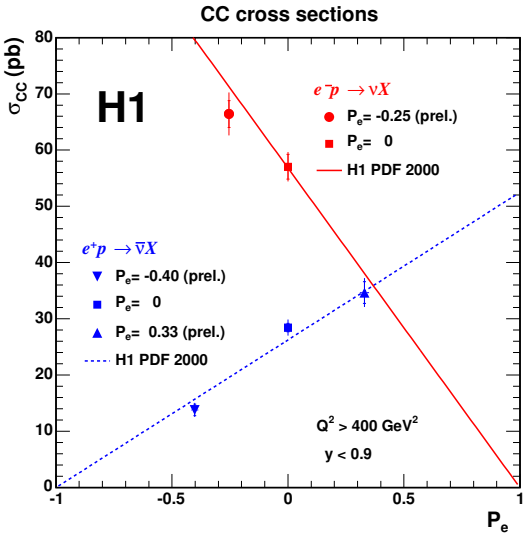

Figure 2.2:
Charged current cross section versus polarisation. HERA-II positron (2003/4) and electron data (2005) for Q^2 >400 GeV^2 and inelasticity y <0.9 are combined with unpolarised lepton data from 1999/2000 (e^+) and 1998 (e^-). The solid lines represent the standard model predictions using particle density functions derived from H1 neutral current data.

e^+p	P	σ_{CC}	$\mathcal{L}$
	0.33 $\pm$ 0.02	34.7 ± 1.9 (stat) ± 1.7 (syst)	15.3 pb^{-1}
	0	28.4 ± 0.8 (stat) ± 1.2 (syst)	65.2 pb^{-1}
	-0.40 $\pm$ 0.02	13.8 ± 1.0 (stat) ± 1.0 (syst)	21.7 pb^{-1}
	-1	-3.7 ± 2.4 (stat) ± 7.7 (syst)	extrapolated

A preliminary analysis of the electron data taken in February and March 2005 can be combined with unpolarised data from 1998 (see also Fig. 2.2) and yields:

e^-p	P	σ_{CC}	$\mathcal{L}$
	0.25 $\pm$ 0.04	66.4 ± 2.4 (stat) ± 3.0 (syst)	17.8 pb^{-1}
	0	57.0 ± 3.9 (stat) ± 2.4 (syst)	16.4 pb^{-1}

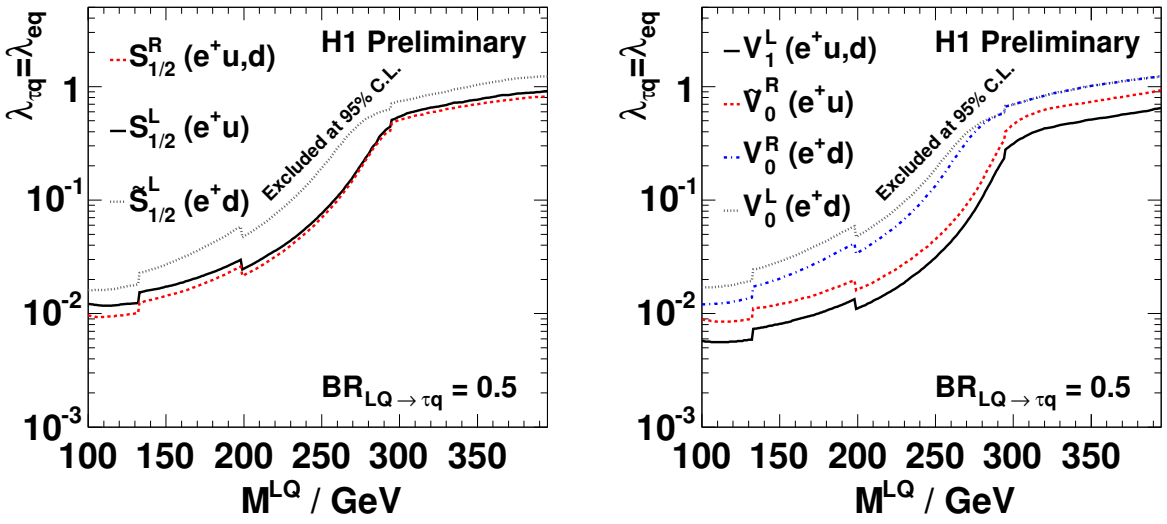

Figure 2.3:
Limits on the coupling strength $\lambda_{\tau q}$ at 95 % confidence level as a function of the LQ mass for scalar (left) and vector (right) LQs in the τ channel.

For neutral currents the dependence of the cross section on the polarisation is less pronounced, since it enters through the vector (v_e) and axial vector (a_e) quark coupling constants in the electroweak interference between γ and Z-exchange. By measuring both electrons and positrons, polarised and unpolarised one can disentangle the individual quark flavors. This program however requires high Q^2 and high statistics.

2.3.2 Search for lepton flavor violation

Lepton-flavor-violating (LFV) processes can be mediated by leptoquarks (LQ) possessing couplings to mixed fermion states. Leptoquarks are color triplet scalar or vector bosons, carrying both lepton (L) and baryon (B) number. The fermion number $F = L + 3B$ is conserved and takes values of $F = -2$ for e^-q and $F = 0$ for e^+q. In a search using the 1999/2000 e^+p-data (integrated luminosity 66.5 pb^{-1}) limits were derived on the Yukawa coupling of seven leptoquarks with $F = 0$ to a μ- or τ-lepton and a light quark, $\lambda_{\mu q,\tau q}$, in the Buchmüller-Rückl-Wyler effective model (36), as well as on the branching ratio, $B_{\mathrm{LQ}\to\mu q,\tau q}$, for the LQ decaying to a μ or τ (33). This analysis covers large parts of the PhD thesis of Linus Lindfeld. The limits are shown in Fig. 2.3, separately for scalar and vector LQ. The analysis uses the high p_T pencil-like (narrow cone and low track multiplicity) jet characteristic for a hadronic decay of a high p_T τ as signature. High p_T dijet events ($p_T > 25$ and > 15 GeV, resp.) have been selected. The 2005 data from e^-p-collisions will open the sensitivity to the other seven LQs with $F = 2$ which are possible in the BRW-model.

In this context also a letter is being prepared (37) presenting the analysis of S. Schmitt, which entails a complete search for LQs coupling to first generation fermions using e^+p data collected at a center-of-mass energy of $\sqrt{s_{ep}} = 300$ GeV, and e^-p as well as e^+p data collected at $\sqrt{s_{ep}} = 320$ GeV, corresponding to integrated luminosities of 37, 15 and 65 pb^{-1}, respectively, and representing the full statistics accumulated by the H1 experiment between 1994 and 2000. The search considered the decays LQ$\to eq$ and LQ$\to \nu q$ which lead to final states similar to those of deep-inelastic neutral and charged current interactions at very high Q^2. Results for scalar LQs are compared to those from other experiments in Fig. 2.4.

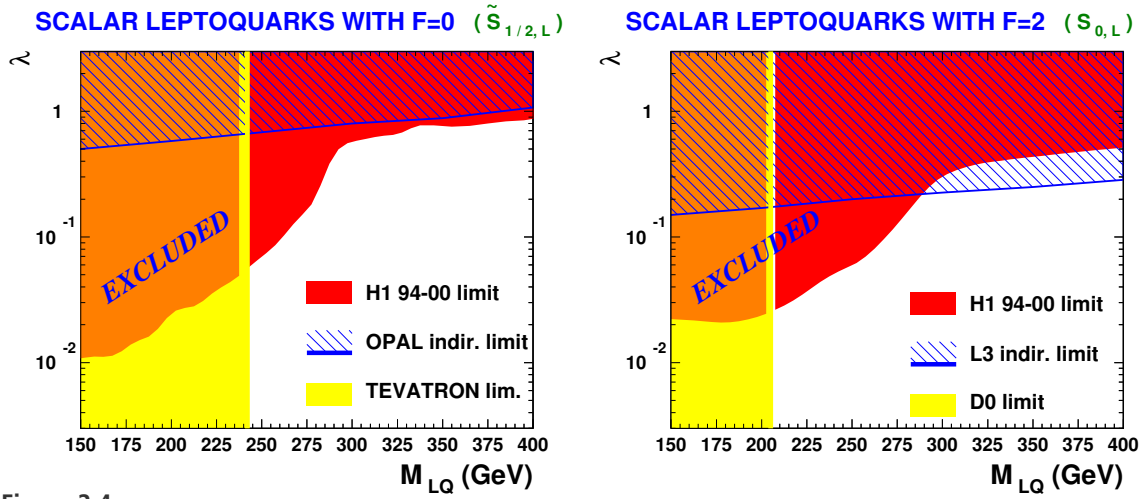

Figure 2.4:
Limits at 95% CL on the Yukawa coupling λ as a function of the LQ mass for scalar LQs with $F = 0$ (left) or $F = 2$ (right) in the BRW model [36]. Shaded and hatched domains are excluded. For $\tilde{S}_{1/2,L}$ the indirect limit from the OPAL-experiment and the combined direct limit from the CDF- and D0-experiments are shown, whereas for $S_{0,L}$ the indirect limit from the L3-experiment and the only available direct limit from the D0-experiment are shown. See ref. [37] for references.

2.3.3 Excited fermions

If leptons and quarks are not elementary particles but composite objects, excited states of these fermions can exist. These states can decay into an ordinary fermion and a gauge boson, e.g. $e^* \to e+\gamma$ or $q^* \to q+g$. At HERA, excited electrons and quarks can be produced by t-channel exchange of a photon or a Z-boson; similarly excited neutrinos can be produced by t-channel exchange of a W-boson. All possible decay channels are accessible with the H1 detector.

Jan Becker analyzed in his PHD thesis the decay of excited quarks into a quark and a photon. The event signature is a high energy photon together with a high energy jet, both pointing predominantly into the forward region of the detector. The dominating standard model background comes from neutral current events with a misidentified electron and from photoproduction events without a scattered electron in the detector. In the latter case prompt photons or isolated neutral mesons (π^0, η) misidentified as photons contribute.

The analysis used 1999/2000 data (integrated luminosity of 63 pb^{-1}) doubling the statistics of a published H1 search (39). It was optimized to get a good signal efficiency for masses of the excited quark larger than 100 GeV with low background from standard model processes.

The photon candidate is required to have a transverse momentum above 40 GeV/c and a scattering angle between 10° and 80°. No track is allowed to point to the photon candidate within 10 cm. Additionally a veto on hits in the proportional chambers is applied. The transverse momentum of the jet has to be larger than 50 GeV/c. This high p_T selection of events has a signal efficiency of roughly 40% and rejects the background very efficiently. In total 7 ± 2.7 events remain, while 8.5 ± 0.4 (stat) ± 3.0 (syst) are expected from the standard model. No excess of the data in the invariant mass is observed (Fig. 2.5a)). The limits derived in this analysis improve the existing H1 limits (39) in the high mass region (Fig. 2.5b) and c)).

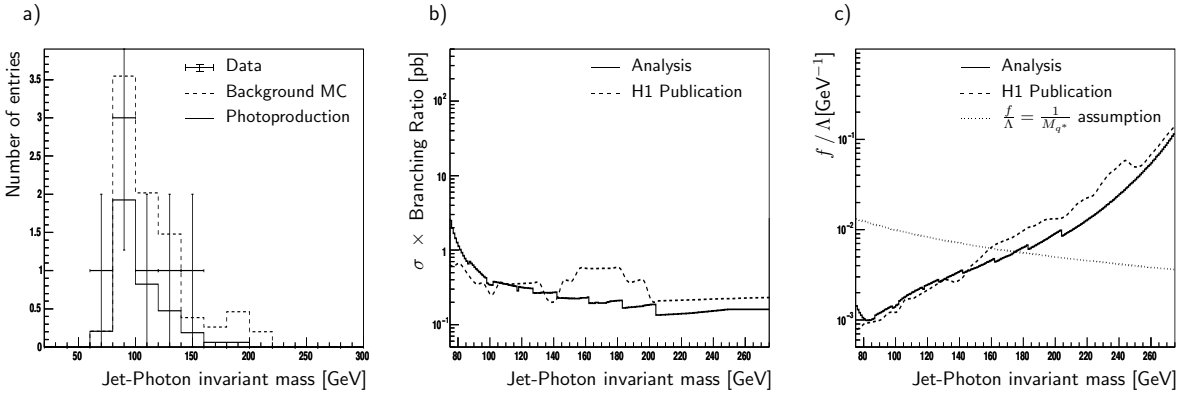

Figure 2.5:
a) Invariant mass calculated from the jet and the photon.
b) Limit on the cross section for an excited quark decaying into a jet and a photon.
c) Limit on the coupling parameters for excited quarks.

[1] **Measurement of Charged Current Cross Sections in Positron Proton Collisions at HERA**, Nicole Werner, PhD Thesis, University of Zürich (2004).

[2] **A Measurement of the QED-Compton Cross Section in Electron-Proton Scattering with the H1-Experiment at HERA**, Nicolas Keller, PhD Thesis, University of Zürich (2004).

[3] **A Multitrack Method for b-Tagging**, Ilaria Foresti, PhD Thesis, University of Zürich (2004).

[4] **The New CIP2K z-Vertex Trigger for the H1-Experiment at HERA**, Max Urban, PhD Thesis, University of Zürich (2004).

[5] **Measurement of Dijet Production at Low Q^2 at HERA**, H1-Collaboration, A. Aktas *et al.*, DESY 03 – 206, hep-ex/0401010, Eur.Phys.J.**C37** (2004), 141 - 159.

[6] **Search for Squark Production in R-Parity Violating Supersymmetry at HERA**, H1-Collaboration, A. Aktas *et al.*, DESY 04 – 025, hep-ex/0403027, Eur.Phys.J.**C36** (2004), 425 - 440.

[7] **Measurement of Anti-Deuteron Photoproduction and a Search for Heavy Stable Charged Particles at HERA**, H1-Collaboration, A. Aktas *et al.*, DESY 04 – 032, hep-ex/0403056, Eur.Phys.J.**C36** (2004), 413 - 423.

[8] **Forward π^0 Production and Associated Transverse Energy Flow in Deep-Inelastic Scattering at HERA**, H1-Collaboration, A. Aktas *et al.*, DESY 04 – 051, hep-ex/0404009, Eur.Phys.J.**C36** (2004), 441 - 452.

[9] **Measurement of the Proton Structure Function F_2 at low Q^2 in QED Compton Scattering at HERA**, H1-Collaboration, A. Aktas *et al.*, DESY 04 – 083, hep-ex/0406029, Phys.Lett.**B598** (2004), 159 - 171.

[10] **Search for Bosonic Stop Decays in R-parity Violating Supersymmetry in e^+p Collisions at HERA**, H1-Collaboration, A. Aktas *et al.*, DESY 04 – 084, hep-ex/0405070, Phys.Lett.**B599** (2004), 159 - 172.

[11] **A General Search for New Phenomena in ep Scattering at HERA**, H1-Collaboration, A. Aktas *et al.*, DESY 04 – 140, hep-ex/0408044, Phys.Lett.**B602** (2004), 14 - 30.

[12] **Measurement of Prompt Photon Cross Sections in Photoproduction at HERA**, H1-Collaboration, A. Aktas *et al.*, DESY 04 – 118, hep-ex/0407018, Eur.Phys.J.**C38** (2005), 437 - 445.

[13] **Inclusive Production of D^+, D^0, D_s^+ and D^{*+} Mesons in Deep Inelastic Scattering at HERA**, H1-Collaboration, A. Aktas *et al.*, DESY 04 – 156, hep-ex/0408149, Eur.Phys.J.**C38** (2005), 447 - 459.

[14] **Measurement of $F_2^{c\bar{c}}$ and $F_2^{b\bar{b}}$ at High Q^2 using the H1 Vertex Detector at HERA**, H1-Collaboration, A. Aktas *et al.*, DESY 04 – 209, hep-ex/0411046, Eur.Phys.J.**C** (2005), in print.

[15] **Search for Light Gravitinos in Events with Photons and Missing Transverse Momentum at HERA**, H1-Collaboration, A. Aktas *et al.*, DESY 04 – 227, hep-ex/0501030, Phys.Lett.**B** (2005), in print.

[16] **A Direct Search for Magnetic Monopoles Produced in Positron-Proton Collisions at HERA**,

H1-Collaboration, A. Aktas *et al.*, DESY 04 – 240, hep-ex/0501039, Eur.Phys.J.**C** (2005), in print.

[17] **Measurement of Dijet Cross Sections for Events with a Leading Neutron in ep Interactions at HERA**, H1-Collaboration, A. Aktas *et al.*, DESY 04 – 247, hep-ex/0501074, Eur.Phys.J.**C** (2005), in print.

[18] **Measurement of Beauty Production at HERA Using Events with Muons and Jets**, H1-Collaboration, A. Aktas *et al.*, DESY 05 – 004, hep-ex/0502010, submitted to Eur.Phys.J.**C** (2005).

[19] **Measurement of Charm and Beauty Photoproduction at HERA $D^*\mu$ Correlations**, H1-Collaboration, A. Aktas *et al.*, DESY 05 – 040, hep-ex/05003038, submitted to Phys.Lett.**B** (2005).

[20] Contributed papers to to ICHEP2004: 32^{nd} Int. Conf. on High Energy Physics Beijing (China), August 16-22, 2004. Only those papers are listed, which have not previously been contributed to other conferences or have been submitted to journals already.

[21] **Measurement of Beauty Production in Deep Inelastic Scattering at HERA**, [20] (5-0165).

[22] **Measurement of Charm and Beauty Production in Deep Inelastic e^+p Scattering at High Q^2 at HERA**, [20] (5-0167).

[23] **Measurement of the Inclusive DIS Cross Section at Low Q^2 and High x Using Events with Initial State Radiation**, [20](5-0170).

[24] **Measurement of Beauty Photoproduction at HERA using Inclusive Lifetime Tagging**, [20] (5-0760).

[25] **Comparison between Diffractive Dijet Electroproduction and Photoproduction**, [20] (6-0177).

[26] **Diffractive D^* Meson Production in Deep Inelastic ep Collisions at HERA**, [20] (6-0178).

[27] **Exclusive Photoproduction of Photons at Large $|t|$**, [20] (6-0183).

[28] **Measurement of the Diffractive Cross Section in Charged Current Interactions at HERA**, [20] (6-0821).

[29] **Search for Events with τ Leptons in ep Collisions at HERA**, [20] (12-0188).

[30] **First Measurement of the Polarisation Dependence of the Total Charged Current Cross Section**, [20] (4-0756).

[31] **Analysis of High Transverse Momentum Particle Production with HERA II Data** , [20] (12-0765).

[32] **Charged and Neutral Current Cross Sections at HERA I and HERA II**, S. Schmitt, Proc. [20], to be published.

[33] **Physics with τ Leptons at HERA**, L. Lindfeld, Proc. 8^{th} Int. Workshop on Tau-Lepton Physics (Tau04), Nara, Japan, September 14-17, 2004.

[34] **The CIP2K First-Level Trigger System at the H1-Experiment at HERA**, M. Urban, J. Becker, S. Schmitt, and U. Straumann, IEEE Trans. Nucl. Sci. **50** (2003), 903 - 908

[35] T. Gehrmann, Institute for Theoretical Physics, University of Zürich, privat communication.

[36] W. Buchmüller, R. Rückl, and D. Wyler, Phys.Lett.**191** (1987), 447.

[37] **Search for Leptoquark Bosons in ep Collisions at HERA**, H1-Collab. A. Aktas *et al.*, to be submitted to Phys.Lett.**B**.

[38] H1-Collab. C. Adloff *et al.* Eur.Phys.J.**C11** (1999), 447 [erratum: ibid. **C14** (1999), 553]; Phys.Lett.**B523** (2001), 234.

[39] H1-Collab. C. Adloff *et al.*, Eur.Phys.J.**C17** (2000), 567.

3 The DØ experiment at the Tevatron $p\bar{p}$ collider: Search for rare decays of the B_s^0-mesons

Ralf Bernhard and Frank Lehner

The full DØ collaboration consists of 86 institutes from 19 countries:
Argentina (1), Brazil (3), Canada (4), China (1), Czech Republic (3), Colombia (1), Ecuador (1), France (8), Germany (6), India (3), Ireland (1), Korea (1), Mexico (1), Netherlands (3), Russia (5), Sweden (4), United Kingdom (3), United States of America (36) and Vietnam (1)

(DØ Collaboration)

Until LHC at CERN starts its operation in 2007, the Tevatron at the Fermi National Accelerator Laboratory, Batavia, USA, is the world's highest-energy accelerator with an available center of mass energy of $\sqrt{s} = 2$ TeV. The so-called Run II of the $p\bar{p}$ collider has started in 2001 and addresses some of the most important questions in particle physics. The most recent physics results involve direct searches for as yet unknown particles and forces, including both those that are predicted in the Standard Model (SM) like the Higgs boson and those that would come as a surprise. Other important aspects of this programme will be the precise measurements of the top quark properties, new accurate determinations of the mass of the W boson and the couplings of the electroweak bosons. Moreover, numerous measurements of various B meson decay modes have already allowed the investigation of B meson properties that are not accessible at other colliders as well as CP-violating effects.

The DØ detector at Tevatron is now fully operational and collision data are taken with a high global efficiency. In 2004 Ralf Bernhard spent a ten-months research period at Fermilab where he participated in detector optimization studies and operation shifts helping a smooth running of the experiment. Presently, about 600 pb^{-1} of $p\bar{p}$ collision data are recorded on tape and we have started with a physics analysis programme of searches for rare B_s^0 meson decays, which will be the main content of Ralf Bernhard's PhD thesis. The study of the B_s^0 meson is presently unique to the Tevatron collider since B_s^0 is not produced at the $\Upsilon(4S)$ resonance at which e^+e^- B-Factories like BaBar and Belle are running. This work represents an important ingredient for the preparation of physics analysis at the upcoming LHCb. Our search programme is dedicated to flavor-changing neutral current (FCNC) B_s^0 decays, that are forbidden in the SM at tree level. However, they proceed through higher order diagrams and have therefore very small SM branching fractions. The FCNC decays of the B mesons are particularly important for probing the quark flavor sector of the SM and for providing severe constraints on several models beyond the SM. For instance, the decay amplitude of $B_s^0 \to \mu^+\mu^-$ can be significantly enhanced in most extensions of the SM: in type-II two-Higgs-doublet models (2HDM) the branching fraction depends only on the charged Higgs mass M_{H^+} and $\tan\beta$, the ratio of the two neutral Higgs field vacuum expectation values, with the branching fraction growing like $(\tan\beta)^4$ (1). In the minimal supersymmetric standard model (MSSM), however, $\mathcal{B}(B_s^0 \to \mu^+\mu^-) \propto (\tan\beta)^6$, leading to an enhancement by up to three orders of magnitude (2) compared to the SM value of $\mathcal{B}(B_s^0 \to \mu^+\mu^-) = 3.5 \times 10^{-9}$, even if the MSSM with minimal flavor violation (MFV) is considered, in which case the CKM matrix is the only source of flavor violation. In minimal supergravity models, an enhancement of $\mathcal{B}(B_s^0 \to \mu^+\mu^-)$ is correlated (3) with a sizeable increase of $(g-2)_\mu$, the anomalous magnetic moment of the muon. A large value of $\tan\beta$ is theoretically well-motivated by grand unified theories

(GUT) based on minimal SO(10) (3; 4). Finally, $B_s^0 \to \mu^+\mu^-$ is also sensitive to supersymmetric models with non-minimal flavor violation structures such as the generic MSSM (5) or R-parity violating supersymmetry (6). Since this decay shows such a strong sensitivity to many new models and its amplitude is theoretically very clean, it allows clearly one of the most sensitive searches for new physics with the statistics presently available at the Tevatron. Moreover, in a long-term perspective, the discovery of this process is definitely one of the most important prospects in the B-physics program of hadron colliders.

So far, we have analyzed 300 pb^{-1} of DØ data that were taken with a special two-muon trigger. For the search of the rare candidate events we have used discriminating variables to best exploit the properties of the signal decay and the multi-variate technique of a random-grid search to optimize the analysis. The signal region itself was kept hidden during the optimization in order to avoid any bias. The events next to the region around the B_s^0 invariant mass were used to determine the background. As a normalization mode we reconstructed $B^\pm \to J/\psi(\to \mu^+\mu^-)K^\pm$ events, as shown in the left part of Fig. 3.1. Since the efficiencies to detect the $\mu^+\mu^-$ system in signal and normalization events are similar systematic effects tend to cancel.

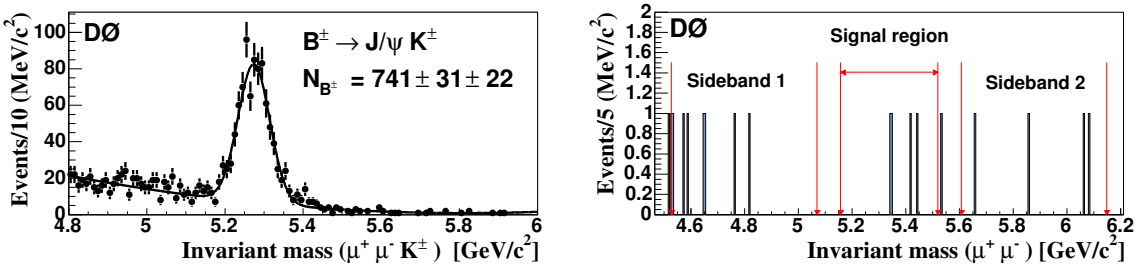

Figure 3.1:
Left: invariant mass distribution for candidates in the normalization channel $B^\pm \to J/\psi K^\pm$.
Right: the remaining sample with our standard discriminating variables.

After unblinding the signal box for 240 pb^{-1} integrated luminosity the mass spectrum shown in the right panel of Fig. 3.1 resulted. We observe four events while 3.7 ± 1.1 are expected from the sidebands. We have published just recently the resulting upper limit for the branching fraction of $B_s^0 \to \mu^+\mu^-$ of 4.1×10^{-7} at a 90% C.L.(7). Our result presently represents the world-best upper limit on this decay and can be used to constrain models beyond the SM. For the Moriond conference 2005 we updated the analysis with more available data and obtained as preliminary result an improved upper limit of 3.0×10^{-7} at a 90% C.L.

The anticipated luminosity at Tevatron will accumulate to 2 fb^{-1}, when LHC starts its operation in 2007. In case of no signal, this amount of DØ data may lead to an expected upper limit on the branching fraction of $B_s^0 \to \mu^+\mu^-$ to 1.2×10^{-7}, if the analysis is re-optimized. Although such a limit will be sufficient to exclude regions of very large $\tan\beta$ in the framework of supersymmetric models, it will still be a factor 30 above the SM branching fraction. Thus, an experimental sensitivity to this rare decay at the level of the SM is clearly out of reach at Tevatron. The LHCb experiment, at the other hand, expects an annual yield of 17 reconstructed $B_s^0 \to \mu^+\mu^-$ decays.

Our second search at DØ concerns the exclusive non-resonant FCNC decay $B_s^0 \to \mu^+\mu^-\phi$, which belongs to the class of the $b \to s\,l^+l^-$ quark transitions caused by electroweak penguin diagrams. The analysis for $B_s^0 \to \mu^+\mu^-\phi$ is still ongoing and the signal region has not yet been examined. The branching fraction of the non-resonant decay is normalized to the known resonant decay $B_s^0 \to J/\psi(\to \mu^+\mu^-)\phi$ which has the same final state. For the Moriond

conference 2005 we have presented the experimental reach with our current 300 pb^{-1} of DØ data (9). Our present exclusion potential is 1.0×10^{-5} (95% C.L.) including systematic uncertainties which is almost seven times better than the published limit (10). We are planning to open the signal box for the summer conferences 2005.

In fall 2005, a new layer of silicon detectors will be inserted into the existing DØ silicon detector. This new layer is very close to the beam pipe and its installation becomes necessary to compensate for the radiation induced damage of the existing silicon device (11). We have contributed to the R&D phase of this new layer and developed together with the Swiss based company Dyconex long flexible fine-pitch cables, which transmit the analog signals from the silicon sensors to the front-end electronics situated at the module's end. After several prototype runs, the production-type cables were successfully procured and tested in summer 2004.

[1] H. E. Logan and U. Nierste, Nucl. Phys. B **586**, 39 (2000).

[2] K. S. Babu and C. F. Kolda, Phys. Rev. Lett. **84**, 228 (2000); A. Dedes *et al.*, FERMILAB-PUB-02-129-T (2002); S. R. Choudhury and N. Gaur, Phys. Lett. B **451**, 86 (1999).

[3] A. Dedes *et al.*, Phys. Rev. Lett. **87**, 251804 (2001).

[4] T. Blazek *et al.*, Phys. Lett. B **589**, 39 (2004); R. Dermisek *et al.*, JHEP **0304**, 37 (2003).

[5] C. Bobeth *et al.*, Phys. Rev. D **66**, 074021 (2002).

[6] R. Arnowitt *et al.*, Phys. Lett. B **538**, 121 (2002).

[7] V. M. Abzov *et al.* [DØ Collaboration], Phys. Rev. Lett. **94** 071801 (2005).

[8] **Update of the upper limit for the rare decay $B_s^0 \to \mu^+\mu^-$ with the DØ detector**, R. Bernhard and F. Lehner, DØ Conference Note 4733, February 2005.

[9] **Sensitivity analysis of the rare decay $B_s^0 \to \mu^+\mu^-\phi$ with the DØ detector**, R. Bernhard and F. Lehner, DØ Conference Note 4732, February 2005.

[10] T. Affolder *et al.* [CDF Collaboration], Phys.Rev.Lett.**83**, 3378 (1999).

[11] F. Lehner, Nucl.Instr.Meth.A **530**, 105 (2004).

4 Rare Kaon Decays at the Brookhaven AGS

H. Kaspar (visiting scientist), P. Robmann, A. van der Schaaf, S. Scheu,
A. Sher (until January 2004) and P. Truöl

Our research program at the Brookhaven National Laboratory's Alternating Gradient Synchrotron (AGS) focuses on rare kaon decays. Only at the AGS intense low-momentum neutral and charged kaon beams are still available today. Though Experiment BNL E-865 finished data-taking in 1998 the analysis of its high statistics data sample on semi-leptonic and leptonic charged kaon decays still supplies novel results. The KOPIO-experiment has been approved for funding by the U.S. National Science Foundation, and its planning concentrates now on the construction of the various detector subsystems and development of a suitable pulsed neutral kaon beam.

4.1 BNL E-865: first observation of the decay $K^+ \to e^+\nu_e\mu^+\mu^-$

in collaboration with:
Paul–Scherrer–Institut, CH-5234 Villigen; Brookhaven National Laboratory, Upton, NY-11973, USA; University of New Mexico, Albuquerque, NM-87131, USA; University of Pittsburgh, Pittsburgh, PA-15260, USA; Yale University, New Haven, CT-06511, USA; Institute for Nuclear Research, Academy of Sciences 117 312 Moscow, Russia

The radiative kaon and pion decays and their internally converted partners
$K_{\ell 2\gamma}: \quad K^+ \to \ell^+\nu_\ell\gamma, \quad K^+ \to \ell^+\nu_\ell\ell'^+\ell'^-, \quad \ell(\ell') = e, \mu$
$\pi_{e2\gamma}: \quad \pi^+ \to e^+\nu_e\gamma, \quad \pi^+ \to e^+\nu_e e^+e^-$
are both an important source of input information as well as a test of the successful chiral perturbation theory (ChPT) (1), the low energy version of quantum chromodynamics. The pion decays were studied during the late eighties in pioneering experiments by the SINDRUM- (2) and the Lausanne-Zürich-collaborations (3) at PSI. In both these collaborations teams from our institute played a prominent role. Radiative pion decay is presently being re-investigated (see Sec. 6.1). Figure 4.1 indicates which processes are to be considered in the construction of the decay amplitudes. The inner bremsstrahlung part, where the virtual photon is radiated either by the decaying meson or by the final state lepton can be calculated in a straightforward and parameter free manner. More interesting is the structure dependent part, which is characterized by the axial vector and vector form factors F_A and F_V and the form factor R, which are the quantities of interest. For example, F_A of the pion fixes one of the terms in

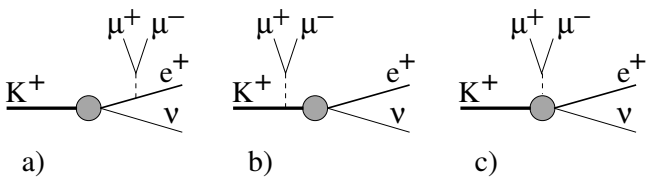

Figure 4.1:
Inner bremsstrahlung (a,b) and structure dependent (c) contributions to the radiative kaon decay $K^+ \to e^+\nu_e\mu^+\mu^-$.

the ChPT-Hamiltonian.

From our experiment E865 (4) we already published results on the radiative decays $K^+ \to \mu^+\nu_\mu e^+e^-$ and $K^+ \to e^+\nu_e e^+e^-$ (5). We have now been able to observe for the first time the decay $K^+ \to e^+\nu_e\mu^+\mu^-$ (6), and determined its branching ratio to

$$B(K^+ \to e^+\nu_e\mu^+\mu^-) = (1.72 \pm 0.37\,(\text{stat.}) \pm 0.17\,(\text{syst.}) \pm 0.19\,(\text{mod.})) \times 10^{-8}$$

In this decay the inner bremsstrahlung contribution is electron helicity suppressed and negligible compared to the structure dependent part, a situation quite different from that in radiative pion decay. ChPT relates F_A and F_V for kaon and pion, and R to the kaon and pion charge radii. Starting from our sample of close to 450'000 triggered $K^+ \to \pi^+\pi^-e^+\nu_e$

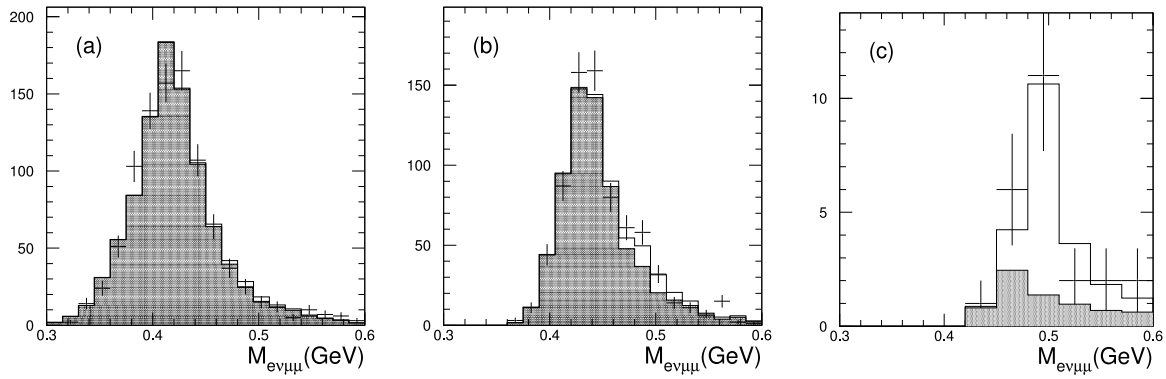

Figure 4.2:
$M_{e\nu\mu\mu}$ invariant mass distribution for events surviving all selection criteria for three bins of the invariant mass $M_{e\mu\mu}$: a) 282.5 to 355 MeV; b) 355 to 427.5 MeV; c) above 427.5. The crosses are the measured data, the histogram is the fitted spectrum consisting of background (shaded) and signal contributions.

(K_{e4}) events (7) 1834 events survived the muon identification cuts, which require a signal in the electromagnetic calorimeter consistent with a minimum ionizing particle and a range in the muon identifier consistent with the measured momentum. This sample is however still dominated by background from K_{e4} or K_τ ($K^+ \to \pi^+\pi^-\pi^+$) decays with misidentified pions and from accidental overlays of two decays with the correct particles in the final state. As is shown in Fig. 4.2 these events are characterized by a lower reconstructed $e\mu\mu$-invariant mass than expected for signal events, their kinematical properties being well understood and represented by the Monte Carlo simulation. The probability that a statistical fluctuation of the background leads to the observed signal of about 17 events with the expected $e\mu\mu\nu$ invariant mass near M_K is less than 10^{-6}. The branching ratio was determined normalizing to K_e4 decay (7). The systematic error arises predominantly from the uncertainty of the muon identification, while the model dependence accounts for the extrapolation to areas of the phase space not accessible in our experiment. The form factors were fixed at the values determined by us in the other radiative kaon decay channels (5). The measured branching ratio is slightly larger than the ChPT-prediction (8) of 1.12×10^{-8}.

[1] S. Weinberg, Physica **96A**, 327 (1979); J. Gasser and H. Leutwyler, Ann. Phys. **158**, 142 (1984); Nucl. Phys. **B250**, 465 (1985); for a recent review see *Effective field theories of QCD*, Proc. 264$^{\text{th}}$ WE-Heraeus-Seminar, Bad Honnef, Germany (2001), J. Bijnens, U.G. Meißner, and A. Wirzba eds., hep-ph/201266, and references therein.

[2] S. Egli *et al.* (SINDRUM-coll.), Phys. Lett. **B222** (1989), 533; ibid. **B175** (1986), 97.

[3] A. Bay *et al.* (Lausanne-Zürich-coll.), Phys. Lett. **B174** (1986), 445.

[4] **A Large Acceptance, High Resolution Detector for Rare K^+-decay Experiments**, R. Appel *et al.* (E865-coll.), Nucl. Instr. Methods Phys. Res. **A479**, 349 (2002).

[5] **Experimental Study of the Radiative Decays $K^+ \to \mu^+\nu_\mu e^+e^-$ and $K^+ \to e^+\nu_e e^+e^-$**, A.A. Poblaguev *et al.* (E865-coll.), Phys. Rev. Lett. **89** (2002), 061803-1.

[6] **First Observation of the Decay $K^+ \to e^+\nu_e\mu^+\mu^-$**, H. Ma *et al.*, subm. to Phys. Rev. **D**.

[7] **High Statistics Measurement of K_{e4} Decay Properties**, S. Pislak *et al.* (E865-coll.), Phys. Rev. **D67**, 072004-1 (2003); Phys. Rev. Lett. **87**, 221801-1 (2001).

[8] J.Bijnens, G. Ecker, and J. Gasser, Nucl. Phys. **B396**, 81 (1993).

4.2 KOPIO: a study of the CP-violating rare decay $K_L^0 \to \pi^0\nu\overline{\nu}$

in collaboration with:
Arizona State University, University of British Columbia, Brookhaven National Laboratory, University of Cincinnati, IHEP (Protvino), INR (Moscow), KEK, Kyoto University of Education, Kyoto University, University of Montreal, University of New Mexico, INFN, University of Perugia, Stony Brook University, TRIUMF, Tsinghua University (Beijing), University of Virginia, Virginia Polytechnic Institute and State University, and Yale University.

The scientific motivations, techniques, and instrumentation associated with the KOPIO measurement of the $K_L^0 \to \pi^0\nu\overline{\nu}$ branching ratio have been discussed in previous annual reports. Many promising approaches to physics beyond the Standard Model (SM) will be tested by

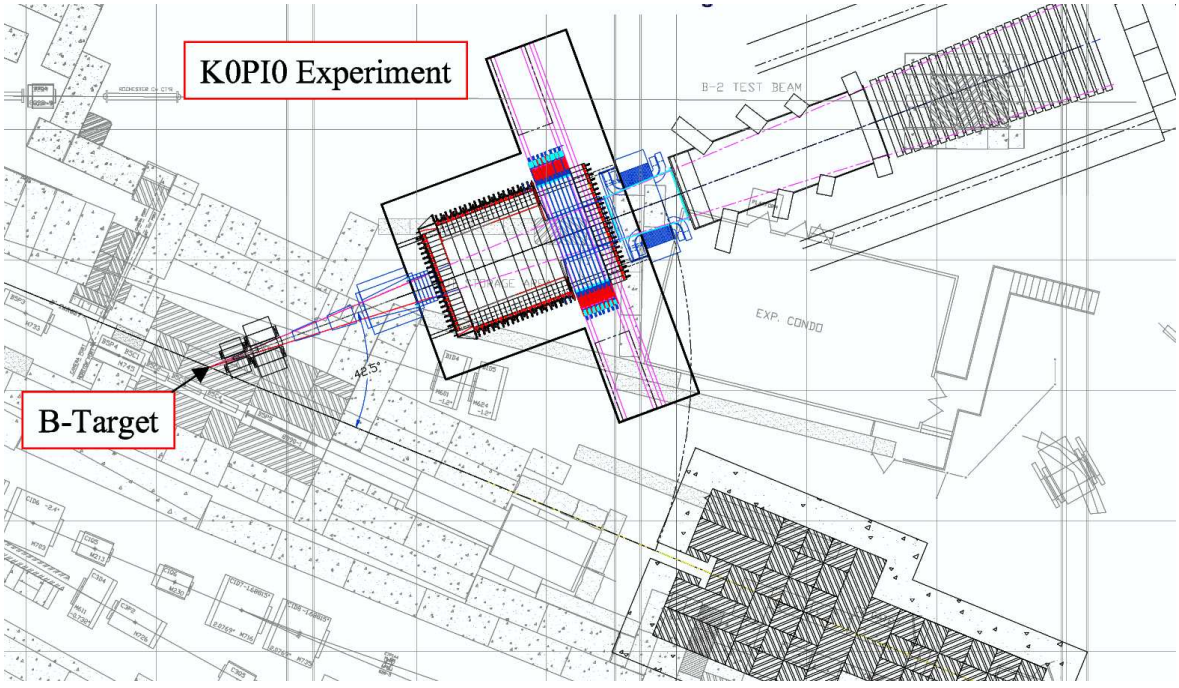

Figure 4.3:
Floor layout of the KOPIO detector. The 25.5 GeV/c proton beam extracted from the AGS hits the KOPIO target before reaching the beam dump shown in the bottom right. The secondary beam line selects neutral particles emitted at 42.5^o using collimators and sweeping magnets. The channel has an acceptance of 90 mr horizontally and 4 mr vertically. Photons are strongly suppressed with the help of a *spoiler*, a 5 cm thick lead plate at the entrance of the channel. See last year's report for details on the setup.

this high sensitivity measurement, and the results will be complementary to measurements at the high energy frontier. For instance, if supersymmetry or other new physics were to be discovered at the LHC, the results from KOPIO would be critical for unraveling whether the flavor structure of this new physics is governed by the SM Yukawa couplings (e.g. Minimal Flavor Violation) or whether there are new sources of CP violation with a new flavor structure. In the absence of a non-SM result, KOPIO will obtain a precision of 10% or better on the branching ratio resulting in the single most precise measurement of CP violation. The basic features of the measurement involve a micro-bunched beam of 10^{14} protons on target during each spill of the AGS used to produce an intense carefully collimated neutral kaon beam (see Fig. 4.3). The detection system employing a unique high efficiency, high resolution pointing calorimeter is used to identify the single π^0 signal in the kaon center-of-mass system while highly efficient photon and charged particle vetos ensure that no other particles were present in coincidence. All important principles of the technique have been tested experimentally with prototypes and/or studied with extensive simulations and construction of the various detector systems will start in October 2005.

Experimental sensitivity

The final error in the measured value of the $K_L^0 \to \pi^0\nu\overline{\nu}$ branching ratio depends on the distribution of the number of signal events v.s. the signal to background ratio (S/B). Main sources of background are the decays $K_L^0 \to 2\pi^0$ and $K_L^0 \to \pi^0\pi^+\pi^-$ when the additional particles remain unobserved. In the case of $K_L^0 \to 2\pi^0$ two components should be distinguished: *even background* results when the observed photons originate from the same π^0, *odd background* results when this is not the case. Even background is characterized by a mono-energetic π^0 in the kaon c.m.s. system: $E^*_{\pi^0} = \frac{1}{2}m_K c^2$. The transformation is made possible by the measurement of the kaon time of flight between production target and decay vertex. Odd background can be suppressed kinematically by requiring $m_{\gamma\gamma} = m_{\pi^0}$ within resolution. For the other backgrounds this condition is automatically fulfilled. $K_L^0 \to \pi^0\pi^+\pi^-$ is limited to low values of $E^*_{\pi^0}$. Main measure against background are hermetic veto systems. Since both the photon and the charged particle inefficiencies are strongly energy dependent S/B depends on the missing energy. Based on these considerations the separation of signal and background depends primarily on the following three quantities:

- $T^*_{\pi^0} \equiv E^*_{\pi^0} - m_{\pi^0}c^2$, the π^0 kinetic energy in the kaon center-of-mass system,
- $E_{\rm miss}$, the missing energy in the laboratory system and
- $m_{\gamma\gamma}$, the 2γ invariant mass.

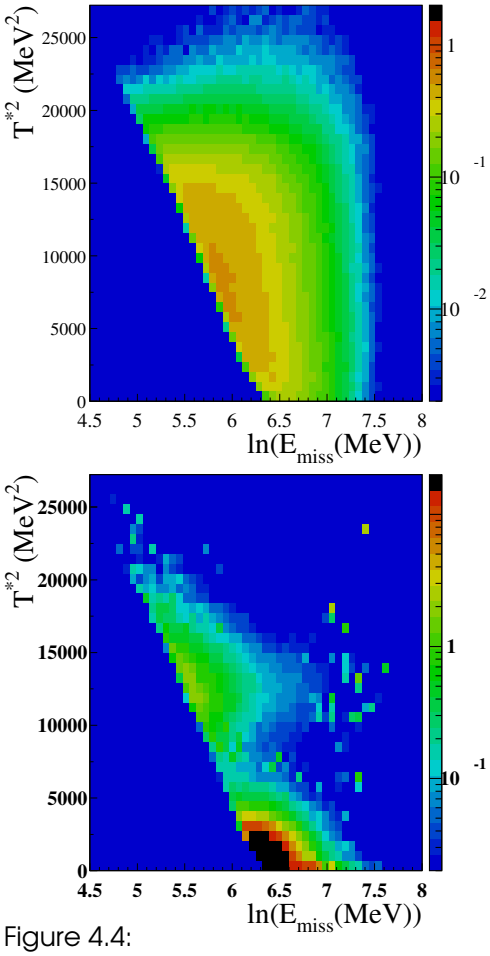

Figure 4.4: **$T^{*2}_{\pi^0}$ v.s. $\ln E_{\rm miss}$ for signal (top) and background (bottom) after suppression of events with veto signals. Whereas signal events show a roughly constant distribution over the allowed phase space, backgrounds are concentrated in a low $T^{*2}_{\pi^0}$ region populated by $K_L^0 \to \pi^0\pi^+\pi^-$ decays and a high $T^{*2}_{\pi^0}$ region populated by $K_L^0 \to 2\pi^0$ even decays.**

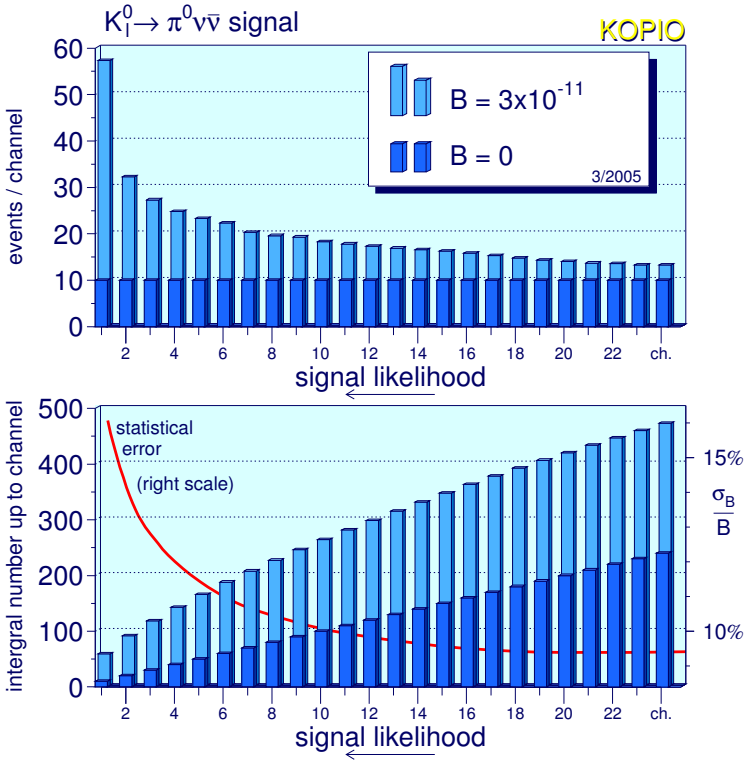

Figure 4.5:
$K_L^0 \to \pi^0\nu\overline{\nu}$ signal for two assumptions for the branching ratio (SM prediction and B vanishing). Events are ordered according to their probability to be signal rather than background. Assuming the central value for the SM prediction the experiment would result in ≈50 *gold-plated* events with S/B around 5. A sample with roughly equal numbers of signal and background events would have $S \approx B$ ≈200.

Figure 4.4 shows simulated distributions of $T^{*2}_{\pi^0}$ v.s. $\ln E_{\rm miss}$ for both signal and total background after suppression of events with signals in the veto systems. From these distributions the probability of an event to be either signal or background can be calculated. The resulting distributions are shown in Fig. 4.5. From these distributions a statistical uncertainty below 10% can be estimated which corresponds to a precision of 5% for the area of the unitarity triangle.

Charged-particle veto system

The purpose of the Charged Particle Veto (CPV) is to provide an efficient identification of background processes in which an apparent $\pi^0 \to 2\gamma$ decay inside the decay volume is accompanied by charged particle emission. Examples of such background processes are $K_L^0 \to \pi^+\pi^-\pi^0$, $K_L^0 \to \pi^0\pi^\pm e^\mp\nu$, $K_L^0 \to \pi^\pm e^\mp\nu\gamma$ in which the $e^\mp$ creates a second photon through Bremsstrahlung or e^+ annihilation in flight, and $K_L^0 \to e^+\pi^-\nu$, again followed by $e^+ \to \gamma$ whereas the π^- creates a photon through $\pi^- p \to \pi^0 n$. In all cases, two particles with opposite electrical charge emerge. Charged-particle detection efficiencies of 99.99% or better are required to keep these backgrounds below 10% in most kinematic regions.

The design of the CPV is based on requirements resulting from extensive simulations of the various background processes and our own tests of the momentum dependence of the detector response to various charged particles ($\pi^\pm, \mu^\pm, e^\pm$). The intrinsic charged particle detection efficiency should be $> 99.99\%$. Inefficiencies are caused by (π^-, xn) reactions, backscattering, or positron annihilation in flight. Our tests show that the efficiency requirement is met if the dead layer in front of the CPV is kept below 20 mg/cm^2 and the detection threshold is kept below 50 keV. The first requirement can only be met when the detectors are situated inside the decay tank and/or beam pipe. With the possible exception of the up-

stream beam hole, the detector has to extend to the full 4π sr. This requires in particular that particles moving downstream within the beam envelope have to be observed as well. In order to separate π^0 decays from (n,π^0) reactions in the CPV from the events of interest the detector elements have to be kept more than 50 cm from the fiducial decay volume. The spread in the time difference between the decay time as reconstructed from the $\pi^0 \to 2\gamma$ decay kinematics and the signals observed in the CPV should be within 12 ns to avoid accidental vetoing by CPV signals from neighboring beam bunches. This requirement sets limits to the intrinsic time resolution and the granularity of the CPV. Depending on the algorithm used to analyze the digitized wave forms, veto signals may get lost when preceded by another signal in the same detector element. These losses are minimized by using fast detectors which are as thin as possible and by distributing the load over many channels. Since access will be limited to less than a few times per year, the loss of a few readout channels must not result in substantial data loss. This requirement can be met by redundancy in the readout of each individual detector element.

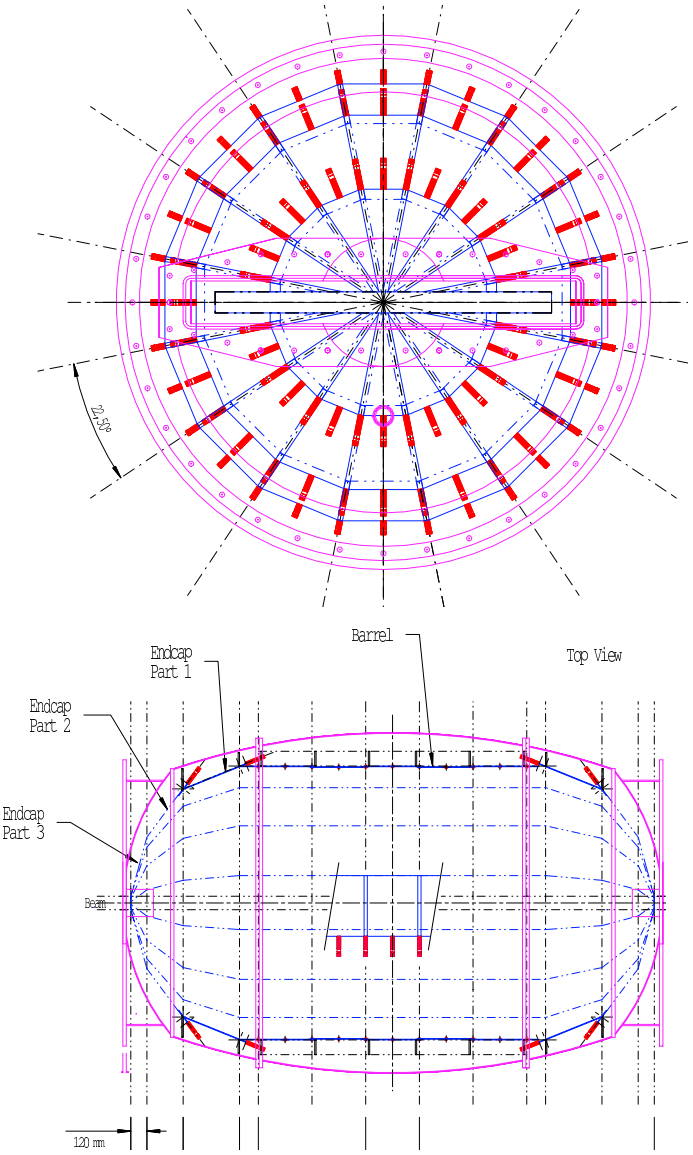

Figure 4.6:
End-cap view (top) and horizontal cross section (bottom) of the barrel CPV.

The Charged Particle Veto consists of three plastic scintillator systems. Our group is responsible for the Barrel CPV (see Fig. 4.6) which consists of 2-mm-thick tiles of Bicron BC408 plastic scintillator covering the walls of the decay tank with the exception of the regions where the beam crosses. The Downstream CPV lines the downstream beam pipe where it crosses the photon detectors. This system is followed by a sweeping magnet and associated veto counters.

Time schedule

The KOPIO construction phase will last about five years starting in October 2005. It is our intention to finish production of the barrel CPV early in the year 2007. Installation at BNL would take place towards the end of 2008.

5 Ultra Cold Neutrons

P. Fierlinger, S. Heule, U. Straumann

in collaboration with:
ETHZ; Fraunhofer Institut, Dresden; ILL, Grenoble; North Carolina State University, Raleigh; PNPI, Gatchina; PSI, Villigen; Virginia Tech, Blacksburg; ETHZ

At the Paul Scherrer Institut (PSI) a new source of ultra cold neutrons (UCN) will be constructed with the goal to improve the sensitivity to the neutron electric dipole moment (nEDM), which is sensitive to possible contributions from new physics. In addition the neutron decay parameters such as its life time may be studied more accurately. Presently, we contribute to the preparation of the UCN source.

UCN (1) have a kinetic energy which is below the Fermi potential of some materials (e.g. Beryllium 258 neV) and thus are totally reflected by walls covered with such material. This neutron energy corresponds to a temperature of 3 mK, a velocity of 6.8 m/s and a wavelength of about 50 nm. When reflected on the walls, however, neutrons are lost with a small probability of order 10^{-4}. This experimental observation does not agree with theoretical predictions, which are several orders of magnitude lower. At the same time depolarization at a level of order 10^{-6} is observed, which is also unexplained.

In the past year we constructed a novel apparatus (DEPOL experiment, PSI project number R-00-03.1, see also (2)) to measure the reflection and polarization loss probabilities of various wall materials. The neutrons are stored inside a vertical tube, with walls coated by the material to be studied. This tube is closed at the bottom by a magnetic field, such that only neutrons with one polarization are kept inside. At the top of the tube the UCN can not escape, since they have not enough energy to overcome the gravitational potential.

This DEPOL experiment (see Sec. 5.1) is the thesis subject of Peter Fierlinger, who in addition developed a Monte Carlo tool to simulate UCN including their gravitational field interaction (see Sec. 5.3) to be used within the framework of GEANT4. Stefan Heule's thesis deals with the production of clean diamond-like coated (DLC) surfaces as an easier alternative to the toxic Beryllium to store UCN (see Sec. 5.2). The use of Diamond as the storage material is motivated by its high Fermi potential of 304 neV.

5.1 A measurement of depolarization and loss probabilities of stored UCN

In this experiment we tested diamond-like coatings (DLC) and Beryllium coatings on Quartz and Aluminium tubes between room temperature and 70 K. We also took data with DLC coated Polyethylene Terephthalate (PET) and Aluminium foils and found excellent storage times. To our knowledge this is the first time that UCN have been stored in containers made from plastic foils. The foils were mounted into the apparatus squeezed into a cylinder like shape in such a way that only the coated surfaces were visible to the neutrons. The experiment took place in spring 2004 at the ILL in Grenoble.

The loss probability per bounce was measured by counting the number of neutrons remain-

Table 5.1: Measured loss and depolarization probabilities per wall interaction on foils (preliminary). Data taken on a Be coated tube in the same setup are given for comparison.

sample	temperature	loss probability η	depolarization probability β
	K	$\times 10^{-4}$	$\times 10^{-6}$
DLC on PET	300	1.63 ± 0.10	15.1 ± 1.0
DLC on PET	70	0.72 ± 0.12	15.7 ± 0.9
DLC on Al	300	3.52 ± 0.06	0.70 ± 0.21
DLC on Al	70	1.73 ± 0.09	0.80 ± 0.25
Be on Al	300	4.2 ± 0.3	11.8 ± 0.5

ing in the storage volume after a certain time, at which the magnetic field is turned off, and the number of neutrons falling out of the tube is counted. Depolarization is measured by observing neutrons leaving the storage volume during the time the magnetic field is turned on. Both measurements require the knowledge of the number of wall interactions during the storage time. This number was calculated using Geant 4 (see Sec. 5.3). We found loss probabilities, which are consistent with the literature values for Beryllium. DLC turns out to have similar or even smaller loss probabilities than Beryllium. The preliminary results of the measurements with the DLC coated foils are given in Tab. 5.1. While loss probabilities seem to be temperature dependent, depolarization probabilities are not. The base material onto which DLC is coated plays an important role. It affects both the losses and the depolarization, but in opposite direction. Possible explanations for these effects are being worked on, including hydrogen contamination with different chemical bond strength on Aluminium and PET.

Storage of UCN in thin foils opens up a wide range of opportunities for new neutron β-decay experiments. Neutron bottles could be made thin enough for the β-decay electrons to pass through them. Non metallic walls allow free design of magnetic and electric fields in the decay volume. We plan to continue this experiment with an improved setup including in situ surface monitoring.

5.2 Characterization of diamond-like carbon coatings

It is planned to produce diamond-like carbon (DLC) coated films at PSI with Pulsed Laser Deposition (PLD). Natural carbon exists in two varieties, Diamond and Graphite. The carbon atoms of Diamond are connected with sp^3-bonds, those of Graphite with sp^2-bonds. Amorphous carbon with a significant amount of sp^3-bonds is called DLC. We have investigated DLC films on different substrates (Aluminium, Silicon and PET). For UCN applications the interesting parameter is the critical velocity v_C (defining the maximum storable velocity in a material container) which is directly related to the mass density ρ and total sp^3 fraction, here denoted by s_{32}. The limits for DLC are therefore ρ=2 g/cm^3, v_C=5.8 m/s for Graphite and ρ=3.5 g/cm^3, v_C=7.6 m/s for pure Diamond. At ρ=2.9 g/cm^3 the corresponding v_C=6.9 m/s is equal to that of Beryllium.

To find an optimum characterization procedure Raman spectroscopy, X-ray absorption near-edge spectroscopy (XANES), X-ray photoemission spectroscopy (XPS), neutron reflectometry and the Laser Acoustic Wave propagation method (LAWave) at the Fraunhofer Institut für Werkstoff- und Strahltechnik in Dresden were used.

Raman spectroscopy (here at $\lambda = 648$ nm) can be used for characterization of DLC films. For amorphous carbon films the Raman spectrum consists mainly of one broad asymmetric peak around wavenumber 1300-1500 cm^{-1}. This peak is deconvoluted into two peaks where one of them can be assigned to a specific graphite feature, called the G band. One can derive s_{32} from the width of the G band which correlates with s_{32} (3). The method works best for s_{32} above 80%. We used XPS to determine s_{32} of the uppermost film layer. It can be directly derived from the XPS spectrum around a binding energy of 285 eV by fitting multiple curves (4). With XPS an accuracy of $\sim$10% for s_{32} can be reached. In order to cross-check the XPS results, measurements with XANES have been performed at the materials beamline at the SLS. The XANES results correctly describe the systematic s_{32} variation of our samples, however, the problem of quantification is not solved yet. One can estimate s_{32} from a special feature in the XANES spectrum which is due to the graphitic structure only (5). Neutron reflectometry has been used to determine the critical velocity directly. In the LAWave method (6), a pulsed laser induces an acoustic surface wave which propagates with a velocity depending on the penetration depth of the wave and the density of the material. The density of the material can be derived from this phase velocity.

In order to quantitatively compare the different characterization methods, a series of DLC coatings with a systematic variation of the s_{32} ratio (on silicon substrates) has been produced by the Fraunhofer IWS in Dresden. As the different methods measure different parameters (e.g. s_{32}, critical velocity), all results have been converted into density. Figure 5.1 shows preliminary density values for eight different samples.

Although reliable errors have not been determined yet, the agreement between the results from the different methods is good (with the exception of sample no. 6). Since the methods have different depth sensitivities (XPS $\sim$3 nm, AMOR $\sim$10 nm, Raman through the full film, LAWave in the order of the film thickness) small deviations are to be expected if the density varies with depth. This might allow to get some information about the depth dependence of the film density.

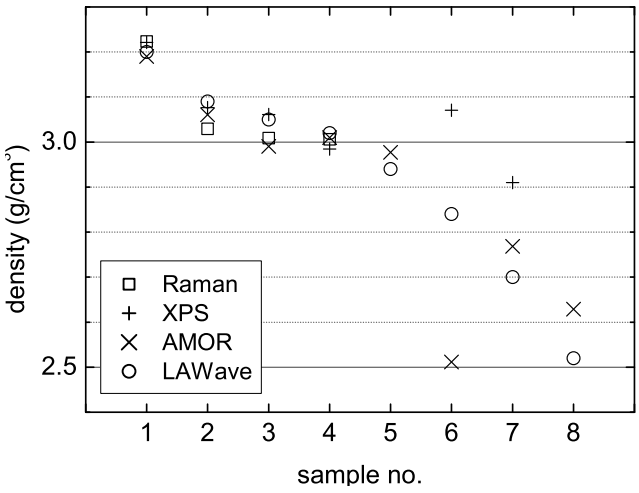

Figure 5.1:
Preliminary results for DLC films with a thickness of $\sim$100 nm (samples 1-4) and $\sim$ 10 nm (samples 5-8), measured with different characterization methods.

5.3 Simulation of ultracold neutron experiments using GEANT4

The Monte Carlo program GEANT4 (7) is a versatile, widely used toolkit for the simulation of particles passing through matter. Its application areas include high energy and nuclear physics experiments, medical, accelerator and space physics studies. As such, it can han-

dle many physically possible processes, including decay and particle production, allowing to combine the trajectory of both, the 'parent' UCN as well as the 'daughter' decay products, e.g. in neutron decay experiments. It therefore appeared very tempting to exploit the GEANT4 advantages - versatility, completeness, easy geometry implementation and professional maintenance - and extend it to the case of UCN. The additions to the code mainly

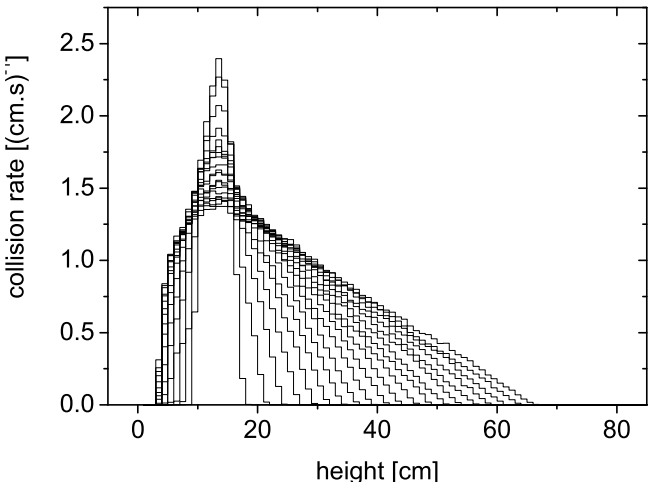

Figure 5.2:
Collision distribution for different neutron energies. The X-axis denotes the height in the tube above B-field maximum, the Y-axis the number of collisions per neutron per second on a 1 cm section of the tube in height. The curves represent energies from 12.5 to 67.5 neV in 2.5 neV steps, where the higher energies reach deeper into the magnetic field and higher up against gravity.

concern gravity and time-varying, inhomogeneous magnetic fields, reflection and scattering for UCN and new geometries(8).

Although neutrons are treated in the standard GEANT4 package we have introduced UCN as a new type of particle, being the only species to be affected by gravity. Gravity is implemented analogous to a constant homogeneous electric field for charged particles and is normalized such that the gravitational energy is $E_g = mgh = (102\,\text{neV/m})\cdot h$. The magnetic interaction is mediated by the magnetic moment of the neutron, $E_m = -\mu\cdot\mathbf{B} = (\pm 60\,\text{neV/T})\cdot B$, where the sign is determined by the relative direction of the magnetic moment and the field. Strongly inhomogeneous, time-varying magnetic fields are included for UCN in the so-called adiabatic limit, i.e. when the Larmor-precession is much faster than the time dependence of the field seen by the neutron moving through the inhomogeneous field.

As an example a vertical tube as has been used in the DEPOL experiment with inner diameter 70 mm closed by a 1.5 T magnetic valve on the bottom is simulated. Neutrons enter the tube from the bottom without magnetic field until the magnetic valve is closed. One spin component of the neutrons is trapped by the magnetic field on the bottom, gravity on the top and the reflecting walls of the tube. The simulation of the tracks inside this volume allows for the determination of the wall collision distribution (Fig. 5.2).

[1] R. Golub, D. J. Richardson, S. K. Lamoreaux,
Ultra-cold Neutrons, Adam Hilger, Bristol, Philadelphia and New York (1991).

[2] T. Bryś *et al.*, PSI Scientific Report 2003/Volume I, p. 137.

[3] A. Stanishevsky and L. Khriachtchev, Diam. and Rel. Mat. **5**, 1355 (1996).

[4] P. Mérel *et al.*, Appl. Surf. Sci. **136**, 105 (1998).

[5] G. Comelli *et al.* , Phys. Rev. B **38**, 7511 (1988).

[6] D. Schneider *et al.* , Thin Solid Films **295**, 107 (1997).

[7] S. Agostinelli *et al.*, Nucl.Instr.Meth.A 506 (2003) 250-303.

[8] **The Simulation of Ultracold Neutron Experiments using GEANT4**, F. Atchison *et al.*, Nucl.Instr.Meth., submitted (2004).

6 Precision Measurements in Rare Pion Decays

P. Robmann, T. Sakhelashvili, A. van der Schaaf, S. Scheu, U. Straumann and P. Truöl

in collaboration with:
CSRT, Faculty of Physics, Sofia, Bulgaria; Department of Physics, University of Virginia, Charlottesville, USA; Dept. of Physics and Astronomy, Arizona State University, Tempe, USA; Institute for Nuclear Studies, Swierk, Poland; Institute for High Energy Physics, Tbilisi, Georgia; JINR, Dubna, Russia; Paul Scherrer Institut, Villigen, Switzerland and Rudjer Bošković Intitute, Zagreb, Croatia

(PIBETA Collaboration)

Early in 2004 the Physik-Insitut joined the PIBETA Collaboration which performs a research project at the *Paul Scherrer Institut* (PSI) in Villigen, Switzerland on rare π and μ decays. Primary objective is the determination of the $\pi^+ \to \pi^0 e^+ \nu_e$ (pion beta decay) branching ratio with a precision of $\approx$ 0.4%, *i.e.* an order of magnitude better than achieved previously. This branching ratio, despite of its very low value of 10^{-8}, allows a direct determination of the CKM quark mixing matrix element V_{ud} with negligible theoretical uncertainties. The uncertainty in V_{ud} is the main limitation in tests of the unitarity of the CKM matrix which, in turn, is an important test of the validity of the Standard Model (SM) of particle physics.

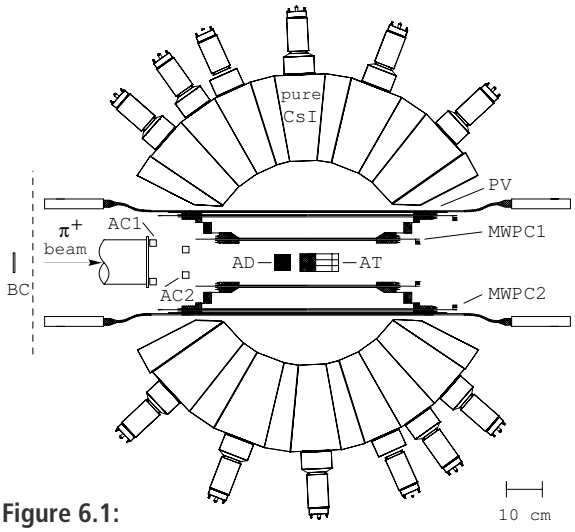

Figure 6.1:
The PIBETA detector.
BC**: beam counter,** AC1,2**: active beam collimators,** AD**: active degrader,** AT**: active target,** MWPC1,2**: cylindrical wire chambers,** PV**: plastic scintillating hodoscope. The pure-CsI calorimeter consist of 240 crystals.**

The pion beta decay branching ratio is determined by observing photons from the subsequent $\pi^0 \to 2\gamma$ decay in a spherical electromagnetic calorimeter consisting of 240 pure-CsI crystals (see Fig. 6.1). The decay rate is normalized to the rate of $\pi^+ \to e^+ \nu_e$ decays observed simultaneously. This way various systematic uncertainties, such as the number of stopped pions, electronic dead time and detector solid angle, can be removed. Data taking for this decay mode took place in the years 1999/2001 and a preliminary result is available (1). Since the Physik-Institut is not part of this effort we will not go in more detail here.

[1] Precise measurement of the $\pi^+ \to \pi^0 e^+ \nu_e$ branching ratio,
D. Pocanic *et al.*, Phys.Rev.Lett.**93** (2004) 181803 [arXiv:hep-ex/0312030].

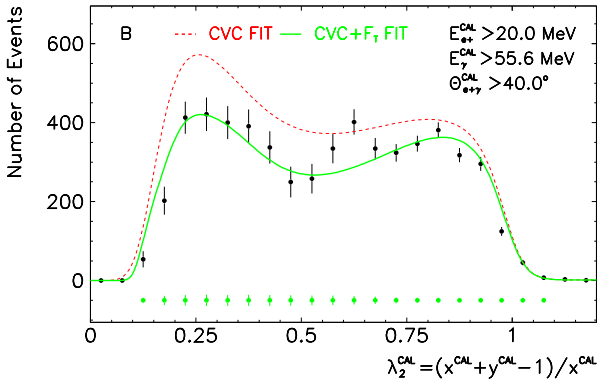

Figure 6.2:
$\pi^+ \to e^+\nu\gamma$ energy distribution for $E_\gamma > 55.8$ MeV and $E_{e^+} > 20$ MeV. x and y are the e^+ and γ energies, respectively, normalized to their endpoints $m_\pi c^2/2$. The quantity $\lambda \equiv (x+y-1)/x$ reaches its minimal value $\lambda = 0$ when e^+ and γ move in the same direction and its maximal value $\lambda = 1$ when e^+ and ν move together.

6.1 The $\pi^+ \to e^+\nu_e\gamma$ anomaly

The $\pi^+ \to e^+\nu_e\gamma$ decay was recorded during $\pi^+ \to \pi^0 e^+\nu_e$ data taking (1). This is the first time that this decay mode has been studied with a setup with almost complete geometric acceptance. Two decades ago we studied this decay (2) and its Dalitz correction $\pi^+ \to e^+\nu_e e^+e^-$ (3) and more recently the corresponding kaon modes $K^+ \to e^+\nu_e e^+e^-$, $K^+ \to \mu^+\nu_\mu e^+e^-$, and $K^+ \to e^+\nu_e\mu^+\mu^-$ (see Sec. 4.1). These decays proceed via a combination of inner bremsstrahlung (IB) and structure dependent (SD) amplitudes. The latter allows a determination of meson form factors, which, in turn, are an important input into chiral perturbation theory.

Based on Dalitz distributions of 42209 events $\gamma \equiv F_A/F_V$ = 0.443(15), or F_A = 0.0115(4) with F_V = 0.0259. However, 20% deviations were observed in the kinematic region of high E_γ and low E_{e^+} (see Fig.6.2). This kinematic region could not be studied in earlier measurements because of the high level of accidental coincidences with positrons from $\mu \to e\nu\overline{\nu}$ decay. To clarify the situation a dedicated measurement (4) was performed at reduced beam intensity for which we contributed an improved active target. A preliminary analysis of these 2004 data indicates a reduction of accidental background by one order of magnitude which allows us to relax the selection criteria. Firm conclusions will have to await further analysis.

[1] **Precise measurement of the pion axial form factor in the $\pi^+ \to e^+\nu\gamma$ decay**, E. Frlež *et al.*, Phys.Rev.Lett.**93** (2004) 181804 [arXiv:hep-ex/0312029].

[2] A. Bay *et al.*, Phys.Lett.B 174, 445 (1986).

[3] S. Egli *et al.*, Phys.Lett.B 222, 533 (1989).

[4] **Study of the $\pi^+ \to e^+\nu\gamma$ anomaly**, PSI Proposal R-04-01.1, E. Frlež and D. Počanić spokesmen, January 2004.

6.2 A precision determination of the $\pi^+ \to e^+\nu$ branching ratio

The $\pi^+ \to e^+\nu$ / $\pi^+ \to \mu^+\nu$ branching ratio is presently the best test of μe universality, *i.e.* the equality of the couplings of $\mu\nu_\mu$ and $e\nu_e$ to the W boson. Recent results in τ decays provide tests for all three generations which start to approach but are still not as sensitive as the 10 year old results from pion decay. As mentioned above this branching ratio is used

as a normalization in the determination of the $\pi^+ \to \pi^0 e^+ \nu$ branching ratio. Independent normalizations based on the number of pion stops are consistent within 1%. This means that the $\pi^+ \to \pi^0 e^+ \nu$ measurement results in a determination of the $\pi^+ \to e^+ \nu$ branching ratio with a precision of 1%. We are confident that a dedicated experiment at lower beam intensity and with improved detection systems in the beam should allow for an improvement by one order of magnitude.

Allowing for violations of universality of the couplings between W and a $l_i \overline{\nu_i}$ pair the tree level partial width of the decay of a pion into such pair is:

$$\begin{aligned} \Gamma^{\rm tree}_{\pi\to e\overline{\nu}} &= \frac{g_e^2 g_{ud}^2 V_{ud}^2}{256\pi} \frac{f_\pi^2}{M_W^4} m_e^2 m_\pi (1-\frac{m_e^2}{m_\pi^2})^2 \\ \Gamma^{\rm tree}_{\pi\to \mu\overline{\nu}} &= \frac{g_\mu^2 g_{ud}^2 V_{ud}^2}{256\pi} \times \frac{f_\pi^2}{M_W^4} m_\mu^2 m_\pi (1-\frac{m_\mu^2}{m_\pi^2})^2 \end{aligned} \tag{6.1}$$

leading to a branching ratio:

$$R^{\rm tree}_{e/\mu} \equiv \frac{\Gamma^{\rm tree}_{\pi\to e\overline{\nu}}}{\Gamma^{\rm tree}_{\pi\to \mu\overline{\nu}}} = (\frac{g_e}{g_\mu} \times \frac{m_e}{m_\mu} \times \frac{1-m_e^2/m_\pi^2}{1-m_\mu^2/m_\pi^2})^2 \tag{6.2}$$

Radiative corrections lower this value by 3.74(1)% (1). Within the SM $g_e = g_\mu = 1$ which leads to a predicted value:

$$R^{\rm SM}_{e/\mu} = 1.2350(5) \times 10^{-4} \tag{6.3}$$

Two experiments (2; 3) contribute to the present world average (4) for the measured value:

$$R^{\rm exp}_{e/\mu} = 1.230(4) \times 10^{-4} \tag{6.4}$$

As a result μe universality has been tested at the level:

$$g_\mu / g_e = 1.0021(16) \tag{6.5}$$

Other constraints on violations of lepton universality can be derived from from W and τ branching ratios. More general quark-lepton universality can be tested (5). Violations of lepton universality have been discussed recently by Antonio Pich (6) and by Will Loinaz *et al.* (7). Figure 6.3 shows a graphic representation of the actual situation. As can be seen from the figure π and τ decays give the best constraints at present.

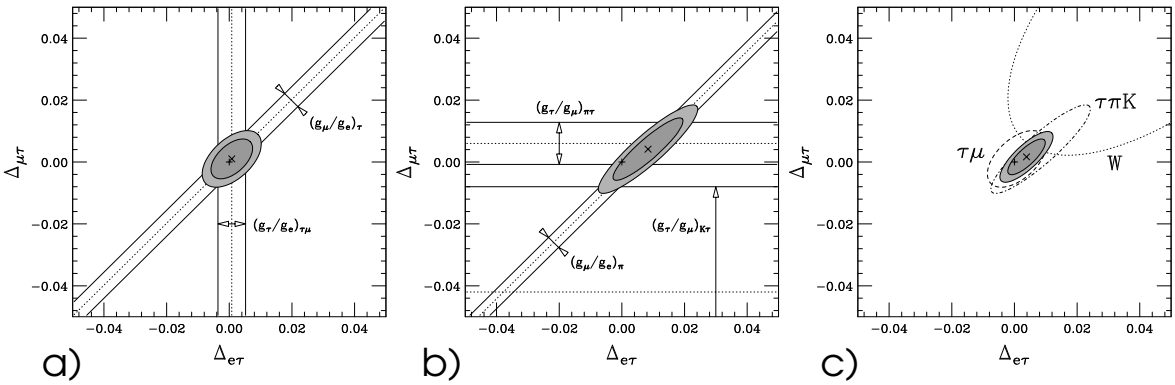

Figure 6.3:
Experimental constraints on violations of lepton universality. $\Delta_{ij} = 2(\frac{g_i}{g_j} - 1)$.
a: from τ decay, b: from π and K decay and c: combined result. From [7].

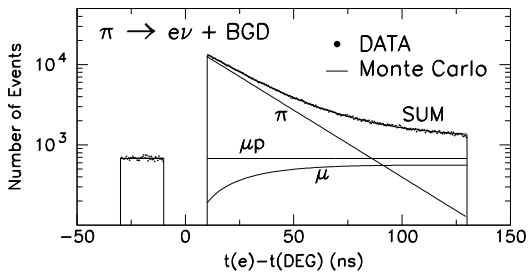

Figure 6.4:
Delay between pion stop and decay. The measured data (dots) are nicely described by $\pi^+ \to e^+$ decay, $\pi^+ \to \mu^+ \to e^+$ decay chain and pile-up (accidental coincidences). The prompt region which is contaminated by hadronic interactions has been removed at trigger level.

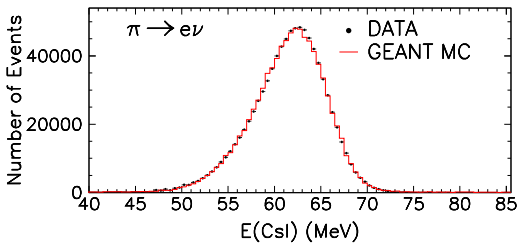

Figure 6.5:
Distribution of CsI total energy for $\pi^+ \to e^+\nu$ decays after background subtraction.

During the years 1999/2001 the PIBETA experiment recorded a huge sample of $\pi^+ \to e^+\nu$ decays. Figures 6.4 and 6.5 show time and energy distributions of decay electrons. Although the measurements were not optimized for this decay mode a clear $\pi^+ \to e^+\nu$ signal is observed with a total systematic error below $\approx$ 1%, i.e. within a factor 2-3 of the dedicated experiments. The main contribution to this uncertainty is in the determination of the number of stopped pions, a quantity which does not enter the determination of the $\pi^+ \to \pi^0 e^+\nu$ branching ratio. The statistical uncertainty associated with the number of observed $\pi^+ \to e^+\nu$ events is totally negligible in this data set. As will be discussed below we are confident that a dedicated experiment with improved beam monitoring and at reduced beam intensity should reach a precision of $O(0.1\%)$, a 3-4 fold improvement compared to the present world average.

Time table

At the January 2005 meeting of the PSI Program Advisory Committee a letter of intent for a measurement of the $\pi \to e\nu$ branching ration (8) was very well received and four weeks of beam time were granted for beam studies and detector tests. A full proposal will be submitted by the end of 2005.

Our group took over the responsibility to develop an ultra-fast beam monitoring system based on 0.6 ns scintillator and microchannel photomultipliers. Waveform digitizers with $\approx$ 5 GHz sampling rates will be used with the aim of reaching a double pulse resolution $O(1\,\text{ns})$ in the target detector. We are investigating options for silicon strip detectors used to track the beam particles which is particularly useful to distinguish pions from halo muons. It is our aim to have most of the necessary R&D done before submission of the proposal.

[1] R. Decker and M. Finkemeier, Nucl.Phys.B 438, 17 (1995).

[2] G. Czapek *et al.*, Phys.Rev.Lett.70, 17 (1993).

[3] D.I. Britton *et al.*, Phys.Rev.Lett.68 (1992) 3000, D.I. Britton *et al.*, Phys.Rev.D 49, 28 (1994).

[4] S. Eidelman *et al.*, (Particle Data Group), Phys.Lett.B 592, 1 (2004).

[5] **Quark-Lepton Nonuniversality**, X.-Y. Li and E. Ma, XXIII ENFPC, Aguas de Lindoia, Brazil (2002), hep-ph/0301006.

[6] **Leptonic Probes of the Standard Model**, A. Pich, hep-ph/0210445,
The Standard Model of Particle Physics: Status and Low-Energy Tests, A. Pich, hep-ph/020611.

[7] **The NuTeV Anomaly, Lepton Unuiversality, and Non-Universal Neutrino-Gauge Couplings**, W. Loinaz *et al.*, Phys.Rev.D 70 (2004) 113004, hep-ph/0403306.

[8] **Precise Measurement of the $\pi^+ \to e^+\nu$ Branching ratio**, D. Pocanic *et al.*, PSI Letter of Intent R-05-01.0.

7 High-precision CP-violation Physics at LHCb

R. Bernet, R.P. Bernhard, J. Gassner, F. Lehner, C. Lois, M. Needham, M. Regli, T. Sakhelashvili, S. Steiner, M. Siegler, O. Steinkamp, U. Straumann, A. Vollhardt, D. Volyanskyy, A. Wenger

in collaboration with:
The silicon tracking group of LHCb: University of Lausanne; Max Planck Institute, Heidelberg, Germany; University of Santiago de Compostela, Spain; Budker Institute for Nuclear Physics (INP), Novosibirsk, Russia and Ukrainian Academy of Sciences, Kiev, Ukraine.

The full LHCb collaboration consists of 51 institutes from Brazil, China, Finland, France, Germany, Italy, The Netherlands, Poland, Romania, Russia, Spain, Switzerland, Ukraine, and the United Kingdom.

(LHCb)

7.1 Introduction

The LHCb experiment aims to perform high precision measurements of CP violating processes and rare decays in the B meson systems. By measuring CP violation in many different decay modes of B_d^0 and B_s^0 mesons the experiment will over-constrain the picture of CP violation given by the Standard Model of particle physics and possibly reveal the effect of new physics. Our group concentrates on the development, construction, operation and data analysis of the LHCb Silicon Tracker as well as on physics analyses.

7.2 The LHCb experiment

The LHCb experiment (1; 2) is designed to exploit the large $b\bar{b}$ production cross section at the Large Hadron Collider (LHC) at CERN in order to perform a wide range of precision studies of CP violating phenomena and rare decays in the B meson systems. The experiment will operate at a moderate luminosity of 2×10^{32} cm^{-2}s^{-1} and will be fully operational from the start of LHC operation in 2007.

In particular, the copious production of B_s^0 mesons, combined with the unique particle-identification capabilities of the LHCb detector, will permit the experiment to perform sensitive measurements of CP violating asymmetries in a variety of decay channels that are beyond the reach of the current generation of CP-violation experiments.

Since the production of b quarks in proton-proton collisions at LHC is strongly peaked towards small polar angles with respect to the beam axis, the LHCb detector is layed out as a single-arm forward spectrometer. Its acceptance extends out to 300 mrad in the horizontal bending plane of the 4 Tm dipole magnet and to 250 mrad in the vertical plane. The forward acceptance of the experiment is limited by the LHC beam pipe that passes through the detector and follows a 10 mrad cone pointing back to the p-p interaction region.

A vertical cut through the LHCb detector is shown in Fig. 7.1. The most important elements are: a silicon vertex detector, tracking system and ring-imaging Cherenkov (RICH) detectors. Excellent particle identification is a key requirement for the experiment. The ability to

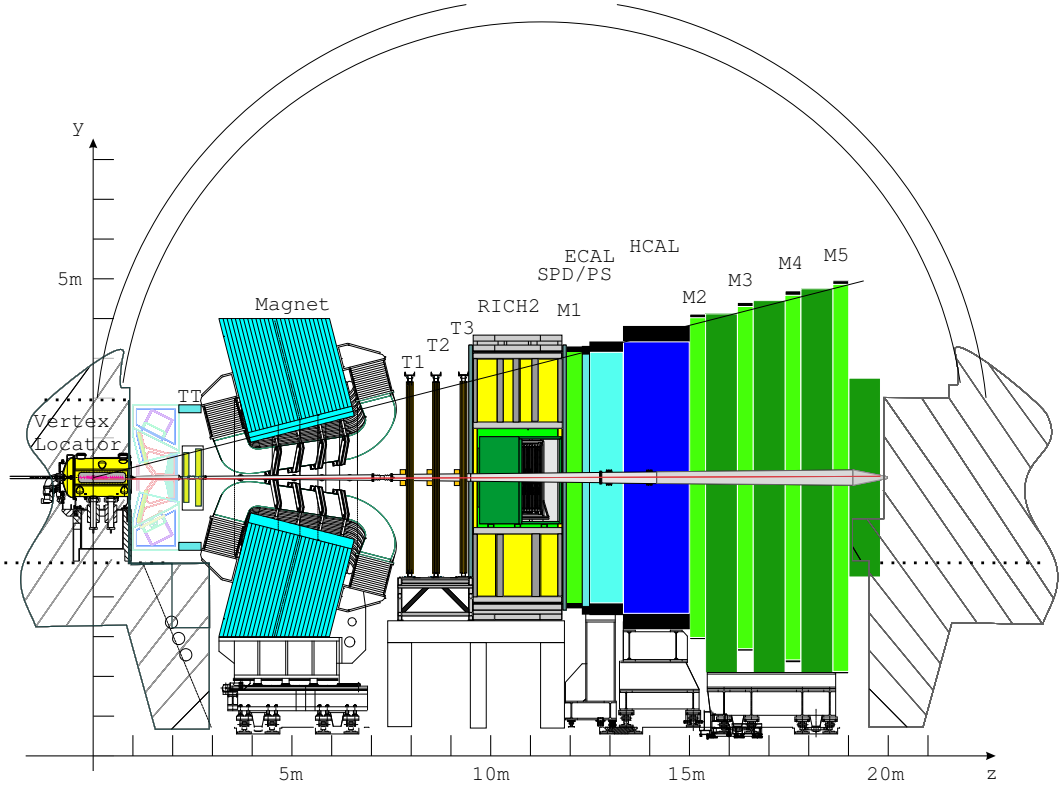

Figure 7.1:Vertical cross section through the LHCb detector.

distinguish final state with kaons and pions is essential in order to suppress specific backgrounds in many channels of interest and also to be able to select kaons for flavour tagging. Since measurements of particle trajectories are used as an input to the RICH reconstruction a highly efficient and well understood tracking system is essential to achieve good particle identification.

7.3 Silicon tracker

Our group has taken a leading rôle in the development, production and operation of the Silicon Tracker. The Silicon Tracker project is led by U. Straumann with O. Steinkamp as his deputy. It consists of two detectors that both employ silicon micro-strip technology but differ in important details of the technical design: The Inner Tracker (3) covers the innermost region around the beam-pipe in the three large tracking stations T1-T3 downstream of the spectrometer magnet; the Trigger Tracker, TT, (4) is located upstream of the spectrometer magnet and covers the full acceptance of the experiment.

The main responsibility of the group is the design and construction of the TT station. A large fraction of our efforts in 2004 were spent in the construction of final prototypes for the TT station and preparation for the detector production. In addition, our group is responsible for the L0 electronics and the development of the optical digital readout link for Inner Tracker and TT station. A prototype of the full readout system, using the final components has been set up and successfully tested in the laboratory.

7.4 TT station

The Trigger Tracker (TT station) fulfills a two-fold purpose: First, it will be used in the Level-1 trigger to assign transverse-momentum information to large-impact parameter tracks. Secondly, it will be used in the offline analysis to reconstruct the trajectories of low-momentum particles that are bent out of the acceptance of the experiment before reaching tracking stations T1-T3.

The TT station consists of four detection layers. Its active area is approximately 160 cm wide and 130 cm high and will be covered entirely by silicon micro-strip detectors. The layers are arranged into two half stations, referred to as TTa and TTb, split in z by a distance of around 30 cm. The layout of a detection layer is illustrated in Fig. 7.2. The areas above and below the beam pipe are each covered by a single seven-sensor long silicon ladder, the areas to the left and to the right of the beam pipe are covered by seven (TTa) or eight (TTb) 14-sensor long ladders. Electronically, each ladder is split into several readout sectors, indicated by different shadings in Fig. 7.2. In the outer part of the detector, where the fluence is low the readout sectors consist of four and three sensors chained together. In the innermost three columns where the the fluence is highest the three sensor sector is split into a one and two sensor sector. M. Siegler has has shown that this layout gives adequate performance in terms of radiation induced leakage currents and shot noise, even after ten years operation in the harsh environment of the LHC, whilst minimizing the number of readout channels (5).

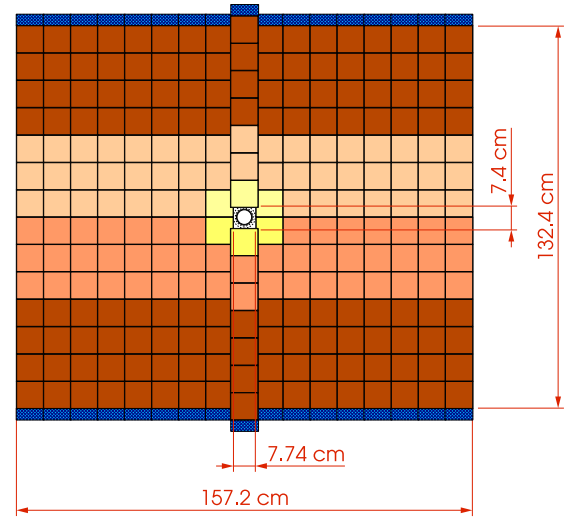

Figure 7.2:
Layout of one detection layer of the TT station. Readout sectors are indicated by different shading.

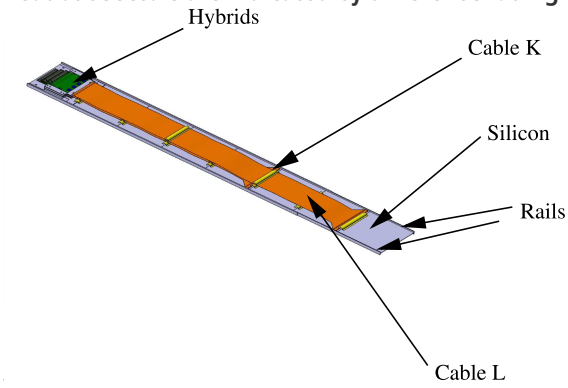

Figure 7.3:
Layout of a half module with two interconnect cables.

All readout electronics and associated mechanics are located at the top end or the bottom end of a ladder, outside of the acceptance of the experiment. The inner readout sectors are connected to their readout electronics via approximately 39 cm and 58 cm long Kapton interconnect cables. An isometric drawing of the basic detector unit, consisting of seven silicon sensors, a Kapton interconnect, and two staggered front-end readout hybrids, is shown in Fig. 7.3. The 14-sensor long ladders that cover the areas to the left and to the right of the beam pipe are assembled from two such detector units that are joined together at their ends. A readout strip pitch of 183 μm will be employed.

A substantial R&D effort has been carried out in our group in order to validate this layout and develop the mechanical design of the long detector modules and of the station frames.

7.5 Prototype tests

To verify the performance of the ladders equipped with interconnect cables two prototype modules have been built (see Fig. 7.4). Initial tests on the prototype ladders were performed in an infra-red laser test stand (6) in our laboratory by D. Volyanskyy and J. Gassner. A focussed 1064 nm laser beam is used to generate charges at well-defined locations in the silicon bulk and permitted systematic studies of signal pulse shapes as a function of various operation parameters of the detector and of the location of the charge deposition. A detailed description of the setup and the results obtained in the laser tests is given in (6).

Further measurements were then performed on the CMS3+Flex ladder at the X7 test-beam facility at CERN, in collaboration with our colleagues from Lausanne and Heidelberg. The analysis of the collected data was coordinated by M. Needham. A detailed description of the test-beam setup and the obtained results is given in (7).

Figure 7.5 shows the S/N distribution obtained for this ladder in the testbeam for tracks passing close to a readout strip. In Fig. 7.6 the dependence of the most likely S/N value on the inter-strip position is presented. It can be seen that for tracks passing close to a readout strip a S/N of 16 is obtained whilst for tracks passing midway between two readout strips a S/N of 14 is found. Such a charge loss has been observed in earlier tests of prototype modules and reproduced in a detector simulation (8). It is mainly attributed to loss of charge carriers at the boundary between the silicon bulk and the silicon oxide layer in between the two readout strips. These results are in good agreement with previous observations. Despite this charge loss full cluster finding efficiency is found across the entire inter-strip region.

The LHCb experiment is expected to operate for ten years in the harsh hadronic environment of the LHC. With time the radiation dose will significantly alter the electrical properties of the sensors. In particular it is known that after irradiation changes in the effective doping concentration and hence the depletion voltage occur (9). In addition, the increased leakage current leads to higher noise and heat dissipation. It is important to test the impact of these changes on the detector performance. To investigate the performance of IT sen-

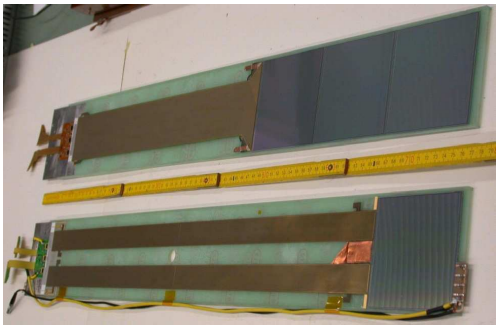

Figure 7.4:
Prototype ladders equipped with Kapton cables: CMS1+Flex (bottom) and CMS3+Flex (top).

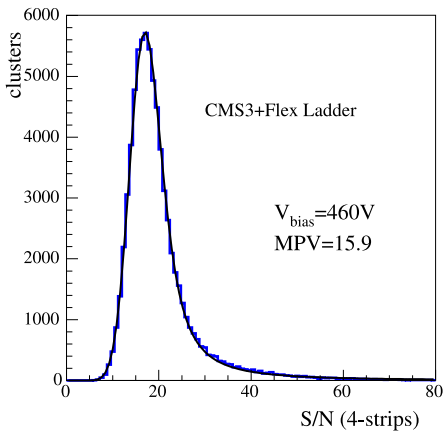

Figure 7.5:
Distribution of S/N derived from the sum of the four strips closest to the extrapolated track impact point for tracks passing close to a readout strip.

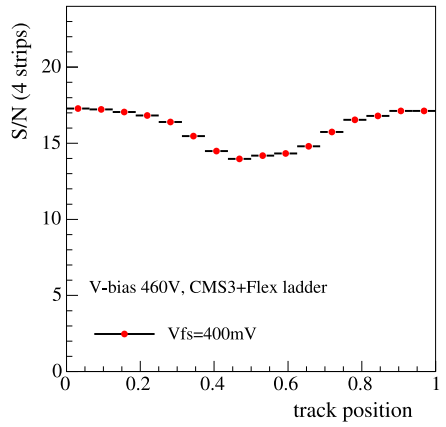

Figure 7.6:
Most likely S/N as a function of the inter-strip position.

sors after irradiation three LHCb multi-geometry prototype sensors were irradiated in a 24 GeV/c proton beam at the CERN PS with proton fluences in the range $2{-}6{\times}10^{13}$ cm^{-2}. The latter corresponds to the expected radiation dose after 20 years of LHCb operation. After irradiation the sensors were electrically characterized by C. Lois (10). Further tests were then carried out in the laser setup in Zürich (11). After irradiation the depletion voltage of the ladder irradiated up to 6×10^{13} cm^{-2} had increased from 70 V to 140 V. At room temperature a sizeable radiation induced leakage current is observed. This current leads to additional shot noise. As expected, both the leakage current (Fig. 7.7) and the shot noise could be suppressed by operating the ladders at temperatures around 5 °C. From these tests it is concluded that even after ten years operation at the LHC the detector will give adequate performance.

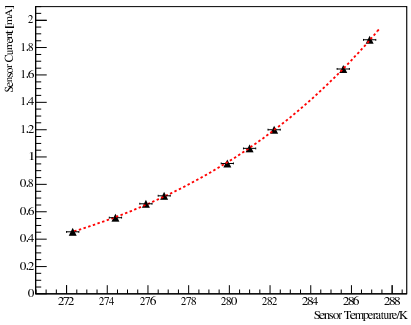

Figure 7.7:
Leakage current versus temperature for the irrad2 ladder

7.6 Preparation for the module production

Work has started in preparation for the final detector production which starts in May 2005. Sensors for both the IT and TT detectors will be first delivered to Zürich. A detailed test program including visual inspection, electrical characterization and metrology will then be carried out to assure the quality of the sensors. The majority of this work will be carried out by students working within our group. Procedures to be followed in this step have been produced by F. Lehner and tested on a preseries of sensors for the TT and IT (12).
Several prototype modules for the TT station have been produced in order to test the procedure to be followed. Bonding tests have also been made and adequate pull strengths achieved.
After production all modules will be tested in a 'burn in' stand being set up by M. Needham together with D. Volyanskyy and A. Wenger. Four TT modules will be tested at a time in a custom built box (Fig. 7.8). Electronics needed to control and readout the system is presently being prepared (Fig. 7.9).

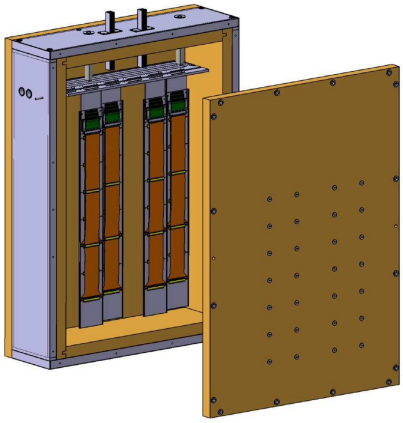

Figure 7.8:Detail of the burn-in box.

Figure 7.9:Detail of the electronics.

7.7 Readout system

The Beetle front-end chip samples detector data at the LHC bunch crossing frequency of 40 MHz and stores the analog data for the latency of the Level-0 trigger. On receipt of a trigger accept, the analog data are multiplexed, read out, digitised and transmitted to the LHCb electronics barrack. For the Silicon Tracker, the design and production of the electronics to do this is a responsibility of our group. Further processing of the data then occurs in the electronics barrack before the data is transmitted to the data acquisition system.

After transmission of the data from the Beetle the first step in the processing chain is to digitize the data. This occurs on digitizer boards located in service boxes placed close to the detector in the LHCb cavern. This electronics has been designed by A. Vollhardt as part of his Ph.D thesis work. This work has included qualifying all the components used for the expected radiation dose of 10 kRad after 10 years at the location of the service boxes (13). Prototypes for the digitizer boards have been produced and successfully tested in the laboratory. Data from the service boxes is transmitted to the electronics barracks using an optical link. Since the L0 Trigger operates at an accept rate of 1.1 MHz, up to 2.6 Tbit/s of digitised detector data have to be transmitted for the Silicon Tracker. A. Vollhardt has designed and tested a low-cost digital optical link using commercially available components for this purpose. Similar developments are underway for other LHCb subsystems and a common working group has been formed by A. Vollhardt. He organizes regular group meetings, in which common solutions are discussed and the selection of commercial components is coordinated.

After transmission to the electronics barracks the data will be processed using L1 electronics boards developed by EPFL, Lausanne. Prototypes of this board have recently become available and have been integrated with the optical link setup in Zurich. This has allowed a first test of the complete readout chain to be carried out.

7.8 Simulation studies

The group is also active in studies of expected LHCb performance in preparation for LHCb startup. This work takes two forms. The first is the studies of LHCb physics reach described in the next section. The second is in the on-going studies of the performance of the tracking system. M. Needham has written a fast and efficient algorithm for searching track seeds in the Inner Tracker ('Tsa') (14). This algorithm is now being extended to Outer Tracker. Work has also been undertaken by A. Wenger and M. Needham to provide and up-to-date estimates of the material budget of the TT station for the LHCb Monte Carlo simulation.

7.8.1 Physics studies

In preparation for data taking the group has started to work on physics simulation studies. Such studies are important in order to understand the physics reach of LHCb, to investigate possible sources of systematic uncertainty and to optimize the performance of the trigger. We have chosen to concentrate our efforts in the area of B_s physics, which is beyond the reach of the current generation of B factories. Currently we are studying two decay modes. The first is the rare decay $B_s \to \phi\mu^+\mu^-$. The measurement of the forward-backward asymmetry of the lepton pair in this decay mode constitutes an important test of the standard model (15). As part of his Ph.D work A. Wenger, supervised by M. Needham, investigates this decay mode. He works to develop an analysis for this decay mode and to determine the annual expected yield and signal-to-background ratio. This work is being undertaken in close co-operation with R. Bernhard who is undertaking a search for this decay at D0 (see Sec.3).

The second decay mode being studied is $B_s \to J/\psi\eta'$. This decay mode can be used to measure the CKM angle χ via a time dependent CP asymmetry measurement. A high precision measurement of this angle is an important check of the standard model (16). This work is being jointly undertaken by D. Volyanskyy as part of his Ph.D. thesis and M.Regli as

part of his Diploma studies. They investigate the physics sensitivity of LHCb for this decay mode by estimating the annual expected yield and the signal-to-background ratio.

7.8.2 Summary and outlook

Tests of final detector modules and preparation for the final detector production has been the major occupation of our group over the last year. Successful prototype tests have been performed in the laboratory and in test-beams and a mechanical design of the station has been completed. Preparations for the production of the detector are ongoing. Series production will commence in May of 2005. Detailed testing and quality assurance will be performed in a burn-in stand being set up in Zurich. The detector will be installed and fully commissioned before the startup of LHC, foreseen for 2007.

A full system test of the final readout electronics has been performed in the laboratory. The system will now be used to test modules in the burn-in stand.

In preparation for Physics data taking, the group has started to work on simulation studies, studying the decay modes $B_s \to \phi\mu^+\mu^-$ and $B_s \to J/\psi\eta'$. These studies will continue over the next years and will permit the group to build up experience of Physics analyses.

[1] **LHCb technical proposal**, CERN/LHCC 998-4.

[2] **LHCb Reoptimised Detector Technical Design Report**, CERN/LHCC 2003-030.

[3] **LHCb Inner Tracker Technical Design Report**, CERN/LHCC 2002-029.

[4] **Layout and expected performance of the LHCb TT station**, J. Gassner, M. Needham, O. Steinkamp, LHCb-2003-140.

[5] **Expected Particle Fluences and Performance of the LHCb Trigger Tracker**, M. Siegler *et al.*, LHCb note 2004-070.

[6] **Measurements of Prototype Ladders for the TT station with a Laser**, J. Gassner *et al.*, LHCb-2004-102.

[7] **Measurements of a prototype ladder for the TT station in a 120 GeV/c π^- beam**, M. Agari *et al.*, LHCb-2004-103.

[8] **Simulation und Messung von Silizium-Streifen-Detektoren**, St. Heule, , Diplomarbeit, Universität Zürich, 2003; see also: **Simulation of Signal Generation in Silicon Micro-strip Detectors for the Silicon Tracker of the LHCb Experiment**, St. Heule and F. Lehner, LHCb-2003-159.

[9] G. Lindstrom *et al.* NIM **A 426** (1999) .

[10] **Measurements on irradiated silicon sensor prototypes for the Inner Tracker of LHCb**, F. Lehner et al, LHCb-2004-104.

[11] **Laboratory Measurements on Irradiated Prototype Ladders for the LHCb Inner Tracker** , C. Lois *et al.*, LHCb-2004-112.

[12] **Quality Assurance of 100 CMS2-OB2 Sensors**, G. Baumann *et al.*, LHCb-2004-105.

[13] **Results of proton irradiation of components for the LHCb Silicon Tracker**, A. Vollhardt *et al.*, LHCb-2004-037.

[14] **Tsa: Fast and efficient reconstruction for the Inner Tracker**, M. Needham, LHCb-2004-075.

[15] T. Hurth, Review of Modern Physics **75** (2003) 1159 .

[16] J.P. Silva and L. Wolfenstein, Phys.Rev.**D 55** (1997) 5331.

8 Particle Physics with CMS at the LHC

Y. Allkofer, C. Amsler, V. Chiochia, A. Dorokhov, C. Hörmann, K. Prokofiev, H. Pruys, C. Regenfus, P. Robmann, J. Rochet, T. Speer, S. Steiner, and D. Tsirigkas[3]

in collaboration with:
ETH-Zürich, Paul Scherrer Institut (PSI) and the CMS Collaboration

(CMS Collaboration)

8.1 Physics programme

The Higgs boson mass is predicted to be smaller than 251 GeV (95 % C.L.) and LEP experiments have set a lower experimental limit of 114 GeV (95 % C.L.). A light Higgs decays mainly to $b\bar{b}$, a heavy Higgs mainly to four leptons via WW or Z^0Z^0 (Fig. 8.1). However, the two-gluon $gg \rightarrow b\bar{b}$ background dominates the signal for a light Higgs. For CMS one of the sensitive channels to search for a light Higgs is $H \rightarrow \gamma\gamma$ (Fig. 8.2). This is the motivation for the large electromagnetic calorimeter made of 80'000 $PbWO_4$ crystals.
The LHC is scheduled to start operations in 2007 at a center of mass energy of $\sqrt{s}$ = 14 TeV. The target luminosity is 10^{34} cm^{-2}s^{-1} which corresponds to an integrated luminosity of about 1 fb^{-1}, achieved every day, assuming full efficiency. This luminosity will hopefully be reached after 2 - 3 years of LHC operation. Figure 8.2 shows the required integrated luminosity for a 5σ Higgs discovery, as a function of mass. Since the final luminosity will not be obtained immediately, the Higgs is not likely to be observed during the commissioning years, unless it is rather heavy (see Fig. 8.2).
The Zurich group has therefore decided to concentrate first on issues related to B meson physics. At the LHC the cross section for $b\bar{b}$ production is five orders of magnitude higher than at the Tevatron and 10^4 $b\bar{b}$ pairs/s will be produced, even with a reduced luminosity of 10^{33} cm^{-2}s^{-1}. Also the physics involving B_s mesons ($\bar{d}s$ and $\bar{s}d$) will not be covered at the current B factories (since the $Y(4s)$ does not decay to $B_s\bar{B}_s$). For B physics the pixel detector we are constructing will be essential to tag secondary vertices from B decays.

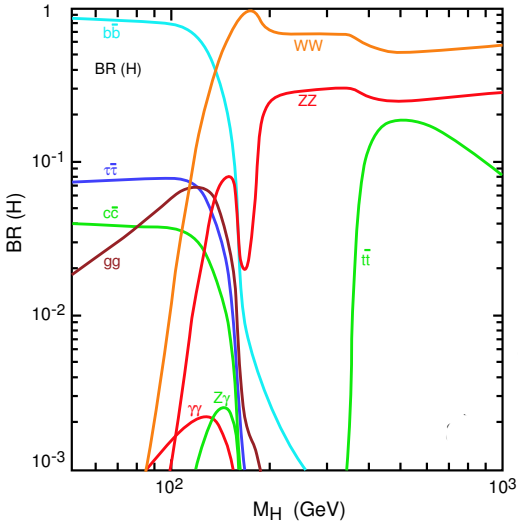

Figure 8.1:
Higgs decay branching ratios as a function of Higgs mass.

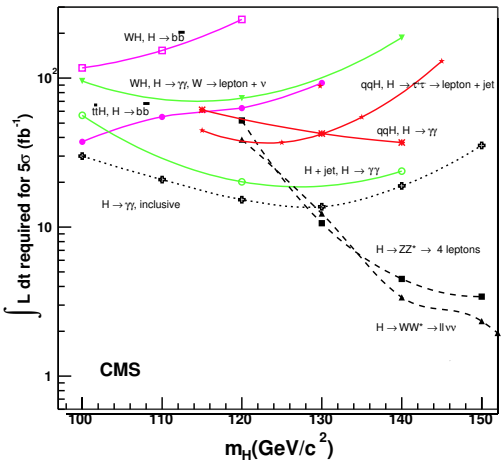

Figure 8.2:
Integrated luminosity required for a discovery with statistical significance of 5σ (1 fb^{-1} represents 1 day of LHC operation at full luminosity and efficiency).

[3]CERN doctoral student

We are preparing (1) a high statistics measurement of the decay channel $B_s \to J/\psi\ \phi$ with $J/\psi \to \mu^+\mu^-$ (or e^+e^-) and $\phi \to K^+K^-$. This channel is one of the golden channels to study many properties of B_s mesons such as CP violation in the B_s system and $B_s - \bar{B}_s$ oscillations. The search for rare B_s-decays such as $B_s \to \mu^+\mu^-$, $B_s \to \mu^+\mu^-\phi$, which have not been observed, opens windows for new physics beyond the standard model. Our experience with the reconstruction of B mesons at CMS will then be quite useful to search for the Higgs in a cleaner environment, such as the associated production $t\bar{t}H, H \to b\bar{b}$, leading to four jets containing b-quarks.

8.2 Performance tests of the silicon pixel detector

To reconstruct B mesons and suppress the dominating light quark and gluon background one has to determine the primary interaction and secondary B decay vertices. The optimum resolution is achieved with the first detector layer as close as possible to the beam-beam collision point. The first layer of our silicon pixel detector is at a distance of $\sim$ 4 cm from the interaction point. The very high particle flux near the primary vertex ($\sim$ 1000 particles every 25 ns) requires a highly granular detector composed of pixels delivering 3D coordinates with resolutions of the order of 15 μm.

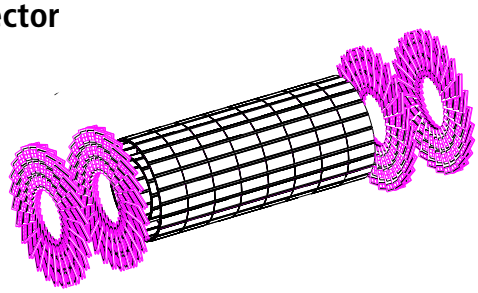

Figure 8.3:The CMS pixel vertex detector.

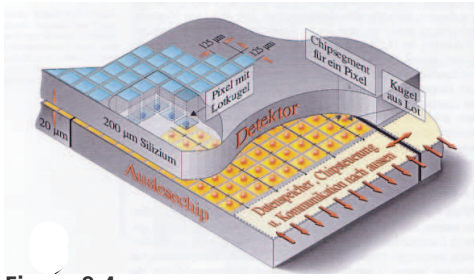

Figure 8.4:
Schematic view of a pixel detector element. Each sensor pixel is connected through an indium solder bump to a pixel unit cell on the readout chip which amplifies and processes the signal. The data are stored at the periphery of the chip where they wait for trigger confirmation.

The pixel detector consists of three concentric cylindrical layers, 53 cm long, with radii of 4.4, 7.3 and 10.2 cm and forward/backward wheels (Fig. 8.3). The latter wheels will be provided by the US collaborators while the barrel layers are built by the Swiss groups. The pixels are mounted on segmented sensor plates with readout chips in 0.25 μm technology, connected by indium bump bonds (Fig. 8.4). The analogue signals are read out to determine the coordinates more accurately, using charge sharing between pixels.

Radiation hardness is the main concern. We are using oxygen enriched silicon substrates which are more resistant to radiation. The pixels are formed by isolated n^+ implants and the pn junction is formed by a large p^+ implant on the backside (Fig. 8.5). The thickness of the sensor is 285 μm and the pixel size is 100 $\times$150 μm^2. The pixels must be separated by p^+ type isolation in order to prevent conductive interconnection between them caused by electron accumulation close to the surface between pixels. Two designs of p^+ dopants separations were tested, the p-spray design (Fig. 8.5, left) for which a moderate boron spray concentration has been diffused between pixels (produced by CiS, Erfurt), and the p–stop ring structure (Fig. 8.5, right) with very high boron concentration surrounding every pixel (manufactured by SINTEF, Oslo). To keep the pixel potential close to the readout chip potential (in the event of a pixel loosing the indium bump connection) the pixels are not completely isolated from each other. The high resistive inter–pixels connection is achieved by a punch–through structure and biasing grid in the the p–spray design and a gap in the p–rings for the p–stop design.

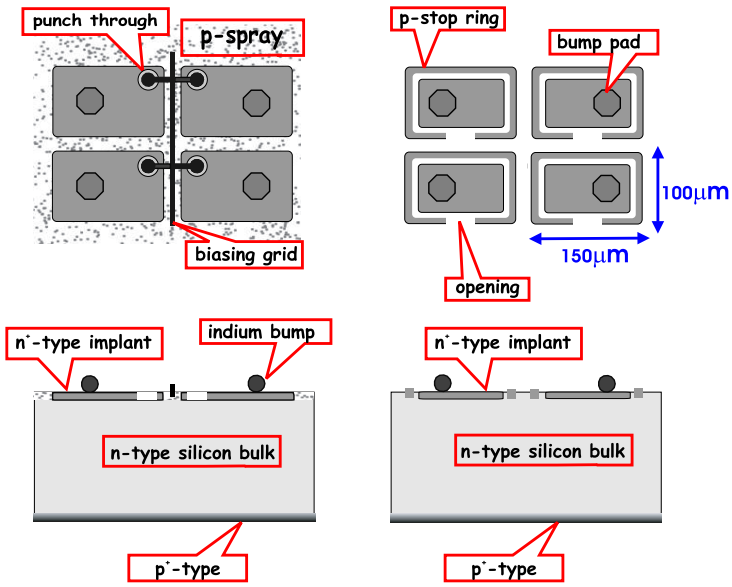

Figure 8.5:
Front view and cross section of the p-spray (left) and p-stop designs (right).

In 2004 we tested the performances of various pixel designs before and after irradiation. The pixel dimensions were of the former design (125 $\times$ 125 μm^2). They were irradiated up to a fluence of 10^{15} n$_{eq}$/cm^2 (neutron equivalent dose per unit surface) with 24 GeV protons from the CERN PS. For comparison the first four years of LHC operation gradually converging to the nominal luminosity correspond to 6 $\times$ 10^{14} n$_{eq}$/cm^2 for the innermost (4.4 cm) pixel layer.
The samples were tested with 150-225 GeV pions in the H2 beam line of the CERN SPS in 2003 and 2004 (2; 3). The beam test setup consisted of our beam telescope (4) made of 8 silicon microstrip detectors (4 measuring the horizontal x and 4 the vertical y impact points) with 50 μm readout pitch and a fast trigger diode. The pixel sensors were bump-bonded to an earlier readout chip (PSI30) and were mounted on a rotating support positioned between the second and third plane of the beam telescope (Fig. 8.6). The samples were stabilized at a temperature of -10 °C by means of water cooled Peltier elements. The hit coordinates on the sensor could be determined from the telescope with a resolution of $\sigma \sim 1$ μm. The telescope was inserted in the gap between two superconducting Helmholtz coils providing a field of 3 T (Fig. 8.7). Measurements were performed with the field parallel to the beam (to measure the Lorentz angle, see below) and perpendicular to the beam (to measure the position resolution).

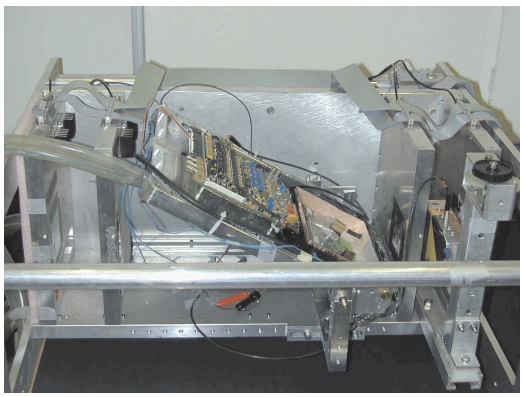

Figure 8.6:
Pixel sensor prototypes and readout inserted between the third and fourth plane of the silicon beam telescope.

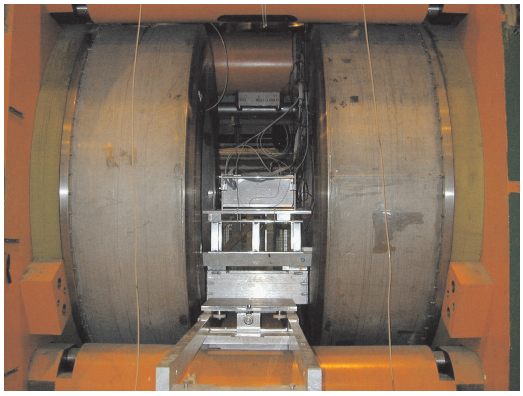

Figure 8.7: *Helmholtz coils providing a magnetic field of 3T.*

With our high resolution telescope it was possible to scan the surface of the sensors and to determine the charge collection efficiency. Irradiated sensors show trapping of charge carriers and the bias voltage has to be increased from typically 100 to 450 V to collect more charge and reach full depletion. Figure 8.8 shows the average charge collected for p-spray and p-stop before and after irradiation. The region with the highest collection efficiency is in the central part of the pixel corresponding to the n^+ implants. The charge collection efficiency is higher than for the p-stop design, about 60 % of that for unirradiated sensors after a fluence of 10^{15} n_{eq}/cm^2. The charge collection efficiency is lower in the punch-through regions in the case of the p-spray design. The p-spray and p-stop designs which were exposed to a fluence of 6×10^{14} n_{eq}/cm^2 have a particle detection efficiency of 99 % with a threshold of 2000 electrons. The respective value for the p-stop design is somewhat lower, 95 %. The p-spray design is therefore preferred over the p-stop.

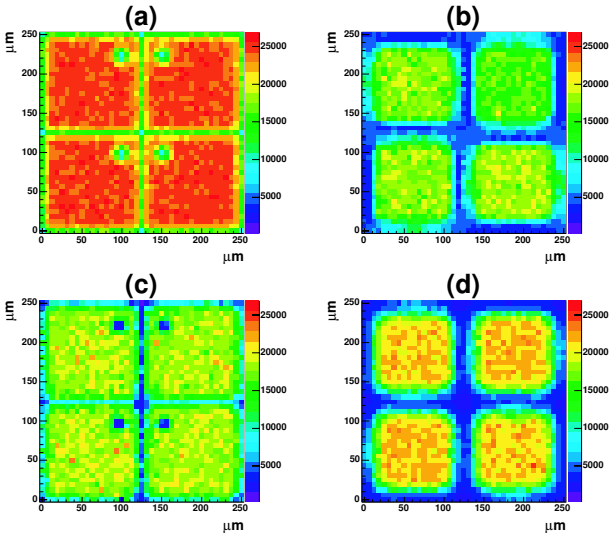

Figure 8.8:
Collected charge over the pixel surface at full depletion. Red (blue) corresponds to high (low) charge levels. The number of collected electrons is shown in the righthand bars. The plots on the left show the p-spray types before (a) and after irradiation with 6.7 $\times$ 10^{14} n_{eq}/cm^2 (b). The plots on the right show the corresponding charge for the p–stop designs.

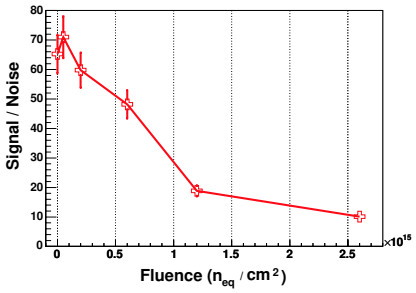

Figure 8.9:
Signal-to-noise ratio measured with the p-spray sensors as a function of irradiation.

The signal-to-noise ratio is about 70 for the unirradiated p-spray sensors, about 50 for the sensors exposed to a fluence of 6×10^{14} n_{eq}/cm^2, and about 10 for a fluence of 2.6×10^{15} n_{eq}/cm^2 (Fig. 8.9). Based on the results of these measurements (3) we have chosen the p–spray design for the barrel sensors. The results from the 2004 tests show that the pixel sensors can be operated up to irradiation fluences of 10^{15} n_{eq}/cm^2. This is much higher than what was originally specified for the CMS pixel detector.

8.3 Charge collection as a function of depth

The charge collection depends on the location of the charge deposit in the sensor bulk. The electron–hole pairs created in the bulk of a fully depleted unirradiated sensor reach the electrodes and contribute to the signal, while for irradiated sensors the trapping centers reduce the probability that charge reaches the electrode. This results in a smaller signal. The charge collection efficiency was measured with high energy pions crossing the sensor at a grazing angle α = 15° with respect to the pixel surface. The pixels at the distance x from the impact point along the beam direction sense the charge deposit at a depth $d = x \tan\alpha$ in the sensor.

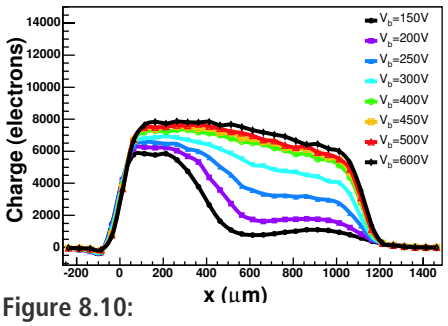

Figure 8.10:
Signal as a function of x for sensors exposed to a fluence of 6×10^{14} n_{eq}/cm^2 for various bias voltages.

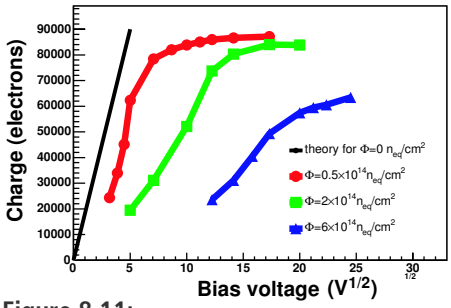

Figure 8.11:
Total collected charge as a function of the square root of the bias voltage far various fluences.

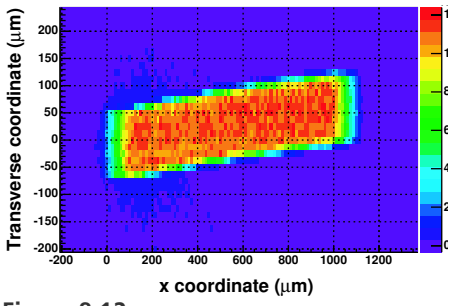

Figure 8.12:
Deflection of the charge in a 3 T magnetic field. The beam enters the sensors from the left.

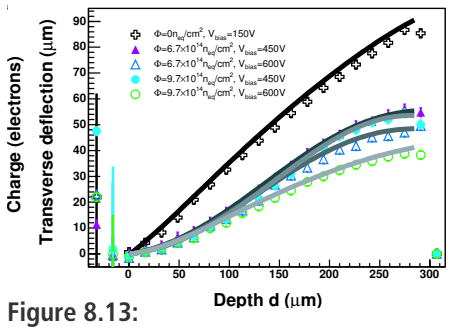

Figure 8.13:
Deflection at the surface versus depth at which the charge was produced, for various fluences.

Figure 8.10 shows the average signal as a function of x for various bias voltages and for a fluence of 6×10^{14} n_{eq}/cm^2. The depletion is believed to start from the implant side after irradiation leading to type inversion. Thus charge should be collected only from the depletion region close to the pixel implant at low bias voltages. However, the measured dependence of the charge collection efficiency (shoulder at high voltages) indicates that even at low bias voltages the charge is collected from both sides of the sensor. This means that for the irradiated sensors the depletion starts from both sides of the sensor bulk. In the conventional picture the total collected charge is proportional to $\sqrt{V_{bias}}$ up to full depletion voltage. The total charge collected is shown in Fig. 8.11 as a function of $\sqrt{V_{bias}}$. These curves do not exhibit the expected $\sqrt{V_{bias}}$ dependence, due the behavior of the electric field which does not vary linearly across the sensor depth, as expected for unirradiated devices. This observation is supported by the direct measurement of the electric field in the sensor bulk (3) and by a detailed simulation (5).

8.4 Lorentz angle as a function of depth

In the presence of a magnetic field the electrons and holes, are deflected from their drift along the electric field lines. We have measured the deflection angle (Lorentz angle θ_L) as a function of depth in the 3 T field provided by the Helmholtz coils of Fig. 8.7, using the technique described in ref. (6; 7). The beam enters the sensor plane at the grazing angle α and the magnetic field is parallel to the beam. Without magnetic field the charge generated at a given depth d would reach the pixel at a distance x along the beam line, as described in previous section. With magnetic field the charge is now deflected towards the adjacent pixel rows. Therefore, a measurement of the charge distribution among adjacent pixels yields the Lorentz angle θ_L as a function of x, and hence sensor depth (8).
Figure 8.12 shows the typical displacement of the collected charge at the surface of the sensor and Fig. 8.13 the displacement of the charge as a function of the depth at which the charge was produced, for various irradiation levels. One observes that the the displacement (and hence θ_L) decreases with irradiation. This is simply due to the increasing electric field needed to fully deplete the sensor. Extrapolating to 4 T one finds a Lorentz angle of $(26.3 \pm 0.8)^\circ$ close

to the pixel implants for the unirradiated sensor (100 V bias) and (11.6 $\pm$ 1.4)° after 6.7 $\times$ 10^{14} n_{eq}/cm^2 (450 V bias).
Figure 8.14 shows how θ_L depends on the sensor depth for various irradiation levels. The Lorentz angle appears to depend on depth. Since θ_L depends on E, B and the mobility (the latter also being a function of E), a measurement of θ_L as a function of depth determines the behaviour of the electric field as a function of depth. Using a well known empirical parameterization of the mobility one can extract the electric field as a function of sensor depth (3). Figure 8.15 shows that the electric field reaches maxima below both surfaces and a minimum in the bulk center.

8.5 Position resolution

The magnetic field was switched perpendicularly to the beam to reproduce the geometry of the CMS barrel sensors and the position resolution of irradiated sensors was measured with high energy pions in a magnetic field of 3 T (3). A simulation of the response of the 125 $\times$ 125 μm^2 was then performed, including the behaviour of the E-field described in the previous section, and verified with data. The simulation was then used to predict the expected charge sharing and the resolution for irradiated 100 $\times$ 150 μm^2 sensors of CMS at 4 T. Due to the widths of the (flat) modules the r.m.s resolution along the $r\phi$ direction (azimuthal angle direction) will vary with ϕ. It lies between 10 μm and 20 μm, depending on irradiation fluence and polar angle (Fig. 8.16). After the first four years of operation the resolution at the innermost barrel layer is still below 20 μm along the $r\phi$ direction and depends weakly on the polar angle. The resolution along the z direction is better than 20 μm. In conclusion, the pixel sensors for CMS will perform according to expectation and those at 4 cm from the collision point will fulfill the requirements at least during the first four years of LHC operation.

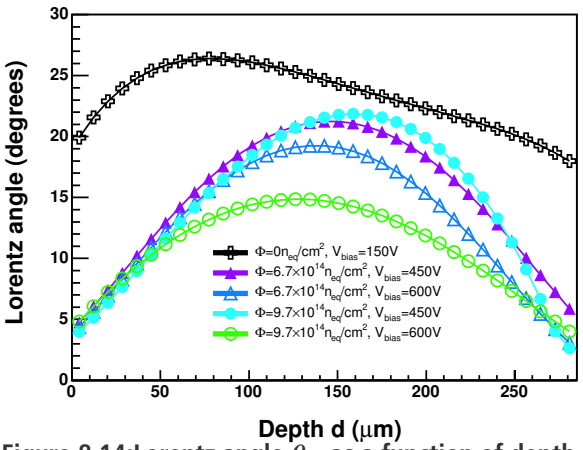

Figure 8.14:Lorentz angle θ_L as a function of depth.

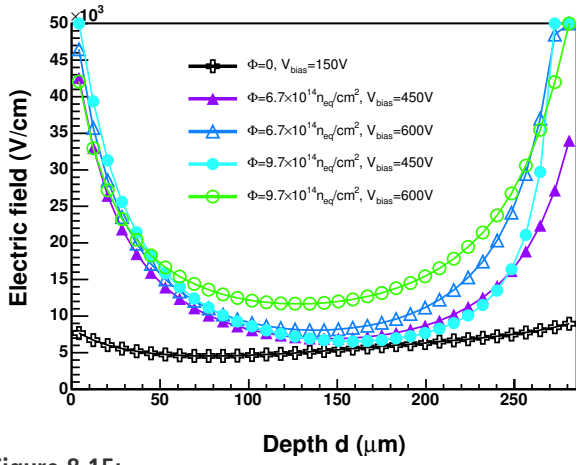

Figure 8.15:
Electric field as a function of depth. The regions immediately below the surfaces ($\sim$ 20μm) are affected by large systematic uncertainties.

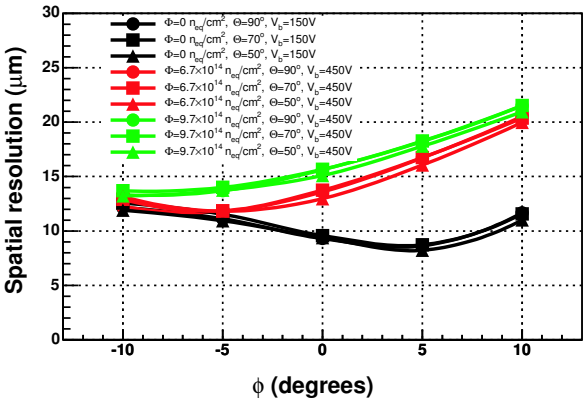

Figure 8.16:
Predicted $r\phi$ position resolution in the CMS pixel barrel as a function of azimuthal angle ϕ, for various polar angles θ and irradiation fluences.

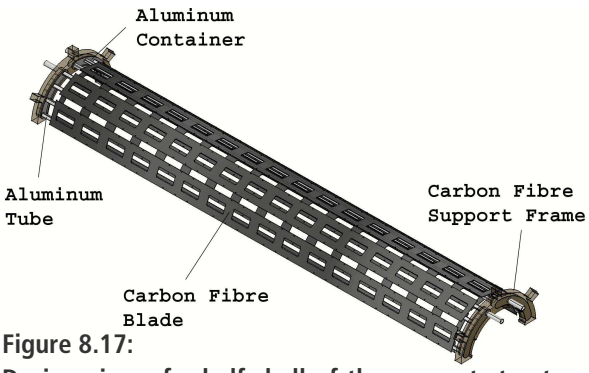

Figure 8.17:
Design view of a half shell of the support structure for the innermost pixel layer.

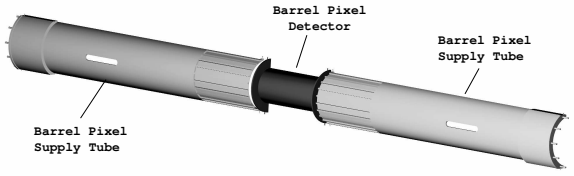

Figure 8.18:
Half shell of the barrel pixel detector system with its two service tubes.

8.6 Mechanical support structure

The design and construction of the mechanical support structure for the CMS pixel detector is performed by our group and our Institute's workshop. The detector support structures (Fig. 8.17) are made of aluminum tubes (wall thickness 300 μm) which are of trapezoidal shape to fit the geometrical constraints. The custom made 240 μm thick carbon fibre blades which support the pixel modules are then glued to the tubes forming the detector segments. Four to five of the aluminium tubes are laser-welded to an aluminum container which distributes the cooling fluid. Laser-welding is done in collaboration with industry. The manifold cools the detector modules to -20 °C using C_6F_{14} as a coolant. On both ends the manifolds are embedded in a carbon fibre support frame which supports the single segments and makes up the detector layer half shell.

We are also building the two 2.2 m long service tubes (Fig. 8.18) which transfer the power, all optical and electrical signals, and the cooling fluid to and from the detector. The power and slow control leads are embedded in the supply tube body. Foam will guarantee rigidity. The full system (pixel detector + service tube) is 5 m long. Two vertically separated half shells will be inserted into the CMS detector on a rail system. The insertion will be rather delicate since it will be done after the installation of the LHC beam pipe.

The design of the detector structure has been completed in 2004. The tools for the production of the different segment parts are also designed and manufactured. In 2005 we will continue with the leakage and cooling tests using the prototype segment of the support structure. Manufacturing of the final pixel segments and half shells will then start. Installation into CMS is foreseen during winter 2007/8, six months after LHC commissioning to avoid radiation damage during the initial injection trials.

8.7 Pixel power distribution

Our group is also responsible for the design of the CMS pixel detector power distribution for the front end electronics (low voltage) and the pixel sensors (high voltage) and cabling. The power lines are integrated in the service tubes discussed in the section above on mechanics.

In 2004 we have constructed a laboratory setup to mimic the behaviour of a section of the CMS pixel detector with respect to beam and settings induced voltage spikes. The system had to cope with sudden (100 ns) current excursions of 2 A in 50 m long power lines. Various solutions were tested to reduce the inductance of the cables. The setup includes a

prototype power supply unit housed in a VME-like crate, a mainframe unit controlling up to six crates, various power cables of the foreseen lengths, a prototype section of the service tube and active loads which reproduce the power consumption of the CMS pixel modules. The tests were performed to optimize the power supply units and the cable specifications to the pixel detector needs, i.e. to determine the need for additional electronics and grounding schemes. The development of the power supply unit is done in collaboration with CAEN, Viareggio, and preliminary results are encouraging.

8.8 Event reconstruction software

The Zurich group has adapted and implemented in the reconstruction software of CMS (ORCA) the Kalman filter (KF). This is a χ^2-square minimization which hence assumes that the track measuring errors are Gaussian distributed. Tracks are normally taken to be straight in the vertex neighborhood. We have improved on the KF by using more realistic helicoidal tracks in the homogeneous field of CMS. However, non-Gaussian noise (e.g. due to δ-electrons) is unavoidable. The distributions of the vertex pulls (difference between simulated and reconstructed values, divided by the measurement error) have a Gaussian core with tails.

We have shown that non-Gaussian noise can be taken into account with a Gaussian-Sum Filter (GSF) (9). Here the distributions of the measurement errors and the estimated quantities are modeled by linear superpositions (components) of Gaussian distributions. The main component describes the core of the distribution and the tails are described by one or several additional Gaussians. Several solutions for the vertex are then calculated with all combinations of components. The final vertex is calculated as the weighted average of all solutions. The algorithm was tested with a simplified simulation in which the tracks parameters were smeared with a mixture of two Gaussians. The hit positions, error estimates and χ^2 are significantly improved.

The sensitivity of the GSF with respect to badly measured tracks or tracks assigned to the wrong vertex (outliers) was extensively studied. These tests demonstrate a higher degree of robustness than χ^2-square estimators and show the adaptive power of the GSF for outliers for which higher weights are assigned to track-components with the largest standard deviations. A novel idea which emerged from these tests was the combination of the GSF with another non-linear filter, the *Adaptive Vertex Filter* (AVF) (10; 11). This filter is referred to as the *Adaptive-GSF* (A-GSF).

For example, an outlying track originating from a second vertex is added to the four tracks from the main vertex. The position of this vertex is shifted by between 0 and 5 mm in the transverse y direction relative to the jet-axis from the main vertex. The

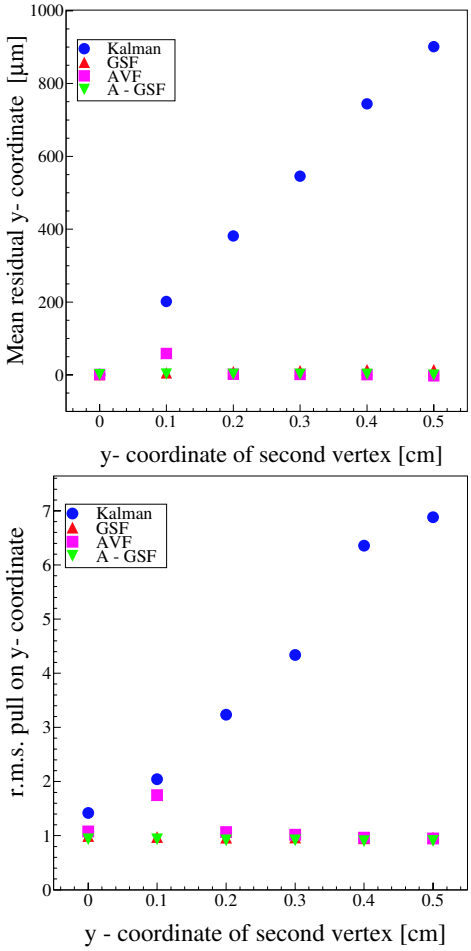

Figure 8.19:
Mean residuals (top) and standard deviations of the pull distributions (bottom) for different transverse positions of a vertex generated by an outlying track.

values of the mean residual distribution and the pull of the estimated vertex are shown in Fig. 8.19. The correct error assignments should lead to r.m.s. pulls of 1. The three non-linear filters are remarkably stable and improve substantially over the KF in terms of resolutions and pulls. For small displacements of the vertex, the AVF is not able to identify all of the outliers and is therefore slightly worse than the GSF and A-GSF. In particular situations the A-GSF performs much better than the GSF, but at the expense of a much longer CPU time.

In 2003/04 we also developed a kinematic fit based on Lagrange multipliers which incorporates additional constraints into the vertex fit to improve the resolutions. These constraints may be the masses of well known (long-lived) hadrons decaying to the observed particles, energy and/or momentum conservation, or collinearity in two-body processes. A further constraint of interest requires the momentum of the reconstructed B meson to be parallel to the vector pointing from the primary to the secondary vertex.

Considerable progress was made this year (1) . A framework for modeling the decay sequence is now provided. The fit allows for instance the reconstruction of complete decay chains, such as $B^- \to D^0 l^- \bar{\nu}_l$, followed by $D^0 \to K^-\pi^+$, $D^0 \to K^-\pi^+\pi^0$ or $D^0 \to K^-\pi^+\pi^-\pi^+$, where only the final long-lived particles are detected. The kinematic fit can also be performed with or without vertex constraint. The software is flexible enough so that new constraints can easily be included by the user.

One decay benefiting directly from such a kinematic fit is $B_s \to J/\psi\ \phi \to K^+K^-\mu^+\mu^-$, in which the Zurich group is particularly interested. This channel provides one of the best ways to determine the height η of the Unitarity Triangle. Here one measures the (CP violating) asymmetry between $B_s \to J/\psi\ \phi$ and $\bar{B}_s \to J/\psi\ \phi$. The CP-violating weak phase $\phi_{CKM} = [\arg(V_{cs}^* V_{cb}) - \arg(V_{ts}^* V_{tb})]$, measured in the rate asymmetry, is equal to $2\lambda^2\eta \simeq 0.03$, where λ is the sine of the Cabibbo angle. A measurement of a significantly larger phase ϕ_{CKM} would indicate contributions from non-Standard Model processes. These parameters may be obtained by a classical maximum-likelihood analysis or by an angular correlation analysis.

Our group is involved in the analysis of this decay with simulated data to estimate the sensitivity of the CMS detector. We have devised a selection strategy that relies on the partial reconstruction of the four charged tracks, already at the stage of the high level trigger (HLT). Indeed, by restricting the track reconstruction to the first 5 hits (to save CPU time) the precision on the track parameters is already sufficient. At the first level the dimuon trigger selects two muons of opposite charges with a transverse momentum above 3 GeV/c, using only the measurements from the muon chambers.

In the HLT the muons stubs are projected into the tracker and all tracks in a cone around a muon candidate are reconstructed. We require the presence of two muons tracks of opposite charges with an invariant mass within 100 MeV of the mass of the J/ψ, as well as two kaon tracks of opposite charges with an invariant mass within 100 MeV of the ϕ mass. The four tracks are required to come from a common secondary vertex by imposing a requirement on the confidence level of the vertex fit. As CMS lacks particle identification (with the exception of muons) all charged tracks have to be considered as possible kaon candidates. This adds a significant contribution to the background from combinatorial ambiguities.

The kinematic fit is applied during offline reconstruction. The r.m.s. resolution in the invariant mass is 14 MeV and the corresponding resolution σ_{ct} on the mean decay path $c\tau$ = 438 μs in the B_s rest frame is 35 μm (Fig. 8.20). A preliminary study shows that approximately 125'000 fully reconstructed B_s candidates will be obtained in the first year of LHC operation at the reduced luminosity of $2 \times 10^{33}\mathrm{cm}^{-2}\mathrm{s}^{-1}$.

We are also investigating the analogous decay $B_s \to J/\psi\,\phi$ where $J/\psi \to e^+e^-$. This decay will increase the B_s sample but the reconstruction of low-momentum electrons is notoriously difficult. All these studies will be incorporated into the physics technical design report requested by CERN in summer 2005.

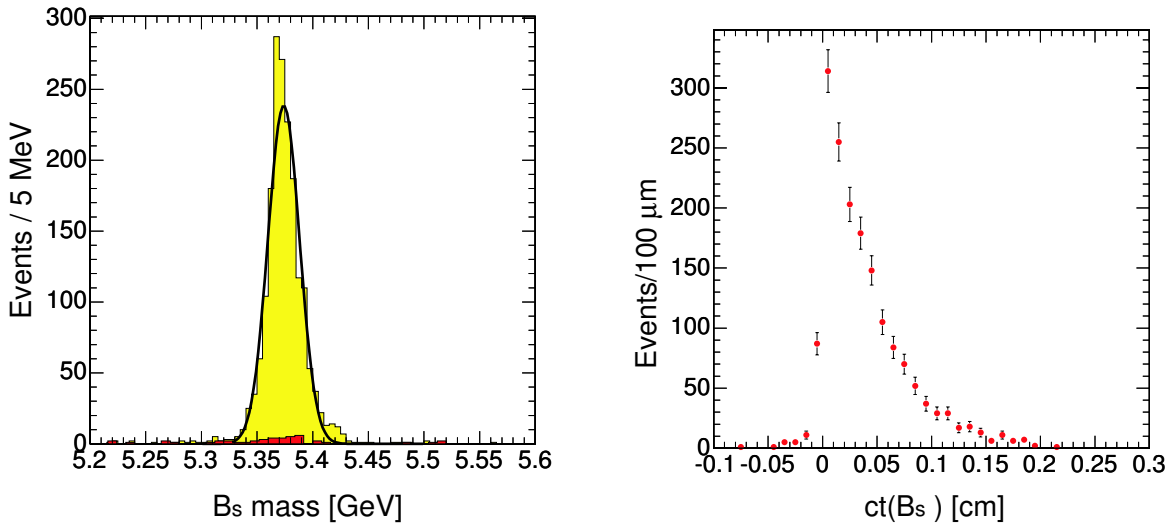

Figure 8.20:
Left: Invariant mass distribution of $B_s \to J/\psi\,\phi$ candidates after the kinematics fit. The small red area is the residual combinatorial background.
Right: ct distribution.

[1] K. Prokofiev, PhD thesis, in preparation.
[2] A. Dorokhov *et al.*, Nucl. Instr. and Meth. in Phys. Research A **530** (2004) 71.
[3] A. Dorokhov, PhD thesis, Universität Zürich, 2005.
[4] C. Amsler *et al.*, Nucl. Instr. and Meth. in Phys. Research A **480** (2002) 501.
[5] V. Chiochia *et al.*, Proc. 2004 IEEE Nuclear Science Symp., prep. physics/0411143.
[6] R. Kaufmann, PhD thesis, Universität Zürich, 2001.
[7] B. Henrich and R. Kaufmann, Nucl. Instr. and Meth. in Phys. Research A **477** (2002) 304.
[8] A. Dorokhov *et al.*, Proc. Vertex 2004 Conf., prep. physics/0412036.
[9] R. Frühwirth and T. Speer, Nucl. Instr. and Meth. in Phys. Research A **534** (2004) 217.
[10] R. Frühwirth, K. Prokofiev, T. Speer, P. Vanlaer and W. Waltenberger, Nucl. Instr. Meth. in Phys. Research **A 502** (2003) 699.
[11] J. D'Hondt, P. Vanlaer, R. Frühwirth and W. Waltenberger, IEEE Trans. Nucl. Sci. **51** (2004) 2037.

9 Superconductivity and Magnetism

D. Di Castro (till November 2004), D.G. Eshchenko, H. Keller, R. Khasanov,
S. Kohout, F. La Mattina (since March 2004), A. Maisuradze (since April 2004),
J. Roos, A. Shengelaya, S. Strässle (since December 2004)

visiting scientists: M. Eremin, V.A. Ivanshin, B. Kochelaev
Emeritus members: M. Mali, K.A. Müller (Honorarprofessor), T. Schneider (Titularprofessor)

in collaboration with:
ETH Zürich (K. Conder, J. Karpinski), Paul Scherrer Institute (K. Conder, E. Morenzoni), Max-Planck-Institute for Solid State Research Stuttgart (A. Bussmann-Holder), IBM Rüschlikon Research Laboratory (J.G. Bednorz), University of Birmingham (E.M. Forgan), University of Rome (A. Bianconi), Kazan State University (A. Dooglav, M.V. Eremin, V. Ivanshin, B.I. Kochelaev), University of Belgrade (I.M. Savić), University of Tokyo (K. Kishio, T. Sasagawa, H. Takagi).

Last year we continued our research activities on the magnetic and electronic properties of novel superconductors and related materials by means of a combination of different complementary experimental techniques, including muon-spin rotation (μSR), low-energy μSR, polarized neutron reflectometry, electron paramagnetic resonance (EPR), nuclear magnetic resonance (NMR), nuclear quadrupole resonance (NQR), as well as SQUID and torque magnetometry. The main goal of our investigation is to provide new information on the *macroscopic* and *microscopic* physical properties of high-temperature cuprate superconductors (HTS), other novel superconductors and related materials, which may help to understand the basic physics of these systems. In addition, we started a new project to investigate electric field effects on the electronic structure of Cr-doped strontium titanate by means of EPR in collaboration with the IBM Rüschlikon Laboratory.

9.1 Studies of isotope effects in novel superconductors

9.1.1 Polaron formation as origin of unconventional isotope effects in cuprate superconductors

High-temperature cuprate superconductors (HTS) are one of the most intensely studied systems due to the yet lacking understanding of the pairing mechanism. The antiferromagnetic properties of the undoped compounds are a consequence of the large Coulomb repulsion at the copper site. The energy scale given by it is the largest, and this has been taken as evidence that it must play a crucial role for the pairing mechanism. Consequently, effects stemming from the lattice have mostly been ignored, especially in view of the fact that the isotope effect on the superconducting transition temperature T_c almost vanishes at optimum doping (1; 2). The failure of BCS theory to account for many of the observed exotic properties has contributed to interpret the pairing mechanism in terms of a purely electronically driven one. However, various unexpected oxygen isotope (^{16}O/^{18}O) effects were reported (3)-(8) which are neither expected within the BCS mechanism nor within models based on strong correlations only. Since the Cu ion is one of the strongest Jahn-Teller systems (9), polaron formation can take place here and be the origin of unconventional isotope effects.

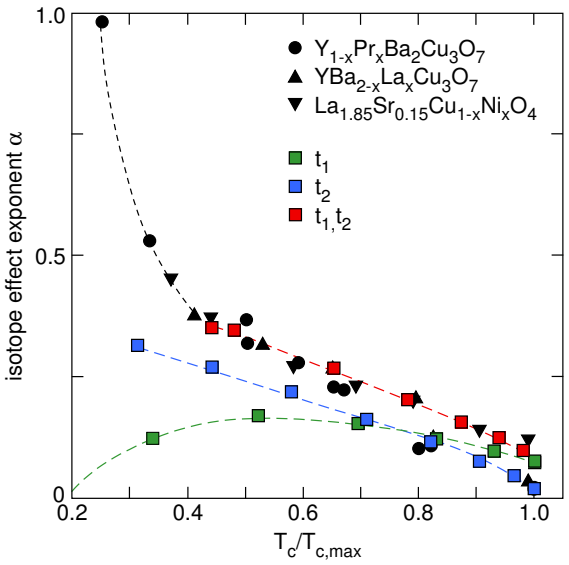

Figure 9.1:
Calculated isotope effect exponent α as a function of $T_c/T_{c,max}$ within the polaronic model [10] ($T_{c,max}$ is the maximum T_c for a given family of HTS). The red squares are calculated by renormalizing both hopping integrals t_1 and t_2 (see Fig. 9.2) through the polaronic coupling. The green squares are calculated by renormalizing t_1 only, whereas for the blue squares t_2 is renormalized, t_1 remains bare. The black symbols are experimental data points for various HTS taken from [7]. The dashed lines are a guide to the eye. The ratio of $t_2/t_1 = 0.3$.

In collaboration with A. Bussmann-Holder (Max-Planck-Institute for Solid State Research, Stuttgart) we investigated the origin of the isotope effects on the superconducting transition temperature and the magnetic penetration depth within polaron theory (10). For this purpose the well-known t-J Hamiltonian is extended to incorporate the hole induced charge channel and the important effects from the lattice. This results in a two-component Hamiltonian, where interactions between the charge channel (local hole plus induced lattice distortion) and the spin channel (antiferromagnetic fluctuations modified by lattice distortions) are explicitly included (10). It is found that the exponential squeezing of the second nearest neighbour hopping integral t_2 carries the correct isotope effect on the superconducting transition temperature T_c, as well as the one on the magnetic penetration depth λ. The average superconducting gap is predicted to have an isotope effect comparable to the one on the penetration depth λ. As an example, Fig. 9.1 shows the calculated isotope effect exponent $\alpha = -\mathrm{d}T_c/\mathrm{d}M$ (M is the oxygen mass) as a function $T_c/T_{c,max}$, together with experimental data (7) for comparison ($T_{c,max}$ is the maximum T_c for a particular family of HTS).

In order to clarify the symmetry of the coupling lattice distortion which causes these isotope effects, various renormalization procedures of the nearest (t_1) and the second nearest (t_2) neighbor hopping integrals were considered. It is evident from Fig. 9.1, that the isotope effect on T_c due to t_1 only, deviates strongly from experimental observations in the underdoped regime where it approaches zero. On the other hand, a renormalization of t_1 and t_2 with $t_2/t_1 = 0.3$ leads to values of $\alpha(T_c/T_{c,max})$ which are in excellent agreement with the experimental isotope effect data on T_c in the range $0.4 \leq T_c/T_{c,max} \leq 1$. However, at low doping the model does not describe the data satisfactory, which is probably due to fact that in a first step the same parameters are used in the model for all doping levels.

From this finding we conclude directly about the lattice distortion which governs the unconventional isotope effects. The half-breathing mode (Fig. 9.2, left panel), which shows anomalous softening (11), is dominated by t_1 and obviously exhibits the wrong isotope dependence. Since symmetry considerations also apply to the perpendicular direction of the half breathing mode, also the full breathing mode can be excluded. The crucial role of t_2 can only be taken into account by considering the Jahn-Teller active Q_2 type mode as the origin of the observed isotope effects (Fig. 9.2, right panel), consistent with the interpretation of earlier EPR results (12). Since the discovery of cuprate HTS (13) was motivated by the idea that Jahn-Teller polaron formation could be a new electron (hole) pairing mechanism, the present results support the original ideas.

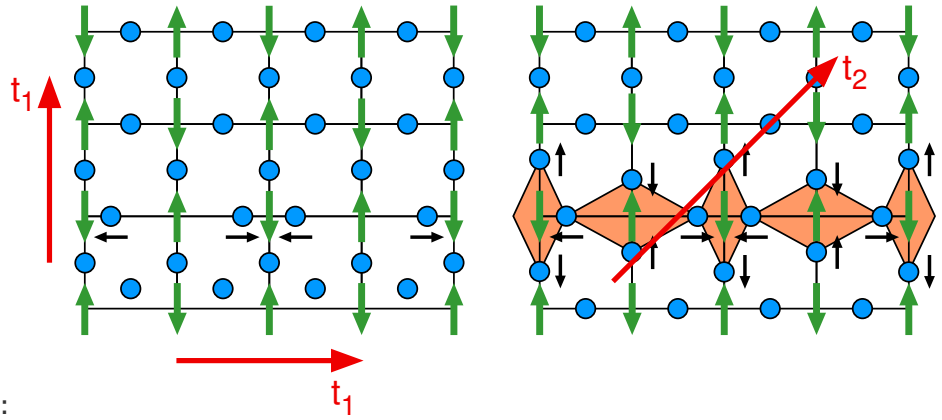

Figure 9.2:
The relevant ionic displacements which are either governed by t_1 only (left panel) or by t_2 only (right panel). Here only displacements in the CuO_2 plane are considered. The blue circles represent the oxygen ions, the green arrows are copper ions with the antiferromagnetic order. The black arrows in the left panel indicate the displacements for the LO half breathing phonon mode. Similarly a full breathing mode could be governed by t_1. The coloured rhombohedra show the displacements (black arrows) of the Q_2 type mode which is dominated by t_2.

[1] J.P. Franck, in **Physical Properties of High Temperature Superconductors IV** (ed. D.M Ginsberg) 189-293 (World Scientific, Singapore, 1994).

[2] D. Zech *et al.*, Nature **385**, 681 (1994).

[3] G.-M. Zhao, M.B. Hunt, H. Keller, and K.A. Müller, Nature **385**, 236 (1997).

[4] J. Hofer *et al.*, Phys. Rev. Lett. **84**, 4192 (2000).

[5] G.-M. Zhao, H. Keller, and K. Conder, J. Phys.: Condens. Matter **13**, R569 (2001).

[6] R. Khasanov *et al.*, Phys. Rev. Lett. **92**, 057602 (2004).

[7] R. Khasanov *et al.*, J. Phys.: Condens. Matter **16**, S4439 (2004).

[8] G.H. Gweon *et al.*, Nature **430**, 187 (2004).

[9] K.A. Müller, in **Magnetic Resonance and Relaxation** (ed. R. Blinc) 192-208 (North Holland Pbl. Inc., 1966).

[10] A. Bussmann-Holder and H. Keller, European Physical Journal B (2005), in press.

[11] M. Tachiki, M. Machida, and T. Egami, Phys. Rev. B **67**, 174506 (2003).

[12] B.I. Kochelaev *et al.*, Phys. Rev. Lett. **79,** 4274 (1997).

[13] J.G. Bednorz and K.A. Müller, Z. Phys.: Condens. Matter **64**, 189 (1986).

9.1.2 Oxygen Isotope effect on electronic phase separation in lightly doped $La_{2-x}Sr_xCuO_4$

Recently our EPR studies of lightly doped $La_{2-x}Sr_xCuO_4$ ($0 \leq x \leq 0.06$) revealed the presence of microscopic electronic phase separation of doped holes (1). However, the mechanism of the electronic phase separation in cuprates is still under debate. Up to now the main attention was paid to purely electronic and magnetic mechanisms, but the existence of phase separation within this approach is still controversial. Therefore, recently Kochelaev *et al.* (2) proposed an alternative mechanism. In the latter the electron-phonon coupling induces anisotropic interactions between the holes, resulting in the creation of extended nano-scale hole-rich regions. If phase separation is related with the electron-phonon coupling, one can expect an isotope effect on the formation of hole-rich and hole-poor

nanoscale regions in cuprates. We decided to check this possibility by studying the microscopic phase separation using EPR in lightly doped $La_{2-x}Sr_xCu_{0.98}Mn_{0.02}O_4$ with different oxygen isotopes (^{16}O and ^{18}O).
Figure 9.3 shows the temperature dependence of the narrow EPR line intensities for x = 0.02 samples with ^{16}O and ^{18}O oxygen isotopes. Previously, we showed that the appearance of this narrow line signals the formation of the hole-rich regions (1). Moreover, the formation energy Δ of these regions can be extracted from the temperature dependence of the signal intensity. One can see a clear difference between EPR signal intensities of the two isotope samples. The obtained results provide strong support for a phonon mechanism of phase separation in lightly doped $La_{2-x}Sr_xCuO_4$.

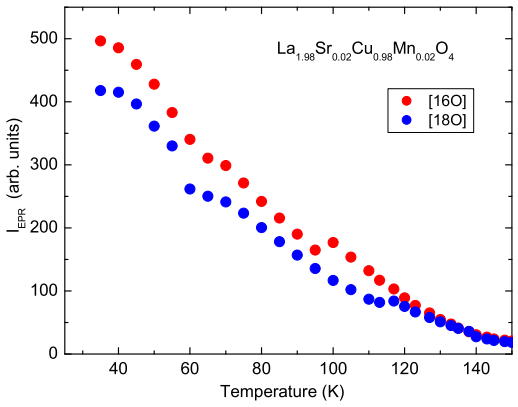

Figure 9.3:
Temperature dependence of the narrow EPR signal intensity for ^{16}O and ^{18}O samples of $La_{1.98}Sr_{0.02}Cu_{0.98}Mn_{0.02}O_4$.

[1] A. Shengelaya *et al.*, Phys. Rev. Lett. **93**, 017001 (2004).
[2] B. I. Kochelaev *et al.*, Mod. Phys. Lett. B **17**, 415 (2003).

9.2 Studies of pressure effects in novel superconductors

9.2.1 Pressure effect on the penetration depth in $YBa_2Cu_4O_8$

One way to explore the role of lattice vibrations in HTS is to perform isotope effect experiments. Previous studies (1)-(4) showed a substantial oxygen-isotope ($^{16}O/^{18}O$) effect on the in-plane penetration depth λ_{ab}, which indicates a non-adiabatic coupling of the electrons to phonon modes involving the movement of the isotope substituted atoms. An alternative way to explore lattice effects in HTS are pressure experiments. The squeezing of the crystal lattice by external hydrostatic or uniaxial pressure affects the lattice parameters, the phonon spectrum, and consequently the electron-lattice coupling. Surprisingly, the pressure effect (PE) on the magnetic field penetration depth has not attracted much attention yet.

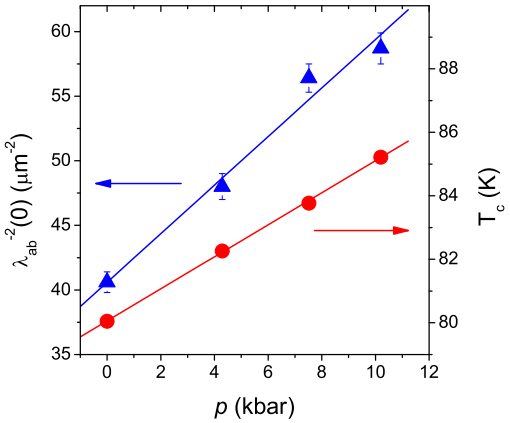

Figure 9.4:
Pressure dependence of the transition temperature T_c (circles) and the zero temperature in-plane magnetic penetration depth $\lambda_{ab}^{-2}(0)$ (triangles) in $YBa_2Cu_4O_8$.
The linear fits yield $dT_c/dp = 0.50(1)$ K/kbar and $d\lambda_{ab}^{-2}(0)/dp = 1.88(13)$ μm^{-2}/kbar.

Here we report the first observation of the pressure effect on the zero temperature in-plane magnetic field penetration depth $\lambda_{ab}(0)$ in a $YBa_2Cu_4O_8$ cuprate superconductor (5). A pronounced PE on both the transition temperature T_c and $\lambda_{ab}^{-2}(0)$ is observed which increases with increasing pressure (see Fig. 9.4). The pressure shift on $\lambda_{ab}^{-2}(0)$ is attributed to (i) the pressure induced charge carrier transfer from the chains to the planes and (ii) the decreasing of the in-plane charge carrier mass m_{ab}^*. At p =10.2 kbar we observed $\Delta\lambda_{ab}^{-2}(0)/\lambda_{ab}^{-2}(0) = 44(3)\%$ and $\Delta m_{ab}^*/m_{ab}^* = -32(3)\%$. Such a large effect on m_{ab}^* implies that lattice effects play an essential role in cuprate superconductors.

[1] G.-M. Zhao, M.B. Hunt, H. Keller, and K.A. Müller, Nature **385**, 236 (1997).

[2] J. Hofer *et al.*, Phys. Rev. Lett. **84**, 4192 (2000).

[3] R. Khasanov, *et al.*, J. Phys.: Condens. Matter **15**, L17 (2003).

[4] R. Khasanov *et al.*, Phys. Rev. Lett. **92**, 057602 (2004).

[5] R. Khasanov, J. Karpinski, and H. Keller, cond-mat/0405643.

9.2.2 Pressure effects on the transition temperature and the magnetic field penetration depth in the pyrochlore superconductor $RbOs_2O_6$

The temperature dependence of the magnetic field penetration depth λ reflects the quasiparticle density of states available for thermal excitations and therefore probes the superconducting gap structure. Observation of a high pressure effect on T_c is a good indication that higher values of T_c in similar compounds may be obtained by "chemical" pressure (by exchanging the appropriate ion with its chemical equivalent having a different ion size). It is not widely appreciated, however, that the pressure dependence of T_c, like the isotope dependence, contains valuable information on the superconducting mechanism itself.

We performed magnetization measurements in the recently discovered superconductor $RbOs_2O_6$ under hydrostatic pressure (1). A pronounced and *positive* pressure effect on T_c with $\mathrm{d}T_c/\mathrm{d}p = 0.090(1)$ K/kbar was observed (see Fig. 9.5), in contrast to the negative pressure shift generally detected in conventional superconductors. This finding was explained within the framework of BCS theory under the assumption that the electron-phonon coupling constant λ_{el-ph} increases with pressure. The absence (within the experimental uncertainties) of a pressure effect on λ suggests that $RbOs_2O_6$ is an adiabatic BCS–type superconductor.

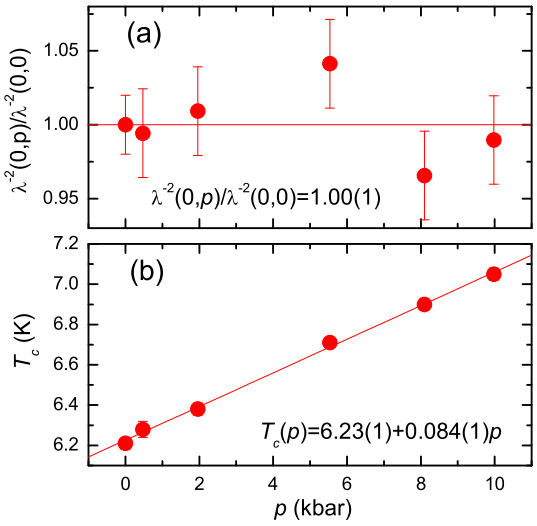

Figure 9.5:
The pressure dependence of $\lambda^{-2}(0)(p)/\lambda^{-2}(0)(p=0)$ (a) and T_c (b) in $RbOs_2O_6$. The solid lines are fits with parameters shown in the figure.

[1] R. Khasanov *et al.* Phys. Rev. Lett. **93**, 157004 (2004).

9.3 Spectroscopic studies of novel superconductors

9.3.1 NMR/NQR investigations of YBCO compounds

We continued our collaboration with the research group of A.V. Dooglav and M. Eremin at the State University of Kazan (Russia). The investigation of the plane ^{63,65}Cu spin-lattice relaxation in superconducting $\mathrm{YBa_2Cu_4O_8}$ at mK temperatures is being completed with a study of the related Ca doped compounds $\mathrm{Y_{1-x}Ba_{2-y}Ca_{x+y}Cu_4O_8(x+y=0.02, 0.05, 0.1)}$ down to 1.5K.

In the superconducting phase of $\mathrm{YBa_2Cu_4O_8}$ the magnetic contribution to the Cu spin-lattice relaxation due to spin fluctuations diminishes because of the superconducting gap (1). At very low temperature this reduced relaxation progressively changes its character from magnetic towards quadrupolar with an unexpectedly large increase in rate below 1K (2). In contrast, $\mathrm{Y_{1-x}Ba_{2-y}Ca_{x+y}Cu_4O_8}$ shows a similar feature shifted to higher temperature regions. The location of this feature on the temperature scale strongly depends on the details of the distribution (x, y) of Ca onto Y or Ba sites (3). With increasing Ca substitution this feature seems to move more near to the superconducting transition temperature. Consequently, spin-lattice relaxation of magnetic character due to spin fluctuations regains its dominance, masking progressively the quadrupolar relaxation contribution.

In our NQR search in cuprates for effects of charge inhomogeneities that seem to exist as self organized objects and are possibly related to the appearance of the pseudo-gap, we recently performed ^{175}Lu NQR measurements on $YBa_2Cu_3O_7$ single crystals. The site symmetry of Lu causes anti-ferromagnetic Cu spin fluctuations to cancel. NQR at this site is therefore exclusively sensitive to charge effects. However, due to the very large nuclear quadruple moment of ^{175}Lu charge fluctuations lead to an extreme shortening of the Lu spin-lattice relaxation time, rendering Lu NQR signals practically undetectable within the experimentally available temperature range. Since high quality powder samples of $LaBa_2Cu_3O_7$ have recently been synthesized successfully by K. Conder and E. Pomjakushina (Paul Scherrer Institute, PSI and ETH Zürich) we were able to resume work on this topic by starting ^{139}La NMR/NQR investigations of $LaBa_2Cu_3O_7$. The nuclear quadrupole moment of ^{139}La is approximately 30 times smaller than the one of ^{175}Lu thus preventing an unfavourable excessive increase of spin-lattice relaxation as observed in the case of Lu. Our preliminary results show an unusual behavior of ^{139}La spin-lattice and spin-spin relaxation in the normal conducting phase of $LaBa_2Cu_3O_7$ below 300K possibly related to charge inhomogeneity effects.

In recent theoretical investigations the appearance of a new phase in cuprates characterized by so-called orbital currents in the CuO_2 planes was predicted (see e.g. (4)). It was suggested to check for their existence by ^{89}Y NMR in the compound $Y_2Ba_4Cu_7O_{15}$, where the Y site is neighboured by unequally doped CuO_2-planes (5). To perform this task we started a study of the temperature dependence of various Y NMR parameters in this compound in order to detect a static or dynamic response to possible orbital currents. We measured the temperature dependence of the Y NMR line shift and line width in normal conducting $Y_2Ba_4Cu_7O_{15}$ and were able to determine within errors an upper limit for a static magnetic field caused by an averaged response to possible orbital currents, which is far below predicted values.

[1] M. Bankay *et al.*, Phys. Rev. B **50**, 6416 (1994).

[2] M. Mali *et al.*, J. Supercond. **15**, 511 (2002).

[3] M. Mali, J. Roos, and D. Brinkmann, Phys. Rev. B **53**, 3550 (1996).

[4] D.A. Ivanov *et al.*, Phys. Rev. Lett. **84**, 3958 (2000).

[5] P.A. Lee and G. Sha, Solid State Commun. **126**, 71 (2003).

Table 9.1: **Summary of the μSR results obtained for $RbOs_2O_6$ ($\mu_0 H$: external magnetic field, T_c: superconducting transition temperature, Δ_0: zero-temperature energy gap, $\lambda(0)$: zero-temperature magnetic penetration depth).**

$\mu_0 H$ (T)	T_c (K)	Δ_0 (meV)	$\lambda(0)$ (nm)
0.1	6.24(3)	0.97(4)	252-256
0.5	6.00(4)	0.87(3)	268-288
1	5.59(2)	0.80(3)	254-295
2.5	4.36(2)	0.58(5)	232-325

9.3.2 Study of the magnetic penetration depth in $RbOs_2O_6$

Since the discovery of superconductivity in pyrochlore related oxides there is no agreement about the nature of superconducting pairing mechanism in these compounds. Investigations of specific heat (1), pressure effects on the magnetic field penetration depth (2) and NMR in $RbOs_2O_6$ (3), as well as band structure calculations of KOs_2O_6 (4) point to a conventional type of superconductivity. In contrast, measurements of the second critical field H_{c2} (5), μSR (6; 7), and specific heat (5) suggest an unconventional type of paring in KOs_2O_6 and $RbOs_2O_6$.

The results of our μSR study of the temperature dependent magnetic penetration depth $\lambda(T)$ in $RbOs_2O_6$ (see Ref. (8) for details) are summarized in Table 9.1 and yield the following findings:

- The absolute value of λ at zero temperature is in the range of 250 nm to 300 nm.
- For temperatures down to 30 mK the temperature dependence of λ is consistent with what is expected for a weak–coupled s–wave BCS superconductor (see Fig. 9.6).
- The shape of $\lambda(T)$ is almost independent of the magnetic field.
- The value of the zero-temperature superconducting gap decreases with increasing magnetic field (decreasing of T_c). The ratio $2\Delta_0/k_B T_c$ was found to be in the range of 3.09–3.60 close to the weak-coupling BCS value 3.52.

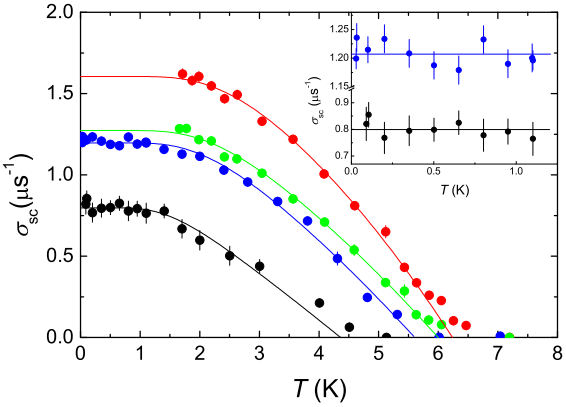

Figure 9.6:
Temperature dependence of the superconducting part of the μSR depolarization rate $\sigma_{sc} \propto \lambda^{-2}$ of $RbOs_2O_6$, measured in fields (field-cooled) of 0.1 T, 0.5 T, 1 T, and 2.5 T (from the top to the bottom). The inset shows the low-temperature region between 0 K and 1.25 K. The constant (within error bars) $\sigma_{sc}(T) \propto \lambda^{-2}$ suggests that $RbOs_2O_6$ is a weak-coupled BCS superconductor. Solid lines represent fits with the expression for the weak-coupling BCS model given in [8].

- The μSR measurements show that at low temperatures the magnetic penetration depth λ is almost (within an accuracy of 10%) field independent, in agreement with what is expected for a superconductor with an isotropic energy gap.

These facts suggest that $RbOs_2O_6$ is *a weak-coupled BCS superconductor with isotropic energy gap*.

[1] M. Brühwiler *et al.*, Phys. Rev. B **70**, 020503(R) (2004).
[2] R. Khasanov *et al.*, Phys. Rev. Lett. **93**, 157004 (2004).
[3] K. Magishi *et al.*, cond-mat/0409169.
[4] R. Saniz *et al.*, Phys. Rev. B **70**, 100505 (2004).
[5] Z. Hiroi *et al.*, J. Phys. Soc. Jpn **73**, 1651 (2004).
[6] R. Kadono, J.Phys.: Condens. Matter **16**, S4421 (2004).
[7] A. Koda *et al.*, cond-mat/0402400.
[8] R. Khasanov *et al.*, cond-mat/0411674.

9.3.3 Tri-layer $YBa_2Cu_3O_7/PrBa_2Cu_3O_7/YBa_2Cu_3O_7$ studies by means of low-energy μSR and polarized-neutron reflectometry

One of the most remarkable unconventional effects in HTS is the recently observed giant proximity effect (see e.g. (1) and references therein). A supercurrent in Josephson junctions was found to run through relatively thick non-superconducting barriers. This contradicts conventional theories which predict exponential suppression of supercurrents with increasing barrier thickness because of the short coherence length of HTS's.
Recent advances in fabrication and characterization of multilayers based on perovskite oxides have opened a new avenue in the investigation of various physical phenomena in superconductor/ferromagnet and superconductor/insulator heterostructures needed in the fabrication of Josephson and proximity effect junctions. Last year we started low-energy μSR measurements in a $33\,\mathrm{nm}/50\,\mathrm{nm}/115$ nm $YBa_2Cu_3O_7/PrBa_2Cu_3O_7/\ YBa_2Cu_3O_7$ structure grown at the University of Geneva. The measurements in a weak magnetic field $\mathrm{B_{ext}}$ = 19.54 mT applied parallel to the surface of the tri-layer sample at a temperature of 5K are presented in Fig. 9.7. Implantation energies of incoming muons were tuned to stop most of the muons in the appropriate layer (3 keV/12.5 keV/30 keV).

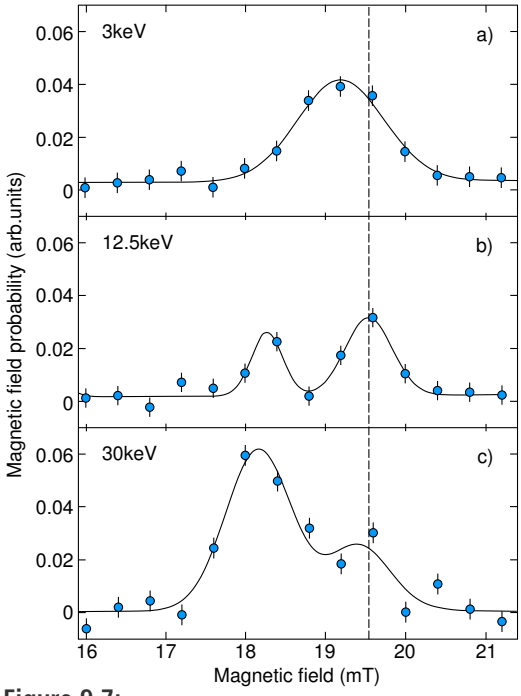

Figure 9.7:
Magnetic field distributions measured at T=5K in external magnetic field Bext=19.54mT (dashed line) in: a) first $YBa_2Cu_3O_7$ layer; b) intermediate $PrBa_2Cu_3O_7$ layer; c) second $YBa_2Cu_3O_7$ layer.

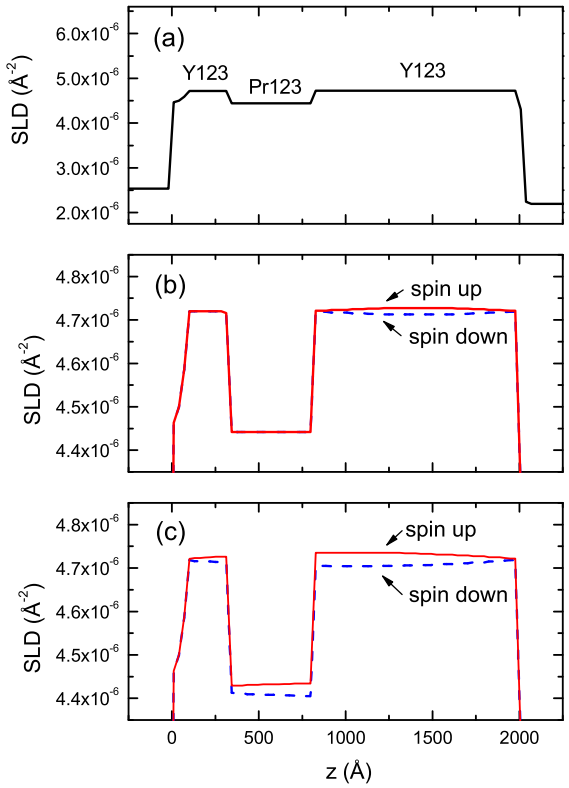

Figure 9.8:
The SLD profiles in the $YBa_2Cu_3O_7/PrBa_2Cu_3O_7/YBa_2Cu_3O_7$ tri-layer sample in the normal state (a) and in the superconducting state (b and c). The solid and dashed lines in (b) and (c) denote the SLD profiles for spin-up and spin-down neutrons, respectively.

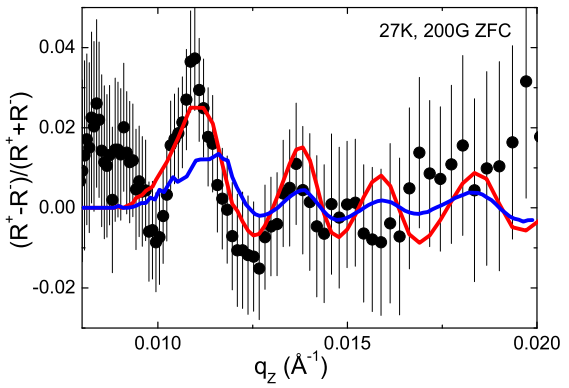

Figure 9.9:
$(R^+ - R^-)/(R^+ + R^-)$ vs. q_z ($T = 27$ K, $H = 200$ G zero-field cooled) for the $YBa_2Cu_3O_7/PrBa_2Cu_3O_7/YBa_2Cu_3O_7$ tri-layer sample. The blue and red lines are calculated for the models presented in Figs. 9.8(b) and (c), respectively.

One can see that the magnetic field is screened not only inside both superconducting layers, but there is a pronounced peak of the internal field distribution function well below the applied magnetic field inside the intermediate antiferromagnetic layer. To check if this behavior is due to the superconductor/antiferromagnet interface we are planning experiments in $PrBa_2Cu_3O_7$ thin films and $YBa_2Cu_3O_7/PrBa_2Cu_3O_7/YBa_2Cu_3O_7$ tri-layers with different thicknesses of individual layers.

In contrast to local techniques used so far in the study of the giant proximity effect, polarized-neutron reflectivity is a bulk method that can help to clarify whether giant proximity, pinholes and/or microshorts are responsible for the observed effects.

Here we report first preliminary studies of the giant proximity effect by means of the polarized neutron reflectivity technique. The tri-layer sample consists of $YBa_2Cu_3O_7/PrBa_2Cu_3O_7/YBa_2Cu_3O_7$ layers with relative thicknesses 33nm/50nm/115nm. First preliminary measurements of neutron scattering lengths density (SLD) profiles of the trilayer sample are shown in Fig. 9.8. In the normal state the SLD profile is determined by neutrons scattered by the nuclei, and it is expected to be equal for spin-up and spin-down polarized neutrons (Fig. 9.8(a)). In the superconducting state the magnetic field is expelled from the superconducting volume of the sample. Thus, in addition to pure nuclear scattering, magnetic scattering occurs and causes the difference in SLD profiles for spin-up and spin-down neutrons. Two simple models were tested. In the first one (see Fig. 9.8(b)), it was assumed that the magnetic field is screened only within the two superconducting $YBa_2Cu_3O_7$ layers, while in the antiferromagnetic $PrBa_2Cu_3O_7$ layer it is equal to the external field. In the second model the whole structure was assumed to be superconducting (see Fig. 9.8(c)). To remove the nuclear contribution in the reflectivity spectra $R(q_z)$, the ratio $(R^+ - R^-)/(R^+ + R^-)$ was determined

as shown in Fig. 9.9. Here q_z denotes the neutron wave vector, and the indexes $+$ and $-$ stay for spin-up and spin-down, respectively. The comparison of the experimental data with the curves calculated for the models presented in Figs. 9.8(b) and (c) leads to the conclusion that most probably the superconducting $YBa_2Cu_3O_7$ layers are coupled through the antiferromagnetic $PrBa_2Cu_3O_7$ layer. This statement is in agreement with our low-energy μSR measurements performed on the very same sample.

[1] I. Bozovic *et al.*, Phys. Rev. Lett. **93**, 157002 (2004).

9.4 Electric field effects in perovskites

9.4.1 Insulator-to-metal transition and resistive memory effect in perovskites induced by electric field

There has been an increased interest in investigating various sorts of *Random Access Memories* that retain stored information after removing the electrical power from the device, i.e., nonvolatile memory. Simpler memory cells presently under intense investigation are using the resistance change of a medium by current or voltage pulses, an effect observed in a large variety of extremely diverse materials.
Starting a collaboration with IBM Rüschlikon Laboratory, we are currently investigating the resistive switching effect that has been found in thin films of perovskites like (Ba,Sr)TiO_3, $SrZrO_3$, $SrTiO_3$ (1).These materials exhibit a charge-induced insulator-to-metal transition with a resistive memory effect. Exposed to an electrical field, the resistance of the doped perovskite is reduced by several orders of magnitude and a conductor is obtained, which is a prerequisite for the memory switching. Consecutive electrical current pulses of opposite polarity switch the resistance of the perovskite reversibly between a high-resistance and a low-resistance state (see Fig. 9.10). These two different states persist after removal of the applied electrical bias with a retention time of up to several years. Single crystals of Cr-doped $SrTiO_3$ (2) with the same memory behavior are used as a model system for this class of materials to study the drastic resistivity changes in the bulk under applied electrical field , the switching between memory levels and to clarify the role of defects with different valencies.

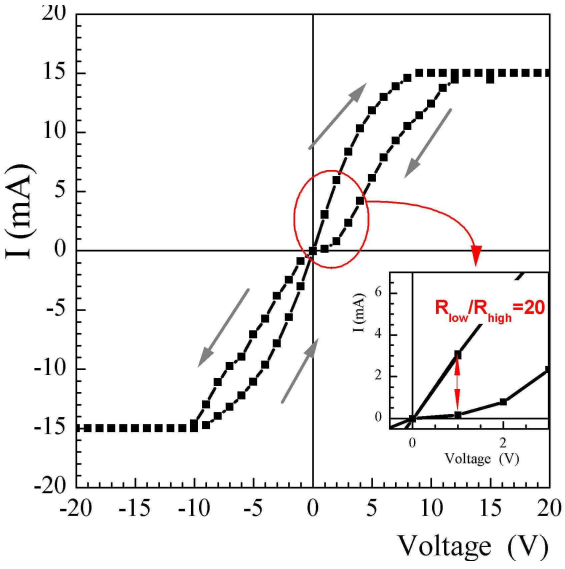

Figure 9.10:
Current-Voltage characteristic (I-V) on Cr-doped $SrTiO_3$ single crystal. Once the insulator-to-metal transition is reached, one finds a hysteresis behavior in the I-V curve.

Changes of the electronic state of the Cr dopant are detected by X-ray absorption spectroscopy on crystals during electrical stressing where it is possible to detect the transformation of Cr^{3+} to Cr^{5+} in a volume close to the metal electrode (anode). It is clear that in this material the Cr ion and its different valence states (3) play a crucial role. Therefore, we decided to study these materials using EPR. In a first step two different $SrTiO_3$:Cr single crystals were measured: annealed in a reducing atmosphere (Ar/H_2) and in an oxidizing atmosphere. It was found that in the oxidized crystals the

majority of Cr ions are in the 5+ valence state. A significant amount of Cr is still seen in the trivalent state. On the other hand, in reduced crystals only Cr^{3+} centers were observed with no evidence of the presence of Cr^{5+}.

In order to study the influences of Cr on the electronic structure of $SrTiO_3$ we performed dielectric and optical absorption measurements. By varying the defect (dopant) concentration (from 0.1 mol% to 0.2 mol%) in single crystals the dielectric properties are modified. Dielectric properties change even more drastically with the Cr valence state. Another evidence of the Cr influence on the electronic structure is the changes of the energy gap between the valence and conduction bands detected by optical absorption in the UV-visible range (from 3.2eV in the undoped samples to 2.5eV in samples with 0.2 mol% of Cr).

[1] A. Beck *et al.*, Appl. Phys. Lett. **77**, 139 (2000)
[2] Y. Watanabe *et al.*, Appl. Phys. Lett. **78**, 3738 (2001)
[3] K.A. Müller *et al.*, Solid State Commun. **85**, 381 (1993)

9.5 New developments in instrumentation

9.5.1 Novel design of piezoresistive torque sensors

Torque magnetometry is a powerful measurement technique, employed in studies of anisotropic and hysteretic magnetic systems. We have been using it successfully for investigations of cuprate superconductors for a decade (1)-(3). During this time, we have also improved this technique several times (4)-(6). The piezoresistive torque detection exploits the resistance change of doped silicon under stress. Since the application of a torque on a suitably formed sensor induces stress in the structure, this allows for an easily detectable and very sensitive determination of the applied torque. Recently we have considered and calculated sensor shapes differing from the initially used cantilever design adopted from atomic force microscopy tips. Our novel design is more flexible and allows expendability compared to those tips. The new square shape of torque sensors allows for the implementation of additional functionality. In Fig. 9.11 a version is shown with the integrated calibration loop and a diode for temperature measurement at the sample position. The fabrication of a sensor, sensitive along two directions, is possible, when all four legs are equipped with piezoresistive paths. Moreover, the sensitivity and robustness can be influenced by modifying the length of the legs. Longer legs result in higher sensitivity, but also cause the sensor to become more fragile and likely to break when a sample is mounted.

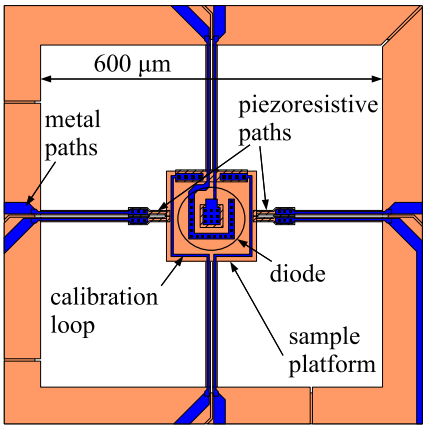

Figure 9.11:
New square shape design with calibration loop and diode for temperature measurement. Piezoresistive paths (hatched areas) are situated on the left and right legs, close to the sample platform. The sensor is embedded in a large $4 \times 5\,\mathrm{mm}^2$ chip. The metallic paths (colored blue) provide the electrical connections.

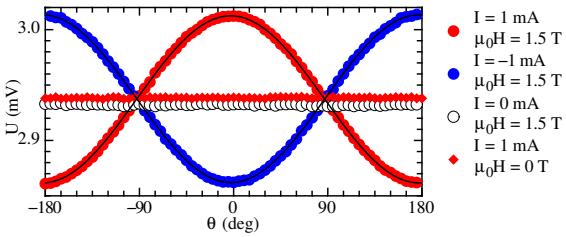

Figure 9.12:
Angle dependent measurements with the new high sensitivity torque sensor shown in Fig. 9.11 in various magnetic field strengths H and calibration loop currents I. Solid lines represent simple cosine-fits. The amplitude of the cosine signal amounts to $2.85 \times 10^{-11}\,\mathrm{Nm}$ in terms of absolute torque.

A metallic loop incorporated on the sample platform allows the induction of a small magnetic moment. Angle dependent measurements in fixed magnetic fields then allow for the relation of the measured voltage to absolute torque magnitudes (example is shown in Fig. 9.12).

[1] D. Zech *et al.*, Phys. Rev. B **54**, 12535 (1996).
[2] M. Willemin *et al.*, Phys. Rev. Lett. **81**, 4236 (1998).
[3] J. Hofer *et al.*, Phys. Rev. Lett. **84**, 4192 (2000).
[4] C. Rossel *et al.*, J. Appl. Phys. **79**, 8166 (1996).
[5] M. Willemin *et al.*, J. Appl. Phys. **83**, 1163 (1998).
[6] C. Rossel *et al.*, Rev. Sci. Instrum. **69**, 3203 (1998).

9.5.2 Automation of the torque measurement setup

Modern scientific work increasingly requires extensive studies in order to detect systematic effects across a large variety of samples and measurement conditions. Measurement automation greatly facilitates such time consuming experiments, but is mostly available only in commercial apparatuses. The control software shipped with such systems is usually created and improved over years by specialized software development teams. Such costly development is seldom within the possibilities of research laboratories, which is why the computer programs used to control custom built experiments are often comparably simple and allow only restricted automation.
A relatively simple program architecture allowed us to create a highly versatile control software system for our custom torque magnetometer (1). Our approach comprises the use of individual programs running in parallel with appropriate means of communication between them. This makes possible the use of an additional program to control the whole system. In our current implementation, this additional program works through a previously created sequence of commands. The nearly arbitrary complexity permitted for such sequences enables us to have the system conduct long measurement series automatically. The basic structure is very general which makes both the application to other instruments and the expansion to more complexity very easy. Currently, we are working on its adaptation to an EPR spectrometer. Since the system is programmed using LabVIEW, an easy to learn graphical programming language, its modification and extension is further facilitated. Thus, the automatic adaptation of experimental parameters based on measurement results during the measurement itself might also be made possible.

[1] S. Kohout, J. Roos, and H. Keller, submitted for publication.

10 Phase transitions, thermal transport and new materials

R. Dell'Amore, A. Engel (since August 2004), M. Reibelt, A. Schilling

in collaboration with:
Ch. Rüegg, Paul Scherrer Institute, K. Krämer, University of Bern, G. Ravikumar, Bhaba Atomic Research Center, Th. Wolf, Forschungszentrum Karlsruhe, K. Il'in, Universität Karlsruhe, P. Canfield, Iowa State University, J. Karpinksi, ETH Zürich, H.-W. Hübers, Deutsches Zentrum für Luft- und Raumfahrt, CSEM Neuenburg, FIRST Lab ETH Zürich.

Besides various activities to extend our experimental possibilities and to complete the equipment used by all the members of our group, we have started a new activity, the study of superconducting thin-film nanostructures. Nanostructuring of materials in general has become a more and more widely used technique to do state-of-the-art experiments. Some of our group members are trained at the FIRST Center for Micro- and Nanoscience at the ETH Zürich, which will enable us to act more flexibly if new developments in solid-state physics require the micro- or nanostructuring of samples or experiments.

10.1 Physics of superconducting thin-film nanostructures and possible applications as fast single-photon detectors

10.1.1 Motivation

Besides the obvious applications of superconducting materials in the field of loss-free current distribution and energy storage the unique properties of the superconducting state also open up a very wide field of electronic and detector applications. In this new project we aim at exploring the physics of narrow superconducting strips and their potential as single-photon detectors eventually covering a spectral range from infrared to high-energy x-ray photons.

Scientific progress always demands faster, more sensitive detectors with a higher energy resolution, ideally all combined within one device that is even scalable to a multi-pixel imaging camera. The recently proposed design of a superconducting single-photon detector (1) based on thin and narrow superconducting strips has promise of better performance with respect to various applications compared to existing technologies. Absorption of a photon in a superconductor leads to the breakage of a Cooper-pair. In general, the photon energy is orders of magnitude larger than the superconducting gap energy, thus creating a highly-excited, non-equilibrium electron. The cascade-like thermalization process results in a large number of quasiparticles within an extremely short timescale on the order of femtoseconds. The thus formed hot-spot has a size that is determined by the photon energy, quasi-particle multiplication efficiency, diffusion of quasi-particles, their decay via recombination and phonon escape into the substrate and the dimensions of the superconductor. Within the hot-spot superconductivity is weakened or even completely suppressed. In a bulk superconductor the hot-spot usually goes unnoticed except when the temperature is right at the superconducting transition and for relatively high photon flux.

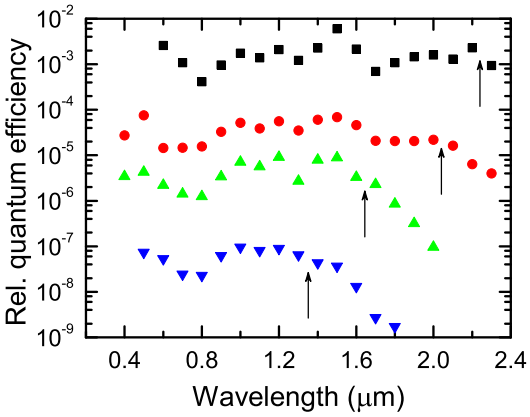

Figure 10.1:
Signal count rates for a photon detector made from a NbN thin film as a function of the wavelength of the incident light. Data were taken for different bias currents; from bottom to top they were set to 0.6, 0.77, 0.8 and 0.89 times the critical current at the operating temperature. For clarity, the data have been shifted along the vertical axis. The cut-off wavelengths are marked by arrows.

In two-dimensional NbN thin-films the hot spot reaches a radius of about 10 nm after absorption of an optical photon. Structures of such narrow dimensions are still out of reach of standard lithography. However, applying a bias current only slightly less than the critical current of the strip, optical and near-infrared photons can be readily detected in 100 nm wide strips, a size achievable using e-beam lithography. The effect of the hot-spot formation may be macroscopically described as a localized reduction of the effective critical current density. If it drops below the applied current density, a complete cross-section of the strip switches temporarily into the normal state and a voltage transient develops between the strip ends.

10.1.2 Photon detection and fluctuations

The original detection model is based on the formation of a normal conducting core within the hot-spot. If the size of this normal core is larger than the superconducting coherence length the applied bias current is redistributed which eventually leads to the formation of the voltage transient. Inherent to this model is a long wavelength cut-off; photons with $\lambda > \lambda_{\text{cut-off}}$ result in hot-spots with a normal core that is too small to trigger the signal. Multi-photon or fluctuation assisted processes may still result in a positive detection event, but with a substantially reduced probability. At higher photon energies, i.e. shorter wavelengths the detection probability should be relatively flat, resembling the absorption probability of these photons within the superconducting strip. The plateau in the detection efficiency at short wavelengths has been experimentally confirmed (see Fig. 10.1) and also the decrease beyond a bias current dependent cut-off wavelength (2). However, the cut-off is not sharp but rather rounded and continuous. Furthermore, knowledge of the dependence of the cut-off wavelength on bias current allows one to calculate the theoretical normal core size of the hot-spot as a function of the photon wavelength. It turns out that these core sizes are far too large in comparison to model estimates (3).

These apparent contradictions prompted us to advance the detection model (4). The key point in our refined detection model is that the formation of a normal core within the hot-spot is not even necessary to trigger a voltage pulse. Instead we considered the reduction of the Cooper-pair density within a cross-section of the superconducting strip that is centered around the point of photon absorption. We could show that a certain number of Cooper-pairs need to be broken for a positive detection event, which is equivalent to a local reduction of the critical current density below the applied current density. Model calculations have shown, that this happens well before the normal conducting core of the hot-spot has

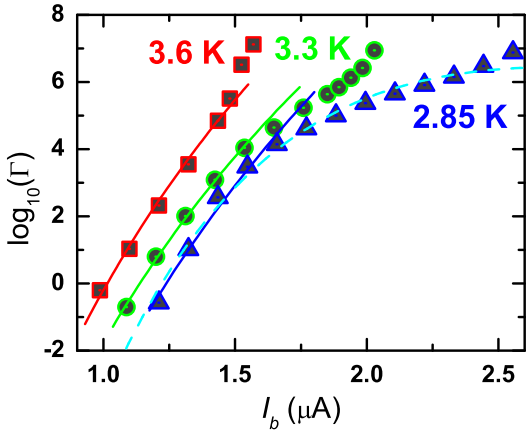

Figure 10.2:
Dark count rates as a function of bias current for different operating temperatures. The dark count rates exhibit a strong current and peculiar temperature dependence. The curves are calculated according to a model based on fluctuating vortex-antivortex pairs. Such a model seems to be promising to explain the observed behavior.

formed and gives a much more consistent description of the experimental data.

Another important issue we have recently addressed are fluctuations of the superconducting order parameter in these nanostructures that make up these photon detectors and which are a major source of dark count events. In Fig. 10.2 signal counts that were recorded with no incident light on the detectors are plotted versus the applied bias current for three different temperatures. There are a whole range of effects that might be responsible for fluctuations that could cause voltage pulses to develop even in the absence of photons. But a deeper analysis of the distinct temperature and current dependence leaves just a few effects as likely candidates able to describe the experimental data. We suggest fluctuating vortex-antivortex pairs as the main source of dark count events (5). In two-dimensional superconductors the occurrence of such vortex pairs is well established and due the Lorentz force caused by the applied current, these pairs may break and start to move towards opposite edges of the strip. This movement in turn will cause a voltage pulse quite similar to those caused by absorbed photons. At high temperatures this model fits the experimental data quite well already. Tweaking the model parameters a little bit, the fit at lower temperatures can improved substantially (dashed curve in Fig. 10.2), however, at the current state, this is purely phenomenological and not based on a sound theoretical model.

10.1.3 Outlook

Improving the detector performance in terms of detection efficiency and spectral range is necessary if such detectors should become viable alternatives for applications. Therefore, we aim to improve technological aspects of the nanostructuring process, not least through the utilization of facilities at the FIRST laboratories at the ETH Zürich. This will be supplemented by the search for alternative materials with possibly superior properties compared to the Nb and NbN films used so far. The fluctuation models also have to be improved and experimentally verified.

[1] A. D. Semenov *et al.*, Physica C, **351**, (2001) 349.
[2] A. Semenov, *et al.*, **Optical Sensing**, volume 5459 (Proc. SPIE Int. Soc. Opt. Eng., 2004), 237.
[3] A. Semenov, *et al.*, Eur. Phys. J. AP, **21**, (2003) 171.
[4] A. Semenov, *et al.*, submitted to Eur. Phys. J., preprint available at cond-mat/0410633.
[5] A. Engel, *et al.*, phys. stat. sol. (c), **2**, (2005) 1668.

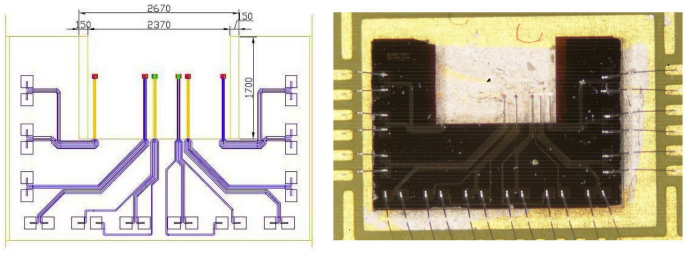

Figure 10.3:
Design and realization of a thermal conductivity chip, designed for two separate measurements (dimensions in μm).

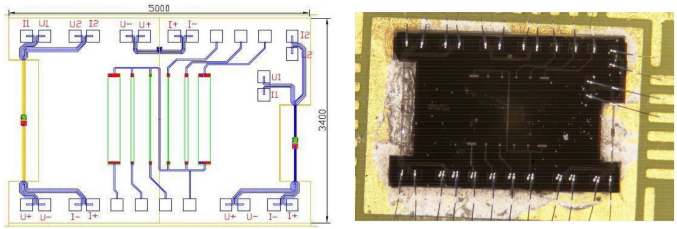

Figure 10.4:
Design and realization of a heat-capacity chip, designed for two separate measurements (dimensions in μm).

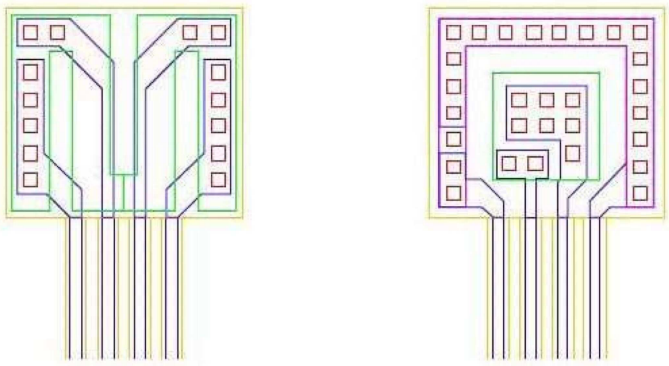

Figure 10.5:
Design and realization of a heater (left) and a thermometer (right). The heater is a p-doped surface, the thermometer is a p-n junction of the same area (78×88 μm^2). (Silicon part in yellow, metallic part in blue, the doped areas are accentuated in purple (n) and green (p), the red squares are the contact pads.)

10.2 Design and development of miniaturized thermal conductivity and heat-capacity experiments

We have designed several miniaturized experiments on silicon chips that will enable us to perform more accurate thermal conductivity and heat-capacity measurements on microscopic samples. A standard steady-state heat flow configuration and an AC calorimetry experiment have been miniaturized to an area of 2.5×3.4 mm^2.

We fabricated these chips on a standard Silicon wafer (in collaboration with CSEM, Neuenburg). For both types of measurements we used p-n junctions as thermometers and p-doped areas as heaters (see Fig. 10.3, Fig. 10.4 and Fig. 10.5). Programming and calibration work will be subject of a future bachelor or a masters thesis.

10.3 Bose-Einstein condensation of magnons in the S=1/2 spin system $TlCuCl_3$?

Last year we have reported on measurements of the thermal conductivity of $\mathrm{TlCuCl_3}$ in its magnetically ordered state, i.e. in magnetic fields above $\mu_0 H_c \approx 5.5\mathrm{T}$ at low temperatures. These measurements were motivated by the search for the manifestation of a Bose-Einstein condensation of magnons (1) that should lead to an enhanced heat transport as it is ob-

served in superfluid helium.

However, in our experiments we could not detect any clear, significant enhancement in the thermal conductivity of $TlCuCl_3$. This may be due to the fact that a low spin-lattice relaxation rate $\frac{1}{T_1}$ does not allow for an efficient coupling of the spin system to the external heat source that heats up the crystal lattice in such an experiment (2). Therefore we decided to design an alternative experiment with the aim to excite the spin system directly. A general feature of condensates is the existence of collective excitations of the quasi-particles. One such a mode is called *second sound*. This phenomenon can be regarded as an oscillation in the local density of magnons creating a standing entropy or temperature wave, in analogy to standing entropy waves observed in superfluid helium. Given the crystal dimensions and the dispersion relation of the magnons in the condensate state (3), such standing wave oscillation frequencies should be of the order of 100 kHz and larger.

We have built a Wheatstone-like bridge set-up to detect possible absorption resonances upon the formation of such standing waves. The probe is composed of two branches of identical coils and resistors, respectively. By sweeping the frequency of the signal and measuring the voltage difference ΔU between the two branches we can detect changes in the self inductance of the coil containing the sample. Such changes are expected as soon as the crystals absorbs energy from the electromagnetic field when a resonance phenomenon occurs. At present we reach a voltage sensitivity of 40 nV, which corresponds to changes in the self inductance of one part in 10^8.

[1] T. Nikuni *et al.*, Phys. Rev. Lett. **84**, 5868 (2000).
[2] O. Vyaselev *et al.*, Phys. Rev. Lett. **92**, 207202 (2004).
[3] Ch. Rüegg *et al.*, Nature (London) **423**, 62 (2003).

10.4 Vortex phases in type-II superconductors

Last year we had investigated the magnetic phase diagram of V_3Si using a high-accuracy differential thermal analysis (DTA) method (1), and we detected a variety of thermal effects that may be ascribed to the formation of different vortex phases. However, we have not yet been able to prove that these effects are signatures of a true thermodynamic phase transition. Since the vortex configurations in V_3Si are expected to be out of thermodynamic equilibrium, we decided to perform so-called "vortex-shaking" experiments (i.e. the application of a small AC magnetic field perpendicular to the main field direction), which have been shown to be effective to drive non-equilibrium vortex states into a thermodynamic equilibrium (2; 3; 4; 5). Because the AC-field coils were not part of the initial design of our experiment and a respective upgrade turned out be unsatisfactory due to large induced screening currents, we decided to build an entirely new heat-capacity probe with many significant improvements compared to the older versions. The new measuring cell is suspended with nylon threads, leading to a better thermal decoupling of the cell. A clamp mechanism enables quick cooling, and two small AC-field coils are mounted on adjustable holders forming a split coil system, with the sample platform placed in between the two AC-coils (see Fig. 10.6).

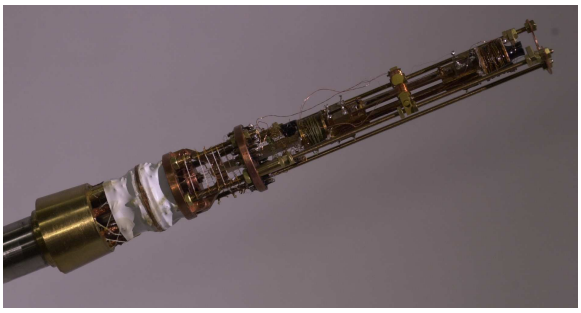

Figure 10.6:
New heat-capacity probe with suspended measuring cell and AC-coils.

Besides continuing the investigations of the phase diagram of V_3Si using this AC-shaking technique, we also intend to test a theory on the "vortex-shaking" effect by Brandt and Mikitik (5). Consider a thin superconducting strip, with a constant homogeneous external magnetic field H_a directed perpendicular to the plane of the specimen (i.e. along z), and an AC-magnetic field $h\cos(\omega t)$ along x, i.e. perpendicular to H_a and to the screening currents inside the sample (see Fig. 10.7). The currents flowing in the critical state of the strip generate a nonuniform distribution of the magnetic induction $B_z(x)$. The AC field periodically tilts the vortices in this state. However, at each point x with a nonzero sheet current $J(x)$ (the current density integrated over the thickness d), the tilt is not symmetric relative to the central plane of the strip, $z = 0$, and during each cycle of the AC field, the asymmetry leads to a shift of the vortices towards the center of the strip ($x = 0$). This process that tends to equilibrate $B_z(x)$ is called flux line "walking" and is illustrated in Fig. 10.7. Quantitatively, vortex shaking in a thin strip should be effective for $h > J_c/2$ (5), irrespective of the shaking frequency ω. As J_c decreases with increasing temperature T, an equilibrium state should be reached as soon as $J_c = 2h$. The effect of the vortex-shaking process has already been observed in magnetization experiments (3; 4), and it should be observable in our experiment as well.

We intend to test the above quantitative predictions on a twinned $YBa_2Cu_3O_7$ single crystal with T_c = 91 K and $m = 8.18$ mg, that does not show the first-order vortex-melting transition as observed in clean, untwinned samples with weaker vortex pinning (work in collaboration with Th. Wolf, Forschungszentrum Karlsruhe). We have estimated the critical-current density j_c of this crystal from magnetization measurements and using the standard Bean model (see Fig. 10.8). At the expected melting transition, $T = 82$ K in $\mu_0 H_a = 5$ T, j_c is already vanishingly small and well within reach of the field amplitudes of our AC-split-coil arrangement. Consequently, the equilibrium first-order melting transition of the vortex lattice should become observable also in this twinned $YBa_2Cu_3O_7$ single crystal.

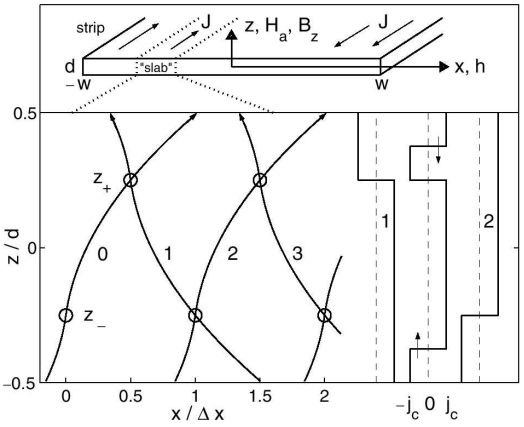

Figure 10.7:
Strip geometry to illustrate the flux line "walking" from left to right through a section of the strip, shown at times $t\omega/\pi = 0, 1, 2, 3$ [5].

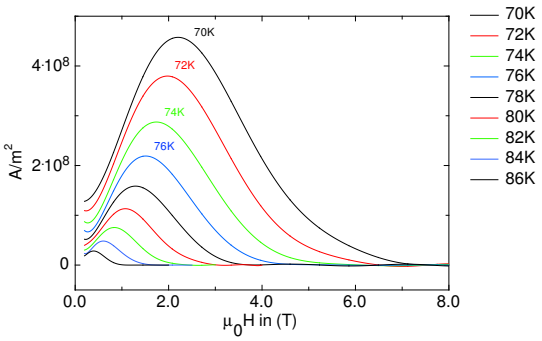

Figure 10.8:
Field dependence of the critical-current density j_c of a twinned $YBa_2Cu_3O_7$ single crystal for different temperatures.

[1] A. Schilling and O. Jeandupeux, Phys. Rev. B **52**, 9714 (1995).

[2] M. Willemin *et al.*, Phys. Rev. B **58**, R5940 (1998).

[3] M. Willemin *et al.*, Phys. Rev. Lett. **81**, 4236 (1998).

[4] N. Avraham *et al.*, Nature (London) **411**, 451 (2001).

[5] E. H. Brandt and G. P. Mikitik, Phys. Rev. Lett. **89**, 027002 (2002).

11 Surface Physics

T. Greber, M. Hengsberger, J. Lobo, R. Schillinger, T. Okuda, M. Muntwiler, A. Tamai,
A. Dolocan, M. Corso, C. Cirelli, M. Morscher, L. Brandenberger, M. Klöckner, J. Osterwalder

The surface physics laboratory is well equipped for the preparation and characterization of clean surfaces, ultrathin films and nanostructures under ultrahigh vacuum (UHV) conditions. Experimental techniques available to us include x-ray photoelectron spectroscopy (XPS) and diffraction (XPD), angle-resolved photoemission spectroscopy (ARPES), two-photon photoemission (2PPE) using femtosecond laser pulses, low-energy electron diffraction (LEED) and scanning tunneling microscopy (STM). At the nearby Swiss Light Source (SLS) we operate two more photoemission spectrometers that were built in our department: a high-resolution ARPES experiment with a three-dimensional spin polarimeter for spin-resolved Fermi surface mapping (the COmplete PHotoEmission Experiment, COPHEE, stationed at the Surface and Interface Spectroscopy beamline of the SLS), and an angle-resolved XPS chamber for near-node photoelectron holography stationed at the Surface and Interface Microscopy beamline of the SLS.

The research carried out during the report period can be grouped into four topics:

- **Electronic states at metal surfaces**
  When we studied the monolayer system of Pb on Cu(111) a couple of years ago for its properties as a surfactant in thin film growth, we realized that the Pb film could be melted on the Cu(111) surface at temperatures below the onset of desorption. A unique opportunity was thus opened to study electronic states in a *liquid* layer by ARPES. The presence of the ordered Cu lattice provides the reciprocal lattice vectors needed for defined electron momentum mapping. The electron dispersion and Fermi surface mapping data described in Section 11.1 give detailed information about the character and the coherence length of the states. It is the first study of its kind and has raised a lot of interest (1). The close-packed (111) surface of gold exhibits a so-called Shockley surface state that propagates almost freely within the surface plane and thus exemplifies a two-dimensional gas of nearly-free electrons (2DEG). This is manifested in a parabolic energy dispersion relation. Due to the high atomic number of Au, this 2DEG is subject to spin-dependent momentum shifts, induced by the Rashba effect that has its origin in the spin-orbit interaction. The COPHEE spectrometer provides direct experimental access to these momentum shifts and the detailed *spin structure* in reciprocal space. Currently, we are trying to learn how such spin structures can be modified by introducing defined structural defects in the surface. Au(17 11 9) is a vicinal Au(111) surface that exhibits a regular array of steps and kinks. On this surface, the surface state spectra are much broader, but with the help of spin resolution, the Rashba-split components can still be resolved (Section 11.2). From these measurements we hope to obtain useful information about spin-dependent scattering processes at defects, and thus eventually on spin-dependent transport properties that are at the heart of the new field of *spintronics*.

- **Monolayer films of hexagonal boron nitride on metal surfaces**
  The preparation of well-defined monolayer-thick films permits us to study the structural, electronic and magnetic properties at an interface between two different materials. On Rh(111) the *h*-BNfilm self-assembles into a remarkable nanostructure in the form of a two-layer *nanomesh*, that may also be useful as a support for *functionalized surfaces*. The

mesh size of 3 nm with 2 nm holes is very interesting. The group has successfully applied for a EU grant (Three-year STREP project "NanoMesh" within the 6th Framework Programme) in which a consortium of 9 European partners are investigating the self-assembly process, alternative production routes and promising applications. A prerequisite for many applications is the *stability* of the formed mesh. In Sec. 11.3 it is demonstrated that the mesh is not only thermally stable, but that is withstands exposure to air and to liquid environments. An obvious step in this research is a screening for other systems that potentially form nanomeshes, maybe with different hole sizes and periodicities. In his diploma thesis, Martin Morscher finds that on Pd(111), boron nitride forms Moiré patterns in several domains rather than a well defined nanomesh (Section 11.4), and can thus be probably removed from the list of interesting candidate systems. The interface character of boron nitride films is best studied on Ni(111), where a commensurate (1x1) single monolayer is formed. Time-resolved 2PPE data from this interface exhibit very interesting dynamical phenomena within a time-window of a few hundred femtoseconds of a photo-excitation process (Section 11.5). An extremely strong enhancement of a well defined signal at temporal coincidence in a two-color pump-probe experiment is indicative of a *two-channel interference*.

- **Adsorbed molecules**
  Molecular monolayers offer a highly interesting route to prepare functionalized surfaces. In a dense layer, the electronic states of the individual molecules may start to interact with each other and form extended states, *molecular band states*, with new properties. On Cu(553), which is vicinal to Cu(111) and exhibits a regular array of steps with terraces in between that are roughly the size of a buckyball, C_{60} molecules form linear chains that alternate in brightness. In the one type of chains we find for the first time the pentagon bonding to the hexagonal terrace surface. ARPES data now indicate that this unusual bonding is accompanied by a very large band width of the highest occupied molecular orbital (HOMO) (Section 11.6). *Chirality* is another important aspect for molecular adsorption. Au(17 11 9) is a naturally chiral surface, i.e. there are kink sites with a chiral center. The question is whether these sites can distinguish left- and right-handed species of a chiral molecule like the aminoacid *cysteine*. Forward-scattering XPD patterns prove to be a unique indicator of chirality, because they display directly the chiral character of the molecule when single enantiomers are adsorbed, Indeed, we find distinct differences in the bonding of the two cysteine species (Section 11.7).

- **Time–resolved electron diffraction**
  The time-resolved low-energy electron diffraction (LEED) experiment, aimed at real-time investigations of *structural rearrangements* at surfaces, has been upgraded by attaching an electron energy analyzer to the vacuum chamber. At the same time, the Croissant measurement software (now commercialized by the start-up company *muntwiler+gresch*) has been implemented that is now common to all our photoemission spectrometers. This allows to measure energy distribution curves of the electrons emitted from the pulsed electron guns (Section 11.8). Effects of the space charge produced by thousands of electrons emitted from the cathode at the same time could thereby be studied in detail by taking energy spectra and by measuring the final electron pulse duration using the pinhole electron-photon pulse correlator (cf. *Annual Report 2003/04*). During the course of the year a new pulsed electron gun was designed and built up which provides a higher electron flux than the previous one while keeping the nominal electron pulse width at the sample in the range of a few picoseconds. First attempts to record time-resolved LEED images after ultrafast heating of Si(111) and In-(4x1)/Si(111) surfaces failed so far because of the low absorption coefficient of silicon for near-infrared light. First studies of the In-

(4x1)/Si(111) system, which exhibits a metal-insulator transition near 120 K, will be pursued using time-resolved photoemission. For the proof-of-principle of time-resolved LEED, C_{60}–monolayers on Cu(111) have been chosen as sample surface. These experiments are currently underway.

[1] Y. Petroff, Science 306 (2004) 2200.

11.1 Electronic structure of a two–dimensional liquid metal

in collaboration with: F. Baumberger, Department of Applied Physics, Stanford University, USA

The vast majority of models in condensed matter physics assumes translational invariance of the elementary building blocks. However, many widely used materials lack such symmetry. They are polycrystalline, amorphous or liquid. In particular, amorphous materials are of growing technological interest for their low production costs and often unique mechanical and electronic properties (1).

Developing a microscopic understanding of these properties remains a prime experimental and theoretical challenge. In a perfect crystal, the electronic wave functions can be classified as Bloch states, *i.e.* plane waves modulated by a lattice periodic function, and many macroscopic properties can be derived from the microscopic properties of the electronic wave functions. In amorphous or liquid materials this does not work. Moreover, the lack of periodicity markedly restricts the information provided by experimental probes that operate in reciprocal space. Consequently many fundamental problems of the electronic structure of liquids remain unresolved. The character of electronic wave functions in liquid metals, and especially to what extent they are itinerant or localized, has so far eluded experimental investigation.

Investigating by ARPES the behavior of a liquid monolayer of Pb supported on a crystalline Cu substrate, we could overcome these difficulties and directly track the localization of the electronic wave

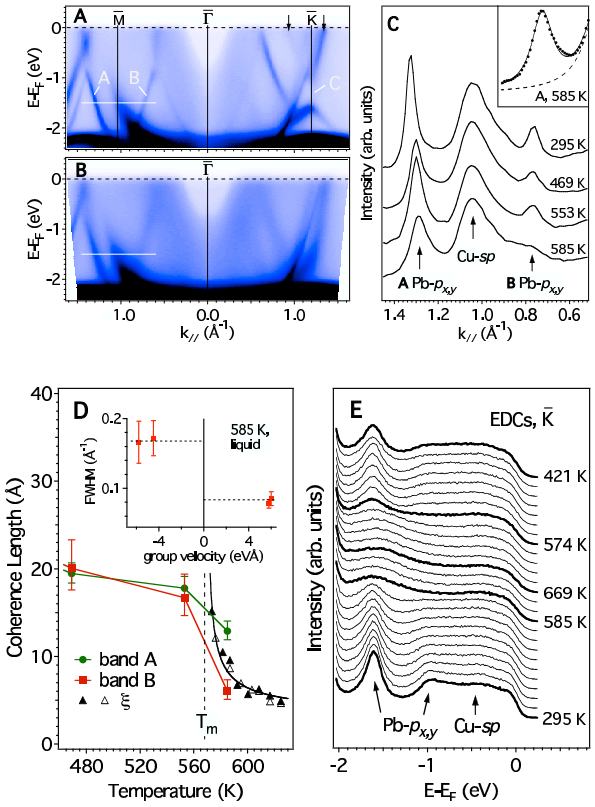

Figure 11.1:
Electron coherence in a melting lead monolayer.
A - C: ARPES data showing the measured electron dispersion and spectral function in the solid and liquid film. The Lorentzian line shape in the liquid phase indicates exponentially localized eigenstates.
D: Line widths and localization lengths are found to depend on the character of the constituting atomic wave functions.
E: Set of EDCs demonstrating the reversible filling and opening of a band gap through the phase transition (for details see Ref. [2]).

functions through the melting transition (2). It is found that states with even symmetry remain coherent over several inter–atomic distances, also well above the melting transition where the structural pair correlation length drops to only 5 – 10$\AA$ (see Fig. 11.1). Contrary, the p–like states with negative group velocity show a decay length in the liquid phase which is shorter than the wave length, *i.e.* may be considered fully localized.

[1] Physics News 689, June 21, 2004, Z.P. Lu, C.T. Liu, J.R. Thompson, and W.D. Porter, Phys. Rev. Lett. **92**, 245503 (2004).

[2] F. Baumberger, W. Auwärter, T. Greber, and J. Osterwalder, Science **306**, 2221 (2004).

11.2 Spin polarized surface states on a kinked vicinal Au(111) surface

in collaboration with:
V. N. Petrov, St. Petersburg Technical University, Russia; L. Patthey, Swiss Light Source, Paul-Scherrer Institut; and J. Henk, Max-Planck-Institut für Mikrostrukturphysik, Halle, Germany

All the noble metal (111) surfaces have an sp-derived Shockley surface state originating from the energy gap around the L-point of the bulk Brillouin zone. These states form a quasi two-dimensional electron gas (2DEG) which is confined in the direction perpendicular to the surface (1). In the case of Au(111) this surface state has been observed to be spin-split into two parabolic sub-bands, shifted in momentum with respect to each other due to the Rashba effect (1; 2; 3). The spin quantization axis is mainly contained in the surface plane, being tangent to the circular constant energy surfaces in momentum space. The sub-bands have opposite spin directions, and the circular symmetry results in zero net magnetic moment (3). In order to study the effects of steps and kinks on the generic spin structure, we have studied the related surface state on Au(17 11 9), which is a chiral surface vicinal to Au(111) with a $15.4°$ miscut angle. The surface unit cell is formed by monoatomic steps separated by $4\frac{2}{3}$ atoms, with a separation between consecutive kinks of $3\frac{1}{2}$ atoms. We observe that the surface state propagates parallel to the average surface. Compared to Au(111), it exhibits a larger electron effective mass, which is consistent with results from previously studied stepped surfaces (4). This mass enhancement is related to the scattering off the step edges. A Fermi surface map measured at room temperature, using a photon energy of 21.2 eV (He-Iα), is shown in Fig. 11.2.

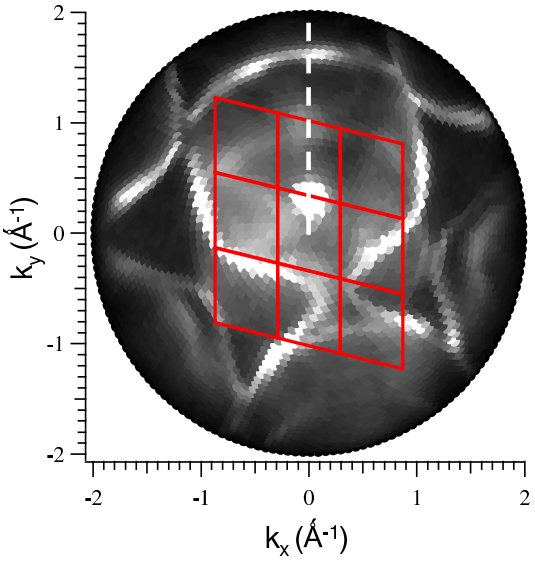

Figure 11.2:
Fermi surface map of Au(17 11 9). The red lines mark the surface Brillouin zones (BZ). The surface state is the bright spot located on the BZ boundary along the white dashed line.

The surface state is found at the boundary of the surface Brillouin zone, shifted away from normal emission in direction of the surface miscut. The binding energy of the bottom of the

surface state shifts from 470 meV in the case of Au(111) to 185 meV for Au(17 11 9). No splitting of the surface state has been found, even when measuring at high energy and angular resolution, due to the intrinsic peak broadening by the broad distribution of terrace sizes and kink separations (5).

By introducing spin resolution in ARPES, the surface state splitting into two components is again observed. These experiments were carried out at the COPHEE (COmplete PHotoEmission Experiment) end-station at the SIS beamline of the Swiss Light Source. This apparatus features two orthogonal Mott detectors which are capable of mapping the three-dimensional spin polarization vector for any value of electron momentum. In a preliminary study it has been found that the surface state spin structure is quite complex; the data are still being analysed. Some data are shown in Fig. 11.3, which represent the three orthogonal spin components along a polar scan, sampling the surface state along the dotted white line shown in the Fermi surface map of Fig. 11.2. The polarization is mainly in-plane for the surface state. The in-plane tangential component shows a Rashba-type momentum shift similar to the case of Au(111). By contrast, there is here also a contribution to the in-plane radial component, which is along the scan direction. Further experiments aimed at resolving the full picture of the surface state spin structure of Au(17 11 9) are underway.

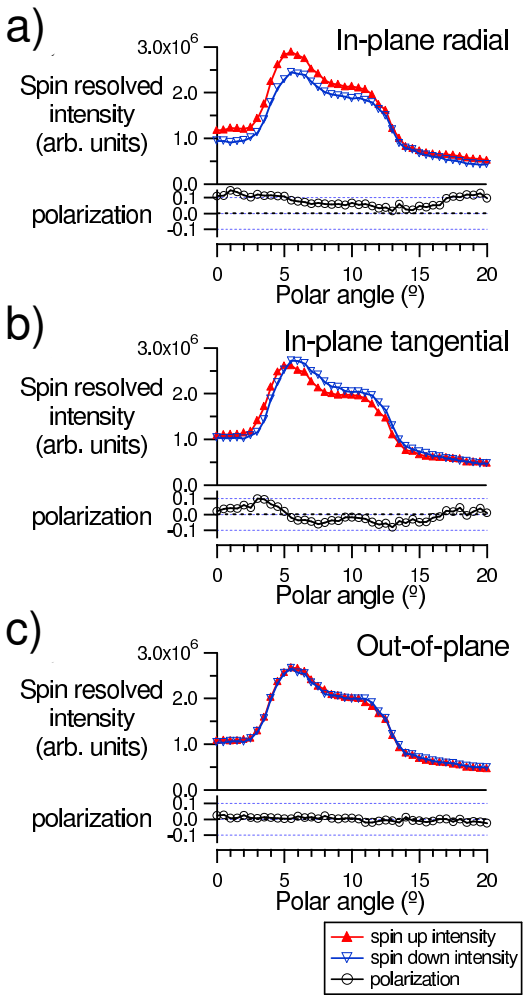

Figure 11.3:
Spin polarization and spin-resolved momentum distribution curves along the white dashed line in Fig. 11.2 for three orthogonal components of the spin polarization vector:
a) in-plane radial polarization,
b) in-plane tangential polarization, and
c) out-of plane polarization.
The scan covers $1\frac{1}{2}$ Brillouin zones.

[1] F. Reinert, G. Nicolay, S. Schmidt, D. Ehm, S. Huefner, Phys. Rev. B **63**, 115415 (2001).

[2] S. LaShell, B. A. McDougall, E. Jensen, Phys. Rev. Lett. **77**, 3419 (1996).

[3] M. Hoesch , M. Muntwiler, V. N. Petrov, M. Hengsberger, L. Patthey, M. Shi, M. Falub, T. Greber, J. Osterwalder, Phys. Rev B **69**, 241401 (2004).

[4] A. Mugarza, J. E. Ortega, J. Phys.: Condens. Matter **15**, S2381 (2003).

[5] F. Baumberger, M. Hengsberger, M. Muntwiler, M. Shi, J. Krempasky, L. Patthey, J. Osterwalder, T. Greber, Phys. Rev. Lett. **92**, 196805 (2004).

11.3 *h*–BN on Rh(111): a stable nanomesh

in collaboration with: O. Bunk, Swiss Light Source, Paul-Scherrer Institut

Recently our group has discovered a new nanostructure (Fig. 11.4a) of *h*–BN on Rh(111) (1). It appears as a two-layer mesh of *h*–BN units, with a periodicity of 3 nm and 2 nm hole size. The nanomesh self-assembles during thermal decomposition of Borazine $(HBNH)_3$ molecules on the hot Rh(111) surface. Hole formation is likely driven by the lattice mismatch of -6.7% between the film and the Rh substrate. The stability of the nanomesh in various environments is an important aspect in view of its possible applications as a template for regular nanostructures or as a functional surface for nanocatalysis or biocatalysis. For this purpose some experiments have been performed during this year in order to test the stability of the nanomesh under exposure to air and to liquids.

Concerning the first aspect, the nanomesh has been prepared in ultra-high-vacuum (UHV) and then exposed to air for 60 hours. LEED and STM images (Fig. 11.4b) show that the structure survived. A short annealing up to 950 K largely removes the contaminants (mostly H_2O, O_2, CO_2 and CO) from the surface and brings the nanomesh back to a highly ordered state. The resistance of the nanomesh to direct contact with liquids was demonstrated by simple wetting experiments. 1 μl droplets of water and of OMCTS (Octamethylcyclotetrasiloxane, $C_8H_{24}O_4Si_4$) were deposited in air on a nanomesh sample by means of a syringe (Fig. 11.4c and 11.4d). The two liquids wet the nanomesh. It can be seen macroscopically that the OMCTS spreads completely on the surface and that the water droplet has a slightly irregular shape. The angle formed by the droplets and the surface, known as contact angle θ (Fig. 11.4e), was measured in a microscope. The resulting values of θ=$51 \pm 1^\circ$ in the case of water and θ<5° for the OMCTS, both resemble the conditions of good wetting ($\theta < 90^\circ$). XPS data clearly show that the boron and nitrogen signals are still present after exposure to liquid water and OMCTS, and after a treatment in boiling (56°) aceton ($(CH_3)_2CO$). Surface

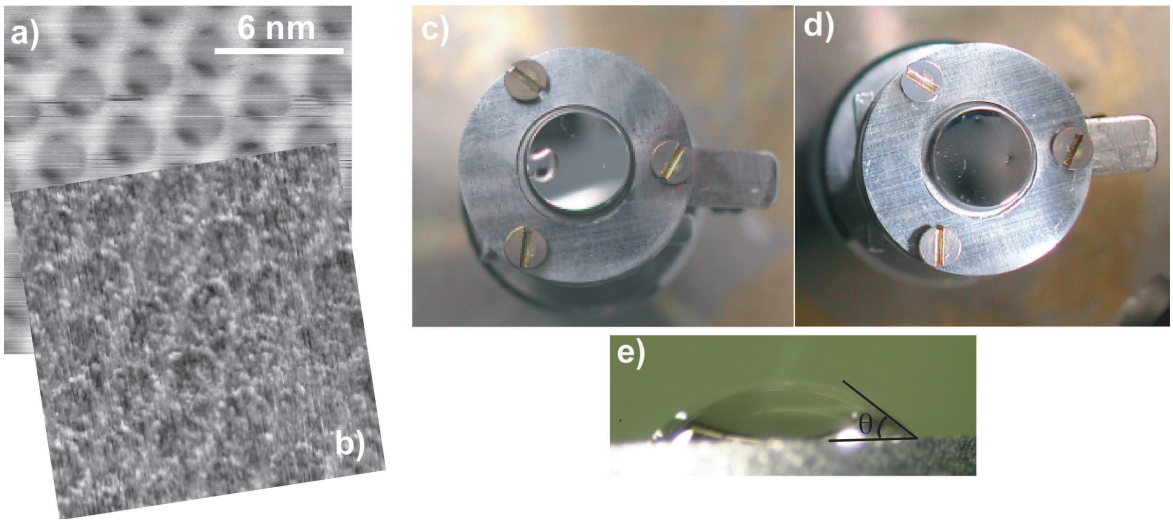

Figure 11.4:
a,b) Constant-current STM images (a: -2 V and 1.0 nA; b: -1V and 1.0 nA) of the *h*–BN nanomesh before and after air exposure ((a) and (b), respectively).
c,d) A 1 μl droplet of water (c) and OMCTS (d) placed on top of the nanomesh.
e) Microscopic side view of the water droplet in c), indicating the contact angle.

X-Ray Diffraction (SXRD) experiments at the Swiss-Light-Source confirm the stability of the *h*–BN nanomesh not only during measurements in a protective He atmosphere but also during exposure to water vapor.

[1] M. Corso, W. Auwärter, M. Muntwiler, A. Tamai, T. Greber, J. Osterwalder, Science 300 (2004) 217.

11.4 Hexagonal Boron Nitride on Pd(111) - Nanomesh or Moiré pattern?

The formation of *h*–BN layers on metal surfaces has been studied in this group for several transition metal substrates. On Ni(111), a commensurate monolayer with a slight corrugation of 0.1 Å due to the small lattice mismatch of 0.4 % is found (1). On Pd(110), several different domains of Moiré patterns are observed. The most spectacular structure is formed on Rh(111): a nanomesh where two mesh layers of boron nitride are stacked in a way to cover most of the substrate (2).
On Pd(111), the lattice mismatch of -9% also causes a coincidence lattice, but no double layer structure is observed. Instead, the boron nitride forms a flat monolayer registered to the Pd surface directions, with a second domain rotated by 30°. Additionally, *h*–BN spots are smeared out to a circle, indicating further *h*–BN domains with random orientations (Fig. 11.5 and refpdfigb). In the STM, several Moiré patterns are imaged, with periodicities ranging from 5 to 25 Å. This is consistent with the random orientations seen in the LEED, because different rotation angles create Moirés with different periodicities. The patterns can be simulated by two superimposed marble patterns with different unit lengths that are rotated against each other, which allows thus to model the STM images. Decoration experiments with C_{60} show that the top layer is flat. The bandstructure is comparable to that for *h*–BN/Ni(111), i.e. there are no strong additional sigma bands like on Rh(111) are measured. There is thus strong evidence for the absence of a double-mesh structure for *h*–BN/Pd(111).

[1] W. Auwärter, T. J. Kreutz, T. Greber, J. Osterwalder, Surf. Sci. 429 (1999) 229.
[2] M. Corso, W. Auwärter, M. Muntwiler, A. Tamai, T. Greber, J. Osterwalder, Science 303 (2004), 217.
[3] M. Corso, T. Greber, J. Osterwalder, Surf. Sci. 557 (2005), L78.

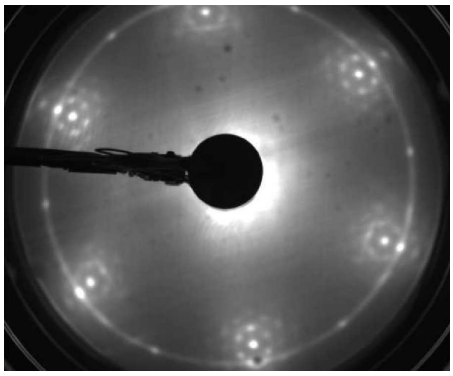

Figure 11.5:
LEED of *h*–BN/Pd(111) showing a superstructure corresponding to 11x11 *h*–BN units plus a second domain rotated by 30°. The circle is caused by azimuthally disordered *h*–BN domains.

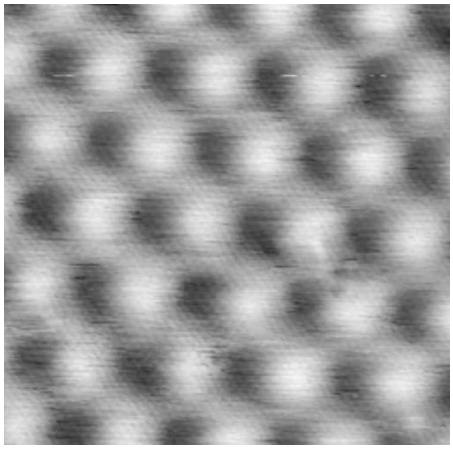

Figure 11.6:
STM image of a Moiré pattern with 27.5 Å periodicity. The apparent corrugation between the darkest and the brightest spots is 1.6 Å and is caused by the strong dependence of the tunneling current on different adsorption sites.

11.5 Time–resolved photoelectron spectroscopy from *h*-BN/Ni(1 1 1)

in collaboration with: W. Schuesslbauer and T. Ruchti, Time-Bandwidth Products AG, Technopark, 8005 Zürich, Switzerland

Deposition of *h*-BN onto Ni(1 1 1) results in atomically flat surfaces (1). The electronic properties of *h*-BN are preserved, leaving an insulating monolayer on a ferromagnetic substrate. In recent experiments, it was found that the charge transfer between the metallic substrate and C_{60} molecules deposited onto *h*-BN/Ni(1 1 1) is strongly temperature dependent: the occupancy of the lowest unoccupied state changes by a factor of seven between room temperature and about 150 K (2; 3). The underlying microscopic mechanism is related to the onset of molecular motion with increasing temperature (3) and raises new questions about the charge transport through the insulating monolayer.

Two-photon-photoemission (2PPE) is the method of choice for addressing such problems since it combines spectroscopic information about occupied and unoccupied states with real-time information about relaxation times through the use of femtosecond laser pulses (see e.g. Ref. (4) and references therein). Two different Ti:sapphire laser systems were used in these experiments: the Coherent Mira oscillator providing 800 nm pulses of 60 fs duration with a repetition rate of 76 MHz at an average power of 500 mW, and a Pallas test system (780–796 nm, 100 fs, 100 MHz, 300 mW) provided by Time-Bandwidth Products. For the time-resolved 2PPE experiments, electrons are pumped into an intermediate level by absorption of a first laser pulse and subsequently probed by excitation out of the intermediate state into the vacuum by a second, temporally delayed pulse (probe). In our case, the fundamental of 780–845 nm wavelength (about 1.55 eV) was used as pump, and its second harmonic, obtained by focusing the fundamental into 0.5–1 mm thick β-bariumborate (BBO) crystals, was used as probe.

Previous experiments, using the second harmonic for both, pump and probe, already revealed an efficient channel for optical pumping out of occupied states close to the Γ-point into a state close to the vacuum level, which was attributed to an image potential state (see Annual Report 2000/01). Furthermore, recent density-functional calculations (5) gave evidence for the existence of an unoccupied π^*-derived band within the *h*-BN–layer, roughly 1.5–1.7 eV above the Fermi level E_F. In the previous single-colour 2PPE-experiments this state showed up as small peak about 1.4 eV above E_F. It will be referred to hereafter as conduction band.

Adding fundamental light in temporal coincidence with the second harmonic changes the spectra dramatically (see Fig. 11.7): the conduction band peak shows up as a giant resonance, enhanced by orders of magnitude with respect to the peak observed without 800 nm light! There is evidence that this enhancement may be explained by resonant interaction of the two excitation channels

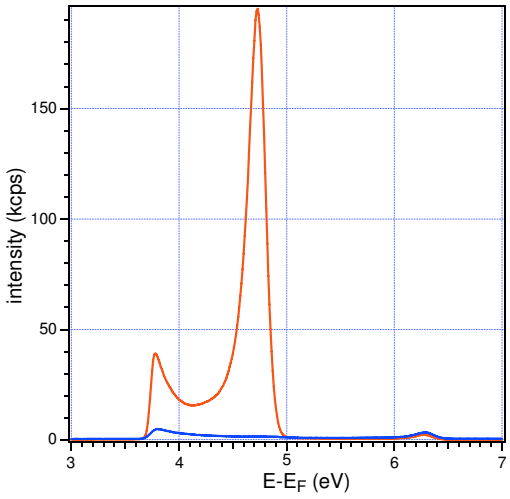

Figure 11.7:
Two-colour 2PPE experiments on *h*-BN/Ni(1 1 1): Comparison of spectra obtained by using only 400 nm light (blue curve) and pulses of 400 nm and 800 nm in temporal coincidence (red curve).

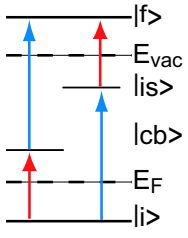

Figure 11.8:
Level scheme for the two resonating excitation channels involving four different states.

$$1: \quad |i\rangle\,(+\hbar\omega_F) \;\rightarrow |cb\rangle\,(+\hbar\omega_{SH}) \;\rightarrow |f\rangle$$
$$2: \quad |i\rangle\,(+\hbar\omega_{SH}) \;\rightarrow |is\rangle\,(+\hbar\omega_F) \;\rightarrow |f\rangle,$$

where $|cb\rangle$ and $|is\rangle$ denote the conduction band and the image state (see Fig.11.8), and ω_F and ω_{SH} the fundamental frequency and its second harmonic, respectively. $|i\rangle$ and $|f\rangle$ are the initial and final state of the excitation, which have to be identical in both interfering processes.

The temporal evolution of the intermediate state population and the dephasing time of the coherent excitations is mapped by varying the time delay between the red and blue light pulses (4), as shown in Fig.11.9. The cross-correlation curves all have an overall width of roughly 200 fs. In these curves, the location of the peak maximum depends on the kinetic energy. Likewise, strong peak shifts and changes of peak shape occur in the energy spectra during a few hundreds of femtoseconds around the time delay zero. The magnitude of this effect cannot be explained by the chirp of the light pulses because measurements at different emission angles, *i.e.* out of resonance, yield much smaller variations with energy and time delay. It is likely that the transient shifts are inherent to the resonant interaction of the two coherent excitations.

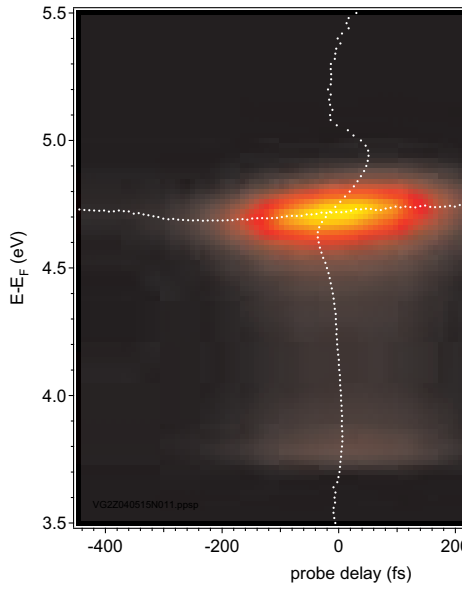

Figure 11.9:
2PPE intensity as function of energy (ordinate) above E_F and time delay of the blue with respect to the red pulse (abscissa); the peak maxima in the spectra and in the cross-correlation curve are shown as white dots.

[1] W. Auwärter, T.J. Kreutz, T. Greber, and J. Osterwalder, Surf. Sci. **429**, 229 (1999).

[2] **Nanostructured magnetic interfaces : case studies and new experiment control software**, M. Muntwiler, Ph.D. thesis, University of Zurich, 2004.

[3] M. Muntwiler, W. Auwärter, A.P. Seitsonen, J. Osterwalder, and T. Greber, Phys. Rev. B **71**, (R)121402 (2005).

[4] X.-Y. Zhu, Surf. Sci. Rep. **56**, 1 (2004).

[5] G.B. Grad, P. Blaha, K. Schwarz, W. Auwärter, and T. Greber, Phys. Rev. B **68**, 085404 (2003).

11.6 Unusually large HOMO dispersion in one-dimensional C_{60} chains

in collaboration with: A.P. Seitsonen, Physikalisch-Chemisches Institut, Universität Zürich

The fabrication of one-dimensional structures on surfaces is attracting considerable interest for possible applications in nano-electronics. Moreover, if electrons are confined to move along a single direction, these systems are expected to show novel and exotic behavior (1). C_{60} molecular chains grown on vicinal copper surfaces offer the possibility to investigate the electronic properties of one-dimensional systems where correlations and electron-lattice interactions are crucial.

In a monolayer of C_{60} on Cu(553), the molecules form long and regular double chains aligned along the step direction of the substrate (2). X-ray photoelectron diffraction data indicate that the molecules have two different and well-defined orientations: molecules adsorb either on the pentagon or on the hexagon ring. The electronic structure of this one-dimensional system has been investigated with angle resolved photoemission (ARPES). Single spectra measured at different emission angles along the C_{60} chains show significant changes in position and line shape of the highest occupied molecular orbital (HOMO) derived peak that are indicative of $\sim$400 meV band dispersion (Fig. 11.10a). In contrast, we do not observe pronounced angular dependence perpendicular to the chains, and the band width is less than 50 meV (Fig. 11.10b). The anisotropy between the two directions reveals that the electronic coupling is predominantly along the molecular chains. Interestingly, such a large HOMO dispersion has never been observed so far in solid C_{60} or in two-dimensional layers, where the reduced band width was explained with the formation of a polaron (3). Density functional theory (DFT) calculations for double molecular chains confirm a very weak coupling across the C_{60} chains (ΓX) and show a band width of 350 meV for the direction along the chains (ΓY). Quite remarkably, there is only one HOMO band, derived from C_{60} molecules sitting on the pentagon, that shows this large dispersion (blue line) and compares well with the experimental data (Fig. 11.11). This suggests that the probability to form a polaron is significantly reduced when the photohole is created in the band with higher dispersion, i.e. with a higher intermolecular hopping rate (4).

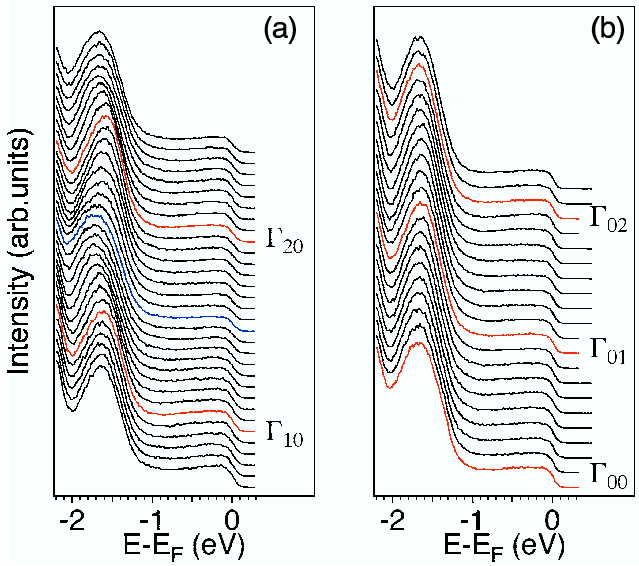

Figure 11.10:
HOMO dispersion in one-dimensional C_{60} chains. Sets of ARPES spectra measured at room temperature along an azimuthal (a) and a polar cut (b), 'parallel' and perpendicular to the chains, respectively (He Iα radiation).

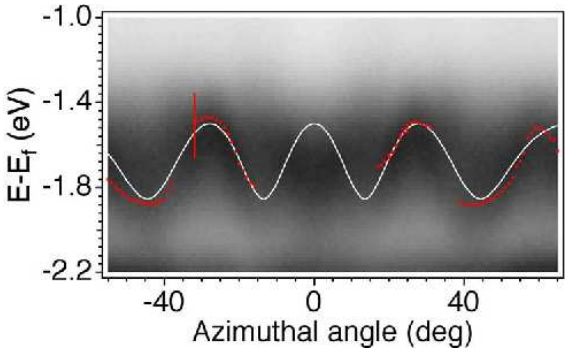

Figure 11.11:
Angular intensity distribution map. The photoemission intensity is displayed as a function of the azimuthal angle on a linear gray scale with black at maximum intensity. One HOMO band from DFT (white curve) and the peak position (red dots) as determined by a Gaussian fit to the data are superimposed.

[1] J. Voit, J. Electron Spectr. Rel. Phen. **117** (2001) 469.
[2] A. Tamai et al., Surf. Sci. **566** (2004) 633.
[3] P.A. Bruehwiler et al., Chem. Phys. Lett. **279** (1997) 85.
[4] V.R. Belosludov et al., Phys. Rev. B **67** (2003) 155410.

11.7 Chiral Heterorecognition: Cysteine on Au(17 11 9)^S

in collaboration with:
Željko Šljivančanin, École Polytechnique Fédérale de Lausanne, and Bjørk Hammer, Department of Physics and Astronomy and iNANO, University of Aarhus, Denmark

Molecular recognition is among the most fundamental processes in nature. In the lock and key model a receptor molecule discriminates a target molecule from all other molecules. For chiral recognition the receptor has to have a chiral center. If the receptor is a surface, recognition is e.g. expressed by an enantiospecific adsorption energy. First experimental evidence that chiral surfaces are enantiospecific on the molecular level came from Attard et al. who demonstrated enantioselective effects on kinked platinum surfaces (1). Near room temperature they found an effect of 13 meV in the electro-oxidation of glucose on chiral Pt(643). These small energy differences are difficult to access. A convenient twist around measuring the energy, is measuring the structure of the adsorbed enantiomers. This has been realized for homorecognition of cysteine by scanning tunneling microscopy (2) and the absolute determination of the chirality of tataric acid on Cu(110) by X-ray photoelectron diffraction (3). In both cases, however, no energy difference between the left handed and the right handed molecules is expected since these experiments were performed on non-chiral $fcc(110)$ surfaces. Here, we demonstrate that L- and D-cysteine adsorb in two distinct structures on chiral Au(17 11 9). From this it can be safely concluded that this system is enantioselective, as it was predicted for cysteine molecules where the carboxyl group is substituted with a phosphino group (4).

The experiments have been performed in a customized end-station for recording 2π X-ray photoelectron diffraction (XPD) data at the X11MA SIM beamline at the Swiss Light Source. With X-ray photoelectron spectroscopy (XPS) the molecules were identified as being in the $SC_\beta H_2 - C_\alpha H - NH_2 - COOH$ state. The coverage was determined to be below one molecule per surface unit cell ($1.08 \cdot 10^{18} \mathrm{molecules\ m}^{-2}$). Figure 11.12 shows the Au(17 11 9) unit cell and 2π X-ray photoelectron diffraction (XPD) patterns from the substrate and the adsorbates. The angular dependence of the photoemission intensities is displayed as stereographic projection using a linear grey scale (high intensities as white).

In Fig. 11.12b) the photoelectron background at 486 eV kinetic energy is shown. From the three most prominent intensity depressions along the $\langle 110 \rangle$ directions, the orientation of the

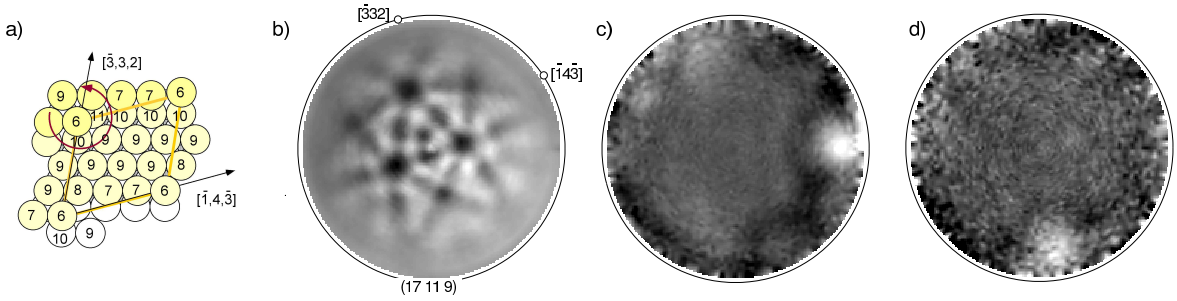

Figure 11.12:
Au (17 11 9) unit cell and angle-scanned 2π X-ray photoelectron diffraction patterns.
a) Unit cell of Au(17 11 9). The coordination numbers of the 14 surface atoms are marked.
b) Inelastic electron diffraction pattern ($E_{kin} = 486$ eV) from which the orientation and the chirality of the substrate is inferred.
c) N 1s $E_{kin} = 368$ eV emission for D-cysteine.
d) N 1s $E_{kin} = 368$ eV emission for L-cysteine.
The single forward scattering peaks in c) and d) indicate distinct single orientations for the two enantiomers.

surface and the C_1 symmetry is inferred. In Fig. 11.12 c) and d) the N 1s ($E_B = 400$ eV) emission patterns of D- and L-cysteine on Au(17 11 9) are shown. We find one dominant forward scattering maximum, though at different emission angles for L- and D-cysteine, respectively. This demonstrates two different bonding geometries and thus chiral heterorecognition or enantio-selectivity of kinks on gold. The forward scattering peaks occur at grazing angles and are identified to point along the $N - C_\alpha$ axis, where C_α is the chiral center carbon atom in cysteine. The observed structures of cysteine on Au(17 11 9) are in good agreement with those derived from density functional theory calculations.

[1] G. A. Attard, A. Ahmadi, J. Feliu, A. Rodes, E. Herrero, S. Blais, and G.Jerkiewicz, J. Phys. Chem. B, **103**, 1381 (1999).
[2] A. Kühnle, T.R. Linderoth, B. Hammer, and F. Besenbacher, Nature **415**, 891 (2002).
[3] R.Fasel, J. Wider, C. Quitmann, K.-H. Ernst and T. Greber, Angew. Chem. Int. Ed. **43**, 2853 (2004).
[4] Ž.Šljivančanin, K.V. Gothelf, and B. Hammer, J. Am. Chem. Soc. **124**, 14789 (2002) .

11.8 Time-resolved electron diffraction

in collaboration with:
H. Over, Physikalisch-Chemisches Institut, Justus-Liebig Universität Gießen, Germany

We continued the development of the time-resolved low-energy-electron diffraction (t-LEED) technique which implies the recording of LEED patterns along the time evolution of a fast surface structural change. Shortly, by hitting the sample with femtosecond laser pulses (pump), one induces fast transient modifications in the surface atomic order which are probed subsequently by means of LEED images recorded with temporally delayed electron pulses. The timescale of such processes is in the range of picoseconds. When the crystal periodicity remains unchanged on the average, the transient temperature jump gives rise to an intensity

drop of the diffraction spots due to the Debye-Waller effect. In contrast, a phase transition involving a new lattice periodicity can be seen as the (dis–) appearance of new spots in the LEED pattern. Either way the pulsed electron diffraction patterns play the role of an ultrafast thermometer, measuring the transient lattice temperature and periodicity.

11.8.1 Upgrade of the current electron gun design

For the purpose of time-resolved electron diffraction experiments, our group previously developed a laser-activated electron gun (1) which was shown to provide a pulse width below 20 ps (2). In the lens-less design of Karrer the collimation of the electrons was realized with a channelplate which results in a exceedingly small yield of electrons. Due to the small laser shot repetition rate and the low onset of space charge effects, this gun was not suited to perform an electron scattering experiment on a surface, where typically one out of 1000 electrons is scattered into the detector. Therefore a new gun design was realized with a nominal pulse width below 5 ps at 100 eV.

Particular attention was paid to minimize the solid angle occupied by the gun head in order to keep a large field of view for placing the laser pump beam and the electron detection. Furthermore, the microchannelplate used to collimate the electron beam (1) was replaced by a mesh and a lens in order to obtain maximum transmission of the gun without loss of time resolution. Figure 11.13 shows a sketch of the new electron gun head. Briefly, the cathode consists of a 20 nm thin atomically flat gold film grown on a sapphire substrate; the 400nm laser light pulses are focused from the back onto the cathode and produce electron pulses via two-photon photoemission. The electrons are then accelerated over a short distance toward a gold mesh (anode) positioned 50 μm in front of the cathode. An additional electrostatic lens is placed to focus the electrons on the sample.

The trajectories of the electrons from the cathode to the sample have been simulated (3) along the 4 mm distance. Together with the measured energy spread of 0.7 eV for 100 eV electrons, this results in a nominal time spread of less than 5 ps for a total flight time of 640 ps.

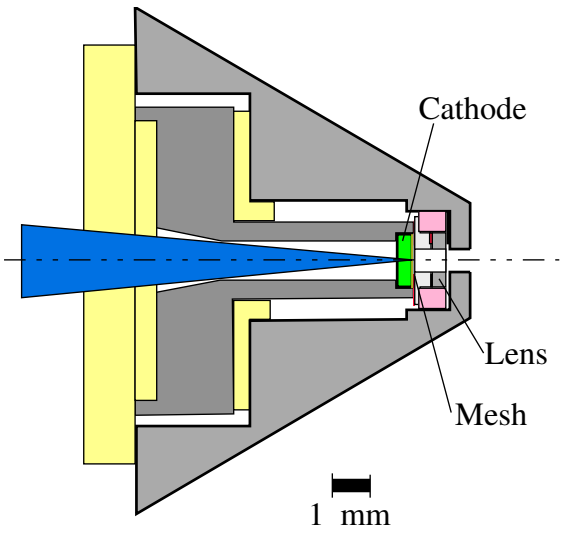

Figure 11.13:Sketch of the new electron gun.

In practice, the temporal broadening of the electron pulses (limiting the final time resolution of the t-LEED experiment) is strongly dependent on the power of the pulsed laser light hitting the cathode: the energy spectra of the electrons show a shift in energy, a broadening, and increasing asymmetry of the peak with increasing power.
This indicates the onset of effects of the large space-charge produced at the cathode within the duration of a laser pulse. The final electron current obtained at the sample position using 400 nm laser pulses of 0.5 nJ per pulse amounts to about 0.5 electrons/pulse. In comparison to the first design that provides $\mathbf{1.4 \times 10^{-4}}$ electrons/pulse for 1.2 nJ, we gain about three orders of magnitude in electron yield.

This new gun enables us to record sharp LEED patterns in a short time: in Fig. 11.14 a LEED pattern of Si(111) 7x7 is shown, obtained with an exposure time of 10 seconds at an electron kinetic energy of roughly 40 eV. The observation of most of the non-integer spots, which lie very close together in reciprocal space, is a clear indication that a well focused and collimated electron beam is sent toward the sample surface.

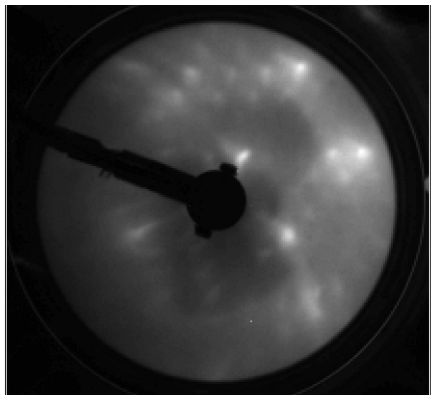

Figure 11.14:
LEED pattern of Si(111) 7x7, recorded with 40 eV electrons from the new electron gun (power 0.75 nJ/pulse, 250 kHz repetition rate, exposure time 10 seconds).

11.8.2 LEED experiments on In-(4x1)/Si(111)

For a first proof-of-principle of this new technique, a surface system exhibiting a sharp phase transition is preferable to a pure Debye-Waller effect due to the magnitude of signal change upon laser excitation. We have therefore selected a new surface system: the indium-(4x1) chain superstructure grown on Si(111) which undergoes a phase transition to an (8x2) reconstruction at about 115 K (4). Previous experiments have shown that the transition occurs within a few degrees K (4; 5), which constitutes a significant advantage of this system over recently studied surface phase transitions like that on Pb/Ge(111).
A vicinal p-doped Si(111) sample with a 2° miscut in the $(11\overline{2})$ direction was used with ohmic contacts placed along $(1\overline{1}0)$ in order to avoid step bunching during resistive heating. Well-ordered (7x7) surfaces (Fig. 11.15) were produced by fast flashes up to 1450 K for 10-15 seconds, followed by annealing at about 1120 K and slow cool down. First t-LEED data from the bare 7x7 silicon sample did not show conclusive results mainly because of the insufficient pump laser power ($\lambda = 800$ nm, 4 μJ/pulse) along with a small absorption coefficient of silicon at this wavelength.
Indium deposition at a rate of 0.05 ML/min while keeping the Si(7x7) substrate at 720 K resulted in a triple-domain (4x1) reconstruction for a $\simeq$1 ML In coverage (Fig. 11.16). The temperature dependence of the (3,3)–spot revealed a Debye temperature of about 117 K. The phase transition could not be observed so far due to bad thermal contact between sample and cryostat, which is currently being improved.

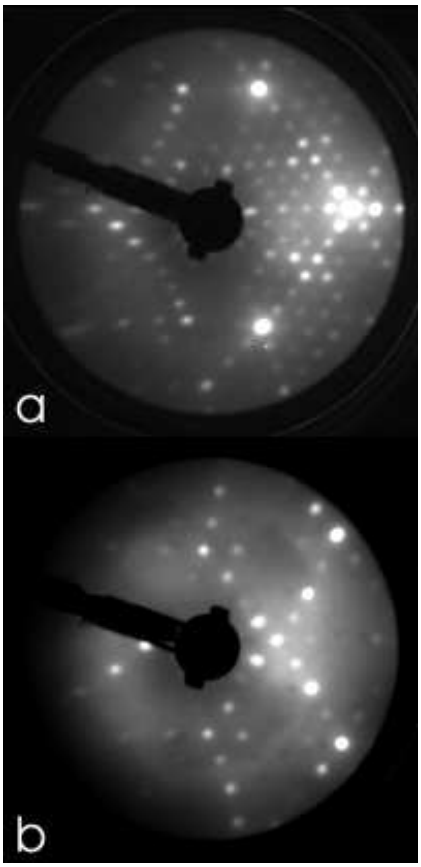

Figure 11.15:
a) LEED pattern of Si(111)-(7x7) surface collected at 66 eV electron energy. b) LEED pattern of the In-(4x1)/Si(111) superstructure at 100 eV. The two patterns were recorded with the standard LEED gun, not with the new gun described in the last section.

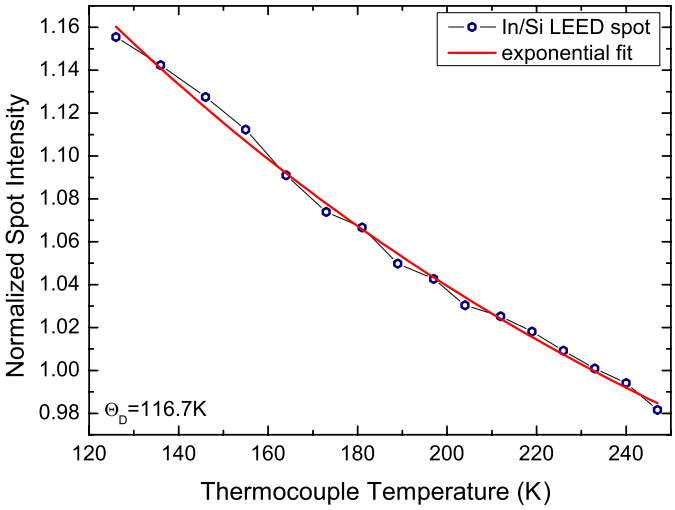

Figure 11.16:
The In-(4x1)/Si(111) (3,3) spot intensity, as a function of temperature, shows a quite low Debye temperature. The intensities were recorded at 65 eV electron energy.

[1] R. Karrer, H.J. Neff, M. Hengsberger, T. Greber, and J. Osterwalder, Rev. Sci. Instr., **72**, 4404 (2001).

[2] A. Dolocan, M. Hengsberger, H.J. Neff, M. Barry, C. Cirelli, T. Greber, and J. Osterwalder, submitted to J. Appl. Phys.

[3] SIMION software package, Idaho National Engineering Laboratory, EG&G Idaho Inc. Idaho Falls.

[4] H.W. Yeom, S. Takeda, E. Rotenberg, I. Matsuda, K. Horikoshi, J. Schaefer, C.M. Lee, S.D. Kevan, T. Ohta, T. Nagao, S. Hasegawa, Phys. Rev. Lett. **82**, 4898 (1999).

[5] O. Gallus, Th. Pillo, M. Hengsberger, P. Segovia, and Y. Baer, Eur. Phys. J. B **20**, 313 (2001).

12 Physics of Biological Systems

Cornel Andreoli, Conrad Escher, Hans-Werner Fink, Michael Krüger,
Tatiana Latychevskaia, Hiroshi Okamoto, Gregory Stevens, Sandra Pascale Thomann.

in collaboration with:
Jevgeni Ermantraut, Clondiag Chip Technologies (Germany); Pierre Sudraud, Orsay Physics (France); Roger Morin, CNRS Marseille (France); John Miao, University of California at Los Angeles (USA); Dieter Pohl, University of Basel; Andreas Plückthun, Peter Lindner, Biochemistry Institute, University of Zurich; Bettina Böttcher, IMBL-European Institute for Molecular Biology, Heidelberg; Andre Geim, Centre for Mesoscience & Nanotechnology, University of Manchester; Werner Kühlbrandt, Max-Planck Institute of Biophysics, Frankfurt.

In the past year the group has been working on quantitative experiments to explore basic aspects of the energetic associated with a single DNA molecule in the liquid phase. A new quantum mechanical concept for reducing radiation damage in electron microscopy has been formulated and implemented. Progress has also been made towards our effort in trying to establish holography with low energy electrons as a new tool for structural determination of individual molecules. A dedicated Low Energy Electron Point Source microscope has been completed for these studies. Preliminary results indicate that it is possible to obtain holograms from unstained viruses. A solid electrolyte ion source has been invented in collaboration with a group at the University of Basel.

12.1 Studies of single DNA molecules in liquids [1]

The DNA molecule is a highly flexible biopolymer, capable of assuming a variety of configurations that are most likely strongly related to its functions in cells of living species. The packing of the DNA in the nucleus of the cell and the dynamics of the various enzymatic reactions require transitions between the configurations of the DNA. Thus, an insight into the free-energy landscape associated with the various configurations of the molecule is at the centre of a basic understanding of its physics and chemistry. Apart from the molecules biological function, the DNA as a biopolymer is also an important object to test and further develop the foundations of polymer physics. Following Kuhn's pioneering work a DNA molecule in a liquid is viewed as a chain of contour length L that is made up of individual elements of Kuhn-length A (often also referred to as persistence length) over which the molecule remains straight. If it costs little or even no energy to change the direction of all Kuhn-length elements in respect to each other, the molecule will assume a random coil equilibrium configuration at finite temperature. The random coil is thus the most likely configuration and its stability is believed to be strongly influenced by the entropy term as the main contribution towards the minimum of its free energy. In contrast, the straight configuration is the most unlikely one with the least number of possible different ways to realize it and thus associated with minimal entropy.

The question we addressed is how the transition from the straight to the random coil proceeds and whether or not this process is thermally activated, i.e. whether or not there is an activation barrier. The ability to observe individual molecules and to monitor their dynamics with video frequency time resolution, pioneered by Steven Chu, has become routine. How-

ever, establishing equilibrium conditions at different temperatures has never been achieved prior to our work, it is a pre-requisite to address the questions in relation to the molecules energetics.

Our experiments have been performed by using such fluorescence video microscopy as exemplified by the sequence of video frames shown in Fig. 12.1 where a λ-DNA molecule, straightened to itscontour length of 16 μm, undergoes a transition to the random coil. After the elapsed time associated with this particular transition, the molecule remains in a random coil configuration indicating that it indeed corresponds to the minimum of the free energy. The question mark in Fig. 12.1 refers to the issue of whether or not the transition from the straight to the random coil is associated with a barrier separating the two states. So far, no direct experimental evidence has established the existence of such a barrier.

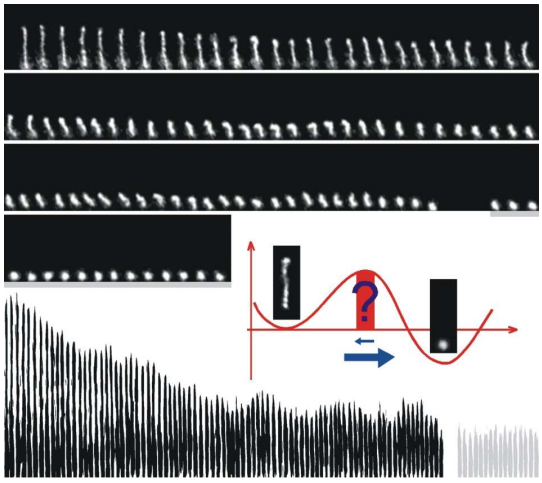

Figure 12.1:
Video fluorescence images taken of a single DNA molecule in the liquid are shown on top. After 85 frames the molecule has completed the transition from the straight to the random coil configuration at 15 ^{o}C. Thereafter, underlined in gray, the random coil remains. The bottom part repeats the raw data set shown on top, just with inverted color and stretched in vertical direction. The straight configuration with a maximum end-to-end separation corresponds to the contour length of about 16 μm for a λ-DNA molecule. It has been created here by employing an electric field after anchoring the bottom end of the molecule to the substrate. After the electric field has been switched off, equilibrium of the solvent is re-established and the DNA molecule evolves towards its equilibrium configuration, the random coil. The arrows in the inlet of the figure represent the very different probabilities of observing transitions between the two configurations and the ? is if there is a barrier separating the two configurations.

For such a task it is necessary to measure the transition time for a large number of events, such as the one illustrated in Fig. 12.1 to derive at a meaningful statistical ensemble for this process. To actually derive quantitative information directly from statistical experiments on the energetics of single molecules, the experimental set-up must be such that thermal equilibrium conditions, free from disturbances by the observation process, are guaranteed at different temperatures. Furthermore, routine methods for anchoring the 16 μm long and 2 nm thick molecules at one end have to be available: first, to provide a proper distance reference, second, to stretch the molecules and third, to be able to derive sufficient statistics and obtain quantitative energy values. This has been achieved in a close collaboration with Clondiag Chip Technologies[4] that provided us with state of the art molecular biology techniques for binding a molecule to a silicon oxide substrate. The experiments take place in a 10 μm thin water film in which stained λ-DNA of low concentration (5 pM) is embedded. The film is carefully sealed to avoid evaporation and associated erratic liquid flow and thus perturbation of the equilibrium conditions, essential for deriving quantitative free energy data, is suppressed.

[4]Clondiag Chip Technologies ®GmbH, Loebstedter Str.103-105, D-07749 Jena, Germany

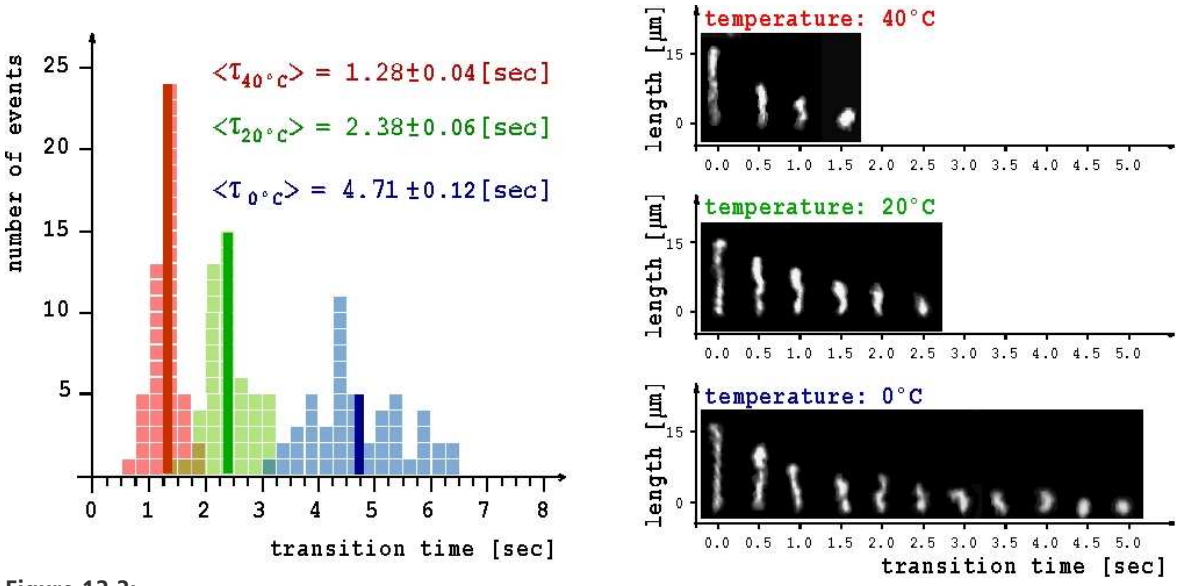

Figure 12.2:
Measurements of the transition time from the straight to the random coil DNA configuration. Right: Every 12th frame of the transition of a straight DNA towards the random coil is shown at 40, 20 and 0 ^{O}C. Left: The corresponding histograms of the distributions for the relaxation times and the average values are shown.

The epoxidated silicon oxide sample binds streptavidin, which in turn provides an anchor for the DNA molecules that are biotinylated at one end. For stretching the λ-DNA to its contour length, an electric field of typically 15 V/cm is employed. The field is provided by two gold lines shadow evaporated onto the substrate. The sample temperature is adjusted and controlled by a peltier stage underneath the sample and needs to be calibrated prior to the experiment. Once the temperature calibration is carried out, the experiments are performed in the following manner. A search is made for a single DNA molecule that is bound at one end to the substrate. This is done by applying an electric field and looking for a straightened molecule. The unbound molecules are just drifting through the field of view towards the electrode at positive potential. After having found a straight molecule, the electric field is switched to zero instantaneously by putting the two electrodes onto the same potential. Equilibrium of the liquid is thus provided immediately compared to the time scale that governs the molecular dynamics of the DNA. This can be verified by visual inspection of the stopping of the motion of unbound DNA molecules. Once this motion has stopped, it is evidence for thermodynamical equilibrium of the solvent in which the DNA then evolves towards the minimum of its free energy. With one particular molecule, typically 5 experiments of stretching and observing the progression towards the random coil configuration are performed. After having collected enough data, similar experiments are carried out at a different temperature. A total of 600 measurements at 12 different temperatures ranging from -5 to +50 ^{o}C were evaluated. In Fig. 12.2 the distribution of the observed relaxation times at three different temperatures are shown together with some sequences taken in the fluorescence video microscope.While the thermodynamically unlikely straight configuration is not observed under ordinary thermal conditions, it can be realized by applying an external electric field and, by switching off the field, the temporal evolution from the initial straight towards the configuration of minimal free energy can readily be measured. In the presence of an activation barrier, the lifetime of this straight configuration, respectively the transition time for the re-formation of the random coil can be written as:

$$\tau = \tau_0 e^{E_{rc}/kT} \tag{12.6}$$

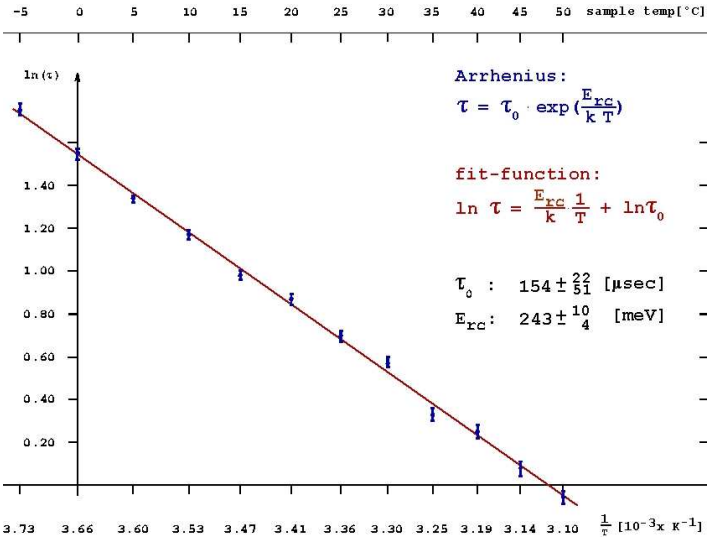

Figure 12.3:
Determination of the activation barrier height and pre-factor. According to Eq. 12.6, the data for the average transition times are represented in a semi-logarithmic plot. A least square fit to a linear dependence reveals the activation barrier E_{rc} and the pre-factor τ_0. The error bars reflect the statistical error of the average transition times (see also the raw data presented in Fig. 12.2).

where E_{rc} denotes the activation free energy barrier for the formation of the random coil. The pre-factor τ_0 is associated with the molecular fluctuations of the solvent. Both quantities are derived from an Arrhenius plot, as shown in Fig. 12.3. Apparently, the formation of the DNA random coil is associated with an activation barrier of the order of 0.25 eV. For a single DNA molecule, embedded in a liquid of constant volume, the Free Energy can be written as: $F = U - T \cdot S$; where U denotes the internal energy of the molecule and is determined by the binding energy between the atoms that make up the molecule; T is the absolute temperature and S the entropy given by the Boltzmann relation $S = k \cdot \ln W$.

The number of possible ways to generate a particular configuration of the DNA chain divided by all possible combinations to generate any configuration of the molecule defines the probability W for this particular configuration and determines its entropy value. Now, it is well known that short DNA molecules can be viewed as rigid rods. That implies that the stacking of the individual nucleotides is such that a straight configuration is energetically favourable and leads to a minimum of U. The response of a small DNA molecule to the Brownian agitation, i.e. the statistical motion of the surrounding solvent molecules, leads to translations and rotations of the rod within the liquid. The entropy plays a minor role and the free energy minimum is almost exclusively given by the internal energy U. For a longer molecule however, the stochastic momentum transfer by the solvent does no longer lead to purely translational and rotational motions of the entire molecule. A longer molecule has to develop kinks as a response to the Brownian agitation. This is purely an effect of size and associated increase of possible configurations. We have thus two extremes. A straight DNA chain corresponding to a minimum of the internal energy U and a small entropy contribution on one side. On the other side, a random coil configuration corresponding to an increased internal energy, which apparently is over-compensated by a large entropy term. The latter is due to the vast number of possible ways to form a random coil for a 16 μm long λ-DNA. At any experimentally accessible temperature between freezing the solvent and melting the molecule, the entropy term apparently dominates and defines the absolute minimum of the free energy.

[1] **Activation Barrier for the DNA Random Coil Formation**, Conrad Escher and Hans-Werner Fink, submitted to Phys.Rev.Lett..

12.2 A new quantum mechanical principle to reduce radiation damage in electron microscopy[1]

Radiation damage severely restricts our ability to study unstained biological specimens in electron microscopy. Reduction of the electron dose in order to keep the specimen intact results in poor image quality due to shot noise. As such, it is widely believed that the amount of extractable information from a single specimen is fundamentally limited. Here we show that this need not be the case when a structural hypothesis of a specimen is available. Quantum mechanical principles then allow the use of a very low electron dose to verify the hypothesis. To realize such a method, one has to control the electron wavefront. We propose to use micro-fabricated diffractive electron optical elements for this purpose. Despite the short electron wavelength, our experiments demonstrate that it is indeed possible to obtain a desired diffractive effect by fabricating such an element. Furthermore, numerical simulations combined with Bayesian statistical analysis were employed to quantitatively assess the strength of this new principle for structural biology. Quantum mechanics states that a measurement of an observable produces a deterministic outcome when a particle is in an eigenstate of the observable. Repetition of the measurement on particles prepared in an identical way quickly yields high confidence about the quantum state due to the absence of noise. The same principle can be applied to the case of electron microscopy, if the state of an electron after the scattering by a specimen is known. One can then design a corresponding electron-optical element that transforms the scattered wave, i.e., the object wave, to a converging spherical wave to produce a spot on an imaging screen. Therefore it is possible to be highly confident about a given structural model with a single electron only, because the chance of detecting an electron at a particular point on the screen by coincidence is low. By repeating the measurement, confidence about the structural model will increase rapidly. This is in a sharp contrast to conventional electron microscopy, which typically takes 10^8 electrons to generate an image with a fair signal to noise ratio. Transforming the object wave into a spherical converging wave can be done solely by linear optical elements (so-called matching filters), as has been studied in the optical image recognition context. Our diffractive element transmission function d is derived from a simple idea that if Ψ_0 is the object wave and Ψ_S is the convergent spherical wave, then d should be a solution of the following equation:

$$\Psi_S = d \cdot \Psi_0 \tag{12.7}$$

Thus, by illuminating the diffractive element d with an object wave Ψ_0, the spherical convergent wave Ψ_S is reconstructed behind the diffractive element, as shown in Fig. 12.4. Ideally, the transmission function of the diffractive element should provide both amplitude and phase modulation satisfying Eq.12.7. However, for micro-fabrication purpose, d must be described by a real and positive function. To overcome this obstacle,

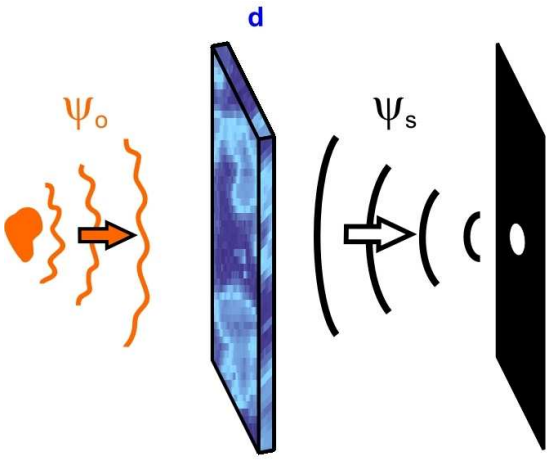

Figure 12.4:
The scheme to transform the object wave Ψ_0 from a specimen to a converging spherical wave Ψ_S by use of the diffractive element d. The structure of the diffractive element is simulated numerically in accordance with Eq. 12.8.

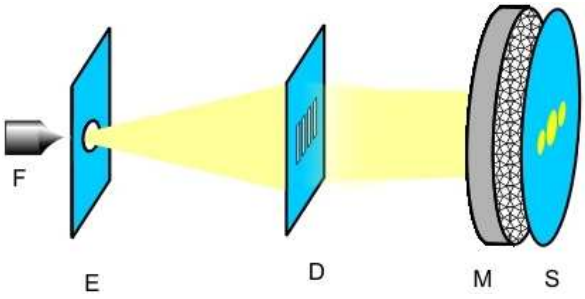

F: W(111) single crystal field emitter
E: carbon thin film extractor with a 1.2 μm diameter hole (Quantifoil R1.2/1.3) located 4 μm away from F.
D: diffraction grating located 360 μm away from E.
M: microchannel plate
S: phosphor screen

Figure 12.5:
Experimental setup. Diffractive elements were fabricated by an FIB apparatus (Orsay Physics), using a 30 keV, 2 pA Ga ion beam. They were milled in carbon support films with a nominal thickness of 12-20 nm (Quantifoil Micro Tools GmbH). Each hole was milled with a Ga ion dose of 4.7 fC, resulting in a diameter of approximately 20 nm. Because of the small diffraction angle, the image on the phosphor screen was magnified by an optical microscope, and subsequently recorded by a CCD camera.

our approach is to take the real part of the quotient

$$d = Re\{\Psi_S/\Psi_0\} + const \tag{12.8}$$

where the constant is added to ensure that d is always positive. To avoid division by zero, d was set to zero where the object wave intensity $|\Psi_0|^2$ is below a certain threshold. Thus, after the diffractive element, the emerging wave $d \cdot \Psi_0$ is proportional to the converging spherical wave Ψ_S and some additional terms.
Two remarks are in order. Firstly, in general we do not know *a priori* the exact place and orientation of a specimen, say a macromolecule. While small changes to the specimen position translates to the lateral displacements of the spot on the screen, the uncertainty of the specimen orientation poses a serious problem. Methods such as trapping the molecules in a well-defined manner may have to be employed. Secondly, if the structural hypothesis is incorrect, the experimenter will obtain an unexpected spot on the screen. However, this information could still be exploited by considering which alternative structural model is most likely to produce the particular spot obtained.
To realize the above scheme, we need freestanding diffractive elements that can be designed and fabricated at will. However, there have been no experimental demonstrations of engineered electron optics based on diffraction. To show that the above scheme can be implemented, we demonstrate electron diffraction by gratings, as well as rudimentary lens action by a diffractive element (see Fig. 12.5).
Figure 12.6 shows the fabricated slits of the gratings as imaged by low energy electron point source (LEEPS) microscopy. The recent wide availability of the focused ion beam (FIB) technology enabled us to fabricate such diffractive elements. The slit-to-slit distance was 100 nm. The array of 4 slits was approximated by a 4x4 array of 20 nm diameter holes with anisotropic hole-to-hole spacing, since it provided better mechanical strength. Since the characteristic feature size of the fabricated structures exceeds typical low energy electron wavelengths by a factor of several hundreds, we must stay in the paraxial optical regime. The high spatial coherence of the electron beam from the sharp field emitter guarantees the electron wave over the whole diffraction grating to be coherent. The relatively large distance of 360 μm between the electron source and the diffraction element ensured that, despite divergence from the point source, the angular spread of the incoming beam was smaller than the expected diffraction angle. The distance between the electron source and the screen was 100 mm, implying that our concept can be implemented without resorting to large instrumentation. Figure 12.7 shows a resultant image of the diffraction experiment performed with

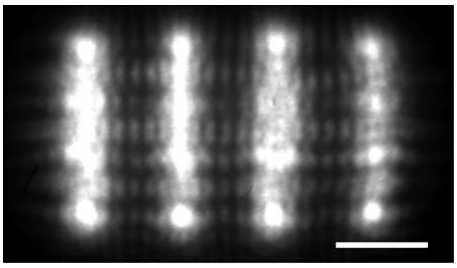

Figure 12.6:
LEEPS image of a diffraction grating taken with 69 eV electrons. Patterns other than the shadow images of the actual holes are due to Fresnel diffraction. Scale bar: 100 nm.

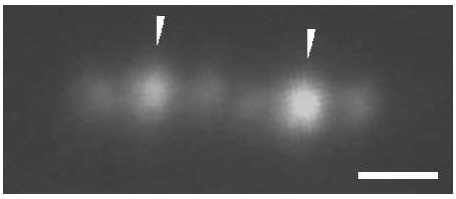

Figure 12.7:
A diffraction pattern produced by two diffraction gratings. Diffraction patterns of each of the gratings exhibits zeroth order spots (indicated by arrows) in between two first order diffraction spots. The electron energy was 149 eV. Scale bar: 3 mrad.

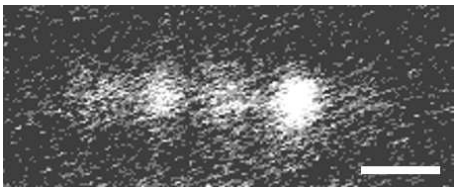

Figure 12.8:
When the electron energy was lowered to 90 eV, the two first order diffraction spots merged. Scale bar: 3 mrad.

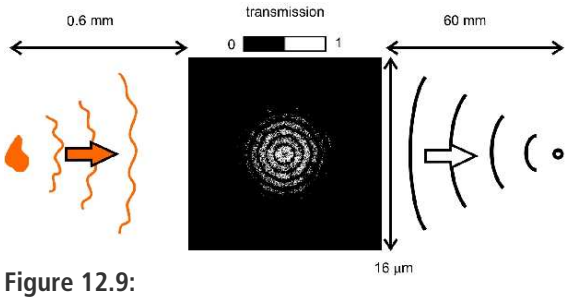

Figure 12.9:
An illustration of the experimental setup used in the simulations. The molecule is assumed to be in a vacuum. The incident electron beam diameter is slightly larger than the molecule. The diffractive element transmission map corresponds to the simulated diffractive element for ribosome 70S using 15 keV electrons.

149 eV electrons. The first order diffraction spots are clearly visible at an angle of 1.9 mrad from the zeroth order spots. This is close to the expected angle of 1.7 mrad derived from the measurement of the slit geometry, taking the electron beam divergence and the finite slit width into account. Furthermore, this angle changed consistently with the electron wavelength, which was varied from 0.073 nm to 0.13 nm, thus confirming that these spots are indeed due to diffraction. Figure 12.8 shows a rudimentary lens action, where the two diffraction spots merged into one when the electron energy was lowered to 90 eV.

To find out how many electrons are needed to identify the correct object with our scheme we set a moderate goal of recognizing the orientation of 70S ribosome[4] out of two possible orientations: a 'right' orientation and a 'wrong' orientation, which differ by 90 degrees. Our hypothesis is that ribosome is in the 'right' orientation, and we compute how many electrons are needed to verify the hypothesis. Figure 12.9 shows the experimental scheme, that was used in our simulations. Two distinct situations were considered. In the first case, the ribosome was treated as an amplitude and phase object, which refers to experiments in the low kinetic energy regime up to about 15 keV. In the second case, the ribosome was modeled as a pure phase object referring to the conventional electron microscopy regime of 100 keV. The diffractive element structures were simulated according to Eq.12.8 and converted to binary format, so that the structures are either fully transparent or opaque, with pixel sizes of 40 nm and 20 nm for 15 keV and 100 keV electrons, respectively. The random electrons arrival positions, obeying a probability distribution given by the intensity on the screen when the ribosome is in the 'right' orientation, were generated by a Monte Carlo method. In both energy cases, when the object is in the 'right' orientation, after a significant amount of electrons have been detected, a spot can be clearly seen on the screen and no special statistical analysis is required. To obtain high confidence of the object identifi-

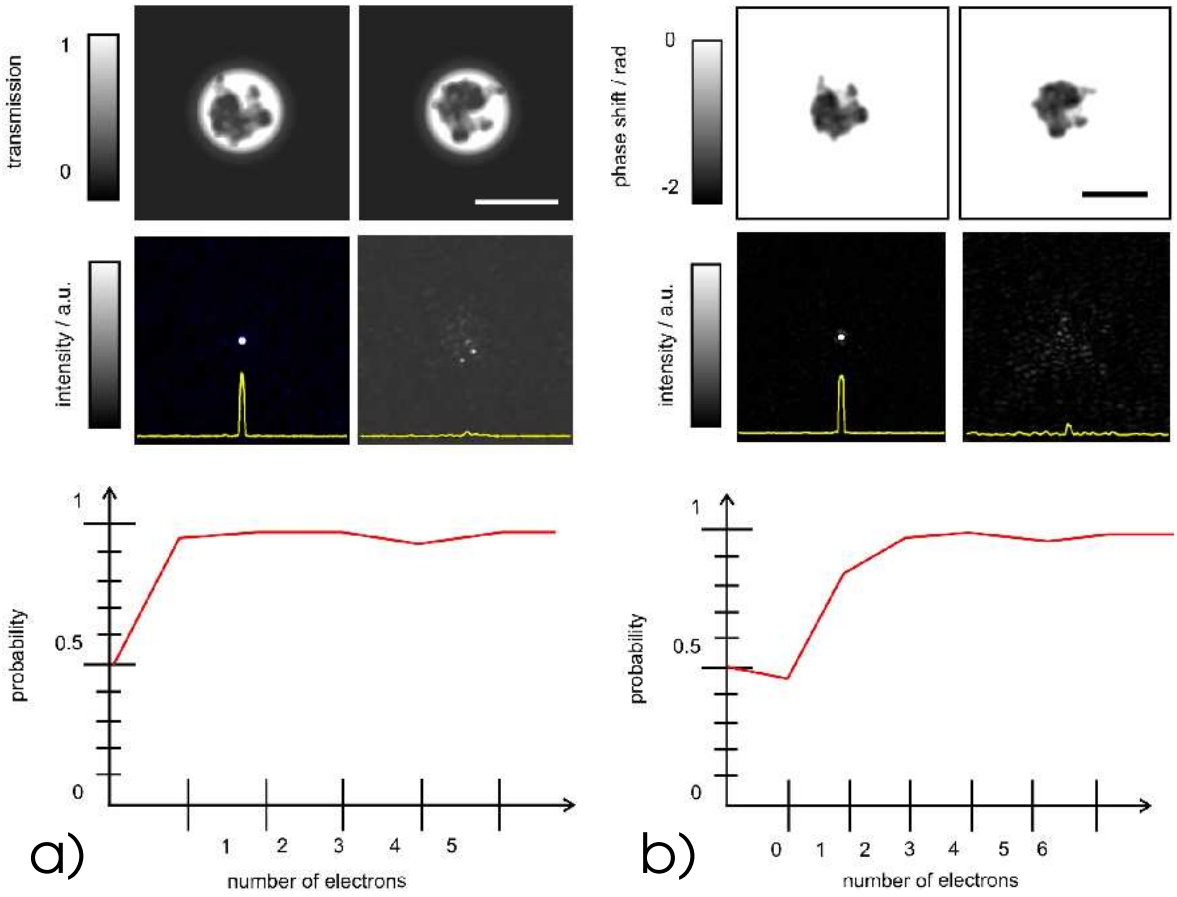

Figure 12.10:
The ribosome S70 at different electron energies can be considered as an amplitude and phase object (at 15 keV, a) or as a pure phase object (at 100 keV, b). The upper pictures show the transmission or phase shifts of the specimens. Scale bar: 20 nm. The pictures in the middle row show the intensity distribution on the screen. The yellow curves are the profiles of the intensity in the middle of the screen. A single spot is observed on the screen when the object is in the 'right' orientation (left picture) and scattered spots when the ribosome is rotated by 90^o (right picture). The graphs in the lower row show the confidence level for the hypothesis about the molecular orientation as a function of the number of electrons detected. The absorption coefficient was calculated using electron inelastic mean free path data. The phase shift was calculated using a known inner potential of the amorphous carbon, which was properly scaled by the equivalent effective carbon density.

cation with a few electrons only, Bayesian statistical analysis was applied to each detected electron. Our numerical experiments have shown that 4±3 electrons are needed at both, 15 keV and 100 keV, to identify the correct object with 95% confidence, see Fig. 12.10a and Fig. 12.10b. However, the absorption by the diffractive element must be taken into account, which changes the number of required electrons to 49±37 electrons at 15 keV and 607±438 electrons at 100 keV. There is considerable leeway for reducing the dose further to a few electrons by placing the diffractive element in between a convergent wave electron source and the specimen. In this case, use of an off-axis configuration would further eliminate irradiation of the specimen by unnecessary electron waves that are due to the zeroth order diffraction.

Apart from practical considerations, a question of fundamental interest is whether or not the above method represents the theoretical limit of radiation damage reduction. As a final remark, we briefly sketch a thought experiment showing that repeated use of an electron could in principle further increase the amount of obtainable structural information for a given radiation damage. Biological samples generally behave as weak phase objects at high electron energies, requiring a high dose especially when we want to discriminate between two similar hypotheses. A radical way to deal with this situation would be to collide an electron wavepacket n times with the specimen, refocusing the electron wave each time. This is essentially equivalent to having a stronger phase object. An incorrect structural hypothesis leads to the failure of subsequent transformation to the spherical wave by the diffractive element, which results in the 'error component' wave with an amplitude proportional to n. This means that the probability of detecting electrons outside the expected region is proportional to n^2, whereas the specimen damage grows as n. Thus, the hypothesis discrimination ability scales as n. This argument indicates that in principle there is room for further reducing radiation damage.

[1] **Controlling radiation damage in electron microscopy**, Hiroshi Okamoto, Tatiana Latychevskaia and Hans-Werner Fink, submitted to Phys.Rev.Lett..

12.3 Structure of individual Bio molecules

Gregory Stevens and Michael Krüger

in collaboration with: Andreas Plückthun and Peter Lindner, Biochemistry Institute

The aim of this project is to develop tools and methods to obtain structural information about individual biological macromolecules using coherent low-energy electrons. Novel methods have been developed to prepare specimens of individual macromolecules and the first low-energy electron holograms have been obtained. These investigations began with a filamentous phage called M13, which is attached to a carbon support film so that individual macromolecules are suspended over holes in the film. We are also using tobacco mosaic virus, because it has a 2.3 nm repeating surface feature that can be used to refine our imaging methods.
Since April 2004, we have designed and built, with the excellent support of our mechanical workshop a bio-LEEPS microscope for making low-energy electron holograms of individual biological molecules. The special requirements of this microscope include ease of use and rapid replacement of the specimen and electron source. Figure 12.11 shows the main parts of the microscope. A 'positioner' to remotely move the electron source in relation to the specimen has been made using three Attocubes, which are a new type of linear motor that utilize a piezo-electric crystal stack in a 'slip-stick' configuration to move macroscopic distances in steps of 50 nm. The positioner is shown with a vibration isolator that prevents vibrations in electrical wiring, and from acoustic noise, from disrupting the relative positions of the electron source and specimen.

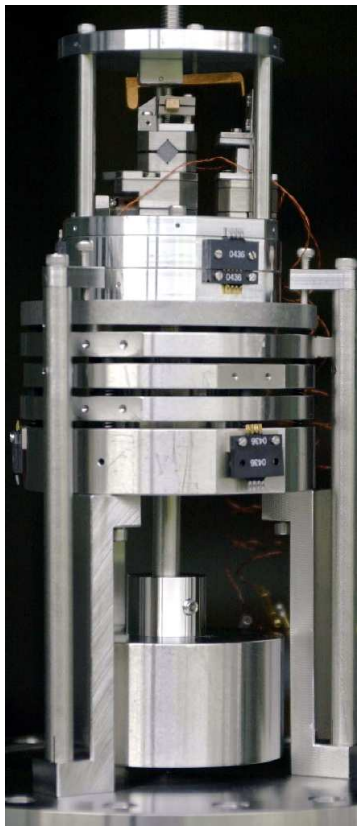

Figure 12.11:
Bio-LEEPS microscope 'positioner' with three Attocube linear motors to move the electron source in relation to the specimen, on a vibration-isolation stack.

Figure 12.12 shows a preliminary low-energy electron hologram of M13 phage suspended across a hole in a carbon film. This sample was prepared in a purpose-built freeze-drying chamber, which allows removal of water from the specimen in a way that minimizes rearrangement of individual macromolecules on a substrate film. Screen defects and an image of a deflecting screen were removed from the hologram by subtracting a background image of the detector screen. Future efforts will be directed to obtaining higher order fringes in the holograms. This may be achieved by improving the stability and coherence of the electron source and the sensitivity of the phosphor detector screen.

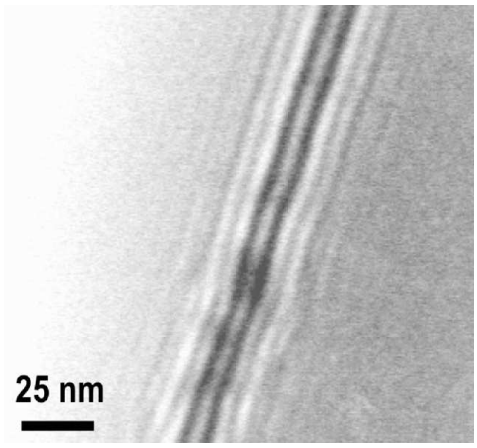

Figure 12.12:
100 eV in-line electron hologram of M13 phage obtained with the bio-LEEPS microscope.

Figure 12.13 shows a conventional cryo-transmission electron microscope (cryo-TEM) image of unstained freeze-dried tobacco mosaic virus and M13 phage suspended across a hole in a carbon film. These images were taken using a low dose imaging method to minimize radiation damage. The ability to image unsupported macromolecules will allow comparison of images obtained in the cryo-TEM with bio-LEEPS images.

Further experiments will address whether the macromolecules are rearranged and/or undergo visible conformational changes during freeze-drying by periodically examining the specimen during freeze-drying in the cryo-TEM. In other experiments, we will label the phage with gold crystals of a known size in order to provide a calibration object for reconstructing the object from the hologram.

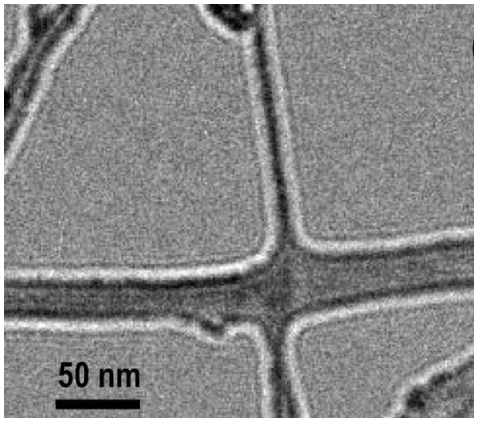

Figure 12.13:
200 keV cryo-transmission electron microscope image of freeze-dried tobacco mosaic virus and M13 phage suspended across holes in holey carbon film. We gratefully acknowledge the Max Planck Institutes of Biophysics for the use of their facilities in making this image.

12.4 A solid electrolyte ion source[1]

A cold source for silver ions has been invented. Source size and brightness are two major properties that allow the use of ions combined with electrostatic lenses to derive at focused ion beams. The current state of the art is represented by gallium ion beams of sizes as small as 5 nm that originate from a liquid metal source. Since these tools are ideally suited for structuring devices on the nanometer-scale, their importance shall increase in the future. Here we present a novel ion source, which is based on mobile silver ions in an electrolyte that are emitted at a well-defined source area of sub-micron dimension and accelerated by an electric field into a vacuum environment. To achieve this, amorphous $(AgJ)(AgPO_3)$ has been shaped into the form of a tip. By using field ion microscopy techniques the emission of silver ions has been investigated and characterized. It turns out that this first cold metal ion source exhibits unique properties with promising perspectives in scientific and technological applications.

There are various possibilities of creating ions, ranging from plasma sources to employing field ionisation to create ions from neutral gas atoms. However, the use of electrostatic

lenses for obtaining focused ion beams in the nanometer-sized regime requires ion sources of high brightness, which excludes conventional plasma sources and gas field ionisation sources. Thus, in view of source size and current per unit emission angle, today's technology is limited to the application of liquid metal ion sources in combination with ion-optical devices to reach focused beams of gallium ions as small as 5 nm.
We have invented a novel type of ion source, namely here the first cold and bright silver ion source which physics of operation is quite different from liquid metal sources. Ions from a conducting solid electrolyte are emitted into the vacuum at a constriction that is provided by geometry. In contrast to the ionisation of neutral species by an electric field, the ionic state is already present in the solid. This implies that at the location of ion emission, an equally high electron current into the source, as is unavoidable in the field ionisation sources and believed to be responsible for the broad energy spread of the ions, is not present in the silver ion source presented here.
The main design criteria for this novel source is associated with shaping the solid electrolyte (AgJ)($AgPO_3$) in such a way as to limit an electric field to a small source size region at which the Ag+ ions can overcome the binding to the solid and get transferred into the vacuum. Two basic designs have been tried and successfully been tested in a Field Ion Microscope.

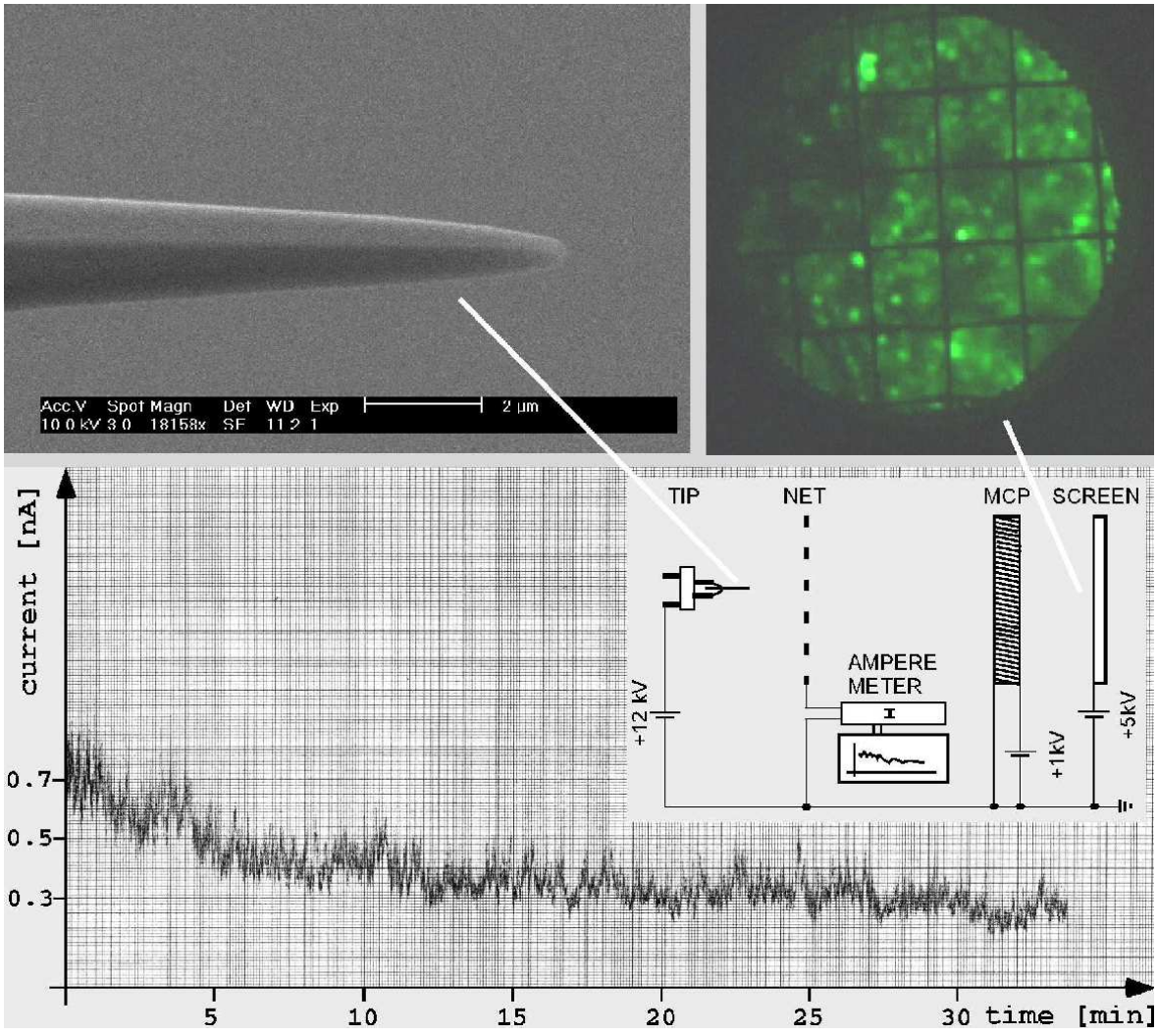

Figure 12.14:
Silver ion emission from an AgJ tip as observed in the Field Ion Microscope; see text for explanation.

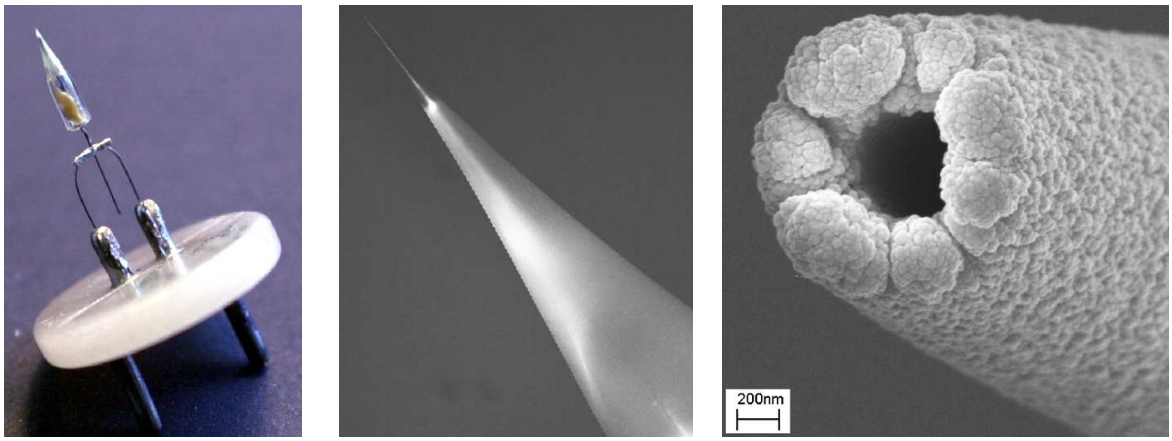

Figure 12.15:
Capillary Silver Ion source shown with increasing magnification. A glass capillary is filled with the conducting electrolyte. The ion emission occurs at the very end of the capillary. The opening of the capillary and with this the emission area can be further reduced by prior depositing silver onto the glass structure. An SEM image of such a capillary opening is shown at the right part of the figure.

Design 1 follows the concept of shaping the electrolyte into the form of a tip by various means of using the molten electrolyte and attaching it to a silver reservoir. It is shown in Fig. 12.14.

The (AgI)($AgPO_3$) material wets a silver wire and is formed into a tip (see SEM image in the upper left of Fig. 12.14) and mounted as a source in the Field Ion Microscope. To measure the emission current out of the tip and simultaneously observe the emission pattern with video frequency on the screen, a grid is assembled between tip and MCP. An Ampere-meter is connected to the grid to measure the current from grid to ground. The cross section of the grid covers about 5% of the beam current and therefore the measured values need to be multiplied by a factor of 20 to determine the total emission current of Ag^+ ions. Design 2 follows the idea of providing a form for the electrolyte to accommodate to, a mantle that provides the appropriate geometry and definition of the source area (see Fig. 12.15). This has been accomplished by filling a fine glass capillary with the molten electrolyte material and then quenching it to its solid amorphous state.

[1] **High brightness solid state ion generator, its use, and method for making such generator**,
Patent filed in March 2005. Invented by: Conrad Escher, Sandra Thomann, Cornel Andreoli and Hans-Werner Fink (University of Zurich), Julien Toquant and Dieter Pohl (University of Basel).

13 Computer Assisted Physics

C. Bersier, T. Mayer, P. F. Meier, S. Renold, E. Stoll, and A. Uldry
guests: T. A. Claxton and M. Eremin

13.1 Effects of strong correlations on the spin susceptibility

in collaboration with: M. Eremin, Kazan State University and I. Eremin, Freie Universitt Berlin

Up to now calculations of the spin susceptibility for cuprates were performed in the framework of weak–coupling approximations. However, it is known that cuprates belong to Mott–Hubbard doped materials where electron correlations are important. We have investigated the effect of strong correlations on high–T_c superconductors. In particular, we have derived an analytic expression for the spin susceptibility below T_c which results for a model system that is closely related to models based on the idea of the formation of copper–oxygen singlets in layered cuprates. Then we numerically evaluated the expression of the susceptibility using parameter values adopted to measurements of the Fermi surface, neutron scattering and NMR data. In Fig. 13.1 the energy dependence of the imaginary part of the calculated susceptibility at the antiferromagnetic wave vector $\mathbf{Q}$ is shown. We observe a large peak near the frequency $\omega \simeq 41$ meV, as observed in neutron scattering measurements. Using the same parameter values we studied the temperature dependence of various NMR properties in the superconducting state including Knight shifts, spin–spin relaxation and spin–lattice relaxation times. Part of this work is published in Ref. (1).

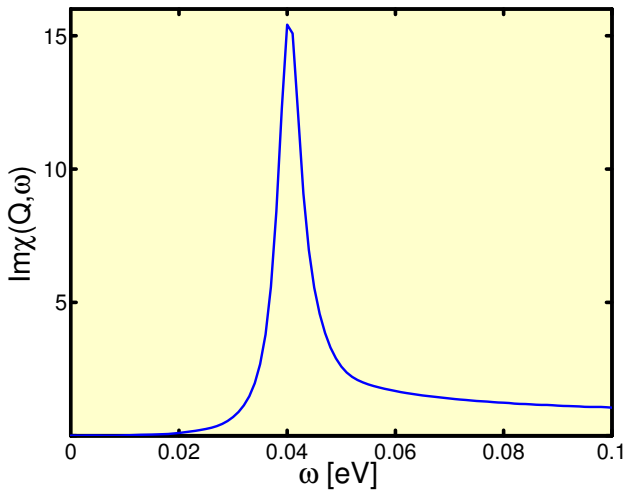

Figure 13.1:
Imaginary part of the susceptibility at the antiferromagnetic wave vector $\mathbf{Q}$.

[1] T. Mayer, M. Eremin, I. Eremin and P. F. Meier, Physica C, **408-410**, 400 (2004).

13.2 Suppression of critical properties in doped cuprates

In high-T_c superconductors dopant atoms supply holes or excess electrons. Electric conduction occurs in the neighborhood of dopants within a circle in the CuO_2 - plane that is several

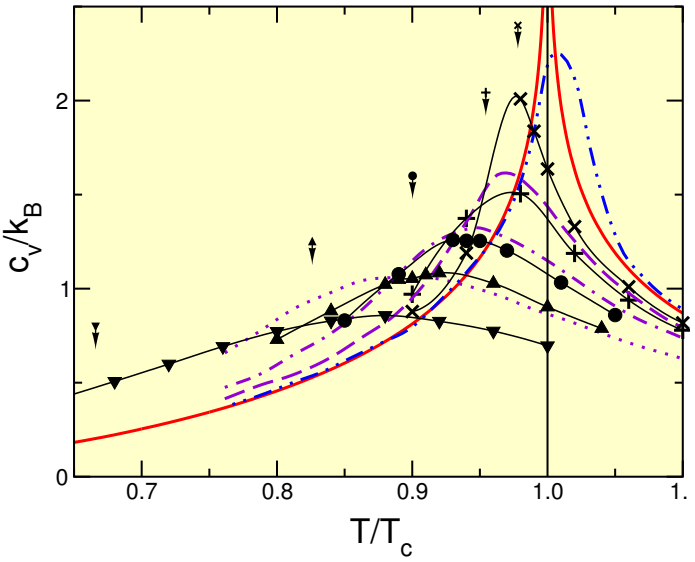

Figure 13.2:
Calculated temperature dependence of the specific heat of $La_{2-x}Sr_xCuO_4$ for Sr concentrations $x = 0.00179$ (crosses), 0.00367 (+ signs), 0.00776 (circles), 0.0124 (triangles up), and 0.0239 (triangles down). The thin full lines are guides for the eyes. The relative uncertainties due to statistical fluctuations of the inhomogeneities and the Monte Carlo processes are of the order of 3 % at each point. The remaining antiferromagnetic lattice has a size of 302×302 sites (lattice constant a), covered with non magnetic discs of a diameter of 6.04 a. Arrows denote the effective Néel temperatures. The red full line corresponds to the exact specific heat of the pure system; the violet dashed, dashed-dotted, and dotted lines have been calculated for a pure $32\times\infty$, $16\times\infty$, and an $8\times\infty$ lattice [2]. The blue dashed double-dotted line corresponds to calculations [3] of a system of 64×64 sites.

lattice constants wide. Percolation of these conducting areas then leads to global conduction. Diffusing d-electrons in these areas can destroy antiferromagnetism. It has been shown (1) that in $La_{2-x}Sr_xCuO_4$ high-T_c superconductors the Néel temperatures decrease with increasing doping even when the systems are simulated with Ising instead of Heisenberg interactions. A system close to the magnetic percolation limit exhibits isolated small clusters responsible for the observed spin glass behavior at low temperatures. The simulations of the specific heat show that the singularities which occur in infinite pure systems, vanish for finite doped systems. It is expected that for infinitely large doped systems the peak heights increase with system sizes, however, the small grain sizes of the cuprates (4) stop such an increase, so that the peak heights decrease and the peak widths grow with doping in these materials (see Fig. 13.2). A similar behavior is also visible for the staggered susceptibility χ and the antiferromagnetic correlation length. Such a growth of the peak widths has also been observed in nuclear quadrupole resonance spectra of doped superconducting $La_{2-x}Sr_xCuO_4$ (5), in contrast to the very narrow peaks of the pure antiferromagnetic insulating La_2CuO_4 (6).

[1] E. P. Stoll, J. Phys. A, **38**, 125 (2005).
[2] Helen Au-Yang and Michael. E. Fisher, Phys. Rev. B, **11**, 3469 (1975).
[3] Arthur E. Ferdinand and Michael. E. Fisher, Phys. Rev., **185**, 832 (1969).
[4] T. Schneider, Journal of Superconductivity: Incorporating Novel Magnetism, **17**, 41 (2004).
[5] Y.-Q Song, M. A. Kennard, M. Lee, K. R. Poppelmeier, and W. P. Halperin, Phys. Rev. B, **44**, 7159 (1991).
[6] T. Imai, C. P. Slichter, K. Yoshimura, and K. Kosuge, Phys. Rev. Lett., **70**, 1002 (1993).

13.3 Charge and spin density distributions around Zn impurities in cuprates

In hole doped cuprates nonmagnetic impurities like Zn and others are detrimental (1) and superconductivity disappears with a few percent of Zn dopants. It is well known that the doping of the cuprates by holes destroys the antiferromagnetic correlations. In contrast, it has been proposed that Zn doping enhances antiferromagnetic correlations (2; 3). Abrikosov (4) following recent numerical calculations of Kaplan *et al.* (5), proposed that Zn, creating an excess positive charge at the copper site, reduces the hole concentration in its vicinity.

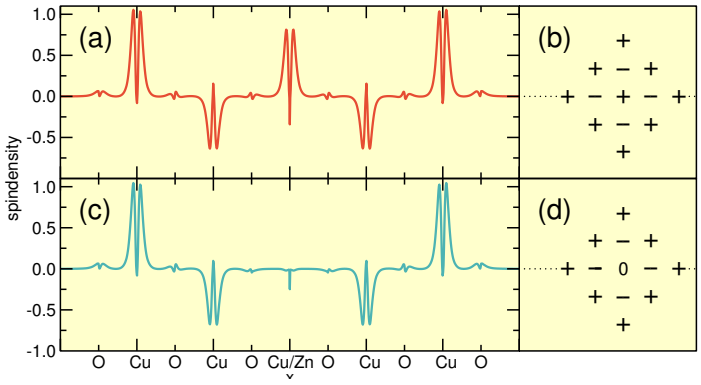

Figure 13.3:
(a) Spin density along the 5 Cu and 6 O in the $Cu_{13}O_{62}/Cu_{12}La_{66}$ Cu cluster with spin multiplicity M=6; (c) spin density with Zn substitution and multiplicity M=5.

We have investigated the effect of zinc substitution on the local electronic structure of several cuprates using first-principles cluster calculations. Clusters comprising until 13 copper atoms in the cuprate plane of La_2CuO_4, $YBa_2Cu_3O_7$, and $YBa_2Cu_4O_8$ were used.
We illustrate the antiferromagnetic spin arrangement with the $Cu_{13}O_{62}/Cu_{12}La_{66}$ cluster for La_2CuO_4. We performed calculations by choosing a spin multiplicity of $M = 6$. In Fig. 13.3a the spin density along the Cu-O bonds in the plane is displayed for an undoped Cu_{13} cluster. In the right panel (Fig. 13.3b) the signs of the Mulliken spin densities at the planar Cu sites are shown which exhibit an antiferromagnetic spin arrangement, with adjacent copper sites having opposite spins. Near the copper, most of the spin density is provided by a singly occupied $3d_{x^2-y^2}$ atomic orbital (AO). Its square has maxima at distances of 0.345 Å from the nucleus but vanishes at the nucleus where the spin densities are provided by s orbitals.
The two copper atoms at the outermost right and left positions in Fig. 13.3a have only one NN copper ion whereas the one in the center has four NN with negative spin densities and the two remaining coppers have four NN with positive spin densities. These differences allow the determination of on-site and transferred hyperfine fields as has been demonstrated in Refs. (6; 7). Near the oxygens, the spin density is provided by the $2p_x$ AO and the contact density is very small for antiferromagnetically arranged copper neighbors.
The introduction of zinc at the cluster center introduces an extra electron into the cluster and it is to be noted that the spin state of lowest energy is now the $M = 5$ state with a corresponding spin density along the Cu-O bonds that is shown in the lower panel of Fig. 13.3c. This leaves the antiferromagnetic arrangement virtually intact although there is a detectable reduction in the spin density on the coppers which are nearest neighbors to the zinc perhaps due to a slight delocalization of the electron of opposite spin on the zinc (see Fig. 13.3c). The Mulliken spin density on the Zn is practically zero, as to be expected (Fig. 13.3d).
The results show that the effects of Zn substitution are rather local as concerns the electronic structure. The charge content on the oxygens surrounding Zn is lower than in the pure compound which we interpret as destroying superconductivity locally in the vicinity of Zn.

We were also able to calculate electric field gradients (EFG) at the Cu sites and compared them to experiment. We find that the EFG values for the nearest neighbor coppers to Zn are larger than in the undoped compounds whereas those of the next nearest neighbors (NNN) are smaller. We also showed that for a Cu nucleus adjacent to a Zn the spin-lattice relaxation rate would be considerably reduced which is not what is observed experimentally. With these two arguments we conclude that the experimentally observed ^{63}Cu satellite peak with lower NQR frequency probably originates from copper nuclei that are NNN to Zn.

[1] G. Xiao, M. Z. Cieplak, J. Q. Xiao, and C. L. Chien, Phys. Rev. B, **42**, 8752 (1990).

[2] M.-H. Julien, T. Fehér, M. Horvatić, C. Berthier, O. N. Bakharev, P. Ségransan, G. Collin, and J.-F. Marucco, Phys. Rev. Lett., **84**, 3422 (2000).

[3] Y. Itoh, T. Machi, C. Kasai, S. Adachi, N. Watanabe, N. Koshizuka, and M. Murakami, Phys. Rev. B, **67**, 064516 (2003).

[4] A. A. Abrikosov, Physica C, **397**, 77 (2003).

[5] I. G. Kaplan, J. Soullard, and J. Hernández-Cobos, Phys. Rev. B, **65**, 214509 (2002).

[6] P. Hüsser, H. U. Suter, E. P. Stoll, and P. F. Meier, Phys. Rev. B, **61**, 1567 (2000).

[7] S. Renold, S. Pliberšek, E. P. Stoll, T. A. Claxton, and P. F. Meier, Eur. Phys. J. B, **23**, 3 (2001).

13.4 Re-assessment of NMR data in the cuprates

The traditional approach to interpreting NMR spin-lattice relaxation rates in the cuprates has been originally developed in 1990 by Millis, Monien and Pines and is generally known as the MMP theory (1). This method is able to model the different temperature dependence of the planar copper and oxygen relaxation rates by identifying two contributions to the spin susceptibility. One is strongly peaked at the antiferromagnetic wave vector and dominates the copper relaxation rate. The other, associated to a Fermi liquid contribution, is essentially wave vector independent and is responsible for the oxygen relaxation. The procedure suffers however from the following drawback: the hyperfine fields are added coherently at the copper site but incoherently at the oxygen site. We put forward a model in which such a distinction needs not be made *a priori*. Rather, the degree of coherency is determined from the value of the correlations between electronic copper spins. Furthermore, no assumption is made from the start on the form of the susceptibility or to what contributes to it.

We come back to a well established expression for the spin-lattice relaxation rate of a nucleus k, ${}^kT_{1\alpha}^{-1} = {}^kU_\beta + {}^kU_\gamma$, when a field is applied in the crystallographic direction α. The relaxation is caused by fluctuating fields ${}^kU_\beta$ and ${}^kU_\gamma$ in the directions perpendicular to the applied field. When the relaxation rates are known experimentally in the different directions, the contributions ${}^kU_\alpha$ can be easily computed. It turns out that the temperature dependence of all ${}^kU_\alpha$ is similar (${}^kU_\alpha$ is growing with increasing temperature), and there is no contrasting temperature difference between the copper and the oxygen contributions.

Using a simple model of fluctuating fields (2), we obtained that ${}^kU_\alpha(T) = {}^kV_\alpha(T)\,\tau_{\mathit{eff}}(T)$. $\tau_{\mathit{eff}}(T)$ is an effective correlation time, and the ${}^kV_\alpha$ in the copper-oxide plane are expressions in terms of the hyperfine field constants and static spin-spin correlations. Typically for the oxygen, ${}^{17}V_\alpha \propto (1 + K_{01}^\alpha)$, where the nearest neighbor antiferromagnetic spin correlation $K_{01}^\alpha = 4\langle S_0^\alpha S_1^\alpha\rangle$ varies between -1 and 0 in function of the temperature. The field at the copper site is given by the on-site contribution, plus the transfered fields from the 4 nearest

neighbors, so that the expression ${}^{63}V_\alpha$ for copper contains also next-nearest neighbor and next-next-nearest neighbor correlations. In the limit of a fully antiferromagnetic system, ${}^{63}V_\alpha$ is simply given by the coherent addition of hyperfine field constants $(A_\alpha - 4B)^2$, whereas in the limit of no correlations, they are incoherently added as $\left(A_\alpha^2 + 4B^2\right)$. The spin correlations provide the interpolation between those extremes in function of the temperature.

In order to make the model numerically tractable, we assumed that the higher order correlations depend on K_{01}^α and decrease exponentially with the distance between spins. By computing the *ratios* of relaxation rates, including those between different nuclei, the τ_{eff} cancel out by assumption. In the case of $YBa_2Cu_3O_7$, where the whole range of data for copper, oxygen and yttrium are available, we were able to fit the hyperfine field constants and determine $K_{01}^\alpha(T)$ between 100 K and 300 K. Using those values we went back to the data and extracted τ_{eff}, which could be extremely well fitted with the function $\tau_{eff}^{-1} = \tau_1^{-1} + \tau_2^{-1}$, where $\tau_1 \propto T$ and τ_2 constant. The linear dependence of τ_{eff} at low temperature hints at a relaxation process dominated by scattering of quasi-particles in a Fermi liquid. At high temperature, $\tau_{eff} \to \tau_2$. In order to determine what dominates the relaxation there, we examined the copper spin relaxation data available for the $La_{2-x}Sr_xCuO_4$ series. As the rates for all dopings, including that of the insulating parent compound, converge to the same constant value at high temperature, we concluded that τ_2 can be associated to the fluctuations of local spins in a paramagnet.

The validity of the model and the fitting formula for τ_{eff} could be convincingly tested by confronting our high temperature predictions with high temperature relaxation rates data in $YBa_2Cu_3O_7$. We analyzed then the underdoped compounds of the YBaCuO series. In particular, some very precise measurements of the copper relaxation rate are available for the $YBa_2Cu_4O_8$ compound. A whole fit could not be done in this substance, since only measurements along the c-axis were made. However, taking the same correlations and hyperfine field constants found in $YBa_2Cu_3O_7$, we can determine τ_{eff} between 100 K and 300 K and fit it with $\tau_{eff}^{-1} = \tau_1^{-1} + \tau_2^{-1}$. This time however, τ_1 is not linear but goes like $\tau_1 \propto Te^{-g/T}$, where g is a further adjustable parameter. The result for the reconstructed relaxation rate is shown in Fig. 13.4, along with the data used for the fit (crosses) and further high temperature data.

Our prediction (solid line) is in striking agreement with the experiment.

In summary, we proposed a way of looking at the spin-lattice relaxation data which is adapted to the anisotropic nature of the cuprate materials. The degree of coherency of the

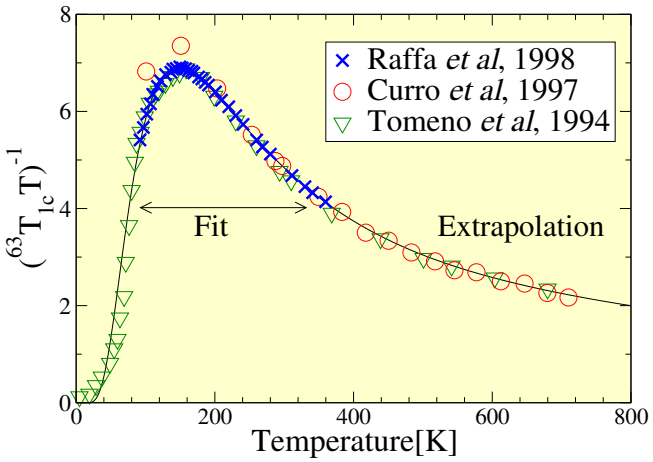

Figure 13.4:
NQR data from Raffa *et al.* [3] for $YBa_2Cu_4O_8$ and fit as in the text (solid line), and comparison with data from Curro *et al.* [4] and Tomeno *et al.* [5].

hyperfine fields is the same at all time for all nuclei, but varies with the temperature in function of the antiferromagnetic spin-spin correlations. The success of the predictions at high temperature confirms the validity of the model, which we believe could help identifying the underlying physical processes in the cuprates.

[1] A. J. Millis, H. Monien and D. Pines, J. Phys.: Condens. Matter, **42**, 167 (1990).

[2] **Principles of magnetic resonance**, C. P. Slichter, Springer, Berlin, 1996.

[3] F. Raffa, T. Ohno, M. Mali, J. Roos, D. Brinkmann, K. Conder and M. Eremin, Phys. Rev. Lett., **81**, 5912 (1998).

[4] N. J. Curro, T. Imai, C. P. Slichter and B. Dabrowski, Phys. Rev. B, **56** , 877 (1997).

[5] I. Tomeno, T. Machi, K. Tai, N. Koshizuka, S. Kambe, A. Hayashi, Y. Ueda and H. Yasuoka, Phys. Rev. B, **49** , 15327 (1994).

14 Mechanical Workshop

K. Bösiger, B. Schmid, B. Lussi, M. Schaffner, R. Meier, P. Treier, R. Reichen (apprentice)

The quality of the mechanical workshop shop is one of the most valuable assets of the Physik-Institut in support of the diverse research and teaching activities. Physicists from collaborating institutions from all over the world have often expressed admiration and shown envy for its work.

Bernhard Schmid, who headed this shop from August 1974 to December 2002 has retired in March 2005. It is appropriate to start this years annual report with a tribute to him and an extension of the best wishes for his future. Bernhard Schmid is to a large extent to be credited for the successful operation of this excellent team. He was instrumental in continously upgrading the machine park, which now includes a number of high-end computer controlled mills and lathes, organized the smooth transfer of the shop to its new location in 1993, coordinated all the larger construction projects for the particle physics experiments (Asterix, Neutrino Mass, Gravitational Constant, H1), taught many generations of incoming physics students the basics of milling, drilling and lathing, lead sixteen apprentices through their four year long training and education required for becoming a certified technician, and last but not least generated an atmosphere of truly collegial understanding and help within his team. He even coolly solved priority conflicts between hotheaded group leaders without loosing them as his friends.

Bernhard Schmid, who retired after heading the workshop for almost 30 years.

The retirement celebrations did not stop the work, as the long list of activities below demonstrates. These include projects for exhibitions, classroom demonstrations, new experiments in the students laboratories, and of course for the research groups.
The modern infrastructure of our mechanical workshop necessary to solve the various demanding problems was complemented by a new folding machine in August (see figure below). In November a practical training for future apprentice was organized. Interested candidates for an apprenticeship had the opportunity to become acquainted with their possible future job.

In the new Bachelor-Curriculum for the Physics students the course in basic mechanical skills continues to be required. Up to three members of the work shop are engaged in this task, which now is concentrated into two-week block courses during the semester break.

The new folding machine installed in the workshop.

Furthermore the workshop maintains the metal and technical material supply store. Again more than 30 institutes made use of this service [5].

Besides work for the internal groups a small fraction of the activities was devoted to special designs, modifications and small series for outside companies.

Some work shop activities

- **Open days of The Faculty of Science**
  June 4 to June 6, 2004
  For this occasion when thousands of visitors came to the institute various installations demonstrating the fundamental laws of physics were designed and built such as a giant version of a chaotic pendulum.
- **Surface Physics**
  (Group Osterwalder, Sec. 11)
  For this group the priorities were on repair and maintenance.
- **Physics of Biological Systems**
  (Group Fink, Sec. 12)
  Various mechanical infrastructure was manufactured and some test setups were built.
- **CMS pixel detector**
  (Group Amsler, Sec. 8)
  All the tooling and parts necessary for the additional laser welding tests were manufactured. We also started with the tooling for the detector-supply tubes.

The giant pendulum in operation.

Segment of the CMS pixel detector support structure.

Cylinder used for the construction of the CMS pixel detector supply tubes.

[5]For a catalogue see http://www.physik.unizh.ch/groups/werkstatt/dienstleistung.html

Cooling plates for the LHCb detectors.

Parts prepared for the installation.

- **LHCb inner tracking detector (Group Straumann, Sec. 7)**
  Different parts for test stands were manufactured. The necessary gluing and production tools were manufactured. The clean room and the assembly hall of the workshop were prepared for the production of the test setups and the final detectors.

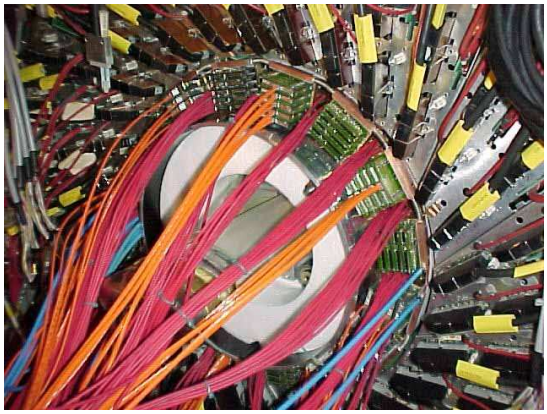

CIP electronics after the re-installation of the detectors.

- **H1 experiment at DESY in Hamburg, Sec. 2**
  Repair and maintenance of the CIP readout electronics.

A complete setup of the improved blood circulation experiment.

- **Physics lectures for medical students (see last year's report)**
  Some of the demonstration experiments had to be repaired and/or improved.

15 Electronics Workshop

W. Fässler, H.P. Meyer, P. Soland and K. Szeker

Several dedicated power supplies were developed and built during the last year. Details of the instruments are shown in the figures to the right. Various repair work, modifications and new designs were executed for all groups at the institute which includes the corresponding documentation. In some cases faulty parts were no longer available so substitutions had to be found. The evaluation and procurement of these parts were often extremely time consuming.

Together with L. Pauli and J. Seiler, who are responsible for the preparation of the experiments in the lecture halls, the workshop maintains and renews the equipment used for demonstration experiments. As a new example the figure below shows curves measured during the demonstration of Bragg`s law for two orientations of the crystal model. These curves can be projected with the beamer during the measurement. The associated electronics were designed and built in the electronic workshop. Different seminars and courses were attended including a wire bonding training to operate the wire bonding machine, which is meanwhile installed at the workshop.

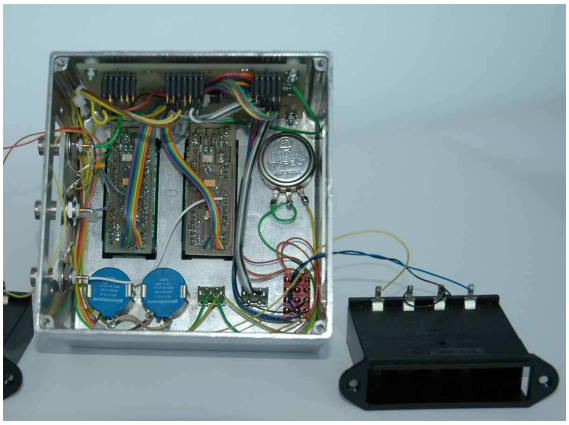

Dedicated constant current- and voltage source.

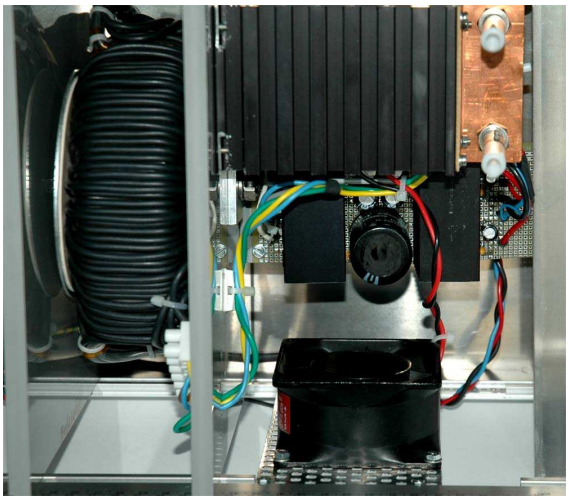

Special heating power supply transformer.

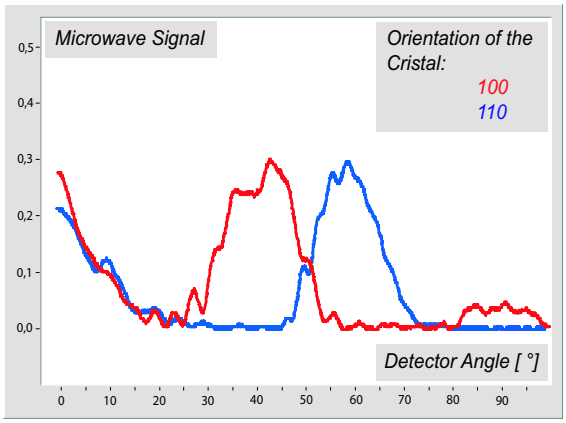

Demonstration of Bragg's law during a lecture on modern physics.

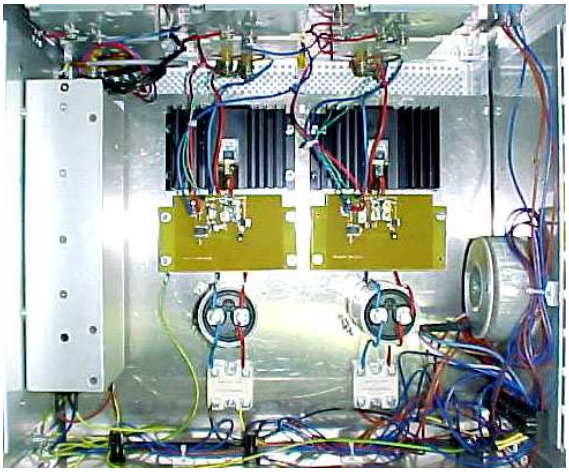

High current DC power supply.

Some examples of our activities in support of the various research projects are:

- **Physics of Biological Systems**
  (Group Fink, Sec. 12)
  Design and construction of a dedicated heating power supply transformer.
- **Superconductivity and Magnetism**
  (Group Keller, Sec. 9)
  A second version of a computer controllable motor power supply was designed. The construction of a NMR spectrometer started. Eventually two complete systems will be built.
- **Particle Physics at DESY/HERA (H1)**
  (Groups Straumann and Truöl, Sec. 2)
  The workshop was involved in the repair and maintenance of the CIP readout electronics for the H1 experiment at DESY in Hamburg.
- **High-precision CP-violation Physics at LHCb**
  (Group Straumann, Sec. 7)
  A programmable delaymodule was evaluated and various PCB layouts were designed.

16 Publications

16.1 Research group of Prof. C. Amsler

Articles

- **Spatial Distribution of Cold Antihydrogen Formation**
  N. Madsen et al. (ATHENA Collaboration), Phys.Rev.Lett.94 (2005) 033403.

- **A measurement of the Lorentz angle in silicon strip sensors at cryogenic temperature**
  I. Johnson, C. Amsler et al., Nucl.Instr.Meth.A 540 (2005) 113.

- **Dynamics of antiproton cooling in a positron plasma during antihydrogen formation**
  M. Amoretti, C. Amsler et al. (ATHENA Collaboration), Phys.Rev.Lett.B 590 (2004) 133.

- **Study of antiproton annihilation on neutrons into $\omega\pi^-\pi^0$**
  C. Amsler et al. (Crystal Barrel Collaboration), Nucl.Phys.A740 (2004) 130.

- **Design and test of the CMS pixel readout chip**
  M. Barbero et al., Nucl.Instr.Meth.A 517 (2004) 349.

- **A Gaussian-sum filter for vertex reconstruction**
  R. Frühwirth, T. Speer, Nucl.Instr.Meth.A 534 (2004) 217.

- **Review of Particles Physics**
  S. Eidelman et al. (Particles Data Group), Phys.Lett.B 592 (2004) 1.

- **Quark Model**
  C. Amsler, Phys. Lett. B 592 (2004) 154.

- **The $\eta(1405)$, $\eta(1475)$, f_1(1420), and f_1(1510)**
  C. Amsler, Phys. Lett. B 592 (2004) 549.

- **Non $q\bar{q}$ candidates**
  C. Amsler, Phys. Lett. B 592 (2004) 848.

- **Tests of silicon sensors for the CMS pixel detector**
  A. Dhorokov, C. Amsler et al., Nucl.Instr.Meth.A 530 (2004) 71.

- **Real-time detector for plasma diagnostic in antimatter experiment**
  C. Carraro et al. (ATHENA Collaboration), Nucl.Instr.Meth.A 518 (2004) 249.

- **Production and detection of cold antihydrogen atoms**
  M. Amoretti, C. Amsler et al. (ATHENA Collaboration), Nucl.Instr.Meth.A 518 (2004) 244.

- **The first cold antihydrogen**
  M. C. Fujiwara et al. (ATHENA Collaboration), Nucl.Instr.Meth.A 532 (2004) 229.

- **Light exotic mesons**
  C. Amsler, Conf. on Quark Confinement and the Hadron Sprectrum, Gargnano, World Scientific (2003) 101.

- **Particle Physics Booklet**
  S. Eidelman et al. (Particle Data Group), Extracted from Phys. Lett. B 592 (2004) 1.

- **Position Dependence of Charge Collection in Prototype Sensors for the CMS Pixel Detector**
  T. Rohe et al., Proc. 2003 IEEE Nuclear Science Symposium, physics/0312009, IEEE-TNS 51-3 (2004) 1150.

- **Detection of antihydrogen with a silicon micro-strip and pure CsI detector**
  I. Johnson et al. (ATHENA Collaboration), Proc. 8th ICATPP Conference, physics/0401034, World Scientific (2004) 473.

Articles in press

- **ATHENA – First Production of Cold Antihydrogen and Beyond**
  A. Kellerbauer et al. (ATHENA Collaboration), Proc. of the Third Meeting on CPT and Lorentz Symmetry, Bloomington, hep-ex/040904, World Scientific.

- **Electric field measurement in heavily irradiated pixel sensors**
  A. Dorokhov, Y. Allkofer et al., Proc. Vertex 2004 Conference, physics/0412036, Nucl.Instr.Meth.A.

- **Fluence dependence of charge collection in irradiated pixel sensors**
  T. Rohe et al., Proc. 5th International Conference on Radiation Effects on Semiconductor Materials Detectors and Devices, physics/0411214, Nucl.Instr.Meth.A.

- **Simulation of Heavily Irradiated Silicon Pixel Sensors and Comparison with Test Beam Measurements**
  V. Chiochia, et al., Proc. 2004 IEEE Nuclear Science Symposium, physics/0411143, IEEE Transactions on Nuclear Science.

- **Final results on the neutrino magnetic moment from the MUNU experiment**
  Z. Daraktchieva et al. (MUNU Collaboration), Phys. Lett. B.

- **Vertex reconstruction in CMS**
  E. Chabanat et al., Nucl.Instr.Meth.

- **The effect of highly ionizing particles on the CMS silicon strip tracker**
  W. Adam et al. (CMS Collaboration), Nucl.Instr.Meth.A .

- **A Gaussian/sum filter for vertex reconstruction**
  T. Speer, Proc. of CHEP 2004, Interlaken.

- **A kinematic fit and a decay chain reconstruction library**
  K. Prokofiev and T. Speer, Proc. of CHEP 2004, Interlaken.

PhD thesis

- **Performance of Radiation Hard Pixel Sensors for the CMS Experiment**
  A. Dorokhov, PhD Thesis, Universität Zürich, (2005).

Invited Lectures

- V. Chiochia: **Simulation of irradiated pixel sensors and comparison with test beam data**
  Invited talk, IEEE Nuclear Science Symposium, Rome, 20.10.04.
- A. Dorokhov: **Pixel sensors under heavy irradiation**
  Invited talk, Vertex 2004 Conf., Menaggio, 16.09.04.
- A.Dorokhov: **Spatial resolution of the CMS pixel detector barrel module**
  Seminar, Paul Scherrer Institut, 04.03.05.
- I. Johnson: **Modeling and measuring the Lorentz deflection in silicon sensors**
  Seminar, CMS tracker workshop, CERN, 19.01.05.
- C. Regenfus: **The CMS pixel detector : a status report**
  Invited talk, Vertex 2004 Conf. , Menaggio, 15.09.04.
- T. Speer: **A kinematic fit library**
  Invited talk, CMS workshop on b/tau Physics, Bari, 28.05.04.
- T. Speer: **A Gaussian-sum filter for Vertex reconstruction**
  Invited talk, CHEP 2004 Conf., Interlaken, 30.09.04.
- T. Speer: **Kinematic fit and decay chain reconstruction library**
  Invited talk, CHEP 2004 Conf., Interlaken, 30.09.04.

ATHENA Collaboration:

M. Amoretti, C. Amsler, G. Bonomi, A. Bouchta, P. Bowe, C. Carraro, C. L. Cesar, M. Charlton, M. Doser, V. Filippini, A. Fontana, M. C. Fujiwara, R. Funakoshi, P. Genova, J. S. Hangst, R. S. Hayano, L. V. Joergensen, I. Johnson, V. Lagomarsino, R. Landua, E. Lodi Rizzini, M. Macri, N. Madsen, G. Manuzio, M. Marchesotti, P. Montagna, H. Pruys, C. Regenfus, P. Riedler, J. Rochet, A. Rotondi, G. Rouleau, G. Testera, A. Variola, D.P. van der Werf

MUNU Collaboration:

Z. Daraktchieva, C. Amsler, M. Avenier, C. Broggini, J. Busto, C. Cerna, F. Juget, D.H. Koang, J. Lamblin, D. Lebrun, O. Link, G. Puglierin, A. Stutz, A. Tadsen, J.-L. Vuilleumier, V. Zacek

CRYSTAL BARREL Collaboration:

C. Amsler, A.V. Anisovich, C.A. Baker, B.M. Barnett, C.J. Batty, M. Benayoun, P. Blüm, K. Braune, T. Case, V. Credé, K.M. Crowe, M. Doser, W. Dünnweber, D. Engelhardt, M.A. Faessler, R.P. Haddock, F.H. Heinsius, N.P. Hessey, P. Hidas, D. Jamnik, H. Kalinowsky, P. Kammel, J. Kisiel, E. Klempt, H. Koch, M. Kunze, U. Kurilla, R. Landua, H. Matthäy, C.A. Meyer, F. Meyer-Wildhagen, R. Ouared, K. Peters, B. Pick, M. Ratajczak, C. Regenfus, J. Reinnarth, A. Sarantsev, U. Strohbusch, M. Suffert, J.S. Suh, U. Thoma, I. Uman, S. Wallis-Plachner, D. Walther, U. Wiedner, K. Wittmack

PARTICLE DATA Group:

S. Eidelman, K.G. Hayes, K.A. Olive, M. Aguilar-Benitez, C. Amsler, D. Asner, K.S. Babu, R.M. Barnett, J. Beringer, P.R. Burchat, C.D. Carone, C. Caso, G. Conforto, O. Dahl, G. D'Ambrosio, M. Doser, J.L. Feng, T. Gherghetta, L. Gibbons, M. Goodman, C. Grab, D.E. Groom, A. Gurtu, K. Hagiwara, J.J. Hernandez-Rey, K. Hikasa, K. Honscheid, H. Jawahery, C. Kolda, Y. Kwon, M.L. Mangano, A.V. Manohar, J. March-Russell, A. Masoni, R. Miquel, K. Monig, H. Murayama, K. Nakamura, S. Navas, L. Pape, C. Patrignani, A. Piepke, G. Raffelt, M. Roos, M. Tanabashi, J. Terning, N.A. Tornqvist, T.G. Trippe, P. Vogel, C.G. Wohl, R.L. Workman, W.-M. Yao, P.A. Zyla

16.2 Research group of Prof. H.-W. Fink

Articles in print

- **Time-resolved spectroscopic fluorescence imaging, transient absorption and vibrational spectroscopy of intact and photoinhibited plant tissue**
  P.B. Lukins, S. Rehman, G.B. Stevens and D.F. George, Luminescence.

- **Axisymmetric Liquid Hanging Drops**
  E.Meister and T.Yu.Latychevskaia, Journal of Chemical Education.

Conference report

- **Using FIB for Sample Preparation in Low Energy Electron Point Source (LEEPS) Microscopy**
  Michael Krüger, poster, 8th European FIB Users Group Meeting (EFUG 2004), EMPA, Dübendorf, Switzerland, 04.10.2004.

Invited Lectures

- Conrad Escher: **Energetics of an individual DNA molecule bound to a solid surface**
  symposium on surface science 2005, Les Arcs (France), 18-03-05.

- Michael Krüger: **Nanostrukturierung mit einem fokussierten Ionenstrahl**
  Raith Lithography User workshop: Regensburg, Germany, 09.03.2004.

16.3 Research group of Prof. H. Keller

Articles

- **Metallic phase in lightly doped $La_{2-x}Sr_xCuO_4$ observed by electron paramagnetic resonance**
  A. Shengelaya, M. Bruun, B.K. Kochelaev, A. Safina, K. Conder, and K.A. Müller, Phys.Rev.Lett.**93**, 017001-1-4 (2004).

- **Absence of a boron isotope effect in the magnetic penetration depth of MgB_2**
  D. Di Castro, M. Angst, D.G. Eschenko, R. Khasanov, J. Roos, I.M. Savić, A. Shengelaya, S.L. Bud'ko, P.C. Canfield, K. Conder, J. Karpinski, S.M. Kazakov, R.A. Ribeiro, and H. Keller, Phys. Rev. B **70**,014519-1-5 (2004).

- **Formation and dynamics of muonium centres in semiconductors – a new approach**
  V.G. Storchak, D.G. Eshchenko, and J.H. Brewer, J. Phys.: Condens. Matter **16**, S4761 - S4778 (2004).

- **Nano-scale thin film investigations with slow polarized muons**
  E. Morenzoni ,T. Prokscha, A. Suter, H. Luetkens, and R. Khasanov, J. Phys.: Condens. Matter **16**, S4583S4601 (2004).

- **The oxygen isotope effect on the in-plane penetration depth in cuprate superconductors**
  R. Khasanov, A. Shengelaya, E. Morenzoni, K. Conder, I.M. Savić, and H. Keller, J. Phys.: Condens. Matter **16**, S4439S4455 (2004).

- **Anisotropic properties of MgB_2 by torque magnetometry**
  M. Angst, D. Di Castro, R. Puzniak, A. Wisniewski, J .Jun, S.M. Kazakov, J. Karpinski, S. Kohout, and H. Keller, Physica C **408-410**, 88-89 (2004).

- **Implications evinced by the phase diagram, anisotropy, magnetic penetration depths, isotope effects and conductivities of cuprate superconductors**
  T. Schneider and H. Keller, New Journal of Physics **6**, 144-1-18 (2004).

- **Anisotropy and internal-field distribution of MgB_2 in the mixed state at low temperatures**
  M. Angst, D. Di Castro, D.G. Eshchenko, R. Khasanov, S. Kohout, I.M. Savić, A. Shengelaya, S.L. Budko, P.C. Canfield, J. Jun, J. Karpinski, S.M. Kazakov, R.A. Ribeiro, and H. Keller,
  Phys. Rev. B **70**, 224513-1-5 (2004).

- **Pressure effects on the transition temperature and the magnetic field penetration depth in the pyrochlore superconductor $RbOs_2O_6$**
  R. Khasanov, D.G. Eshchenko, J. Karpinski, S.M. Kazakov, N.D. Zhigadlo, R. Brütsch, D. Gavillet, D.Di Castro, A. Shengelaya, F.La Mattina, A. Maisuradze, C. Baines, and H. Keller,
  Phys.Rev.Lett.**93**, 157004-1-4 (2004).

- **Evidence for charged critical fluctuations in underdoped $YBa_2Cu_3O_{7-\delta}$**
  T. Schneider, R. Khasanov, and H. Keller, J. Phys.: Condens. Matter **16**, L437-L442 (2004).

- **Finite-size and pressure effects in $YBa_2Cu_4O_8$ probed by magnetic-field penetration-depth measurements**
  R. Khasanov, T. Schneider, R. Brütsch, D. Gavillet, J. Karpinski, and H. Keller, Phys. Rev. B, **70** 144515-1-7 (2004).

- **Comment on "Superconducting anisotropy and evidence for intrinsic pinning in single crystalline MgB_2**
  M. Angst, R. Puzniak, A. Wisniewski, J. Roos, H. Keller, and J. Karpinski, Phys. Rev. **70**, 226501-1-3 (2004)

- **Direct Observation of Nonlocal Effects in a Superconductor**
  A. Suter, E. Morenzoni, R. Khasanov, H. Luetkens, T. Prokscha, and N. Garifianov, Phys. Rev. Lett. **92**, 087001-1-4 (2004).

- **Long range electron spin polarization in the Ag layer of a Fe/Ag film**
  H. Luetkens, J. Korecki, E. Morenzoni, T. Prokscha, A. Suter, M. Birke, N. Garifianov, R. Khasanov, T. Slezak, and F.J. Litterst, J. Magn. Magn. Mater. **272-276**, 1128-1129 (2004).

- **Antiferromagnetic transition in epitaxial strained La_2CuO_4 thin films**
  A. Suter, J.-P. Locquet, E. Morenzoni, T. Prokscha, D.G. Eshchenko, N. Garifianov, R. Khasanov, H. Luetkens, and J.W. Seo, J. Magn. Magn. Mater. **272-276**, 110-111 (2004).

- **Two Band Superconductivity in MgB_2: Basic Anisotropic Properties and Phase Diagram**
  M. Angst and R. Puzniak, in *Focus on Superconductivity*, ed. B. P. Martines, Vol. **1** (Nova Science Publishers, New York, 2004) (pp. 1-49).

- **Relationship between and implications of the isotope and pressure effects on transition temperature, penetration depths and conductivities**
  T. Schneider, phys. stat. sol. (b) **242**, 58-77 (2005).

- **Evidence for charged critical behavior in the pyrochlore superconductor $RbOs_2O_6$**
  T. Schneider, R. Khasanov, and H. Keller, Phys. Rev. Lett. **94**, 077002-1-4 (2005).

- **Implications of the isotope effects on magnetization, magnetic torque and susceptibility**
  T. Schneider, J. Phys.: Condens. Matter **17**, L161 - L167 (2005).

Articles in press

- **Clean and Dirty Superconductivity in Pure, Al doped, and Neutron Irradiated MgB_2: a Far-Infrared Study**
  M. Ortolani, D. Di Castro, P. Postorino, I. Pallecchi, M. Monni, M. Putti, and P. Dore, Phys. Rev. B (2005).

- **Muon-Spin-Rotation Measurements of the Penetration Depth in the Infinite-Layer Electron-Doped Cuprate Superconductor $Sr_{0.9}La_{0.1}CuO_2$**
  A. Shengelaya, R. Khasanov, D. G. Eshchenko, D. Di Castro, I. M. Savić, M. S. Park, K. H. Kim, Sung-Ik Lee, K.A. Müller, and H. Keller, Phys. Rev. Lett. (2005).

- **Evidences for polaron formation in cuprates**
  A. Bussmann-Holder, H. Keller, and K.A. Müller, in *Structure and Bonding Vol. 114*, A. Bussmann-Holder and K.A. Müller, eds., Springer-Verlag Berlin Heidelberg (2005).

- **Unconventional isotope effects in cuprate superconductors**
  H. Keller, in *Structure and Bonding Vol. 114*, A. Bussmann-Holder and K.A. Müller, eds., Springer-Verlag Berlin Heidelberg (2005).

- **Essential heterogeneities in hole-doped cuprate superconductors**
  K.A. Müller, in *Structure and Bonding Vol. 114*, A. Bussmann-Holder and K.A. Müller, eds., Springer-Verlag Berlin Heidelberg (2005).

- **Polaron formation as origin of unconventional isotope effects in cuprate superconductors**
  A. Bussmann-Holder and H. Keller, European Physical Journal B (2005).

- **Pressure effect on the in-plane magnetic penetration depth in $YBa_2Cu_4O_8$**
  R. Khasanov, J. Karpinski, and H. Keller, J. Phys.: Condens. Matter (2005).

Conference reports

- **Single Crystal ^{11}B-NMR Study of Magnesium Diboride**
  J. Roos, S. Strässle, M. Mali, H. Keller, J. Karpinski,
  AMPERE/EENC joint meeting, Lille, France, 6 - 11 September 2004.

Invited lectures

- H. Keller: **Unconventional isotope effects in strongly correlated cuprate superconductors**
  Max-Planck Institute for Solid State Research, Stuttgart, Germany, May 12, 2004.

- H. Keller: **Oxygen-isotope effect on the magnetic penetration depth in cuprate superconductors**
  5th International Conference on New Theories, Discoveries and Applications of Superconductors and Related Materials, Chongqing, China, June 11-16, 2004.

- H. Keller: **Unconventional isotope effects in cuprate superconductors**
  Spectroscopies in Novel Superconductors (SNS2004), Sitges, Spain, July 11-16, 2004.

- H. Keller: **Unconventional isotope effects in cuprate high-temperature superconductors**
  Nanoscale properties of condensed matter probed by resonance phenomena, Kazan, Russia, August 15-19, 2004.

- A. Shengelaya: **Microscopic Phase Separation and Two Type of Quasiparticles in Lightly Doped $La_{2-x}Sr_xCuO_4$ Observed by Electron Paramegnetic Resonance**
  Nanoscale properties of condensed matter probed by resonance phenomena, Kazan, Russia, August 15-19, 2004.

- H. Keller: **Unconventional isotope effects in cuprate superconductors**
  2004 E-MRS Fall Meeting Warsaw, Warsaw, Poland, September 5-10, 2004.

- H. Keller: **Unconventional isotope effects in cuprate superconductors**
  4th International Conference on Nanoscale Heterogeneity & Quantum Phenomena in Complex Matter (STRIPES04), Rome, Italy, September 26 - October 2, 2004.

- D. Di Castro: **Study of the pressure and isotope effects on the magnetic penetration depth of MgB_2**
  4th International Conference on Nanoscale Heterogeneity & Quantum Phenomena in Complex Matter (STRIPES04), Rome, Italy, September 26 - October 2, 2004.

- H. Keller: **Unconventional isotope effects in cuprate superconductors**
  EPFL Lausanne, Switzerland, February 1, 2005.

- H. Keller: **What did we learn from isotope effect experiments?**
  MaNEP Topical Meeting, Neuchâtel, Switzerland, February 11, 2005.

- H. Keller: **Unconventional isotope effects in high-temperature cuprate superconductors**
  American Physical Society (APS) March Meeting 2005, Los Angeles, U.S.A., March 21-25, 2005.

16.4 Research group of Prof. P. F. Meier

Articles

- **Hybrid mean field and alloy analogy treatment of the Hubbard model**
  A. Uldry and R. J. Elliott, J. Phys.: Condens. Matter **16**, S5221 (2004).

- **Spin susceptibility in the superconducting state of cuprates**
  T. Mayer, M. Eremin, I. Eremin and P. F. Meier, Physica C **408-410**, 400 (2004).

- **Percolation, fractal behavior and high-T_c superconductors**
  E. P. Stoll, J. of Superconductivity **17**, 79 (2004).

- **From next nearest neighbor site percolation to continuum percolation: Application to high T_c superconductors**
  E. P. Stoll, Int. J. Mod. Phys. C **15**, 321 (2004).

- **Suppression of critical properties in doped cuprates**
  E. P. Stoll, J. Phys. A **38**, 125 (2005).

Conference report

- E. P. Stoll:
  Critical properties in high-T_c superconductors below the insulator-conductor transition
  SPG Tagung, Neuchâtel, 03.03-04.03.04.

Invited Lectures

- P. F. Meier: **Re-assessment of NMR data in cuprates**
  Workshop on Unconventional Superconductors, University of Miami, Coral Gables, Miami, USA, 15.01.04.

- P. F. Meier: **First-principles calculation of the charge and spin density distribution in cuprates**
  Chongqing University, Chongqing, China, 11.06.04.

16.5 Research group of Prof. J. Osterwalder

Articles

- **Spin- and angle-resolved photoemission spectroscopy study of the Au(111) Shockley surface state**
  M. Muntwiler, M. Hoesch, V. N. Petrov, M. Hengsberger, L. Patthey, M. Shi, M. Falub, T. Greber, J. Osterwalder, J. Electron Spectrosc. Relat. Phenom. 137-140, 119-123 (2004).

- **One-dimensional chains of C_{60} molecules on Cu(221)**
  A. Tamai, W. Auwärter, C. Cepek, F. Baumberger, T. Greber, J. Osterwalder, Surf. Sci. 566-568, 633-637 (2004).

- **Localization of surface states in disordered step lattices**
  F. Baumberger, M. Hengsberger, M. Muntwiler, M. Shi, J. Krempasky, L. Patthey, J. Osterwalder, T. Greber, Phys. Rev. Lett. 92, 196805-1-4 (2004).

- **On the dissociation of N_2O after electron attachment**
  H.U. Suter and T. Greber, J. Phys. Chem. B, 108, 14511-14517 (2004).

- **Spin structure of the Shockley surface state on Au(111)**
  M. Hoesch, M. Muntwiler, V. N. Petrov, H. Hengsberger, L. Patthey, M. Shi, M. Falub, T. Greber, J. Osterwalder, Phys. Rev. B 69, 241401(R)-1-4 (2004).

- **Spin-orbit coupling in the L-gap surface states of Au(111): spin-resolved photoemission experiments and first-principles calculations**
  J. Henk, M. Hoesch, J. Osterwalder, A. Ernst, P. Bruno, J. Phys.: Condens. Matter 16, 7581-7597 (2004).

- **Electron coherence in a melting lead monolayer**
  F. Baumberger, W. Auwärter, T. Greber, J. Osterwalder, Science 306, 2221-2224 (2004).

- **Applications of a new Hamiltonian of interaction to one-dimensional and two-dimensional structures**
  A. Dolocan, V. Dolocan, Int. J. Mod. Phys. 18(2), 185-209 (2004).

- **Cr-doped TiO_2 anatase: a ferromagnetic insulator**
  T. Droubay, S. M. Heald, V. Shutthanandan, S. Thevuthasan, S. A. Chambers, J. Osterwalder,
  J. Appl. Phys. 97, 046103-1-3 (2005).

- **h-BN on Pd(110): a tunable system for self-assembled nanostructures?**
  M. Corso, T. Greber, J. Osterwalder, Surf. Sci. 577, L78-L84 (2005).

- **Rocking motion induced charging of C_{60} on h-BN/Ni(111)**
  M. Muntwiler, W. Auwärter, A. P. Seitsonen, J. Osterwalder, T. Greber, Phys. Rev. B 71, 121402(R)-1-4 (2005).

Articles in press

- **Growth of Cr-doped TiO_2 films in the rutile and anatase structure by oxygen-plasma assisted molecular beam epitaxy**
  J. Osterwalder, T. Droubay, T. Kaspar, J. Williams, C. M. Wang, S. A. Chambers, Thin Solid Films, (2005).

Diploma and PhD theses

- **Hexagonal boron nitride on Pd(111): nanomesh or Moiré pattern ?**
  Martin Morscher, Diploma Thesis, Physik-Departement, ETH Zürich, 2005.

Contributed conference presentations

- **Ultraschnellen Prozessen auf der Spur: Physik auf der Skala von Nanometern und Pikosekunden (Poster)**
  M. Hengsberger, Symposium zum Forschungskredit, Universität Zürich, 26.3.04.
- **Hexagonal boron nitride on metals: how does it grow? (Poster)**
  T. Greber, Lorentz Center Workshop on Collective Phenomena, Leiden, The Netherlands, 17.6.04.
- **How steps affect the Shockley surface state on vicinal Cu(111) - and vice versa**
  T. Greber, Lorentz Workshop on Collective Phenomena, Leiden, The Netherlands, 21.6.04.
- **Bilayer nanomesh of h-BN on Rh(111) (Poster)**
  M. Corso, Nanospectra Summer School, Porquerolles, France, 20.-30.6.04.
- **Bilayer nanomesh of h-BN on Rh(111) (Poster)**
  M. Corso, 16th International Vacuum Congress, Venice, Italy, 1.7.04.
- **One-dimensional C_{60} chains: molecular arrangement and electronic properties**
  A. Tamai, 16th International Vacuum Congress, Venice, Italy, 2.7.04.
- **Spin-polarized surface states on Ni(111)**
  J. Lobo-Checa, SLS Users Meeting, PSI, 5.10.04.
- **Electronic structure of C_{60} molecular chains on a stepped Cu surface**
  A. Tamai, SLS Users Meeting, PSI, 5.10.04.
- **Time-resolved low-energy electron diffraction from large molecules on surfaces**
  C. Cirelli, DPG 69th Annual Meeting, Berlin, 4.3.05.
- **Observing enantio-selective absorption: D and L cysteine on Au(17 11 9)**
  R. Schillinger, DPG 69th Annual Meeting, Berlin, 7.3.05.
- **Chiral heterorecognition: cysteine on Au(17 11 9)**
  T. Greber, Symposium on Surface Science (3S), Les Arcs, France, 15.3.05.

Invited lectures

- M. Muntwiler: **Metal-insulator-metal interfaces based on hexagonal boron nidride on Ni(111)**
  X.-Y. Zhu Group Seminar, Department of Chemistry, University of Minnesota, Minneapolis, USA, 29.3.04.
- J. Osterwalder: **Valence band photoemission**
  6 hours of lectures, ICTP School on Synchrotron Radiation, International Center of Theoretical Physics, Trieste, Italy, 3.-7.5.04.
- J. Osterwalder: **C_{60} monolayers on nanostructured surfaces**
  Colloquium, Université de Neuchâtel, 24.5.04.
- M. Hengsberger: **Tracking ultrafast dynamics in solid surfaces: electron diffraction**
  Seminar, Physikalisch-Chemisches Institut der Universität Zürich, 27.5.04.
- J. Osterwalder: **Organizing C_{60} molecules on 1D and 2D nanotemplates**
  16th International Vacuum Congress, Venice, Italy, 1.7.04.

- J. Osterwalder: **Probing electrons confined to nanometer dimensions**
  SLS Users Meeting, PSI, 4.10.04.

- T. Greber: **Elektronen an Grenzflächen: Wie sie sich und Atome bewegen**
  Kolloquium, Université de Fribourg, 7.10.04.

- J. Osterwalder: **Spin-polarized photoemission**
  2 hours of lecture, School on Magnetism and Synchrotron Radiation, Mittelwihr, France, 12.10.04.

- T. Greber: **Hexagonal boron nitride on metals: a baseplate for molecular electronics**
  Hutter Group Seminar, Physikalisch-Chemisches Institut der Universität Zürich, 20.10.04.

- T. Greber: **Observing molecules with photoelectron waves: from forward scattering to near node photoelectron holography**
  Kolloquium, Max-Planck Institut für Festkörperforschung und Universität Stuttgart, 16.11.04.

- T. Greber: **Nanomesh: a new boron nitride allotrope with small holes**
  Seminar, EPF Lausanne, 9.3.05.

16.6 Research group of Prof. A. Schilling

Articles

- **Fluctuations and dark count rates in superconducting NbN single-photon detectors**
  A. Engel, A. Semenov, H.-W. Hübers, K. Il'in, and M. Siegel, phys. stat. sol. (c) 2, (2005) 1668.

- **Critical current of Nb and NbN thin-film structures: The cross-section dependence**
  K. Il'in, M. Siegel, A. Semenov, A. Engel, and H.-W. Hübers, phys. stat. sol. (c) 2, (2005) 1680.

- **Anisotropic field dependence of the magnetic transition in Cu2Te2O5Br2**
  A.V. Sologubenko, R. Dell'Amore, H.R. Ott, and P. Millet, Eur. Phys. J. B 42, (2004) 549.

- **Vortices in low-T_c layered Ta_xGe_{1-x}/Ge superconductors**
  A. Engel and B. J. Ruck, in *Frontiers in Superconductivity Research*, B. P. Martins, ed., Nova Science Publ. Inc. (2004) 199.

Talk

- A. Engel: **Energy Resolution of a Superconducting Quantum Detector**
  SPIE Europe International Symposium Astronomical Telescopes, Glasgow, Scotland, United Kingdom, 21.-25.6.2004.

Conference Contributions

- **Fluctuations and dark count rates in superconducting NbN single-photon detectors**
  A. Engel, poster, E-MRS 2004 Fall meeting, Warsaw, Poland, 6.-10.9.2004.

16.7 Research group of Prof. U. Straumann[6]

Articles

- **An apparatus for the investigatiuon of solid D_2 with respect to ultra-cold neutron sources**
  K. Bodek, B. van den Brandt. T. Brys, M. Daum, P. Fierlinger, P. Geltenbort, M. Giersch, P. Hautle, R. Henneck, M. Kasprzak, K. Kirch, J. A. Konter, G. Kuehne, M. Kuzniak, A. Pichlmaier, D. Raetz, A. Serebrov, J. Zmeskal, Nucl.Instr.Meth.A533, 491 (2004).

- **Search for Supersymmetry with Gauge-Mediated Breaking in Diphoton Events at DØ**
  V. M. Abazov *et al.* (DØ Collaboration),
  Phys. Rev. Lett. **94**, 041801 (2004); hep-ex/0408146; FERMILAB-Pub-04/198-E.

- **Search for New Particles in the Two-Jet Decay Channel with the DØ Detector**
  V. M. Abazov *et al.* (DØ Collaboration),
  Phys. Rev. D Rapid Comm. **69**, 111101 (2004); hep-ex/03080 33.

- **Improved Measurement of the Top Quark Mass**
  V. M. Abazov *et al.* (DØ Collaboration),
  Nature **429**, 638 (2004); hep-ex/0406031, FERMILAB-Pub-0 4/083-E.

- **Observation and Properties of the $X(3872)$ decaying to $J/\psi\pi^+\pi^-$ in $p\bar{p}$ collisions at $\sqrt{s} = 1.96$ TeV**
  V. M. Abazov *et al.* (DØ Collaboration),
  Phys.Rev.Lett.**93**, 162004 (2004); hep-ex/0405004, Fermilab-Pub-04/061-E.

- **Search for Pair Production of Light Scalar Top Quarks in $p\bar{p}$ Collisions at $\sqrt{s} = 1.8$ TeV**
  V. M. Abazov *et al.* (DØ Collaboration), Phys.Rev.Lett.**93**, 011801, (2004); hep-ex/0308033.

- **Search for Doubly-charged Higgs Boson Production in the Decay $H^{++}H^{--} \to \mu^+\mu^+\mu^-\mu^-$ with the DØ Detector at $\sqrt{s} = 1.96$ TeV**
  V. M. Abazov *et al.* (DØ Collaboration),
  Phys.Rev.Lett.**93**, 141801 (2004); hep-ex/040415; FERMILAB-PUB-04/045-E.

- **Search for 3- and 4-Body Decays of the Scalar Top Quark in Proton Anti-Proton Collisions at $\sqrt{s} = 1.8$ TeV**
  V. M. Abazov *et al.* (DØ Collaboration), Phys. Lett. B **581** (2004) 147-155.

- **Combination of CDF and DØ results on W boson mass and width**
  V. M. Abazov *et al.* (DØ Collaboration), Phys. Rev. D **70**, 092008 (2004);
  hep-ex/0311039v2.

- **Search for Narrow $t\bar{t}$ Resonances in $p\bar{p}$ Collisions at $\sqrt{s} = 1800$ GeV**
  V. M. Abazov *et al.* (DØ Collaboration),
  Phys.Rev.Lett.**92**, 221801 (2004); hep-ex/0307079; FERMILAB-Pub-03-225.

[6] for H1 publications see Sec. 16.8

- **Measurement of the B_s^0 lifetime in the exclusive decay channel $B_s^0 \to J/\psi\Phi$**
  V. M. Abazov *et al.* (DØ Collaboration),
  Phys.Rev.Lett.**94**, 042001 (2005); hep-ex/0409043; FERMILAB-Pub-04-225-E.
- **Measurement of the WW Production Cross Section in $p\bar{p}$ Collisions at $\sqrt{s} = 1.96$ TeV**
  V. M. Abazov *et al.* (DØ Collaboration),
  Phys.Rev.Lett.**94**, 15180 (2005); hep-ex/0410066; FERMILAB-Pub-04-293-E.
- **Search for the Flavor-Changing Neutral Current Decay $B_s^0 \to \mu^+\mu^-$ in $p\bar{p}$ collisions at $\sqrt{s} = 1.96$ TeV with the DØ Detector**
  V. M. Abazov *et al.* (DØ Collaboration),
  Phys.Rev.Lett.**94**, 071802 (2005); hep-ex/0410039; FERMILAB-Pub-04-215-E.
- **Search for $Wb\bar{b}$ and WH Production in $p\bar{p}$ Collisions at $\sqrt{s} = 1.96$ TeV**
  V. M. Abazov *et al.* (DØ Collaboration),
  Phys.Rev.Lett.**94**, 091802 (2005), hep-ex/0410062, FERMILAB-Pub-04-288-E.
- **Measurement of $\sigma(p\overline{p} \to Z)\mathrm{Br}(Z \to \tau\tau)$ at $\sqrt{s} = 1.96$ TeV**
  V. M. Abazov *et al.* (DØ Collaboration),
  Phys.Rev.D **71**, 072004 (2005), hep-ex/0412020, FERMILAB-Pub-04-381-E.
- **Measurement of the Top Quark Mass In All-Jet Events**
  V. M. Abazov *et al.* (DØ Collaboration),
  Phys.Lett.B B606 (2005) 25-33, hep-ex/0410086, FERMILAB-Pub-04-305-E.
- **Investigation on Radiation Damage on Silicon Detectors for the DØ Run IIb upgrade**
  F. Lehner, Nucl.Instr.Meth.A 5300 (2004) 105.
- **Measurement of the Λ_b Lifetime in the Decay $\Lambda_b \to J/\psi\Lambda$ with the DØ Detector**
  V. M. Abazov *et al.* (DØ Collaboration),
  Phys.Rev.Lett.**94**, 102001 (2005); hep-ex/0410054; FERMILAB-Pub-04-286-E.
- **A search for anomalous heavy-flavor quark production in association with W bosons**
  V. M. Abazov *et al.* (DØ Collaboration),
  Phys.Rev.Lett.**94**, 152002 (2005); hep-ex/0411084; FERMILAB-Pub-04-359-E.
- **A Measurement of the Ratio of Inclusive Cross Sections $p\bar{p} \to Zb/p\bar{p} \to Zj$ at $\sqrt{s} = 1.96$ TeV**
  V. M. Abazov *et al.* (DØ Collaboration),
  Phys.Rev.Lett.**94**, 161801 (2005); hep-ex/0410078; FERMILAB-Pub-04-297-E.

Articles in print

- **Measurement of the Ratio of B^+ and B^0 Meson Lifetimes**
  V. M. Abazov *et al.* (DØ Collaboration),
  Phys.Rev.Lett.; hep-ex/0410052; FERMILAB-Pub-04-284-E.
- **Measurement of Dijet Azimuthal Decorrelations at Central Rapidities in $p\bar{p}$ Collisions at $\sqrt{s} = 1.96$ TeV**
  V. M. Abazov *et al.* (DØ Collaboration),
  Phys.Rev.Lett.; hep-ex/0409040; FERMILAB-Pub-04/217-E.
- **Helicity of the W Boson in lepton + jets $t\bar{t}$ events**
  V. M. Abazov *et al.* (DØ Collaboration),
  Phys.Rev.Lett.; hep-ex/0404040, FERMILAB-PUB-04-057-E.

PhD theses

- **The new CIP2k z-Vertex Trigger for the H1 Experiment at HERA**
  Max Christoph Urban, PhD Thesis, Physik-Insitut, Universität Zürich, 2004.

- **A Measurement of the QED-Compton Cross-Section in Electron-Proton Scattering with the H1 Experiment at HERA**
  Nicolas Keller, PhD Thesis, Physik-Insitut, Universität Zürich, 2004.

- **Measurement of the Charged Current Cross Section in Positron-Proton Collisions at HERA**
  Nicole Werner, PhD Thesis, Physik-Insitut, Universität Zürich,2004.

Conference reports

- Frank Lehner: **New Results from B Physics and Observation of the $X(3872)$ state at DØ**
  XII. International Workshop on Deep Inelastic Scattering, April 14-18, 2004, Strbske Pleso, Slovakia.

- Ralf Bernhard: **Search for rare B decays at the Tevatron**
  DPF 2004, UC Riverside, California, USA, Aug. 26 - 31, 2004. Proceedings submitted to Int. J. Mod. Phys. A, hep-ex/0411020.

- Ralf Bernhard: **Search for the rare decay $B_s \to \mu\mu$ with the DØ detector at the Tevatron**
  poster session, XXXII SLAC Summer Institute, Aug. 2 - 13, 2004.

- Ralf Bernhard: **Search for flavor-violating decay $B_s \to \mu\mu$**
  APS Spring Meeting, Denver, May 1-4, 2004.

- Ralf Bernhard: **Sensitivity analysis of the rare decay $B_s \to \mu\mu$ with the DØ detector**
  2004 PHENOMENOLOGY SYMPOSIUM, University of Wisconsin-Madison, April 26-28, 2004.

- Dima Volyanskyy: **A search for the Bs->J/psi eta' decay at LHCb**
  KINR Open Annual Conference, Kiev (Ukraine), January 26-30th 2004.

- DØ Collaboration: **Search for the Flavor-Changing Neutral Current Decay $B_s \to \mu\mu$ in pp collisions at $\sqrt{s}$ = 1.96 TeV with the DØ Detector**
  DØ conference note 4514, 2. August 2004
  http://www-d0.fnal.gov/Run2Physics/WWW/results/B/B06/B06.pdf

- Linus Lindfeld: **Physics with tau leptons at HERA**
  TAU'04 International Workshop on Tau Lepton Physics, Nara, Japan, 17 September, 2004. Proceedings submitted to Nuclear Physics B - Proceedings Supplements

- Peter Fierlinger: **Storage of Ultracold Neutrons**
  SPS Meeting 03.-04.03.2004, Neuchatel.

- Peter Fierlinger: **Geant4 Simulations for Ultracold Neutrons**
  Frühjahrstagung der Deutschen Physikalischen Gesellschaft, 08.-12.3.2004, Köln.

- Peter Fierlinger: **Geant4 Simulations for Ultracold Neutrons**
  International Conference on Precision Measurements with Slow Neutrons, NIST Gaithersburg, 05.-07.04.2004.

- Peter Fierlinger: **A New Experiment to Measure the Depolarization and Loss Probability of UCN on Diamond Like Carbon**
  International Conference on Precision Measurements with Slow Neutrons, NIST Gaithersburg, 05.-07.04.2004.
- Max Urban: **Design of a z-Vertex Trigger and its Operation Experience in the H1 Experiment at HERA**
  10th Workshop on Electronics for LHC and future Experiments, 13. - 17. September 2004, Boston, USA., Proceedings: CERN-LHCC-2004-030.
- Achim Vollhardt: **LHCb Silicon Tracker electronics: from R&D to Preproduction**
  10th Workshop on Electronics for LHC and future Experiments, 13. - 17. September 2004, Boston, USA., Proceedings: CERN-LHCC-2004-030.
- O.Steinkamp: **Silicon Strip Detectors for the LHCb Experiment**
  5th International Symposium on the Development and Application of Semiconductor Tracking Detectors, Hiroshima, June 14-17, 2004.

Collaboration notes

- **Update on the upper limit for the rare decay $B_s^0 \to \mu^+\mu^+$ with the DØ detector**
  R. Bernhard and F. Lehner, DØnote 4696, January 2005.
- **Sensitivity Analysis of the rare decay $B_s^0 \to \mu^+\mu^-\phi$ with the DØ detector**
  R. Bernhard and F. Lehner, DØnote 4695, January 2005.
- **Search for the Flavor-Changing Neutral Curren t Decay $B_s^0 \to \mu^+\mu^-$ in $p\bar{p}$ collisions at $\sqrt{s} = 1.96$ TeV w ith the DØ detector**
  R. Bernhard and F. Lehner DØnote 4514, July 2004.
- **Mechanical Characterization of a TT Half-Module Prototype**
  F. Lehner et al., LHCb-2005-070.
- **Laboratory Measurements on Irradiated Prototype Ladders for the LHCb Inner Tracker**
  C. Lois, R. Bernhard, M. Needham, A. Vollhardt, A. Wenger, LHCb-2004-112.
- **Quality Assurance of 100 CMS2-OB2 Sensors**
  G. Baumann et al., LHCb-2004-105.
- **Measurements on irradiated silicon sensor prototypes for the Inner Tracker of LHCb**
  F. Lehner et al., LHCb-2004-104.
- **The LHCb Silicon Tracker**
  H.Voss et al., LHCb-2004-077.
- **Tsa: Fast and Efficient Reconstruction for the Inner Tracker**
  M.Needham, LHCb-2004-075.
- **Expected Particle Fluences and Performance of the LHCb Trigger Tracker**
  M. Siegler et al., LHCb-2004-070.
- **Silicon Strip Detectors for the LHCb Experiment**
  O.Steinkamp, LHCb-2004-054.
- **The LHCb Silicon Tracker Project**
  J.Blouw et al., LHCb-2004-051.

- **Raw Data Format and Readout Partitioning for the Silicon Tracker**
  M.Needham, O.Steinkamp, U.Straumann and A.Vollhardt, LHCb-2004-051.

16.8 H1 Publications by the groups of Straumann and Truöl

Articles

- **Measurement of Dijet Production at Low Q^2 at HERA**
  H1-Collaboration, A. Aktas *et al.*,
  DESY 03 – 206, hep-ex/0401010, Eur.Phys.J.**C37** (2004), 141 - 159.

- **Search for Squark Production in R-Parity Violating Supersymmetry at HERA**
  H1-Collaboration, A. Aktas *et al.*,
  DESY 04 – 025, hep-ex/0403027, Eur.Phys.J.**C36** (2004), 425 - 440.

- **Measurement of Anti-Deuteron Photoproduction and a Search for Heavy Stable Charged Particles at HERA**
  H1-Collaboration, A. Aktas *et al.*,
  DESY 04 – 032, hep-ex/0403056, Eur.Phys.J.**C36** (2004), 413 - 423.

- **Forward π^0 Production and Associated Transverse Energy Flow in Deep-Inelastic Scattering at HERA**
  H1-Collaboration, A. Aktas *et al.*,
  DESY 04 – 051, hep-ex/0404009, Eur.Phys.J.**C36** (2004), 441 - 452.

- **Search for Bosonic Stop Decays in R-parity Violating Supersymmetry in e^+p Collisions at HERA**
  H1-Collaboration, A. Aktas *et al.*,
  DESY 04 – 084, hep-ex/0405070, Phys.Lett.**B599** (2004), 159 - 172.

- **Measurement of the Proton Structure Function F_2 at low Q^2 in QED Compton Scattering at HERA**
  H1-Collaboration, A. Aktas *et al.*,
  DESY 04 – 083, hep-ex/0406029, Phys.Lett.**B598** (2004), 159 - 171.

- **A General Search for New Phenomena in ep Scattering at HERA**
  H1-Collaboration, A. Aktas *et al.*,
  DESY 04 – 140, hep-ex/0408044, Phys.Lett.**B602** (2004), 14 - 30.

- **Measurement of Prompt Photon Cross Sections in Photoproduction at HERA**
  H1-Collaboration, A. Aktas *et al.*,
  DESY 04 – 118, hep-ex/0407018, Eur.Phys.J.**C38** (2005), 437 - 445.

- **Inclusive Production of D^+, D^0, D_s^+ and D^{*+} Mesons in Deep Inelastic Scattering at HERA**
  H1-Collaboration, A. Aktas *et al.*,
  DESY 04 – 156, hep-ex/0408149, Eur.Phys.J.**C38** (2005), 447 - 459.

Articles in print

- **Measurement of $F_2^{c\bar{c}}$ and $F_2^{b\bar{b}}$ at High Q^2 using the H1 Vertex Detector at HERA**
  H1-Collaboration, A. Aktas *et al.*, DESY 04 – 209, hep-ex/0411046, Eur.Phys.J.**C** (2005).

- **Search for Light Gravitinos in Events with Photons and Missing Transverse Momentum at HERA**
  H1-Collaboration, A. Aktas *et al.*, DESY 04 – 227, hep-ex/0501030, Phys.Lett.**B** (2005).

- **A Direct Search for Magnetic Monopoles Produced in Positron-Proton Collisions at HERA**
  H1-Collaboration, A. Aktas *et al.*, DESY 04 – 240, hep-ex/0501039, Eur.Phys.J.**C** (2005).

- **Measurement of Dijet Cross Sections for Events with a Leading Neutron in ep Interactions at HERA**
  H1-Collaboration, A. Aktas *et al.*, DESY 04 – 247, hep-ex/0501074, Eur.Phys.J.**C** (2005).

H1-collaboration

A. Aktas, V. Andreev, T. Anthonis, S. Aplin, A. Asmone, A. Astvatsatourov, A. Babaev, S. Backovic, J. Bähr, A. Baghdasaryan, P. Baranov, E. Barrelet, W. Bartel, S. Baudrand, S. Baumgartner, J. Becker, M. Beckingham, O. Behnke, O. Behrendt, A. Belousov, Ch. Berger, N. Berger, J.C. Bizot, M.-O. Boenig, V. Boudry, J. Bracinik, G. Brandt, V. Brisson, D.P. Brown, D. Bruncko, F.W. Büsser, A. Bunyatyan, G. Buschhorn, L. Bystritskaya, A.J. Campbell, S. Caron, F. Cassol-Brunner, K. Cerny, V. Chekelian, J.G. Contreras, J.A. Coughlan, B.E. Cox, G. Cozzika, J. Cvach, J.B. Dainton, W.D. Dau, K. Daum, B. Delcourt, R. Demirchyan, A. De Roeck, K. Desch, E.A. De Wolf, C. Diaconu, V. Dodonov, A. Dubak, G. Eckerlin, V. Efremenko, S. Egli, R. Eichler, F. Eisele, M. Ellerbrock, E. Elsen, W. Erdmann, S. Essenov, P.J.W. Faulkner, L. Favart, A. Fedotov, R. Felst, J. Ferencei, L. Finke, M. Fleischer, P. Fleischmann, Y.H. Fleming, G. Flucke, A. Fomenko, I. Foresti, G. Franke, T. Frisson, E. Gabathuler, E. Garutti, J. Gayler, C. Gerlich, S. Ghazaryan, S. Ginzburgskaya, A. Glazov, I. Glushkov, L. Goerlich, M. Goettlich, N. Gogitidze, S. Gorbounov, C. Goyon, C. Grab, T. Greenshaw, M. Gregori, G. Grindhammer, C. Gwilliam, D. Haidt, L. Hajduk, J. Haller, M. Hansson, G. Heinzelmann, R.C.W. Henderson, H. Henschel, O. Henshaw, G. Herrera, M. Hildebrandt, K.H. Hiller, D. Hoffmann, R. Horisberger, A. Hovhannisyan, M. Ibbotson, M. Ismail, M. Jacquet, L. Janauschek, X. Janssen, V. Jemanov, L. Jönsson, D.P. Johnson, H. Jung, M. Kapichine, J. Katzy, N. Keller, I.R. Kenyon, C. Kiesling, M. Klein, C. Kleinwort, T. Klimkovich, T. Kluge, G. Knies, A. Knutsson, V. Korbel, P. Kostka, R. Koutouev, K. Krastev, J. Kretzschmar, A. Kropivnitskaya, K. Krüger, J. Kückens, M.P.J. Landon, W. Lange, T. Laštovička, G. Laštovička-Medin, P. Laycock, A. Lebedev, B. Leißner, V. Lendermann, S. Levonian, L. Lindfeld, K. Lipka, B. List, E. Lobodzinska, N. Loktionova, R. Lopez-Fernandez, V. Lubimov, H. Lueders, D. Lüke, T. Lux, L. Lytkin, A. Makankine, N. Malden, E. Malinovski, S. Mangano, P. Marage, R. Marshall, M. Martisikova, H.-U. Martyn, S.J. Maxfield, D. Meer, A. Mehta, K. Meier, A.B. Meyer, H. Meyer, J. Meyer, S. Mikocki, I. Milcewicz-Mika, D. Milstead, A. Mohamed, F. Moreau, A. Morozov, J.V. Morris, M.U. Mozer, K. Müller, P. Murín, K. Nankov, B. Naroska, Th. Naumann, P.R. Newman, C. Niebuhr, A. Nikiforov, D. Nikitin, G. Nowak, M. Nozicka, R. Oganezov, B. Olivier, J.E. Olsson, D. Ozerov, V. Palichik, C. Pascaud, I. Panagoulias, T. Papadopolou, G.D. Patel, M. Peez, E. Perez, D. Perez-Astudillo, A. Perieanu, A. Petrukhin, D. Pitzl, R. Plačakytė, B. Portheault, B. Povh, P. Prideaux, N. Raicevic, P. Reimer, B. Reisert, A. Rimmer, C. Risler, E. Rizvi, P. Robmann, B. Roland, R. Roosen, A. Rostovtsev, Z. Rurikova, S. Rusakov, F. Salvaire, D.P.C. Sankey, E. Sauvan, S. Schätzel, F.-P. Schilling, S. Schmidt, S. Schmitt, C. Schmitz, L. Schoeffel, A. Schöning, V. Schröder, H.-C. Schultz-Coulon, K. Sedlák, F. Sefkow, I. Sheviakov, L.N. Shtarkov, Y. Sirois, T. Sloan, P. Smirnov, Y. Soloviev, D. South, V. Spaskov, A. Specka, B. Stella, J. Stiewe, I. Strauch, U. Straumann, V. Tchoulakov, G. Thompson, P.D. Thompson, F. Tomasz, D. Traynor, P. Truöl, I. Tsakov, G. Tsipolitis, I. Tsurin, J. Turnau, E. Tzamariudaki, M. Urban, A. Usik, D. Utkin, S. Valkár, A. Valkárová, C. Vallée, P. Van Mechelen, N. Van Remortel, A. Vargas Trevino, Y. Vazdik, C. Veelken, A. Vest, S. Vinokurova, V. Volchinski, B. Vujicic, K. Wacker,

J. Wagner, G. Weber, R. Weber, D. Wegener, C. Werner, N. Werner, M. Wessels, B. Wessling, C. Wigmore, Ch. Wissing, R. Wolf, E. Wünsch, S. Xella, W. Yan, V. Yeganov, J. Žáček, J. Zálešák, Z. Zhang, A. Zhelezov, A. Zhokin, J. Zimmermann, H. Zohrabyan, and F. Zomer

16.9 Research group of Prof. P. Truöl [7]

Articles

- **Limits for the Central Production of θ^+ and Ξ^{--} Pentaquarks in 920-GeV pA Collisions**
  HERA-B Collaboration, I. Abt *et al.*,
  DESY-04-148, hep-ex/0408048, Phys.Rev.Lett.**93** (2004), 212003 - 212007.
- **Search for the Flavor Changing Neutral Current Decay $D^0 \to \mu^+\mu^-$ with the HERA-B Detector**
  HERA-B Collaboration, I. Abt *et al.*,
  DESY-04-086, hep-ex/0405059, Phys.Lett.**B596** (2004), 173-183.
- **Physics with Low-Energy Muons at a Neutrino Factory Complex**
  J. Aysto, A. Baldini, A. Blondel, A. de Gouvea, J. Ellis, W. Fetscher, G.F. Giudice, K. Jungmann, S. Lola, V. Palladino, K. Tobe, A. Vacchi, A. van der Schaaf, K. Zuber, (Stopped Muons Working Group) in: *ECFA/CERN Studies of a European Neutrino Factory Complex*, A. Blondel *et al.* (ed.), CERN-2004-002, ECFA-04-230, Apr 2004, 47pp.

Report

- **ECFA/CERN Studies of a European Neutrino Factory Complex**
  Edited by A. Blondel, G. Buchalla, M. Campanelli, J. Ellis, J.J. Gomez-Cadenas, G. Giudice, P. Gruber, H. Haseroth, P. Hernandez, A. Kataev, S. Kraml, M. Mangano, M. Mezzetto, W.J. Murray, A. van der Schaaf, CERN-2004-002, ECFA-04-230, Apr 2004, 379pp.

PhD Thesis

- **A Multitrack Method for b-Tagging**
  Ilaria Foresti, PhD Thesis, Universität Zürich, 2004.

[7] for H1 publications see Sec.16.8